Study of the optoelectronic properties of atomically thin WSe2

Marco Manca

Université Fédérale
Toulouse Midi-Pyrénées

THÈSE

En vue de l'obtention du

DOCTORAT DE L'UNIVERSITÉ DE TOULOUSE

Délivré par l'Institut National des Sciences Appliquées de Toulouse

---

Présentée et soutenue par

Marco MANCA

Le 18 juin 2019

Study of the optoelectronic properties of atomically thin WSe2

Ecole doctorale : **SDM - SCIENCES DE LA MATIERE - Toulouse**

Spécialité : **Physique**

Unité de recherche :
LPCNO-IRSAMC - Laboratoire de Physique et Chimie des Nano-Objets

Thèse dirigée par
Bernhard URBASZEK et Thierry AMAND

Jury

Mme Jaqueline Bloch, Rapporteure
M. Stéphane Berciaud, Rapporteur
M. Vincent Paillard, Examinateur
M. Clement Faugeras, Examinateur
M. Bernhard URBASZEK, Directeur de thèse
M. Thierry Amand, Co-directeur de thèse

Université Fédérale
Toulouse Midi-Pyrénées

THÈSE

En vue de l'obtention du

DOCTORAT DE L'UNIVERSITÉ DE TOULOUSE

Délivré par l'Institut National des Sciences Appliquées de Toulouse

---

Présentée et soutenue par

Marco MANCA

Le 18 juin 2019

Study of the optoelectronic properties of atomically thin WSe2

Ecole doctorale : **SDM - SCIENCES DE LA MATIERE - Toulouse**

Spécialité : **Physique**

Unité de recherche :
LPCNO-IRSAMC - Laboratoire de Physique et Chimie des Nano-Objets

Thèse dirigée par
Bernhard URBASZEK et Thierry AMAND

Jury

Mme Jaqueline Bloch, Rapporteure
M. Stéphane Berciaud, Rapporteur
M. Vincent Paillard, Examinateur
M. Clement Faugeras, Examinateur
M. Bernhard URBASZEK, Directeur de thèse
M. Thierry Amand, Co-directeur de thèse

Abstract

Transition Metal Dichalcogenides (TMDs) are a family of layered materials with potential applications in optics and electronics. Following the discovery of graphene, a great number of techniques were developed for the study of atomically thin 2D crystals. Using these techniques TMDs were characterized and extraordinary physical properties were discovered: when thinned down to a monolayer, TMDs become direct band gap materials, therefore strongly facilitating light emission. The direct bandgap of these semiconductors is situated on the edge of the Brillouin zone, at the K-point. This is different from standard semiconductors for optoelectronics like GaAs where the bandgap is in the centre of the Brillouin zone. The optical properties are dominated by excitons, Coulomb bound electron-hole pairs, and light-matter interaction is extremely strong with up to 20% of light absorption per monolayer.

In addition to a bandgap, the other main differences between TMD monolayers and the semi-metal graphene are strong spin-orbit coupling and broken inversion symmetry. As a result, the optical transitions across the bandgap have chiral selection rules. Circularly right polarized light addresses transitions in the K^+ valley, whereas circularly left polarized light addresses the K^- valley, where the K^+ and K^- valley are related by time reversal symmetry. The spin states in the valence and conduction bands are well separated in energy by the spin-orbit interaction. This makes it possible to optically address specific spin and valley states in momentum space and monitor their dynamics. As a result monolayer TMDs are exciting model systems for spin and valley physics: these research fields are termed spintronics and valleytronics. This motivated our work on the exact understanding of the optical transitions, their polarization selections rules and the different exciton states. Another strong point of layered materials is the possibility of assembly them in Van der Waals heterostructures producing nano-meter thin materials with novel properties.

In the first chapter we introduce the family of 2D crystals and we explain why they are promising for fundamental science and potential applications in optics and electronics. In particular we will introduce and describe the optoelectronics properties of transition metal dichalcogenides.

In the second chapter we will focus on the experimental techniques used for studying the materials. We describe the sample fabrication techniques based on exfoliation. Details on the confocal microscopy set-ups and the optical spectroscopy techniques will be given.

Chapter 3 focuses on the TMD monolayer material WSe_2. Based on a new fabrication technique using hexagonal boron nitride for encapsulation, the WSe_2 monolayers show sharp optical transitions that can be analysed in detail. Information on optically dark and bright excitons is obtained, as well as mea-

surements on the excited exciton states. Coupling of excitons to phonons is discussed for photoluminescence excitation experiments.

In chapter 4 we will introduce upconversion spectroscopy, an original spectroscopy technique that is based on exciting a low energy transition and detecting emission from a high-energy transition. It is shown that this non-linear optical process is based on a very specific form of exciton-exciton scattering. Upconversion is used to extract detailed information on excited exciton states.

In chapter 5 we will study WSe_2 monolayers in a device that allows us to control the carrier density inside the monolayer through an applied gate voltage. This allows detailed studies of exciton complexes in the p-type, n-type and the intrinsic regimes. The formation of charged excitons is discussed.

In chapter 6 we give an outlook on future work and open questions in optoelectronic properties of atomically thin semiconductors.

Abstract in french

Les dichalcogénures de métaux de transition (TMDs) constituent une famille de matériaux lamellaires riches de potentialités en optique et en électronique. A la suite de la découverte du graphène, un grand nombre de techniques ont été développées pour l'étude de cristaux dits bidimensionnels, matériaux dont l'épaisseur ne dépasse pas quelques plans atomiques. Grâce à ces techniques, la caractérisation des TMDs a permis la découverte de leurs propriétés physiques exceptionnelles : amincis à l'état de mono-feuillets, les TMDs semi-conducteurs deviennent des matériaux à bande interdite directe, donc très efficaces pour l'absorption ou l'émission de lumière. Le gap direct de ces semi-conducteurs est situé aux points K, à la frontière de la zone de Brillouin. Les propriétés optiques sont dominées par les excitons (paires électron-trou liées par l'attraction de Coulomb) et l'interaction lumière-matière y est extrêmement forte, l'absorption d'un faisceau lumineux pouvant atteindre 20% par monocouche.

Outre l'existence du gap, les TMDs se différencient du graphène par leur fort couplage spin-orbite, ainsi que par la rupture de la symétrie d'inversion. En conséquence, les règles de sélection pour les transitions optiques à travers le gap ont un caractère chiral. Les états de spin opposés dans les bandes de valence et de conduction sont significativement clivés en énergie du fait de l'interaction spin-orbite. Cette propriété permet d'exciter optiquement des états de spin et de vallée spécifiques dans l'espace réciproque et de suivre leur comportement dynamique. Ainsi, les TMDs mono-feuillets constituent-ils des systèmes modèles très attractifs pour l'étude de la physique des états de spin et de vallée. Ce fut la motivation principale de notre travail qui a porté sur la compréhension précise des transitions optiques, leurs règles de sélection en polarisation, ainsi que celle des différents états excitoniques.

Dans le premier chapitre, nous présentons la famille des cristaux bidimensionnels (2D) et montrons en quoi ils sont prometteurs tant du point de vue de la physique fondamentale que pour leurs applications potentielles en optique et en électronique. Dans le deuxième chapitre, nous nous focaliserons sur les techniques expérimentales utilisées pour l'étude ces matériaux. Nous y décrirons les techniques de fabrication basées sur l'exfoliation, et décrirons les ensembles expérimentaux de microscopie confocale et de spectroscopie optique utilisés.

Le troisième chapitre est consacré à l'étude du diséléniure de tungstène en mono-feuillets (WSe_2). Sur la base d'une nouvelle technique de fabrication utilisant le nitrure de bore hexagonal (hBN) pour encapsuler le feuillet, nous avons pu analyser en détail des monocouches de WSe_2 qui présentent alors des transitions optiques caractérisées par des raies spectrales étroites. Nous avons ainsi obtenu des informations sur les états d'excitons "noirs" et "brillants", et avons pu effectuer des mesures sur les états excitoniques excités.

Dans le quatrième chapitre nous présentons la spectroscopie de conversion des photons, technique originale basée sur l'excitation d'une transition située à basse énergie et la détection de l'émission à haute énergie qui en résulte. Nous montrons que ce processus d'optique non-linéaire repose sur la forme spécifique de l'interaction mutuelle entre excitons.

Dans le chapitre 5, nous étudions des monocouches de WSe_2 insérées dans un dispositif permettant de contrôler la densité des porteurs qui y résident en appliquant une tension sur une grille. Ceci permet l'étude détaillée de l'apparition des divers complexes excitoniques chargés dans les régimes dopés de type n, p ou intrinsèque.

Enfin dans le chapitre 6, nous présentons quelques perspectives pour les études futures et les questions ouvertes concernant les propriétés optoélectroniques des semi-conducteurs bidimensionnels.

Contents

Chapter 1

Brief introduction to transition metal dichalcogenides

"There's plenty of room at the bottom"

This very famous quote by Richard Feynman, the title of one of his equally famous lessons [1], has stimulated many developments in the field of nanotechnology. However, it was only after 20 years that this field really start to take off, producing papers, results and quoting Feynman's lesson as a motivation to proceed [2, 3, 4, 5].

In this lesson, Feynman explored the possibility of manipulating the atoms directly, building nanoscale machines, improving the concept and the design of microscopes to observe smaller and smaller objects, creating much denser computer circuitry and using particle beams to define 2D patterns [1].

More in general, the idea behind the phrase was that many phenomena were still to be understood about the properties of matter when the size starts to decrease and reach the nanoscale. In particular, plenty of quantum mechanical effects completely change how a material or its fundamental components behave.

The tendency of reducing the size of a system has given the start and made the fortune of the computer industry. From machines as big as a room with no margin of profit, we end up having devices in our pocket that are orders of magnitude more powerful than the computer which brought the mankind to the moon. This was made possible by merely reducing the size of the transistors, the fundamental components of computers [6]. in contrast, very little has been done to change the logic or the working principles which are at the base of computation.

Similarly, pushed by the possibility of exploring new fascinating phenomena, the scientific community also moved in the direction of reduced dimensionality. Semiconductors in which one dimension becomes comparable with the size of the wavefunction of the electron were created and they were referred to as quantum wells. In these systems the electrons can move freely in 2 dimensions whereas movement in the other direction is quantized. This effect is called quantum confinement. Subsequently, the reduction of the size was extended to

two dimensions, in systems called quantum wires and to all the three (quantum dots). These system started to be called 2D, 1D and 0D materials respectively, as the electron inside them can only propagate in two dimensions, just in one, or can't propagate at all.

Let's focus on the quantum wells. These systems have always been made sandwiching a semiconductor with a small band-gap in between two layers (called barriers) of another semiconductor whose bandgap is larger. In other words the valence band maximum (conduction band minimum) of the first semiconductor is at higher (lower) energy than the valence band maximum (conduction band minimum) of the other semiconductor. This band alignment is called type I.

Historically, the most studied quantum wells were GaAs layers sandwiched between AlGaAs barriers. Manipulating the light-matter interaction in these III-V nanostructures has an important impact in our everyday life as we use for example quantum well lasers for fiber based telecomunication networks (internet, telephones). The quantum wells are grown using epitaxy [7]. However, because of intermaterial mixing and imperfection in the surfaces the thickness of the GaAs layer could not be arbitrarily reduced: the size never reached the ultimate 2D limit, which means a single atom thick well. This has recently been achieved in a completely different class of materials that will be investigated in this thesis.

Layered crystals are a group of materials which are formed by a series of atomic planes stacked one on top of the other. Precisely speaking the single plane doesn't need to be one atom thick but rather a single unit cell thick. Strong covalent bonds between the atoms keep the single plane together while the force which is responsible for the interplane cohesion is the attractive van der Waals force. In principle it is thus possible to separate a single layer of the crystal from the rest of the bulk and obtain a true two-dimensional sheet: the perfect quantum well.

The study of few layer crystals and even single monolayers actually dates back several decades [8, 9, 10, 11], but it was just with the isolation of a single layer of graphite, graphene [12, 13, 14], that the research on 2D and few layer crystals evolved in a very active field with more than ten thousands papers published every year [15].

After the Novoselov paper in 2004 [12], many techniques for producing, characterizing, and manipulating atomically thin flakes were developed, which in turn led to a fast growth of the field. This great interest was a consequence of the compelling properties that the graphene exhibited. Graphene is a semimetal in which the electrons act as masless Dirac fermions [16, 14] and which is extremely electrically [17] and thermally conductive [18]. Moreover, it is impermeable to molecules [19], it is very elastic and it is mechanically strong [20].

Following these facts the community started to investigate different layered materials hoping that other extraordinary properties could be found in different monolayers. It was discovered that many of them could actually be exfoliated down to the single layer limit and that the monolayers were stable under ambient conditions. It was possible to find metals like VS_2 [21], semiconductors like MoS_2 [13], insulators such as hexagonal BN [22], superconductors ($NbSe_2$) [23], ferroelectrics like In_2Se_3 [24] and ferromagnets like CrI_3 [25].

The possible applications of these new ultra-thin materials are manyfold, especially when one thinks to combine them into van der Waals heterostructures [15]. These are artificially built materials obtained by stacking different

monolayers one on top of the other in a designed order, as shown in Fig. (1.1).

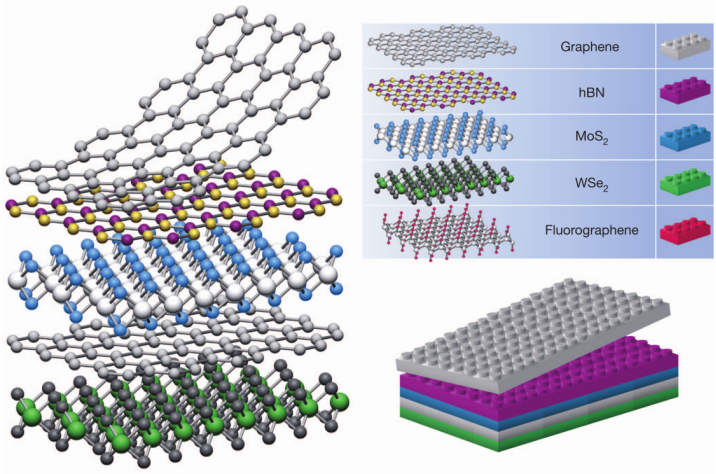

Figure 1.1: The figure, reprinted from reference [15], shows in a very effective way how single layer crystals can be combined for building a van der Waals heterostructure.

Among all the 2D crystals the family which is of particular interest for us is the one of transition metal dichalcogenides. The aforementioned MoS_2 is part of it. In the following we will introduce the main properties of a sub-class of this family and later, in the central chapters of this manuscript we will discuss mainly one of its members: tungsten diselenide WSe_2.

1.1 Transition metal dichalcogenides

Transition metal dichalcogenides (TMDs) are a family of about 60 crystals, the majority of which has a layered structure [9]. In particular, the group which attracts considerable attention is the group VI of semiconducting dichalcogenides with chemical formula MX_2 where M stands for metal (molibdenum or tungsten) and X represent a chalcogen (sulphur, selenium or tellurium). The crystal structure of these materials is shown in panel (a) of Fig. (1.2). From now on we will refer to this sub-group simply as TMDs.

These materials, when thinned down to the monolayer limit, are stable enough in ambient conditions to perform optical and electrical characterization. Already in 2005, Novoselov et al. [13] showed that it was possible to isolate a single layer of MoS_2, which was classified as a semiconductor.

But it was only five years after, with the simultaneous work of Splendiani [27] and Mak [28] that this specific TMD really started to attract the interest of the scientific community. Indeed, the two groups discovered that a MoS_2 monolayer is a direct band gap semiconductor, which gives rise to an optical transition in the visible part of the spectrum. This is interesting because in the bulk form, and even considering a bilayer, the material is an indirect bandgap semiconductor, as shown in panel (b) of Fig. (1.2). This switch between indirect to direct bandgap strongly enhances the light-matter interaction of the material and in particular leads to an increase of its luminescence efficiency. In

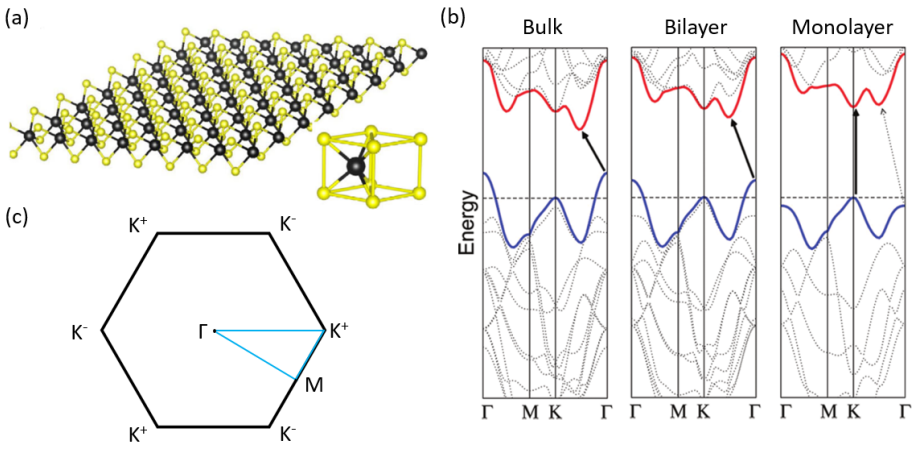

Figure 1.2: (a) 3D model of the crystal structure of a TMD monolayer and corresponding unit cell. Yellow spheres represents a chalcogen atom while the black ones represent the metal. The picture was taken from reference [26] (b) Calculated bandstructure of bulk, bilayer and monolayer MoS_2. The three panels show that the semiconductor undergoes a transition from indirect to direct band-gap. The figure was taken from reference [27]. (c) Sketch of the hexagonal brillouin zone where the main points are indicated. The light blue lines mark the directions along which the bandstructure in panel (b) is calculated.

other words, a MoS_2 monolayer exhibit an intense photoluminescence signal, contrarty to bilayer or bulk MoS_2, as shown in Fig. (1.3).

The band extrema in monolayer MoS_2 are interestingly located away from the center of the Brillouin zone, the so-called Γ point. They are instead at the K points, which are indicated in panel (c) of Fig. (1.2). It can be seen that the Brillouin zone of MoS_2 looks similar to the one of graphene. However, instead of the dirac cones exhibited by graphene, a bandgap is present at the K points of MoS_2. As we will see below, in subsection (1.1.2), a second fundamental difference between the two materials is that in the TMD the K points are divided in two non-equivalent groups which are called K^+ and K^- and which are related by time-reversal symmetry.

In bulk MoS_2 the valence band maximum (VBM) is located in Γ while the conduction band minimum (CBM) is located half way between the points Γ and K instead [29, 30]. The electronic states in the center of the Brillouin zone are formed mainly by the p_z orbitals of the chalcogen atom and the d_{z^2} orbitals of the transition metal. On the contrary, the K valley states are very strongly localized in the metal atom plane. The valence band states are mainly composed of transition metal atom $d_{x^2-y^2} \pm id_{xy}$ states while the conduction band ones by and d_{z^2} states. Both of them are slightly mixed with the chalcogen $p_x \pm ip_y$ orbitals [31, 32, 33]. This can be observed in Fig. (1.4) where the atomic orbital contribution to the conduction and valence band states are shown [33].

The transition between indirect to direct band gap in the monolayer limit happens because the orbitals contributing to the formation of the states in the Γ point and in the Γ−K middlepoint are extending out of the plane and so those of different layers spatially overlap. Thus, the reduction of the number of layer

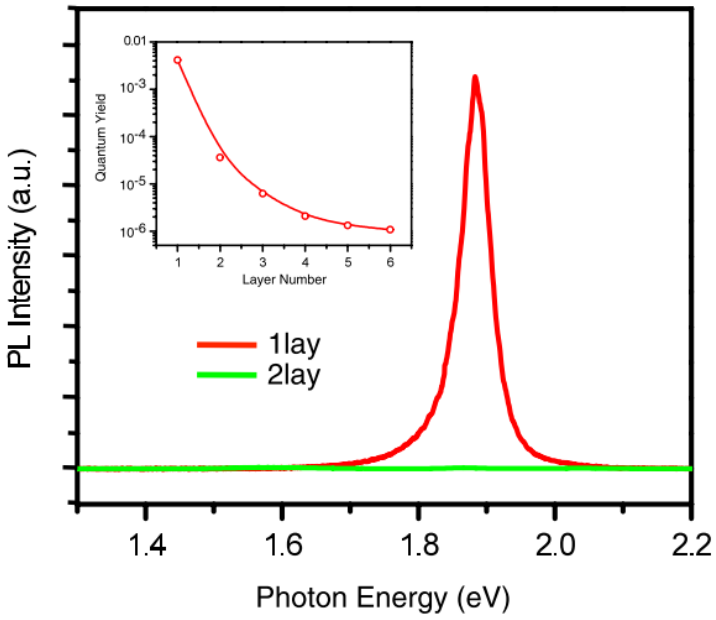

Figure 1.3: The picture shows the PL emission from monolayer (red) and bilayer (green) MoS_2. In the inset the quantum yield as a function of the number of layers is reported in a semi-log scale. The image was taken from reference [28].

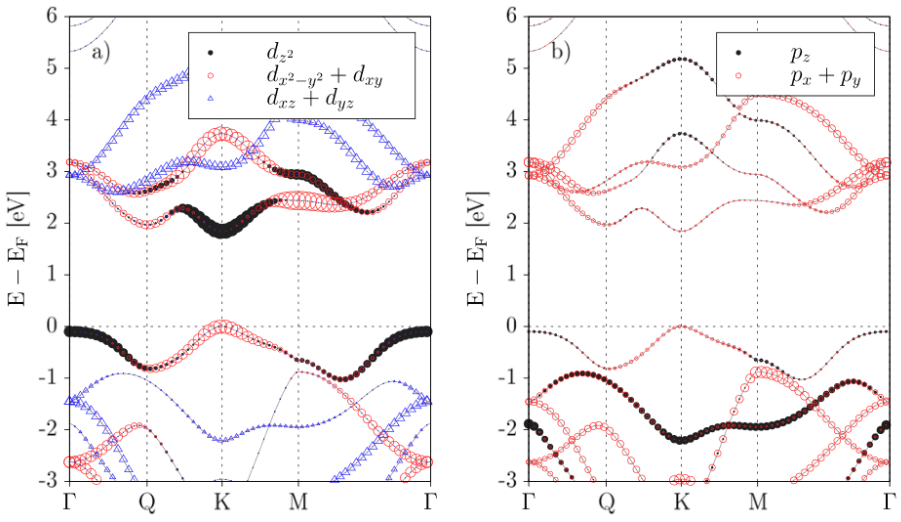

Figure 1.4: The image shows the atomic orbital weights in the energy bands of MX_2 In particular, panel (a) shows the d orbitals of the metal atom, while in panel (b) the p orbitals of the chalcogen atoms are presented. The size of each symbol is proportional to the weight of the atomic orbital. Spin-orbit coupling was neglected in these calculations. The image was taken from reference [33].

increases the energy separation between the two points, while the orbitals of the K points, lying in the metal plane are basically unaffected by the number of layers and their energy separation is constant. Eventually, when only a monolayer remains, the energy of the indirect gap is shifted upwards whereas the direct gap at the K points is now the lowest lying transition.

The shift between indirect to direct bandgap in the monolayer limit was enough to justify further investigations in TMDs. Indeed, the strong light-matter interaction exhibited by the single monolayer (up to 20% in the appropriate spectral region) made researcher dream about atomically thin phototransistors [34], sensors [35], logic circuits [36, 37], LEDs and light harvesting devices [38, 39, 40, 41]. Please note that the other TMDs of the group VI, such as WS_2, $MoSe_2$, WSe_2 and $MoTe_2$, exhibit the same indirect to direct band-gap transition and share with MoS_2 many other properties as we will further discuss. In Fig. (1.5) and in Fig. (1.6) some of the results of the calculation performed by Kormanyos et al. [33] are grouped. In these two tables the band dispersions, the effective masses and the spin orbit splitting of both conduction and valence bands for the six materials are presented.

Most of these important parameters still need to be confirmed experimentally, which motivate the experiments carried out during this thesis.

1.1.1 Excitons

MoS_2 and the other TMDs present very strong excitonic effects because they have a direct band gap and they are atomically thin. Normally, in a semiconductor, an electron can be excited to the conduction band leaving an empty state in a sea of other electrons in the valence band. This many body system can be effectively described introducing the concept of a hole, a quasi particle with a positive charge. The electron and the hole are attracted to each other by the Coulomb interaction. In particular, as the dielectric screening is small in a 2D system, and as a consequence of the quantum confinement, the Coulomb attraction between the electron and the hole is very strong in TMDs and give rise to a bound state called exciton which is schematically depicted in panel (c) of Fig. (1.7).

These quasi-particles were originally discovered in Cu_2O [42] and have been already extensively studied in classical quasi-2D system such as the quantum wells. However, the binding energy between the electron and the hole in TMDs is one to two orders of magnitude larger than in those systems, typically around 500 meV [43, 44, 45, 46, 47]. This makes the excitonic features in the optical spectrum of TMDs dominant, even at room temperature.

The way in which excitons alter the optical spectra can be easily understood thinking about the nature of the quasi-particle. In absence of excitonic effects the absorption by a semiconductor would look like a step-function: no photon is absorbed for energies below the bang-gap but some will be when the energy is larger. Following the excitation, the electron is promoted to the conduction band and is not influenced by the vacant state it left behind. However, if the Coulomb interaction in the material is strong enough to create excitons, it means that there is a state at lower energy, as the electron and the hole are bound. This means that, in absorption, a peak will appear and it will have smaller energy compared to the band-gap value E_g. This energy difference is the exciton binding energy E_B.

	MoS_2	$MoSe_2$	WS_2	WSe_2	$MoTe_2$	WTe_2
$m_{cb}^{(1)}/m_e$ (HSE,LDA)	0.46	0.56	0.26	0.28	0.62	0.26
$m_{cb}^{(1)}/m_e$ (PBE,PBE)	0.47	0.58	0.27	0.29	0.61	0.25
$m_{cb}^{(2)}/m_e$ (HSE,LDA)	0.43	0.49	0.35	0.39	0.53	0.39
$m_{cb}^{(2)}/m_e$ (PBE,PBE)	0.44	0.50	0.36	0.40	0.51	0.38
$C_{3w}^{(1)}$ (eVÅ^3) (HSE,LDA)	−3.36	−3.11	−2.8	−3.02	−3.85	−5.86
$C_{3w}^{(1)}$ (eVÅ^3) (PBE,PBE)	−3.57	−2.94	−1.8	−2.44	−3.95	−17.54
$C_{3w}^{(2)}$ (eVÅ^3) (HSE,LDA)	−3.34	−3.12	−3.14	−3.23	−3.86	−4.90
$C_{3w}^{(2)}$ (eVÅ^3) (PBE,PBE)	−3.49	−2.86	−2.54	−2.97	−4.04	−9.67
$2\Delta_{cb}$ (meV) (HSE,LDA)	3	22	−32	−37	36	−52
$2\Delta_{cb}$ (meV) (PBE,PBE)	3	20	−31	−37	32	−54
n_{cb} (10^{12} cm^{-2}) (HSE,LDA)	0.54	4.5	4.68	6.03	7.97	8.48

Figure 1.5: Band dispersion parameters and spin-splittings at the K^+ and K^- points in the conduction band (CB) from DFT calculations. $m_{cb}^{(1)}$ ($m_{cb}^{(2)}$) is the effective mass of the $K_{cb}^{(1)}$ ($K_{cb}^{(2)}$) band where (1) and (2) indicate the two sub-bands. Similarly, $C_{3w}^{(1)}$ and $C_{3w}^{(2)}$ are the values of the trigonal warping parameters in the two conduction sub-bands. m_e is the free electron mass and $2\Delta_{cb}$ is the spin orbit splitting. n_{cb} is the electron density above which the upper spin-split CB starts to fill. The table was taken from reference [33].

	MoS_2	$MoSe_2$	WS_2	WSe_2	$MoTe_2$	WTe_2
$m_{vb}^{(1)}/m_e$ (HSE,LDA)	−0.54	−0.59 (−0.64)	−0.35	−0.36	−0.66	−0.34
$m_{vb}^{(1)}/m_e$ (PBE,PBE)	−0.54	−0.60 (−0.60)	−0.36	−0.36	−0.62	−0.32
Exp	−0.6±0.08[a]	−0.67±0.4[b]				
$m_{vb}^{(2)}/m_e$ (HSE,LDA)	−0.61	−0.7 (−0.72)	−0.49	−0.54	−0.82	−0.58
$m_{vb}^{(2)}/m_e$ (PBE,PBE)	−0.61	−0.7 (−0.69)	−0.50	−0.54	−0.77	−0.54
Exp	−0.6±0.08[a]	−0.75±0.3[b]				
$C_{3w}^{(1)}$ (eVÅ^3) (HSE,LDA)	6.16	5.67	4.59	6.47	5.44	6.77
$C_{3w}^{(1)}$ (eVÅ^3) (PBE,PBE)	6.08	5.21	6.07	5.79	5.46	17.61
$C_{3w}^{(2)}$ (eVÅ^3) (HSE,LDA)	5.78	5.42	5.50	5.18	5.14	4.83
$C_{3w}^{(2)}$ (eVÅ^3) (PBE,PBE)	5.71	5.064	5.04	4.78	5.09	9.08
$2\Delta_{vb}$ (meV) (HSE,LDA)	148	186	429	466	219	484
$2\Delta_{vb}$ (meV) (PBE,PBE)	148	184	425	462	213	480
Exp (meV)	≈140[c]	≈180[e]	≈400[g],	≈400[g]		
	≈150[d]	≈180[f]	380[h]	≳460[k]		
	160[m]	≈200[m]	410[i]	400[l]		
	140[n]		400[j]	510[m]		
	140[p]		400[l]	∼500[q]		
	138[r]	202[r]	379[r]	404[r]		
			391[t]	412[t]		
				430[x]		

Figure 1.6: Band dispersion parameters and spin-splittings at the K^+ and K^- points in the valence band (VB) from DFT calculations. $m_{vb}^{(1)}$ ($m_{vb}^{(2)}$) is the effective mass of the $K_{vb}^{(1)}$ ($K_{vb}^{(2)}$) band where (1) and (2) indicate the two sub-bands. Similarly, $C_{3w}^{(1)}$ and $C_{3w}^{(2)}$ are the values of the trigonal warping parameters in the two valence sub-bands. m_e is the free electron mass and $2\Delta_{vb}$ is the spin orbit splitting. Some experimental values are also shown. The table was taken from reference [33].

Radiative recombination of excitons is at the origin of the strong PL signal from a TMD monolayer. The photon energy E_{PL} of the emission is at a lower energy compared to the free carrier bandgap as:

$$E_{PL} = E_g - E_B \tag{1.1}$$

This electron-hole pair, bound by Coulomb attraction, has certain similarities to the hydrogen atom and also with positronium. The relative motion of the electron and the hole is characterized by a principal quantum number n. So just as in the case of the hydrogen atom, different orbits are possible, giving rise not only to the lowest lying $n = 1$ state but also to excited states corresponding to $n = 2, 3 \ldots$. Excited exciton states were indeed observed in TMDs monolayers [46, 47]. Their presence can be detected in optical spectroscopy as a series of transitions in between the values of E_{PL} and E_g. These exciton states form a series similar to the Rydberg series of a hydrogen atom, as schematically depicted in panel (a) of Fig. (1.7). The experimental observation of the series performed by Chernikov et al. [46] is instead shown in panel (b).

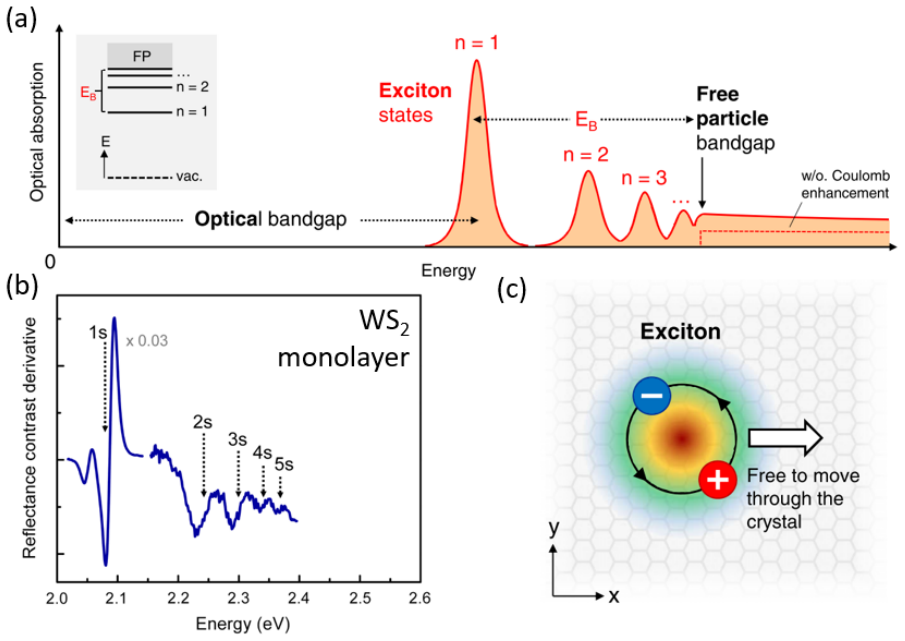

Figure 1.7: (a) Scheme of the optical absorption of an ideal 2D semiconductor including the exciton and its series of excited states at lower energy than the electronic band gap. The inset shows an energy level scheme of the exciton states, in analogy with the hydrogen atom. The principal quantum number n identify the excited states. The energy difference between the most tightly bound exciton (n=1) and the free-particle band gap is the binding energy E_B. The figure was taken from Wang et al. [26]. (b) Experimental differential reflectivity spectrum of a WS_2 monolayer at $T = 4\,\mathrm{K}$. The series of excited exciton states is clearly visible. Data taken from Chernikov et al. [46]. (c) Schematic real-space representation of an exciton showing the strong spatial correlation of the two constituents. The arrow indicates the center-of-mass wave vector responsible for the motion of the exciton as a whole. Figure taken from reference [26].

Note that because of the presence of strong exciton resonances the position of the free carrier bandgap E_g cannot be determined directly by optical experiments. However, if some excited states are visible one can use appropriate models to extrapolate this value. This is exactly what it was done with the hydrogen atom where the position and spacing of the spectral lines was used to determine the Rydberg binding energy. For an ideal 2D model the binding energy of the different elements of the series evolves as:

$$E_B^{\mathrm{n}} = \frac{\mu e^4}{2\hbar^2 \epsilon_{eff}^2 (n - 1/2)^2} \tag{1.2}$$

in an hydrogenic series with n= $1, 2, 3, \ldots$ [48, 49], where μ is the reduced mass of the electron-hole system and ϵ_{eff} is the effective dielectric constant (an average between the dielectric constant of the monolayer and the one of the external environment). However, as shown in optical spectroscopy experiments [46, 50] the exciton excited states in TMDs don't follow the simple model of Eq. (1.2) as we will discuss more in details in Chapter 3 in section (3.3).

This happens as a consequence of the inhomogeneous dielectric environment in which the exciton is immersed. Indeed, the dielectric screening is not solely determined by the dielectric constant of the monolayer itself but is strongly influenced by the the surrounding environment. Therefore, the effective strength of the Coulomb interaction for an electron-hole pair in the $n = 1$ state is not the same as in higher excited states, as states with different spatial extensions sample different dielectric environments. For this reason, it is more apporiate to use a potential that doesn't follow the Coulomb $1/r$ law [51], as first suggested by [52, 53]. More details will be provided in Chapter 3, but we stress that the sensitivity of the monolayer to the dielectric environment in which it is immersed can effectively be used to tune the exciton binding energy and thus the spectral position of the excitonic transitions.

1.1.2 Spin-valley coupling

Following the first steps described above, which show how promising TMDs are in the field of optoelectronic, another fundamental result in the study of TMDs was obtained by Xiao et al. [54] and by Cao et al. [55]. Their theoretical prediction of the band-structure showed that the absence of inversion symmetry exhibited by the monolayers divides the six K valleys of the Brillouin zone in two inequivalent groups which can be addressed with different states of circular polarization of light. We will call the two groups valley K^+ and K^-, where the first group can be addressed by the σ^+ component of circularly polarized light of suitable energy while the second by the σ^- one.

Moreover, Xiao et al. [54] also considered that the strong spin-orbit coupling induced by the relatively heavy metal atoms (and by the fact that their d orbitals are involved in the formation of the electronic states) give rise to an interesting coupling between the spin and valley properties of the material.

It can be shown that the valence band is splitted in two sub-bands. In each sub-band just one of the possible spin states is allowed and the order is reversed in two adjacent K valley of the Brillouin zone (as they are related by time reversal symmetry). The situation is well depicted in panel (a) Fig. (1.8).

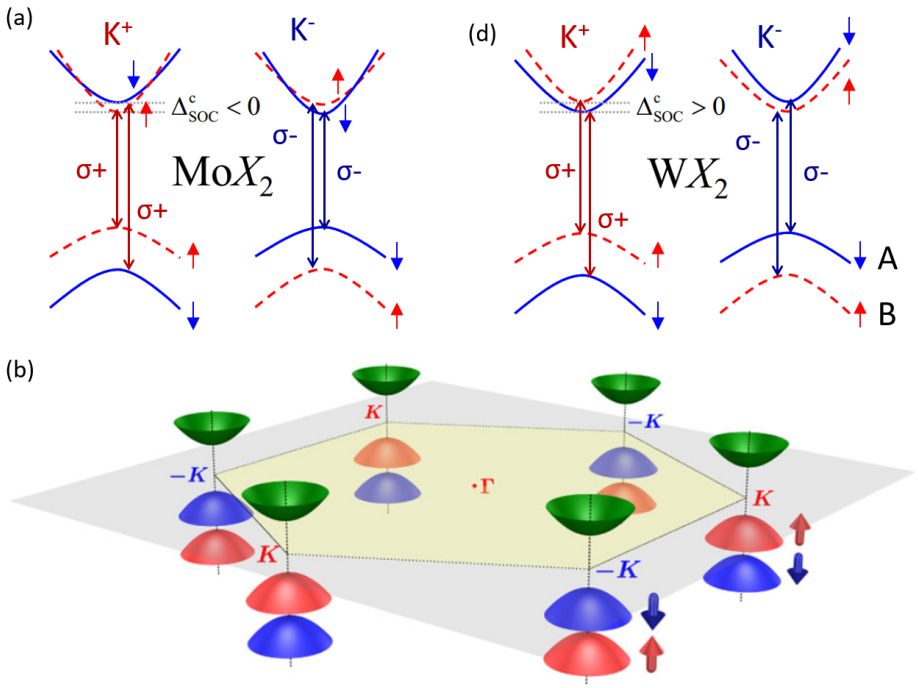

Figure 1.8: (a) The sketch shows the spin-orbit splitting of the valence and conduction band in both valleys K^+ and K^-, for both the molibdenum and the tungsten compounds. Notice how the order of the conduction band splitting is reversed when the metal is changed. The double point arrows indicate both the A- and B-exciton interband transitions and the color symbolyze the chiral optical selection rules. The figure was taken from Wang et al. [26] (b) Sketch of the first hexagonal Brillouin zone in TMDs (the conduction band splitting is ignored for simplicity). The picture was taken from reference [55].

The splitting in the valence band is very large, typically 0.2 eV for the MoX_2 and 0.4 eV for WX_2 compounds [32, 43, 54, 56, 57]. It was shown later that also the conduction band is splitted but the energy difference between the two sub-bands is one order of magnitude smaller (tens of meV) [33, 54, 58, 59, 60, 61] as shown in Fig. (1.5). For the moment, let's ignore the conduction band splitting, as done in panel (b) of Fig. (1.8). Thanks to the presence of two valence bands there are two possible electronic transitions.

The first and the most intense is from the topmost valence band to the conduction band, while the second transition happens between the lower valence band and the conduction band. Because excitons are dominant in these materials, the presence of two electronic transitions implies the existence of two exciton series. Intuitively, the energy separation between these two exciton states is roughly equal to the spin-orbit splitting of the valence band Δ_{vb}. From now on we will call the exciton whose hole occupies the top valence sub-band A-exciton, while the other will be called B-exciton. Both of them leave their signature in TMDs optical spectra, as it will be shown in Chapter 2.

Shifting our attention from panel (b) of Fig. (1.8) to the top panel (a), we can see that the situation is slightly more complicated as the conduction band

is split as well. In particular the order of the spin state in the conduction bands of molibdenum and tungsten compounds is reversed.

If we consider optical absorption, the reversed order of the spin states in the two material is not very important as we can always excite an electron to one of the two conduction sub-bands. However, in the emission spectra, the spin selection rules have important consequences in the intensity of the transitions. If we consider the molibdenum compounds, the spin-allowed A-exciton transition happens between the topmost valence band and the lower lying conduction band. This means that the optically bright transition (i. e. the spin allowed one) is favoured as it represents the recombination of an exciton in which both the electron and the hole occupy their lowest energy state [58, 60]. The opposite happens for the B-exciton where the lowest lying state is optically dark as it is spin forbidden.

In contrast, for WS_2 and WSe_2 the lower conduction band has opposite spin with respect to the top valence band. Hence the lowest lying transition is optically dark. Both trends are in agreement with the temperature dependence evolution of the photoluminescence signal measured from the monolayers [62, 63, 64, 65]. More details on bright and dark excitons will be provided in Chapter 3.

Another reason why the research on TMDs is so fascinating are the original polarization selection rules for the optical transitions. In III-V semiconductor nano-structures such as InAs quantum dots or GaAs quantum wells it is possible to optically initialize carrier spin states by using circularly polarized laser light [66].

In TMD monolayers it is possible to address either K^+ or K^- valleys in momentum space by choosing σ^+ or σ^- polarized laser light, respectively. [54, 55, 67, 68, 69, 70]. These valley dependent selection rules have been predicted and experimentally verified in 2012. As can be seen in Fig. (1.8), by choosing a suitable laser energy also specific spin states can be targeted.

Controlling the valley degree of freedom has already been tried in other solid state systems before [71, 72, 73, 74], but the strong point of TMD monolayers is that strongly contrasting valley properties can be very easily implemented experimentally, simply by changing the polarization of a standard excitation laser such as a helium-neon laser.

In a single particle picture, without taking excitonic effects into account, it could be expected that a carrier remains in a specific valley for two reasons: first, scattering with a large change in momentum has to occur. Second, the carrier has to change its spin, so if we consider for example the valence states in WSe_2, the $\sim 400\,\mathrm{meV}$ energy difference of the spin-orbit splitting has to be overcome. Based on these arguments, it was very interesting to measure the valley relaxation times of carriers (not excitons) in WSe_2 monolayers, and first studies indicate indeed that optically initialized hole polarization is maintained over several microseconds [75, 76].

The above arguments on polarization relaxation do not hold for excitons, which can depolarize without evoking individual carrier spin flips, on very short time scales of the order of picoseconds. Here, the main depolarization mechanism is driven by electron-hole Coulomb exchange, as in the case for 2D excitons in GaAs quantum wells [77, 78]. The reason for observing a high degree of circular polarization is therefore a competition between ultrafast recombination and depolarization. As will be discussed later, PL emission times are in the order of 1 ps, which is therefore comparable to polarization relaxation times for

excitons and hence their emission is partially polarized. The highly polarized stationary PL spectra from monolayers following circularly polarized laser excitation have inspired more sophisticated experiments on valley polarization using pump-probe techniques and modifying emission properties in optical microcavities, for example, which allow continuing progress in our understanding of valley dynamics [79, 80, 81].

1.2 Conclusions

In this chapter we introduced the physical system which will be the subject of this whole manuscript: transition metal dichalcogenide monolayers. We showed how the research in these materials is a continuation and extension of research on quasi-2D systems such as the quantum wells. We motivated the interest in these system by briefly describing their fundamental properties: the fact that they are direct bandgap semiconductors and the spin-valley locking which allows us to create carriers in inequivalent valleys of the momentum space (K^+ or K^-) by means of light of different circular polarization.

We also described the strong excitonic effects which dominates the optical spectra of TMD monolayers. The energy scale of the binding energy is extremely large, one to two orders of magnitude larger than the one of excitons in III-V quantum wells.

Chapter 2

Experimental Techniques

The purpose of this chapter is to give an overview of the experimental systems and techniques which were used throughout this PhD thesis. The experimental work performed in our laboratory can be roughly divided in sample fabrication and sample analysis. The first part of this chapter will describe the ways in which it is possible to obtain a single atomic layer starting from a bulk crystal. All of them are quite simple and inexpensive and that is one of the reasons why the research on 2D crystals and transition metal dichalcogenides (TMDs) in particular, received a great boost in recent years and can be pursued by many groups.

After the description of the sample fabrication techniques we will introduce our experimental set-ups. The main ingredients for our study of TMDs are experiments performed at low temperatures and the understanding of light-matter interaction at the nanoscale. Thus, our instrumentation consist of a cryostat, in which the samples are kept at $T = 4\,\mathrm{K}$, several laser sources which provide the excitation light, and a microscope for allowing light excitation and detection on the μm scale. This is necessary as TMD monolayer samples fabricated by exfoliation are only a few micrometers in size. These instruments will be briefly described in the following. Moreover, we will introduce the optical spectroscopy techniques which will be extensively used throughout this manuscript.

In the last part of the chapter we will instead focus on the optical spectroscopy of TMD monolayers. We will show the photoluminescence and the reflectivity contrast spectra of the materials exfoliated on Si/SiO_2 substrates. From these data it will be clear that an improvement in the fabrication technique was needed. This improvement was indeed achieved by encapsulating the monolayers in hexagonal boron nitride (hBN). The process will be described in Chapter 3

2.1 Sample fabrication

The technique used to obtain a single monolayer flake starting from a bulk crystal is called micro-mechanical cleavage but it is often referred to as exfoliation or "scotch-tape" technique. Indeed, the only necessary instruments for obtaining a monolayer are a bulk crystal and an adhesive tape.

The technique was used by Geim and Novoselov [12] for obtaining a graphene

flake starting from a bulk crystal of graphite. Their work largely inspired the study of different 2D materials, the number of which has increased greatly in the last 15 years.

The working principle of the micro-mechanical cleavage technique is very simple: in layered crystals the in-plane bonds between the atoms are much stronger than the weak Van der Waals force which keeps the different atomic layers together. Thus, the adhesive force exercised by a scotch tape is enough to separate atomic sheets from a bulk crystal without breaking them. In particular, it may be possible to obtain a single layer, which will be atomically thin.

In practice a bulk crystal of a layered material is put on an adhesive tape and repeatedly peeled off. Then the scotch tape is put in contact with a substrate, generally a silicon wafer with a thin silica (SiO_2) layer on top. The small flakes present on the adhesive tape will be exfoliated as well, thanks to the van der Waals force between the crystal layers and the substrate. In other word, after having put the adhesive tape in contact with the substrate some flakes can be found on the surface of the latter.

It is straightforward to see that this technique is not deterministic, in the sense that it is not possible to predict if and where a single layer will be removed from the bulk material. Thus, after having deposited some flakes on a substrate, it will be necessary to scan its surface looking for a monolayer. This procedure is made difficult by the fact that the single layer will be surrounded by hundreds of flakes of random thickness. Moreover, the area which has to be scanned is of the order of one cm^2 while the average monolayer is generally a few μm in size. However, once the monolayer has been found by analysing the optical contrast using a white light source it can be investigated with different experimental techniques.

2.1.1 Transfer or stamp technique

The micro-mechanical exfoliation technique as we described it is aleatory and it leads to monolayers with very small surface area of the order of a few μm^2 for TMD flakes. Such a value makes the optical study of the material complicated: even with a μPL set-up, the available area has similar dimensions as the exciting laser spot.

For these reasons the community made efforts in order to improve the fabrication procedure. In particular, after the exfoliation of the bulk crystal on the scotch tape, researchers started to transfer part of the flakes on a polymeric organosilicon, the Polydimethylsiloxane (PDMS) [82]. This passage can be done by simply putting the two surfaces in contact. The reason why PDMS has been chosen is that its viscosity varies as a function of how fast one tries to detach an object in contact with it. In particular, the faster the peel off, the stronger the adhesive response of the polymer will be. In this way after having put in contact the scotch tape with the PDMS stamp, flakes are transferred from one to the other by quickly separating them. Subsequently, a flake can be transferred to a substrate by slowly lifting the PDMS from the surface of the wafer, thus minimizing the adhesive force of the polymer. A sketch showing the different steps of the procedure we just described is presented in Fig. (2.1)

This technique is very useful for obtaining monolayers of bigger size, which can range from $10 - 100\,\mu m^2$ [82] and even more. Moreover, it can be readily modified to partially solve the indeterministic nature of the technique. Indeed,

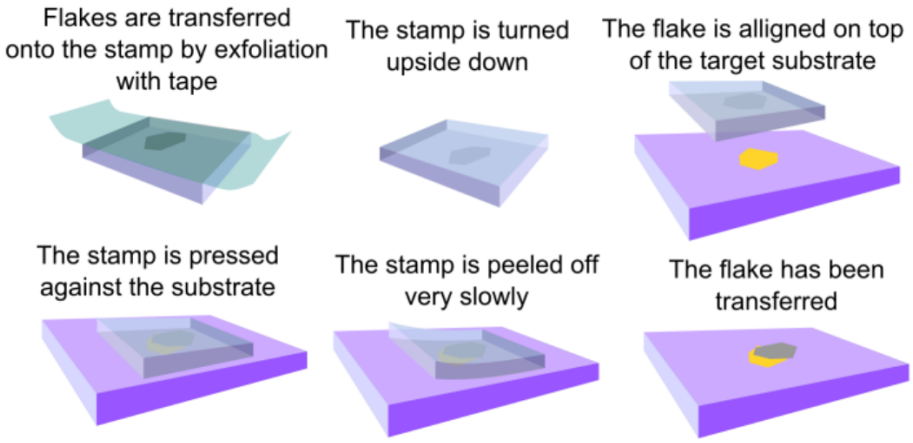

Figure 2.1: The image shows how flakes exfoliated on a scotch tape can be transferred on a Polydimethylsiloxane (PDMS) stamp. Hence, a monolayer can be located on PDMS and then deterministically transferred on an arbitrary substrate, thanks to PDMS viscoelastic properties. The image was reprinted from reference [82]

the PDMS is transparent. It is thus possible to scan its surface and to locate a monolayer which can be subsequently transferred on an arbitrary substrate in a specific location using a micromechanical manipulator.

This is the technique used in our laboratory. In particular a small PDMS sheet is attached to a glass slide. The flakes present on an adhesive tape (previously exfoliated from a bulk crystal) are then transferred on the polymer by putting them in contact. The PDMS sheet is carefully checked under an optical microscope. For doing that the glass slide is mounted on an xyz micrometer stage. In particular, the PDMS is placed on the bottom of the glass slide and its surface is imaged through the glass and the polymer itself. In Fig. (2.2) the PDMS surface with several TMD flakes of random thickness is shown.

The whole PDMS surface is thus scanned and once the monolayer has been found it can be deterministically transferred. This is done by placing the target substrate (generally a silicon wafer covered by a $\approx 90\,\text{nm}$ layer of silicon dioxide) on top of a second xyz micrometer stage. The surface of the wafer can be easily imaged thanks to the transparent nature of the glass and of the PDMS, thus allowing us to decide where to deposit the monolayer. After careful alignment the PDMS and the substrate are put in contact and slowly separated from each other. In this way it is possible to detach the monolayer from the PDMS and transfer it on the silicon wafer.

The technique we described assumes the possibility to actually see the monolayer. This issue is not trivial as we are talking of a layer which is just $0.6\,\text{nm}$ thick. Fortunately, the strong light-matter interaction exhibited by TMDs make it possible to identify a monolayer by simple optical contrast. However, an optical microscope with a high quality imaging camera is needed for being able to imagine a single atomic layer of TMDs. An image of a TMD monolayer on PDMS is shown in panel (b) of Fig. (2.2).

Our setup allows us to measure the room temperature micro-photoluminescence of a flake which is on PDMS. Indeed, the detection of a PL signal is an unam-

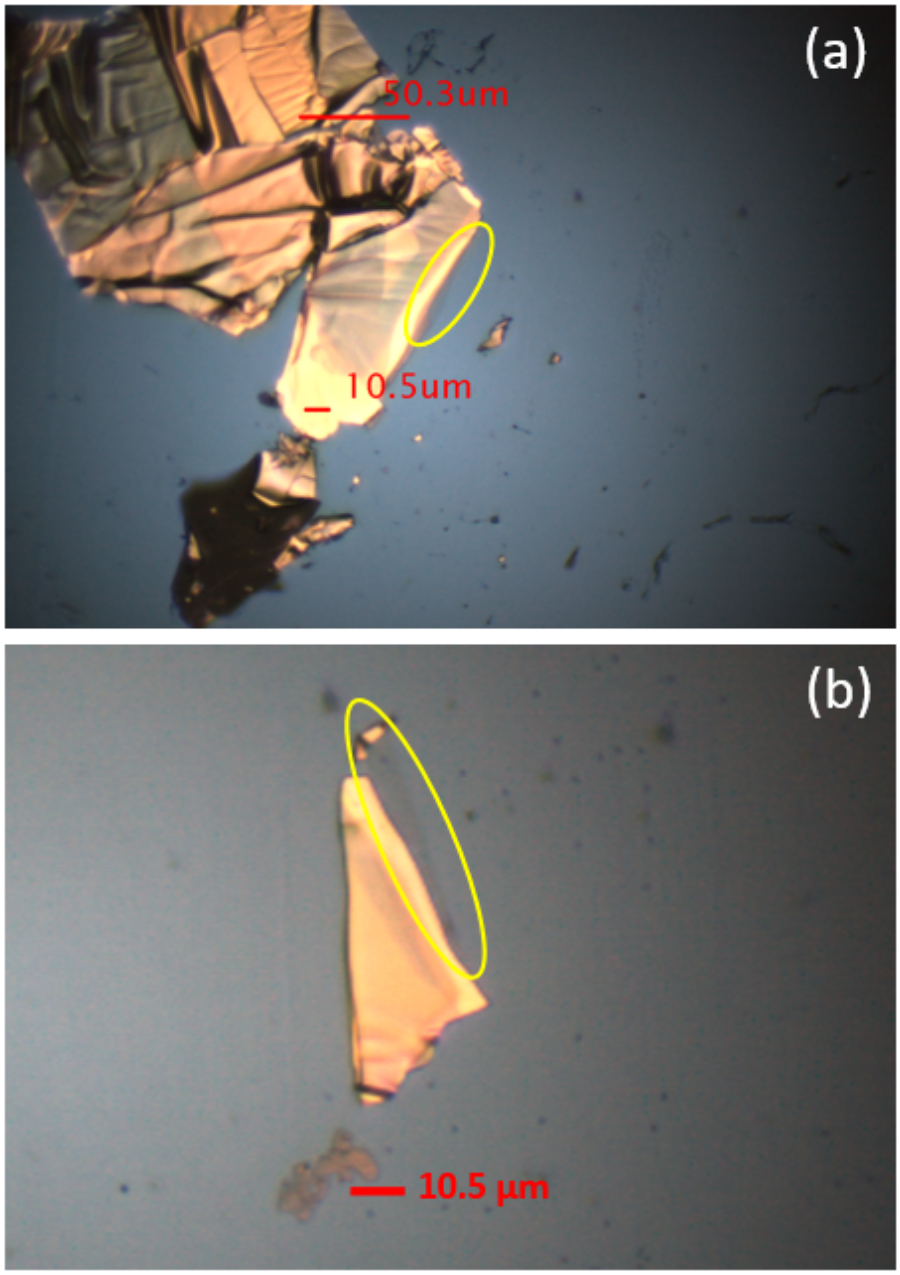

Figure 2.2: (a) The picture is a micrograph of several flakes of random thickness of TMD WSe_2 exfoliated on a PDMS stamp. Among them a monolayer can be identified by analyzing the optical contrast. Note the scale bar: the area to be scanned is of a few cm^2, thus making the location of a monolayer a time consuming task. (b) Optical micrograph showing a monolayer of $MoSe_2$ attached to a thicker flake on PDMS. The monolayer appears as a slightly darker area on the right side of the thick orange flake and has been marked by a yellow line.

biguous sign of the single layer nature of the flake we are looking at, because of the fact that the bilayers or the multi-layers have an indirect bandgap and their PL is thus strongly quenched. This is with the exception of $MoTe_2$, where the nature of the gap of the bilayer is still under discussion [83, 84].

To conclude, we also stress that after the deposition a thermal annealing is generally performed to enhance the adhesion of the monolayer to the substrate. The annealing is done by placing the substrate on a hot plate at 150 °C in air at ambient pressure. More details about the importance of this passage will be provided in the following section.

2.1.2 Van der Waals hetersostructures

One of the great strength of 2D crystals is the possibility to combine different monolayers, stacking them one on top of the other. The result is an artificial material which has been assembled in a choosen sequence and which has been called van der Waals heterostructure [15].

In these engineered materials the single building block (an atomically thin layer) is kept together by the covalent bonds in the atomic plane, while the van der Waals force is sufficient to assure the stability of the stack. Considering the great variety of layered crystals, the possibilities of building different heterostructures are numerous and promise to lead to great breakthroughs in both fundamental research and applications.

However, one has to keep in mind that not all layered crystals are stable under ambient condition and that monolayers are even more fragile and can oxidise, decompose, corrode and so on. Moreover, adsorbates may contaminate the single layer surface. Thus, when a second layer is placed on top of the first the properties which where envisaged may be affected by the presence of these interlayer impurities. Nevertheless, these contaminants are usually squeezed into μm size "bubbles" by the van der Waals force itself, thus making possible to have large areas free of contaminants [85]. Thermal annealing is also very useful for improve the mobility of the adsorbates making their confinement easier.

Ideally, for fabricating these heterostructures one would desire van der Waals epitaxy [86] in which each layer is simply grown on top of another. However, the weak nature of the van der Waals force compared to the one of covalent bonds make the epitaxial fabrication of a single layer very challenging [15]. Moreover, the growth condition of each material should be compatible with the one already present on the substrate. For these reasons the efforts to epitaxially grow a specific heterostructure are currently a complex research field.

Thus, for research purposes, the manual stack of atomic layer is advantageous to have access to new properties. For example, with the transfer technique described above, the fabrication of a van der Waals heterostructure is straightforward. Indeed, after having deposited the first layer, one has just to repeat the procedure and deposit the second layer on top of the first using a different PDMS stamp. This is why it is very important to control the position of the deposition with great accuracy. Moreover, the simplicity and the fact that the technique is very cheap, gave to many research groups the opportunity to fabricate their own samples.

The most common heterostructures fabricated in our laboratory are the so-called encapsulated samples [87] a TMD monolayer is placed between two flakes of hexagonal boron nitride (hBN), a layered insulator with a wide bandgap

around 6 eV [88]. hBN crystals of very high quality are brovided by our collaborators at NIMS, Tsukuba [89]. The considerably improved optical quality as compared to unencapsulated samples will be detailed in Chapter 3.

In practice, a hBN bulk grain is put on a scotch tape and repeatedly peeled off. Hundreds of flakes are then transferred from the scotch to the PDMS, with the procedure detailed above. Then, using the optical microscope in our transfer station we can look for a suitable flake, which has to be flat and with a thickness of approximately 100 nm (this value may change depending on the application). The flake is then transferred to a substrate, and annealed (at 150 °C in air for ten minutes). An image of an hBN flake exfoliated on a Si/SiO_2 wafer is shown in panel (a) Fig. (2.3).

After the hBN bottom layer has been transferred on the substrate we need to repeat the procedure for a TMD monolayer. Once it has been located it can be precisely transferred on top of the hBN flake as shown in panel (b) of Fig. (2.3). Finally a second thinner (≈ 10 nm) hBN flake will be used to cap the TMD monolayer, isolating it from the external environment. Notice that the thermal annealing is repeated after every passage of the fabrication process.

Another kind of heterostructure which is possible to fabricate in our laboratory is a device for controlling the charge density inside a TMD monolayer. The silicon of the substrate is connected to a source meter and acts as a back gate while the top surface is patterned with gold electrodes. The bottom hBN flake is then exfoliated close to one electrode and, after the deposition of the monolayer, a thin graphite flake is used to connect it with the macroscopic gold electrodes. In the end, a capping hBN layer is used to protect the single TMD layer. In this scheme, applying a voltage between the top and the back gate will modify the charge density of the monolayer thus allowing us to explore different effective doping regimes. As we will see, in Chapter 5, this will modify the optical properties of the material: close to the charge neutrality the spectrum is dominated by the neutral exciton recombination line (the A-exciton, also labelled as X^0). However, in case of significant doping, charged excitons (or trions) are formed and they may become the dominant feature in the optical spectrum of a TMD monolayer. These three particles complexes consist of a charge (an electron or a hole, depending on the type of doping) bound to a neutral exciton and have already been observed in quantum wells kept at low temperature [209]. We will discuss about these particles in Chapter 5.

Note that with little variation on this structure it would be possible to built a device in which we can apply different electric fields to the material without changing the doping level, for studying the variation of its optical response. For building these double gated structures [90] it suffices to start the stack with a graphite flake which has to be contacted with an electrode. Then the hBN/TMD/hBN heterostructure is built and a second graphite (contacted with another electrode) is used to complete the heterostructure. In this way the two hBN layers will act as dielectric spacers. The charge density would not be modified but the TMD monolayer will be exposed to an electric field.

This is just one more example of the versatility of van der Waals heterostructures. Using more 2D materials in different configurations and stacking orders promise to allow the built of many devices and engineered materials which will boost both research and applications [91].

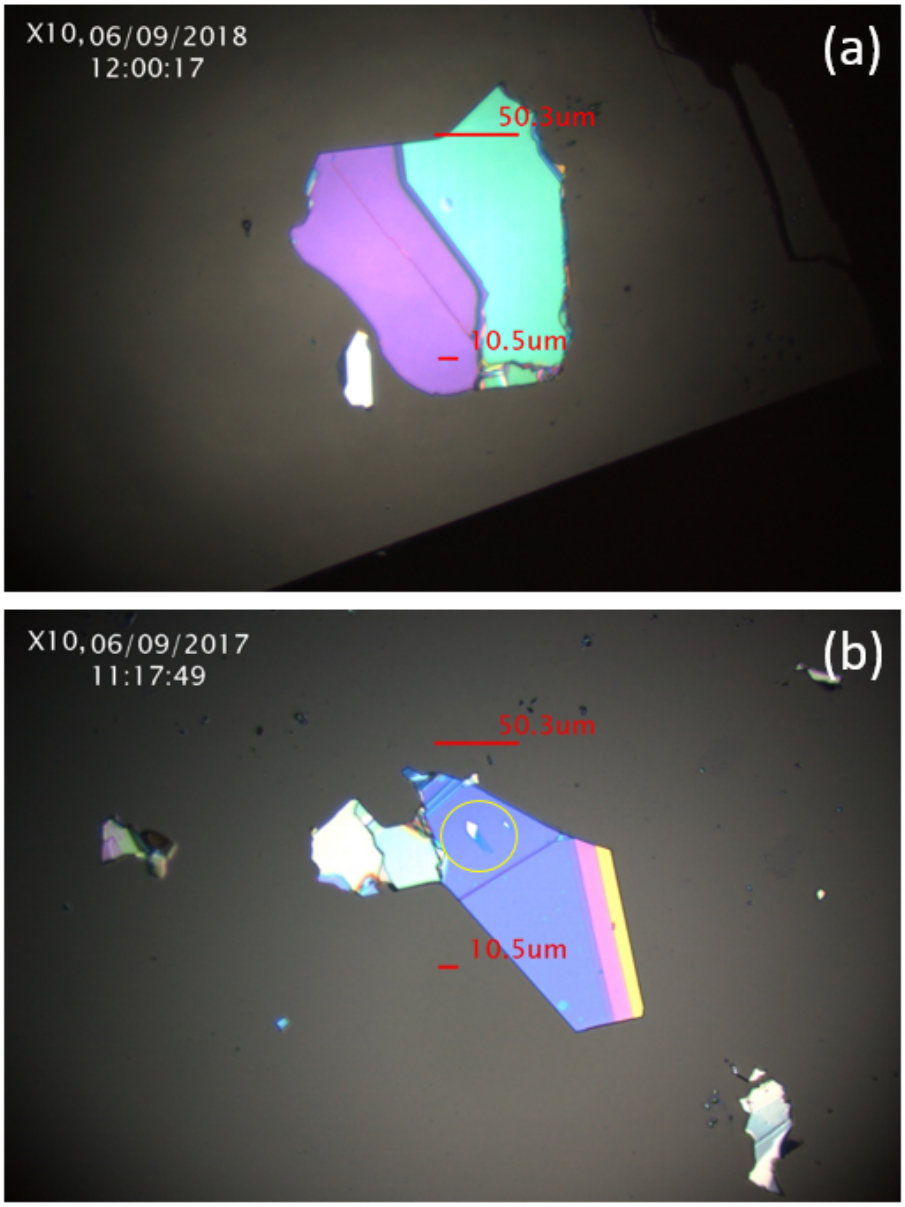

Figure 2.3: (a) hBN flake with a marked height step, exfoliated on a silicon wafer covered by 90 nm of SiO_2. (b) Same as (a) but a WSe_2 flake with a monolayer has been deposited on the hBN.

2.2 Low temperature optical spectroscopy set-ups

In this section we will describe the main scientific instruments which were extensively used for this PhD reseach work. In particular, we performed optical spectroscopy studies of atomically thin semiconductors at low temperature. The set-ups employed need to satisfy some important requirements.

In particular, the samples have to be kept at cryogenic temperatures. Indeed, as described in Chapter 1, the properties of TMD monolayers are dominated by excitons. The presence of lattice vibration alter the optical properties of the material, in particular inducing thermal broadening of the transitions. Thus, to uncover more details it is better to perform the studies at low temperature where phonon occupation numbers are low.

A second requirement is that of a high spatial resolution, as the area of the flakes to analyse, generally doesn't exceed some tens of μm^2. A few years ago, before the use of the PDMS transfer technique, the size was even smaller. To achieve sufficient excitation power density and to be able to uncover any spatial variation of the optical properties around the flake it is thus necessary to have a laser excitation spot close to the limit of diffraction. For obtaining this resolution a high magnification objective is necessary.

Moreover, in order to characterize a sample despite its small size it is necessary to move it with respect to the microscope objective, and it is necessary to do it in all three spatial directions with a very high precision. This can be achieved thanks to three piezoelectric motors which allow us to control the sample position in the three spatial axis and in particular to position the excitation laser with nanometric resolution.

However, if the set-up is so sensitive to the position of the exciting laser it is fundamental to reduce the external vibrations which have the effect of moving the excitation spot and averaging the spectra over a larger area of the monolayer: the result would be the same of having a larger excitation spot. For this reason the cryostats used show low mechanical vibrations.

Another fundamental requirement for the purpose of this PhD research work is high polarization resolution. This is necessary to uncover the spin and valley-polarization properties of charge carries in transition metal dichalcogenides. This means that exciting a TMD monolayer with a circulary polarized laser will induce an electronic transition only in one of the two K valleys. In particular the degree of circular polarization of the exciting laser light has been kept as high as 99% during all of our experiment. The main element used for controlling the polarization are half and quarter waveplates, Glan-Taylor prisms and liquid crystal retarders. More detail can be found later in this chapter, in subsection (2.2.2).

2.2.1 Cryostats

A cryostat is a device which is used to maintain a sample at cryogenic temperatures. There are three families of cryostats the bath cryostats, the continuous-flow ones and the closed-cycle cryostats.

In bath cryostats the sample is put in thermal contact with a cryogenic liquid bath. The gas which evaporates from the bath can be collected or dispersed. The main disadvantage of this technique is that the bath needs to be periodically refilled which is time consuming and expensive, especially if the temperature which is needed to be reached required the use of liquid helium.

The continuous-flow cryostats use instead the exhausted vapour flow for cooling the sample. The vapour boils from a liquid reservoir which still needs to be refilled. Thus, this technique presents the same disadvantages than the bath one.

In the end, the closed-cycles cryostats do not need a bath of cryogenic liquid. The vapour used for cooling down the sample is brought at low temperatures using an external compressor. The cooled gas circulates on a line and is thermally contacted with the sample, from which it absorbs heat. Once the gas has been warmed up it circulates back in the compressor where it's cooled down again and reused in the next cycle. The main drawbacks of this techniques arise when, as in our case, we want to look at small objects with high spatial resolution. This latter is reduced by the vibrations of the cryostat which have the effect of moving the detection spot. For this reason, the external compressor is often designed to be a low-vibraton one which means that the amount of mechanical vibrations that can be transmitted to the cryostat chamber are minimized. This is the kind of cryostats used for this work: closed cycle and low-vibration.

In particular the majority of the data presented in this thesis were acquired in a single low vibration closed He-cycle cryostat, the attoDRY700 from attocube systems. Its compact design and simplicity to use make it a very versatile instrument for studying TMDs monolayer when a magnetic field is not required. In this latter case other two more complex cryostats are used. In the following we will mainly describe the attoDRY700 as the other two cryostats (from attocube as well) share with it many features. We will highlight the difference at the end of this subsection.

A picture of the attoDRY700 in our lab is shown in panel (a) of Fig. (2.4).

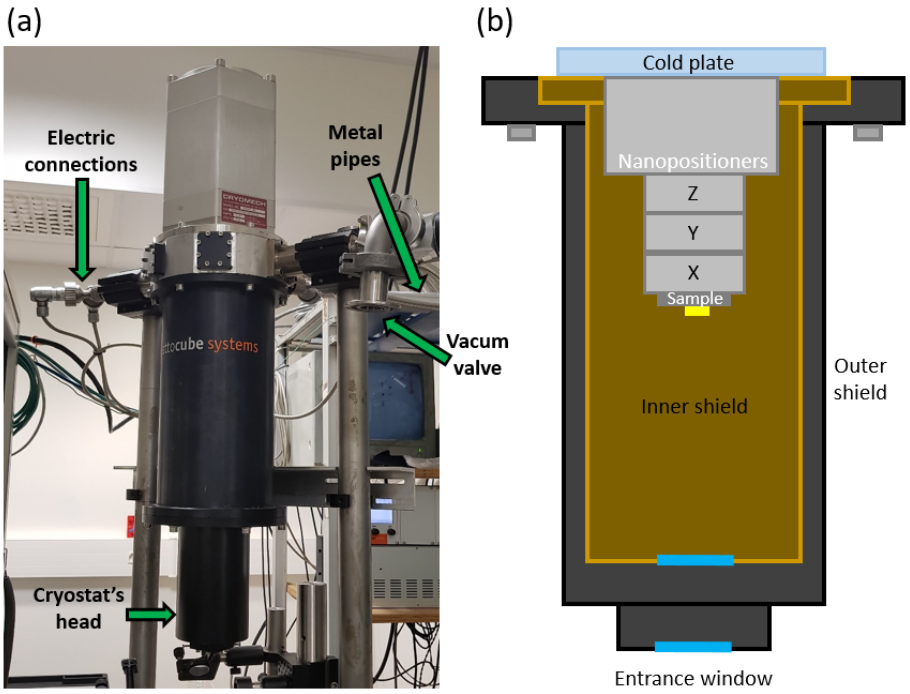

Figure 2.4: (a) Picture of the attoDRY700 cryostat as installed in our laboratory. (b) Sketch of the head of the cryostat.

From it, it is possible to see the main part of the cryostat. The bottom part is the head and it is the only part which needs to be removed in order to load a

sample. On the right one can see the vacuum valve which is used to evacuate the chamber of the cryostat. Barely visible, two metal pipes connects the system to a compressor (not shown). The cold helium gas flows in these two pipes from the cryostat head, where it absorbs heat, to the compressor where is cooled down again. On the left, vacuum electrical connectors are indicated. Thanks to them it is possible to operate the piezoelectric motors, a temperature sensor, a heater and eventually other electric connections for charge tunable devices.

In panel (b) of Fig. (2.4) a cutaway drawing of the cryostat's head is shown. It consist of two concentric shields surrounding the stack of piezoelectric motors. When the cryostat is operated the first shield separate the vacuum inside the chamber from the ambient pressure. The inner shield has instead the purpose to protect the sample form thermal radiation, which would increase the sample temperature. At the bottom of each shield, a glass window is opened for allowing the optical excitation and detection of the sample, which is performed on the same optical line. The sample is thermally contacted, thanks to a cold finger, to the cold plate which is in turn in thermal contact with the flowing helium gas. In this way it is possible to cool the sample down to approximately $T = 4\,\mathrm{K}$.

The design of the other two cryostats in our laboratory is completely different. They are the attoDRY1000 and the attoDRY2000 from attocube systems. They present the possibility to apply a magnetic field on the sample. In particular the attoDRY1000 allow us to apply up to 9 T along z direction perpendicularly to the monolayer plane (parallel to the excitation/detection line) while the attoDRY2000 has a vector magnet which can provide 5 T along z and 2 T along x and y.

The volume to cool down to cryogenic temperatures in these two magnetocryostats is much larger than the one in the attoDRY700 because also the magnets needs to be at very low temperature to operate. That's why the starting procedure (evacuation plus cooling) requires longer time than the attoDRY700. Moreover, the different geometry forced us to build a completely different microscope for the excitation and the detection of signals. Indeed, while the attoDRY700 can be mounted on an optical table, thus giving us plenty of space for placing all the necessary optical elements. The other two cryostats are placed directly on the floor and the optical excitation/detection line has to pass through the top window.

This is the reason why two microscopes based on the Thorlabs cage system were built. Their main drawback is the mechanical stability over a long period of time and the fact that the number of optical elements which can be installed is limited in order to have a stable structure. To improve our set-up we recently replaced these microscopes with small removable breadboards which can be fixed on the top of the cryostats thanks to new adapters recently developed by attocube systems. However, all the data acquired in magneto-cryostats during this PhD work where obtained with the old cage-based system [92, 93, 94].

2.2.2 Confocal microscope and polarization resolved measurement

Confocal microscopy is an optical imaging technique which aims at increasing optical resolution and contrast of a micrograph by using point illumination (diffraction limited spot) and a spatial pinhole to prevent out-of-focus light to reach the detector [95, 96]. The name confocal stems from the fact that the

illuminated spot has to be in an optically conjugate plane with the pinhole. In practice, in a confocal system, the excitation and the detection paths pass through the same objective. A sketch explaining how this technique can effectively improve the spatial selectivity of a microscope is shown in Fig. (2.5)

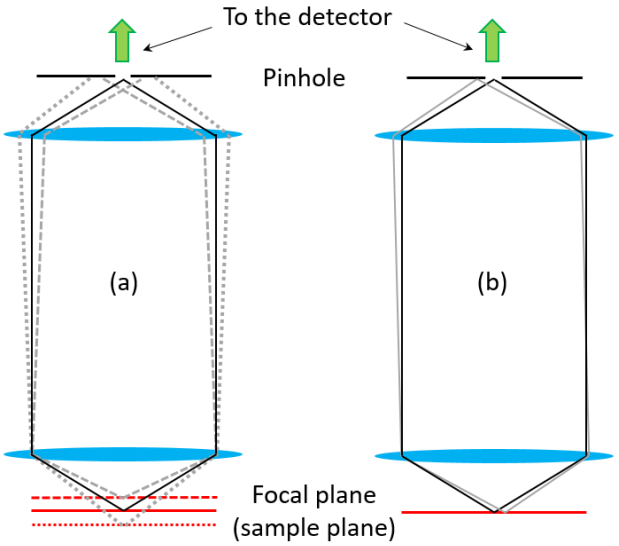

Figure 2.5: Sketch which shows the working principle of the confocal microscopy. In (a) the light emitted out of the focal plane is rejected by the presence of the pinhole. In (b) the light emitted by the focal plane but outside the excitation/detection spot is rejected as well as it is not focused on the pinhole. In this way only the signal coming from the excited region can be detected.

In panel (a) light emitted from three different planes is shown. Only the middle plane (represented by a continuous red line) is in an optical conjugated position with the pinhole. Thus, the lens system focuses the light coming from this plane exactly on the plane of the pinhole. The light coming from the other two planes instead is focused before or after the pinhole and is thus strongly suppressed. Indeed, this light is focused by the lens system outside the pinhole aperture.

In panel (b) of Fig. (2.5) it it shown instead how the light emitted from the focal plane (which is the sample plane) but from a region outside the focal spot is rejected as well by the pinhole.

In our set-ups a pinhole is actually not present. In the case of the attoDRY700 set-up (shown in Fig. (2.6)) its role is played by the entrance slit of the spectrometer, while in the two magneto-cryostats both excitation and detection are performed with optical fibers. The core of the detection fiber, which diameter is just $5\,\mu$m, acts as an effective pinhole.

Our set-up is structured in this way. Several excitation sources can be coupled to a single excitation line and their power density can be varied thanks to a tunable optical density (OD) filter. Specific low-pass, high-pass and band-pass filters or other ODs can be added when needed. The excitation light is deflected by two mirrors, which have the purpose to walk the beam for making the excitation and detection spots coincide. Subsequently, the excitation light

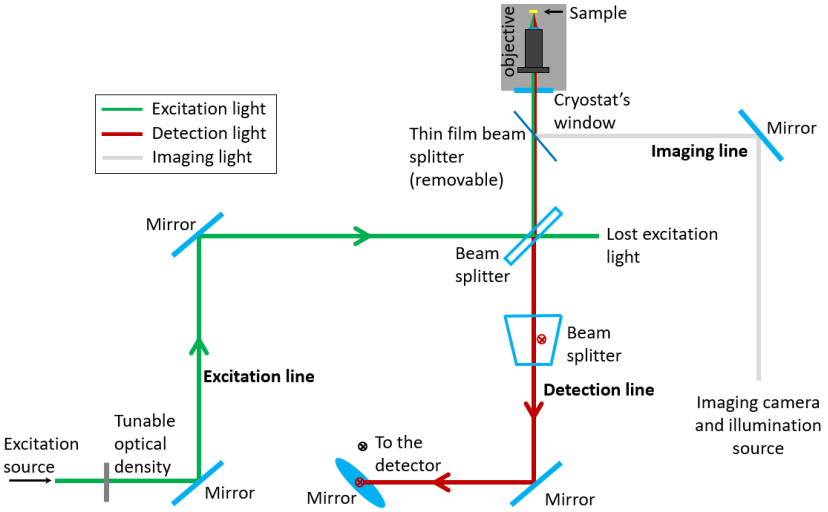

Figure 2.6: Sketch of the attoDRY700 set-up and optical microscope.

beam crosses a beam splitter which reflects part of the light and sends it inside the cryostat. Here the excitation light is focused by the objective and reach the sample. Note than a movable thin film beam splitter is present in Fig. (2.6). This beam splitter is used only while imaging the sample to overlap the imaging and illumination optical path with the excitation/detection line.

The emitted light from the sample (and the reflected excitation light) passes through the objective, exits the cryostat, passes through the first beam splitter and then crosses a second. Those two are rotated by $\pi/2$ (orthogonally to the optical axis) with respect to each other to compensate possible distortion of polarization (and hence distortion of intensity, if the emitted light is polarized) that each beam splitter may have induced. After, two other mirrors are present (for walking the detection beam) and in the end the light is sent to the detector i.e. the spectrometer and CCD camera. This is the detection line.

The imaging line consist of a camera and bright LED emitting light centred at 635 nm for illumination. This allows to perform optical measurements in specific sample regions of complex van der Waals heterostructures.

As we discussed before, spatial resolution is fundamental when performing μPL experiments. It is given by the size of the detection spot and by our ability in precisely positioning the sample in the three spatial directions. Thanks to the piezoelectric nanopositioners, purchased from attocube systems, we are able to move the sample with a precision of 10 nm over 5 mm at $T = 4$ K, even in high magnetic fields. In other words our precision is only limited by the detection spot, whose size is two orders of magnitude larger.

The size of the spot depends on the objective and in particular on its numerical aperture (NA). This quantity is defined as $NA = n \sin\theta$ where n is the refractive index of the environment (1 in our case) and θ is the maximal half-angle of the cone of light that can enter or exit the lens.

Our objective is achromatic, multi-lens, suitable for measurements performed at 4 K (as it is inside the cryostat chamber) and its numerical aperture is 0.82. It has been purchased from Sysmex-Partec. The achromaticity is very important

as the linewidth of the optical transitions in TMDs and their spectral separations are large. The use of a single aspheric lens (as tested before I joined the group) lead to distorted PL spectra in which the intensity ratio of the peaks was depending on the distance between the objective and the sample.

Using a reformulation of the Rayleigh criterion we can estimate our spatial resolution as:

$$\Delta_x = \frac{0.61\lambda}{NA} \tag{2.1}$$

which is equal to 470 nm in the case of a excitation/detection with a helium-neon laser ($\lambda = 632.8$ nm). This quantity gives us the minimum distance at which two different point sources can be distinguished. Δ_x is strongly related to the ability of the microscope to selectively excite and detect objects separated by a small distance. This quantity is called spatial selectivity. Using a 5 μm period grating made of aluminium reflective stripes, the spatial selectivity achieved by our system was measured to be 700 ± 70 nm. This quantity is the full width at half maximum of our excitation laser beam.

From the theory of gaussian beams it can be shown that the "beam diameter" is approximately 1.7 times the FWHM and it is thus equal to 1.2 μm. This quantity is very important because the beam diameter is by definition the size of the spot in which 95 % of the incident power transit. This is also call the $1/e^2$ diameter of the gaussian beam.

Another fundamental requirement for studying the optical properties of transition metal dichalcogenides is the ability to resolve polarization both in a circular and in a linear basis. Doing so with our set-up is straightforward once some elements are added, as shown in panel (a) of Fig. (2.7)

On the excitation line a Glan-Taylor (GT) polarizer is added. It posses an optical axis and all the light polarized parallel to it is transmitted while the other component is reflected by 45° with respect to the propagation axis and thus exits the excitation line. In particular we chose this axis to be parallel to the ground (orthogonally to the plane of the paper). From now on we will refer to this direction as the s-direction.

Before the Glan-Taylor a half-waveplate ($\lambda/2$) is added. This element rotates the direction of polarization and in particular its purpose is to align the incident laser polarization (which is linearly polarized in a random direction) with the optical axis of the Glan-Taylor, thus maximising the power which will emerge after the GT. Note that in this way the exciting laser light will always be polarized in the s-direction.

In contrast, the emitted light from the sample contains most probably both the directions of polarization. For selecting one of the two another half-waveplate and a second GT are added to the detection path. The optical axis of the second Glan-Taylor is chosen to be perpendicular to the one of the first. Thus, the detected light is always polarized in the p-direction.

Now, the $\lambda/2$ in the detection path has the purpose to align part of the light emitted by the sample with the p-direction (which is the only component which will pass through the Glan-Taylor). Suppose we want to detect the p-polarized component of the light emitted by the sample. Then we just have to rotate the half-waveplate in such a way that its neutral axis is aligned with the p-direction. Thus, the p-polarized component will pass through the $\lambda/2$ and the GT unaffected and it will be detected.

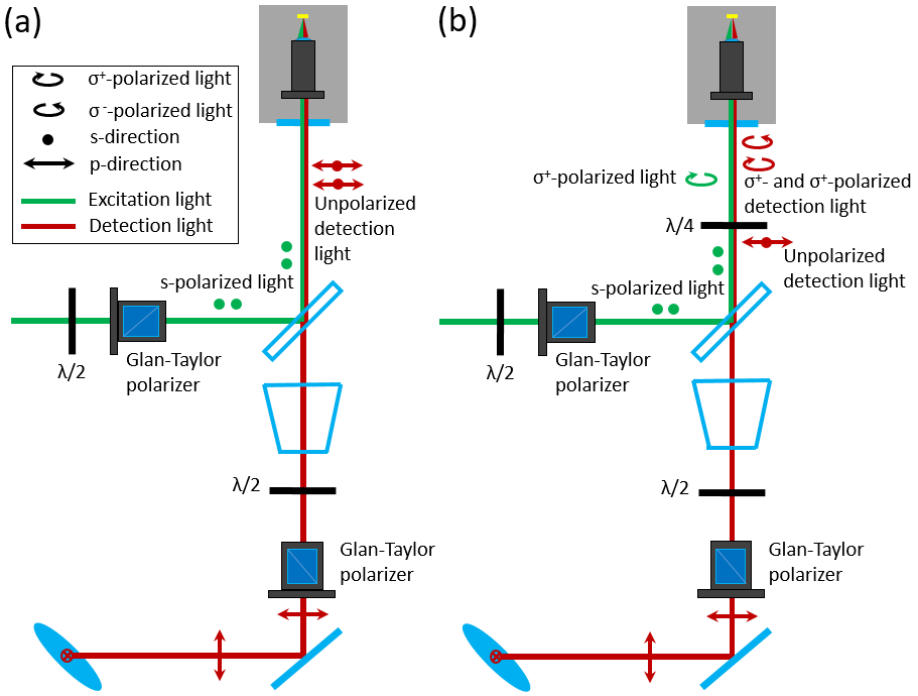

Figure 2.7: Sketch of the modified set-up for allowing the detection of the polarization in a (a) linear and (b) circular basis.

If instead we want to detect the s-component of the light emitted by the sample we have to put the neutral axis of the half-waveplate at 45° with respect to both s and p-directions. As it is known the half waveplate rotates the polarization of light by 2θ where θ is the angle between the neutral axis and the incident light polarization direction. In such a way the incident s-component is rotated by 90° and it is thus aligned with the p-direction. Hence, it can pass through the Glan-Taylor and be detected. Therefore, the way in which we can collect either the s- or p-component of the light emitted by the sample is turning the detection half-waveplate. Note that for intermediate directions of the neutral axis of the $\lambda/2$, the polarization emission at an arbitrary direction can be detected.

Exciting and detecting in a circularly polarized basis is done by simply adding a quarter-waveplate ($\lambda/4$), with a neutral axis oriented at 45° with respect to both s and p-direction, before the window of the cryostat. This is shown in panel (b) of Fig. (2.7). Once the s-polarized excitation light has passed the $\lambda/4$ it will be converted in a circularly polarized wave which will excite the sample. We call this state σ^+. The light emitted from the sample will be both σ^+- and σ^--polarized and it will cross the $\lambda/4$ a second time. In particular the σ^+ component will become a p-wave.

Exactly as before, if the detection half-waveplate has its optical axis parallel to p-direction this p-polarized light will cross the detection GT and will be detected. However, what we are actually detecting is the σ^+ emission from the sample.

Similarly, if the detection half-waveplate has its optical axis at 45° with respect to p-direction the light which will be coupled to p is the one polarized along s, which in turn represent the σ^- emission from the sample.

Summarizing, for detecting light which is co-circularly (cross-circularly) polarized with the laser we have to put the detection half-waveplate neutral axis along (at 45° with) p-direction.

Once the intensity of the polarization components of the light emitted by the sample is detected it is possible to define the degree of linear and circular polarization in the following way:

$$P_{lin} = \frac{I_s - I_p}{I_s + I_p} \quad , \quad P_c = \frac{I_{\sigma^+} - I_{\sigma^-}}{I_{\sigma^+} + I_{\sigma^-}} \tag{2.2}$$

Where I is the intensity of the detected signal and the subscript indicate the polarization component. If the first (second) value is different from 0 it means that the signal is linearly (circulary) polarized. This is true in case of perfect linear (circular) excitation and in case every optical element (such as the objective and the cryostat windows) doesn't alter the polarization state of the light. We measured that the degree of linear and circular polarization in excitation is as high as 99.9 %.

Taking into account the repeatability of the waveplates manual positioning, the small retardance changes as a function of the wavelength and the error in the fitting of the data we estimate the errors on both polarization degrees in detection to be around ±2 %.

2.2.3 Detection set-up

Once the signal coming from the sample has been collected and its polarization analysed it is sent to a detector. It consists of a spectrograph in which light passes through a slit, is then dispersed by a monochromator and detected by a CCD (charge-coupled device) camera.

The monochromator is an Acton SpectraPro 2500i purchased from Princeton Instruments. Three different gratings mounted on a turret can be selected in accordance with the experimental needs. Their specifications are listed in the Tab. (2.1)

Table 2.1: The table shows the characteristic of the three gratings used in our monochromator.

Grating (grooves/mm)	Spectral range (nm)	Dispersion (nm/mm)	Pixel resolution (at 700 nm) (μeV)
300	174	6.5	290
600	85	3.2	72
1200	41	1.52	38

To calculate the best spectral resolution we can achieve, we can image on the CCD the slit illuminated by a monochromatic light source, (i. e. a laser) when using the most dispersive grating. The observed full width at half maximum of the peak is 1.47 pixels (grating at zero order) which corresponds to 40 μm. The

difference between this value and the theoretical pixel resolution is due to the imaging system.

The CCD (Roper Scientific) is an "epitaxial silicon" layer with a squared active area of $20 \times 20\,\mu$m divided in 100×1340 pixels. Each pixel is defined by a gate electrode, separated by the silicon layer by a thin insulator (SiO_2) and it is thus a capacitor (a p-doped metal-oxide-semiconductor field effect transistor or MOS-FET). In each pixel incident photons are converted into electron hole pairs. The photoexcited electrons are then separated from holes by the voltage applied by the gate and stored in the capacitor. Then they are transferred from one pixel to another and in the end to a charge amplifier. The value is then converted into a voltage and finally digitalised.

To reduce the thermal noise (dark current) the chip is refrigerated by means of a liquid nitrogen bath. The operation temperature is approximately 150 K. Moreover, the CCD is built in the so called back-illuminated geometry in which the light reaches the photocatode without passing through the wiring system where the intensity of the signal would significantly drop. The quantum efficiency which can be achieved is as high as 95% at 750 nm. This is achieved thanks to the material used, the epitaxial silicon: an high resistance silicon on an highly doped silicon substrate which minimizes the distance in which the charge generated by photons can diffuse without being counted as a signal. The use of a high resistance silicon substrate is referred to deep depletion. The spectral range which can be detected is comprised between 120 and 1100 nm.

2.2.4 Excitation light sources

In this sub-section we will describe the excitation light sources used throughout this PhD research. In particular they are mainly lasers and a white light source used for exciting the sample in the contrast reflectivity measurements.

This latter is a halogen white-light lamp with a power stabilizer to prevent fluctuation in the exciting power density. As the source is not a point and has instead the shape of a filament, we need to use a system of lens and pinholes to create a collimated beam of well defined size. This is important to minimize the diameter of the excitation spot on the sample.

The most commonly used laser is a helium-neon. The wavelength is 632.8 nm (1.96 eV). If an higher excitation energy is needed we can also use a green laser with excitation wavelength 532 nm corresponding to an energy of 2.33 eV.

Another laser which has been extensively used is the SolsTiS from the company M squared. This continuous wave (CW) Titanium Sapphire laser posses exceptional characteristic which we will briefly describe. First it is very compact: its dimensions are approximately $24 \times 14 \times 9$ cm. The output power is up to 2 W. Several optical elements are used to reduce it, as for our work powers of few μW are sufficient.

Most importantly, it provides broad continuous tuning from 700 nm to 1000 nm with an ultra narrow linewidth which is much narrower than our detector spectral resolution: it is smaller than 100 kHz which corresponds to less than 0.2 fm at 780 nm. This exceptionally narrow linewidth allows an ultra-precise selection of the exciting wavelength which is kept stable for several hours. In our experiment the wavelength is known down to the 0.1 pm and its stabilized by a wave-meter.

When tunable excitation is needed below 700 nm an optical parametric oscillator (OPO) purchased from APE (Angewandte Physik & Elektronik) is used. This laser is synchronously pumped by a mode-locked Ti:Sapphire laser and generates a train of picosecond or femtosecond pulses. The possibility of replacing the active crystal give us the chance of obtaining laser light in the visible range $505-750$ nm or in the infrared one ($1-1.6\,\mu$m). Experiments presented in this manuscript where performed using the visible light generated by this laser.

2.2.5 Main optical spectroscopy techniques

In the final part of this section we will put aside the instrumentation to focus on the optical techniques which will be extensively used throughout this manuscript. It is thus fundamental to understand them and to know which kind of information it is possible to obtain by using them.

The first technique we will describe is the differential reflectivity (reflectivity contrast or DR/R) and it is the only technique which doesn't require the use of a laser. This technique is used instead of absorption as the Si/SiO_2 substrate does not allow simple transmission measurements. The idea is to excite a sample with a white light source and to detect the reflected light. If the sample absorbs light at a certain wavelength, the collected light will show a dip in the spectrum.

Sometimes, the dips present in simple reflectivity are too weak to be identified directly. Moreover, the signal could be generated by the substrate. That's why a second spectrum is acquired from a region close to the sample but not on it. This second spectrum is called reference. The signal and the reference are subtracted (from here the name differential reflectivity) and then normalized by dividing the result by the reference. A scheme clarifying the process is shown in Fig. (2.8).

The sample is an encapsulated WSe_2 monolayer (see Chapter 3) and its reflectivity is shown in panel (b). Please note the intensity of the main transition, which is clearly visible even before the calculation of the DR/R spectrum. This is an indication of the strong light absorption by the TMD monolayer. In panel (a) we can see instead the light reflected by the heterostructure from a position (green spot in panel (c)) in which the monolayer is absent. No transition is visible and what we observe is the spectral shape on the white light source and the instrumental response. Finally the differential reflectivity spectrum is shown in panel (d). The visibility of the peaks is clearly enhanced.

Reflectivity is very helpful to uncover the energy of the main A- and B-exciton transitions. In reflectivity we are sensitive to transitions with large oscillator strength and large density of states [49].

The other technique which will be used used extensively is photoluminescence (PL). A laser with energy larger than the bandgap is used to excite the sample. The electrons (or excitons in our case) relax and recombine radiatively and the emitted photons are detected.

The PL spectrum presents in general much more features than the reflectivity one. This happens because defects states inside the energy band-gap are often present. In this general case the electron can relax (emitting one or more phonons) to one of these defect states and then recombine radiatively. Hence, more peaks than the one related to the main exciton transitions may appear at lower energy. Moreover, if the relaxation time to these defects states is much

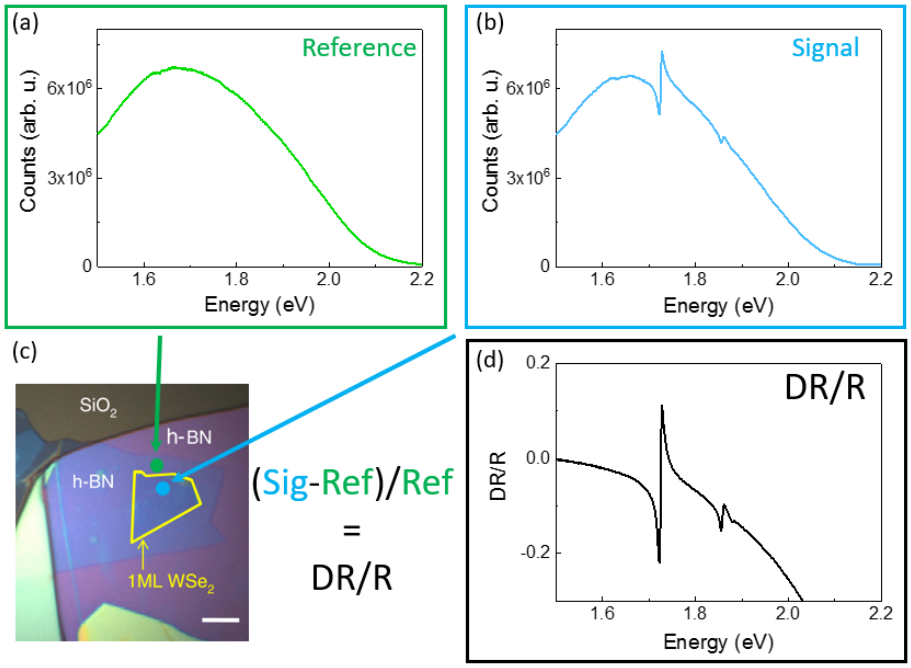

Figure 2.8: Scheme useful for explaining how a differential reflectivity spectrum is obtained. In (a) we show the acquired spectrum from outside the sample, which is called reference (Ref). Then we get the spectrum from the sample, the signal (Sig) shown in (b). The positions on the heterostructure (an encapsulated WSe_2 monolayer at $T = 4\,\mathrm{K}$) from which the two spectra are taken are shown in the microcraph in (c) as coloured circles. The two spectra are subtracted and divided by the reference. This give us the reflectivity contrast (DR/R) shown in panel (d).

faster than the radiative recombination time in the bottom of the conduction band, the exciton peak may not be visible at all.

A consequence of this is that in photoluminescence the intensity of the peaks is not an indication of the density of states or of the oscillator strength. While in reflectivity the main peak is always the one related to the transition with higher density of states, in PL this is not the case, as the intensity of the peaks is a consequence of complex interplays between different processes in the material. Indeed, in PL, we probe the population of a state, so usually lower laying transitions are favoured.

Sometimes it is possible to observe photoluminescence from states at higher energy than the lowest lying exciton transition (excited states). This signal is referred as hot photoluminescence and it is generally very weak.

A more complex but extremely useful technique is photoluminescence excitation which we will often call with its acronym: PLE. This technique consist in collecting photoluminescence spectra as a function of the excitation energy. If all the other parameters are kept constant this dependence can give us information about the absorption of the material and the subsequent relaxation process to the emitting state.

To explain this technique, let's consider a simple model system in which a

defect level is located inside the band gap of a semiconductor. If we excite the material with a laser which energy is higher than the bandgap, we will promote some electrons from the valence to the conduction band. These electrons will relax to the bottom of the conduction band and some of them will be trapped by the defect. If the defect allows radiative recombination we will see a PL emission due to the electron going back in a valence state. This is the PL signal we want to monitor.

If we scan the laser excitation energy across the bandgap suddenly we will be unable of promoting electrons across the gap which in turn will not occupy the defect state and will not recombine emitting light: the PL intensity will drop to zero. This idea can be observed in panel (a) of Fig. (2.9).

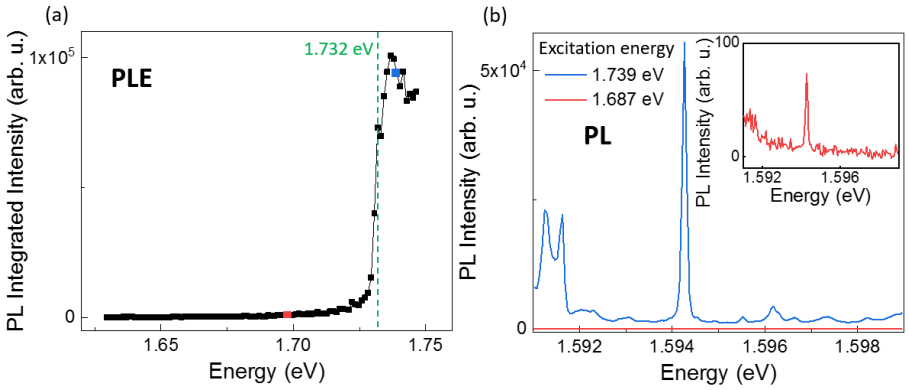

Figure 2.9: (a) Each black square represent the integrated PL intensity of the emission of a GaAs quantum dot at $T = 4\,\mathrm{K}$ at a specific excitation energy. (b) $T = 4\,\mathrm{K}$ PL spectrum of the quantum dot excited above the band-gap (in blue) and below it (in red). The drop of the signal is so intense that the peak is no longer visible, if not in a magnified graph (inset).

The sample under study is a single GaAs quantum dot embedded in a $Al_{0.15}Ga_{0.85}As$ matrix. It effectively acts as a defect: when the energy we use for excitation is above the one of the band-gap of the matrix (which is 1.732 eV at 4 K [97]), we generate conduction electrons which are then trapped inside the dot. We thus observe PL emission, as shown by the blue curve in panel (b). However, once the excitation energy is moved below the value of the energy gap the emission is strongly suppressed (of about 5 orders of magnitude). Each square in the graph shown in panel (a) is obtained by calculating the area under the quantum dot emission peak. It is thus an integrated photoluminescence intensity. A symilar system, not detailed in this manuscript, has been studied to investigate nuclear and spin dynamics in original GaAs droplet dots [94].

A textbook example of PLE in presence of excitons can be observed in an encapsulated WSe_2 sample which PL spectrum for above band gap excitation is shown in panel (a) of Fig. (2.10).

The transition at higher energy is related to the recombination of the neutral A-exciton. At lower energy two more transitions are visible. Many details about encapsulated WSe_2 samples will be provided in Chapter 3. For the moment what is interesting is showing the results of a PLE experiment in which the exciting laser energy is moved across the neutral exciton transition (labelled X^0) and

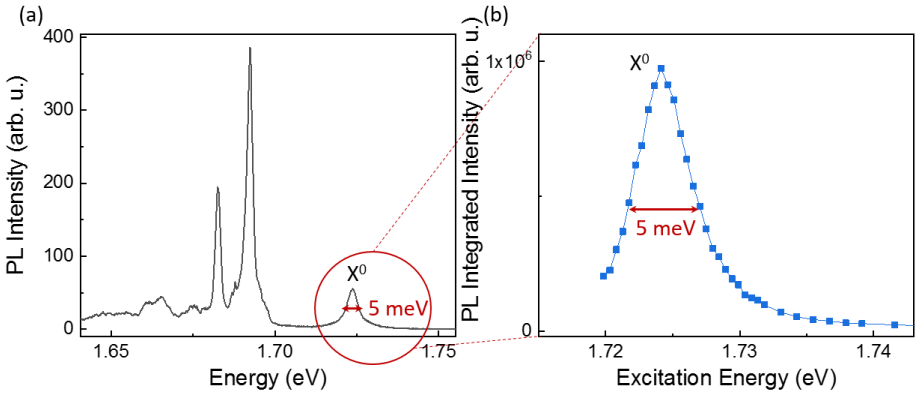

Figure 2.10: (a) Photoluminescence spectrum of an encapsulated WSe_2 sample, obtained by above bandgap excitation ($E_{laser} = 1.96\,\text{eV}$). The high energy peak is due to the radiative recombination of the excitons. (b) Integrated photoluminescence intensity of the two other transition appearing in the PL spectrum. The shape is clearly the one of a peak and is a consequence of the increased absorption of light by X^0. All the data are obtained at $T = 4\,\text{K}$.

the intensity of the two other peaks is monitored. If we plot the integrated PL intensity of the two other transitions as a function of the exciting energy we observe a peak which correspond to the absorption peak of the neutral exciton. This is shown in panel (b) of Fig. (2.10).

As explained before (in the case of the band gap absorption) the light absorption is strongly increased when the exciting energy matches an electronic transition. Once many excitons (electrons) are created they can relax to low lying energy states. If this relaxation is sufficiently efficient the PL signal from these low lying states will be enhanced. This is the concept behind photoluminescence excitation which is therefore a measure for the absorption and energy relaxation. If the latter is inefficient, there is no PL signal despite strong absorption.

2.3 Optical spectroscopy of TMDs

In this last section we will start presenting the first spectra of transition metal dichalcogenide monolayers. Since the beginning of the research on these crystals, the monolayer were transferred in many different substrates but, in particular on Si/SiO_2 wafers. This happened for two reasons: from one side these substrates improve the optical contrast, thus making easier to locate a monolayer [13, 98], from the other they are compatible with the microelectronic standards [99]. This is the reason why many of the experimental results which we will present here were obtained in sample exfoliated in Si/SiO_2 wafers.

Once a monolayer is transferred, the sample can be loaded in the cryostat and can be cooled down to low temperature, around 4 K. The first basic characterization is done using differential reflectivity because the spectra are easier to interpret. The results can be seen in Fig. (2.11) where the results for the four most prominent members of the TMDs family can be seen.

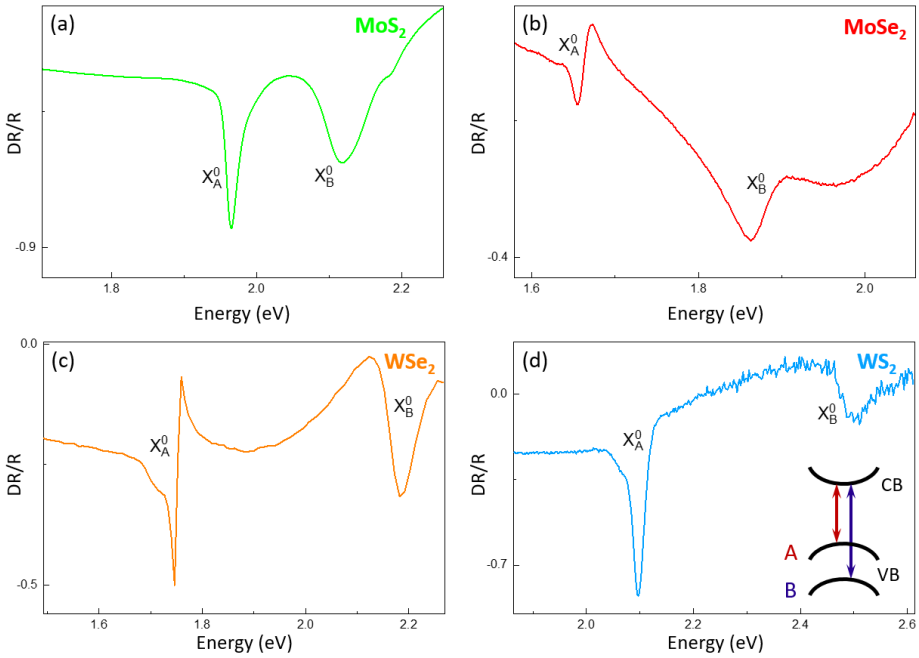

Figure 2.11: Reflectivity spectra of (a) MoS_2, (b) $MoSe_2$, (c) WSe_2 and (d) WS_2 monolayer exfoliated on Si/SiO_2, obtained while exciting the samples at $T = 4\,K$ with a white halogen lamp. Each spectrum shows two transitions, the A- and B-excitons. Their origin is due to the presence of the spin-orbit splitting of the bands, as shown in the inset. The spectra come from unpublished data from our laboratory.

As it is clearly observed, each material shows two transition in its reflectivity spectrum. As discussed in Chapter 1 a consequence of the large spin-orbit splitting of the valence band is the presence of two types of neutral excitons which we called A- and B-exciton and which are labelled X^0_A and X^0_B respectively. Please note how the energy separation changes from the molibdenum to the tungsten compounds, from about 200 meV to aproximately 400 meV [32, 43, 54, 56, 57]. This energy separation is mainly determined by the spin-orbit splitting of the valence band but in addition, differences in exciton binding energies for A- and B-excitons can play a role, as well as the small conduction band spin splitting.

Thanks to the reflectivity characterization it is thus possible to assign a spectral position to the excitons. Hence, we will have a reference to identify the emission peak of the neutral A-exciton in PL. Indeed, after reflectivity, a fundamental characterization consist in checking the photoluminescence spectrum of the four TMD materials. The emission response under σ^+ laser excitation, can be observed in Fig. (2.12), where both the co-circularly polarized and cross-circularly polarized components are displayed.

To identify the peaks it is necessary to use different approaches. As already mentioned, the neutral A-exciton can be labelled by simply controlling the spectral position of the peak at higher energy and comparing it with the value obtained from the reflectivity spectrum. The absence of Stokes shift leads to a good accordance between the two. This accordance is less good for MoS_2 and the reason will be explained later.

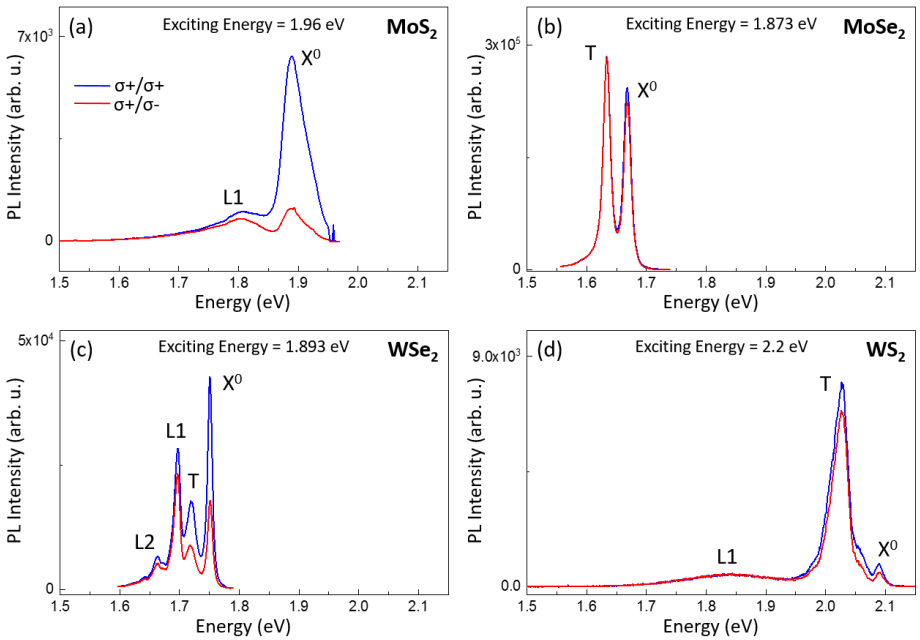

Figure 2.12: Circularly polarized components of the photoluminescence spectrum of a (a) MoS_2, (b) $MoSe_2$, (c) WSe_2 and (d) WS_2 monolayer exfoliated on Si/SiO_2, obtained while exciting the samples at $T = 4\,K$ with a σ^+ polarized laser. The excitation energy is different for the four samples and it is indicated in each panel. Note that in labelling the A-exciton we drop the subscript A as in PL there is no ambiguity. The neutral A-exciton is thus indicated simply as X^0.

The peaks labelled as L are localized states, excitons localized around a defect. We can deduce that by measuring the spectrum of the monolayer as a function of temperature. As the thermal energy of the excitons increase their chances to escape from the defects potential well increase accordingly and the peaks disappear. The trion or charged exciton (a three particles complex labelled as T) is instead identified in devices in which is possible to effectively dope the material and by theoretical predictions of its energy separation from the neutral exciton X^0. More details about this complex will be provided in Chapter 5. Notice that the B-exciton is not considered: hot PL emission from this state is very weak as excitons prefer to relax to the A-exciton level and then recombine radiatively.

As discussed in Chapter 1 the peculiar bandstructure of TMDs lead to polarization specific selection rules. As a consequence one of the two inequivalent K valleys can be addressed only by one of the two circularly polarized light components, σ^+ or σ^-. As the polarization lifetime is comparable or longer than the recombination one, the unbalance of exciton population created by a polarized laser in the two polarization states is partially conserved in some members of the TMDs family. The results is that the PL emission is co-circularly polarized with respect to the laser as clearly observed in panel (a) and (c) of Fig. (2.12).

What is evident from these spectra is the low optical quality of the samples. Indeed, many defect related peaks are presents and the linewidth of the

transitions is very large, from $\approx 10\,\text{meV}$ of $MoSe_2$ and WSe_2 to the approximately $50\,\text{meV}$ of MoS_2. Moreover, the spectral position of the neutral exciton in MoS_2 is very variable from monolayer to monolayer and has been find in between $1.88\,\text{eV}$ and $1.90\,\text{eV}$ at $4\,\text{K}$ [55, 70, 100, 101]. This poor optical quality is a fundamental problem when one thinks about applications of TMDs in optoelectronics. The situation is even worse when one realizes that the material with lower optical quality is also the most naturally aboundant, thanks to the diffusion of the mineral molybdenite [102].

However, it has been shown by Cadiz et al. [103] in our group that the linewidth of MoS_2 can be reduced down to the value of $10\,\text{meV}$ and that the peak shown in panel (a) of Fig. (2.12) is actually not associated with the neutral exciton recombination, contrary to many reports in the literature. For doing this a super-acid treatment [104] of the Si/SiO_2 substrate was performed before the transfer of the monolayer. The effect of this treatment is to strongly increase the photoluminescence intensity of MoS_2 monolayers at room temperature. On the other side, the intense defect related peak visible at $4\,\text{K}$ is reduced and the intensity of both trion and X^0 is increased, as shown in panel (b) of Fig. (2.13).

The cyan and green curves in panel (b) show the photoluminescence emission of two MoS_2 monolayers exfoliated on a pristine Si/SiO_2 substrate. As we can see a main, broad peak appears at low energy while two smaller and narrower peaks, the trion and the neutral exciton, are slightly visible. These two peaks becomes dominant when a monolayer is exfoliated on a substrate which has been previously treated with the super acid bis(trifluoro-methane) sulfonimide (TFSI). In contrast, the broad emission at lower energy almost disappear.

Please note also that the spectral position of X^0 is $1.96\,\text{eV}$, in better agreement with the reflectivity measurements. Many experimental studies on this monolayer have been performed exciting the material with an helium-neon laser which energy is exactly $1.96\,\text{eV}$. This corresponds to a resonant excitation scheme.

If we consider the monolayers labelled C and D in panel (b) of Fig. (2.13) we already notice a great difference between their spectrum and the one we showed in Fig. (2.12). The reason is that the first two spectra have been obtained with very low laser excitation power. Indeed, in a different work in our group, Cadiz et al. proved that laser excitation can induce irreversible changes in the optical spectrum of monolayer MoS_2, even for power densities considered low and safe for the material [105]. These results are shown in panel (c) and (d) of Fig. (2.13).

The neutral exciton emission is totally quenched and also the trion and the defect peak intensities are reduced. A peak at 1.9 is the dominant feature in the spectrum after the monolayer has been exposed to high power density. Note how this spectrum (the red curve in panel (c) of Fig. (2.13)) is very similar to the one shown in Fig. (2.12). Please note also that the power used for altering the optcal response of the MoS_2 monolayer so dramatically was used in many experiments [101, 106, 107, 108, 109, 110, 111].

Changes of the PL emission as a functon of the incident power have been observed for monolayer $MoSe_2$ [105] and WS_2 [112, 113] as well. These results seem to prove that the optical stability of the TMDs and their environment is too fragile in unprotected samples. We will show in the next chapter that considerable more stable and robust samples in terms of laser damage threshold can be obtained through encapsulation in hexagonal boron nitride [114].

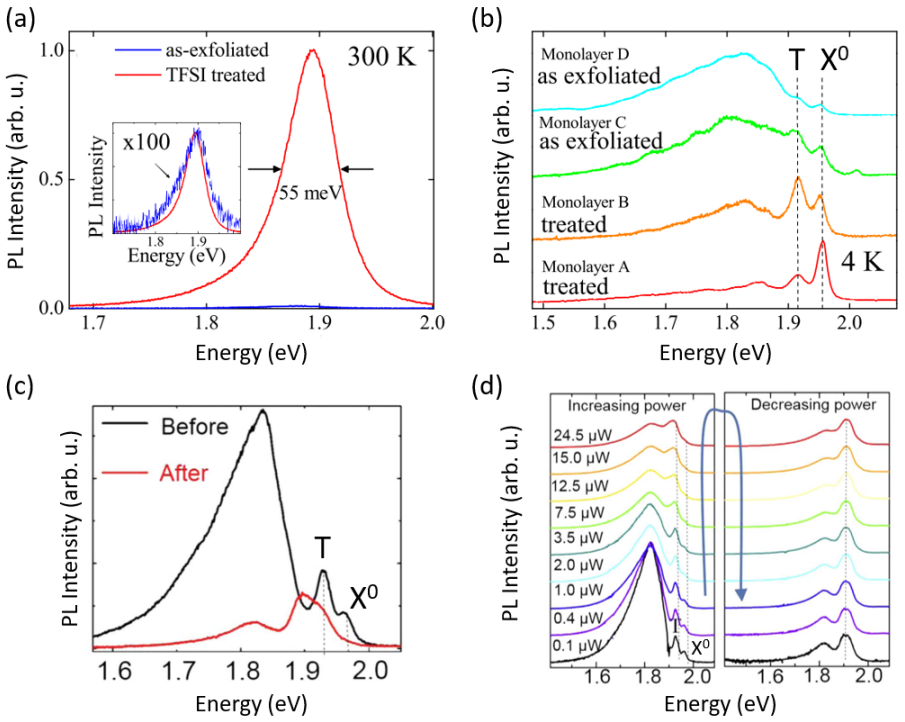

Figure 2.13: (a) Comparison of room temperature photoluminescence signal from a MoS_2 monolayer exfoliated on Si/SiO_2 with one which was treated with the super-acid TFSI. (b) Comparison of the 4 K PL spectra of four MoS_2 monolayers, two exfoliated on a pristine Si/SiO_2 and two on substrates which were treated with the acid. (c) Comparison between the low excitation power PL spectrum of the same MoS_2 monolayer before and after it was exposed to high power densities at $T = 4$ K. (d) Evolution of the low temperature PL spectrum of a MoS_2 monolayer as a function of the laser power density. Panel (a) and (b) are reprinted from Cadiz et al. [103] while (c) and (d) from [105].

2.4 Conclusions

We dedicated this chapter to the description of the experimental set-ups and techniques we used for studying transition metal dichalcogenide monolayers. We start with the description of the original technique which was used for separate a single layer from a bulk crystal: the micro-mechanical cleavage or exfoliation technique. We then describe how this technique was improved and how we fabricated the samples which will be analysed in the following chapters.

We then introduced our instruments, such as the cryostats where the sample are kept in vacuum at 4 K, the confocal microscopes with high spatial and polarization resolution, the detection set-up and the main light sources used for exciting the monolayers.

We then described the main optical techniques which will be extensively used in the next chapters. These techniques are our main tool for investigating the samples and understanding the physics which govern these atomically thin crystals. In the end the first optical spectra obtained with those techniques are

presented. They show how optical spectroscopy of TMDs looked like before the beginning of this PhD project.

Chapter 3

Optical transitions in WSe_2 monolayers

In the previous chapters, when we introduced the members of the TMDs family, we showed their photoluminescence and reflectivity spectra and we presented data from initial monolayer samples exfoliated on SiO_2 substrates which were obtained before the works described in this manuscript were performed. The topic of this chapter is instead an extensive description of the improvements made in characterizing monolayer WSe_2 and its recently uncovered optical properties.

Indeed, in the last three years great advancements have been made in terms of sample fabrication, which resulted in an improved optical response by all the TMDs [115, 116, 117, 114, 118, 119, 120, 121, 122, 123]. In the photoluminescence (PL) spectra, some peaks which were thought to be defect related, disappeared and new much narrower transitions were observed instead. The drastic reduction of the linewidth, which lately reached the homogeneous broadening limit around 1 meV at $T = 4\,\mathrm{K}$, allowed the whole community to obtain more information from the optical spectra of TMD monolayers but also forced it to perform anew all the basic characterization. As part of the community we spend many months in doing so and this chapter collects all the main results we achieved in studying the new WSe_2 monolayers samples. However, many questions raised by the better definition of the optical transitions remain still without an answer. Encouraging a discussion about those questions is also among the purposes of this chapter.

We will start describing the encapsulation in hexagonal born nitride (hBN): the fabrication technique which allowed us to access the intrinsic properties of TMD monolayers. We will then focus our attention on WSe_2 and, after having discussed the optical spectra obtained from these new samples, we will proceed at the identification of the optical transitions, using all the spectroscopy techniques available. Particular attention will be paid to a peak appearing at 1.68 eV in photoluminescence, on the low energy side of the main A-exciton transition (1.72 eV), which will be identified as the dark exciton: a spin-forbidden transition with an out of plane optical dipole. In differential reflectivity we will extensively investigate the excited A-exciton states. In the end we will discuss the exciton-phonon coupling in this material which appears to play a very important role.

3.1 Exciton states in high quality samples

hBN encapsulation is the process of building a van der Waals heterostructure in which a TMD monolayer is exfoliated on top of a bulky hBN crystal (typically around 100 nm thick) and subsequently covered by a second, much thinner, hBN cap layer (≈ 10 nm).

This technique is not new. Already in 2010 it was shown by Dean et al. that putting graphene in between two layers of hBN resulted in a vast improvement of electron mobility [124]. The reason why that happened will be addressed in the following but using hBN as a substrate proved itself to be a very effective technique for improving the optical and electronic quality of many 2D materials. The first material that we exfoliated on high quality hBN crystals [89] was WSe_2 [116] but then we proceed to do the same with all the other members of the TMDs family. The drastic change of the optical quality is shown in Fig. (3.1).

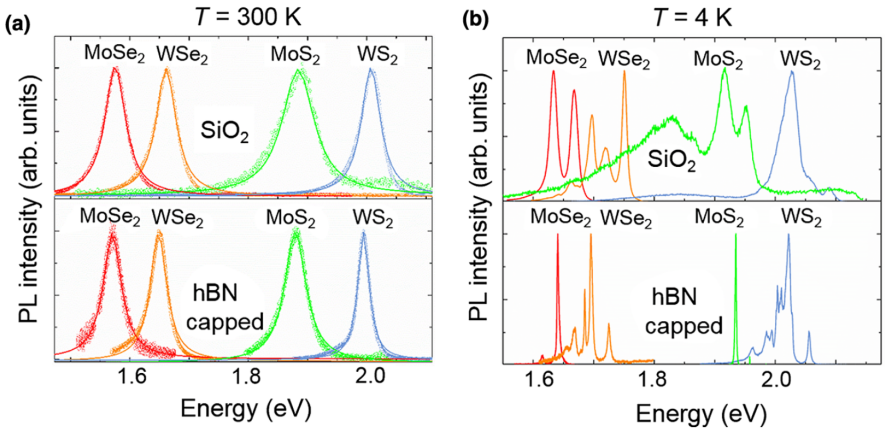

Figure 3.1: PL spectra of four TMDs at (a) $T = 300$ K and (b) at $T = 4$ K. In the upper part of both panels we show the PL spectra of the monolayer exfoliated on SiO_2. In the lower part, the monolayer is exfoliated on top of a thick (~ 100 nm) hexagonal boron nitride flake and subsequently covered with a thin (~ 10 nm) hBN layer. The heterostructure is placed on top of a Si/SiO_2 wafer. The figure is reprinted from Cadiz et al. [114].

As one can see, the linewidths of the neutral exciton transitions (but of the other transitions as well) for the samples exfoliated on SiO_2 are broad as they are dominated by inhomogeneous broadening. If we consider the data at room temperature, the full width at half maximum (FWHM) of the neutral exciton in monolayers $MoSe_2$ and WSe_2 is typically around 50 meV and it is even larger for MoS_2. The FWHM of all TMDs are reduced when the flakes are exfoliated on hBN, being MoS_2 still the one with the larger linewidth. When moving at $T = 4$ K the situation improves for some of the materials exfoliated on Si/SiO_2, but not for the sulphide compounds whose FWHM is about 50 meV even at low temperature [106, 70, 125, 100, 55, 101, 126, 127, 128]. But if we consider the flakes exfoliated on hBN at $T = 4$ K all of them present a very sharp linewidth, less than 5 meV. All the values are reported in Tab. (3.1).

As we already pointed out, the first material to be encapsulated in hBN was

Table 3.1: The table shows the values of the FWHM of the neutral exciton X^0 for the four members of the TMDs family after hBN encapsulation, for the sample set analyzed in [114].

Material	Linewidth (meV) at 300 K	Linewidth (meV) at 4 K
$MoSe_2$	$34-36$	$2.4-4.9$
WSe_2	$32-34$	$3.9-4.2$
MoS_2	$44-46$	$2.0-4.5$
WS_2	$23-25$	$4.3-4.8$

WSe_2 and its 4 K spectrum has been already presented in panel (b) of Fig. (3.1). From now on, this chapter will focus mainly on this material so it is useful to isolate its spectra on Si/SiO_2 and on hBN from the other TMDs and to present them in Fig. (3.2)

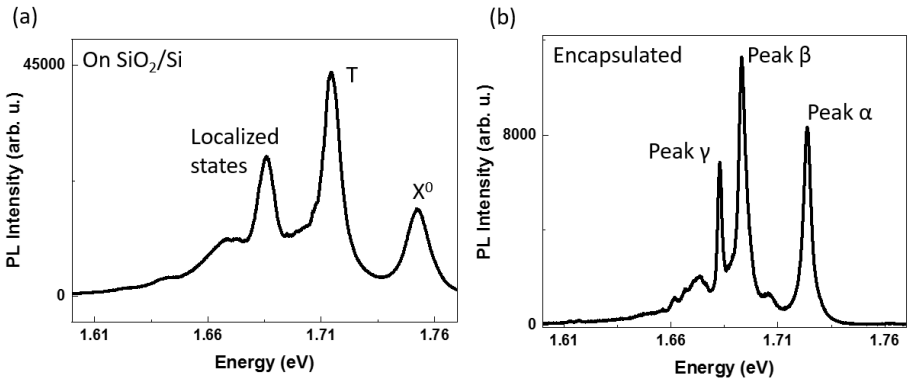

Figure 3.2: (a) Photoluminescene spectrum of a WSe_2 monolayer exfoliated on a Si/SiO_2 substrate. The labels indicate the peaks according to literature identification: from right to left we have the neutral exciton X^0, the trion T and a peak ascribed to localized excitons. (b) Photoluminescence spectrum of a WSe_2 monolayer encapsulated in hBN. Both spectra are obtained exciting the sample with a helium-neon laser (632.8 nm) at $T = 4$ K.

The main difference between the two spectra presented in panel (a) and (b) of Fig. (3.2) is the reduction of the linewidth of the transitions. Even if an identification of the peaks required detailed studies (which will be presented later) we can already anticipate that the most energetic peak, labelled peak α in Fig. (3.2) (b), is the neutral exciton, X^0. A clear identification of the second peak (peak β) is still missing but was tempting to identify it as a trion (T) for comparison with the spectrum from the sample on Si/SiO_2 shown in section (2.3) in Chapter 2.

When exfoliated on silicon dioxide the neutral exciton has a linewidth of ~ 13 meV which is reduced to ~ 4 meV in-between hBN. Also the trion shows a marked reduction of the linewidth, from ~ 10 meV to 4 meV while the low energy peak is even narrower, reaching a FWHM of only 2 meV. Moreover, the

whole spectrum is redshifted by approximately 30 meV, which is a surprisingly small shift when we consider the change of the dielectric environment. We will discuss this below.

If it is clear that encapsulation improves the optical quality of the TMDs monolayer, understanding why this happens is less trivial. When Dean et al. exfoliated graphene on an hBN layer they attributed the improved transport response of the material to the fact that hBN surface is atomically flat and free of dangling bonds and charge traps [124]. It is indeed well known that SiO_2 has a rough surface which can create ripples in the monolayer exfoliated on top of it and that impurities and charge traps are present. The charged states can locally influence the dielectric environment felt by excitons in the monolayer which, by definition, lay close to the surface and whose field line are mainly outside the slab itself. Thus, their size and binding energy are randomly modified by the random variation of the surrounding environment. This in turn lead to an inhomogeneous broadening of the linewidths.

Another effect of the encapsulation is a change of the dielectric constant. This should in principle lead to a great difference in the energy position of the neutral exciton but as pointed out above the change is just of 30 meV. This happens because the modification of the dielectric environment changes both the size of the free-particle bandgap and the exciton binding energy. It is believed that these two contributions almost cancel out in TMD monolayers, leading to only a small global redshift of the neutral exciton peak [129, 130].

3.1.1 Identification of the neutral exciton

Now that the main effects observed on the PL spectrum of an encapsulated WSe_2 monolayer have been discussed let's concentrate on how the peaks can be identified. As anticipated the peak at higher energy (1.72 eV) is the neutral A-exciton X^0 and this can be shown immediately by comparing the PL spectrum with a differential reflectivity one, shown in Fig. (3.3)

As already explained in Chapter 2 the transitions appearing in differential reflectivity measurements are those which present a strong density of states and a large oscillator strength and thus correspond to real electronic transitions. The only transition appearing in this part of the spectrum corresponds to the absorption of photons by the neutral A-excitons. The energy position of this transition agrees very well with the one of the peak at higher energy in PL, at 1.72 eV. Thus, it will be called neutral exciton or X^0 from now on.

Please note how the width of the transition in reflectivity is much narrower than the one for samples exfoliated in Si/SiO_2: compare with Fig. (2.12) in Chapter 2. It is also worthy to underline how the energy matching of the peaks with the two optical techniques implies the absence of any Stokes shift and thus of any localization of the X^0 complex.

Another way to probe the absorption of light by the encapsulated WSe_2 monolayer is photoluminescence excitation (PLE). As already discussed in Chapter 2, it consist in exciting a sample with a laser which is tunable in energy and in detecting the photoluminescence emission of the sample at a different energy. When the laser energy matches a transition with large absorption probability, the detected emission will be greatly enhanced. We thus perform the following experiment: we scan our tunable Ti:Sapphire laser (see section (2.2)) through the X^0 transition of a WSe_2 monolayer encapsulated on hBN and we detect the

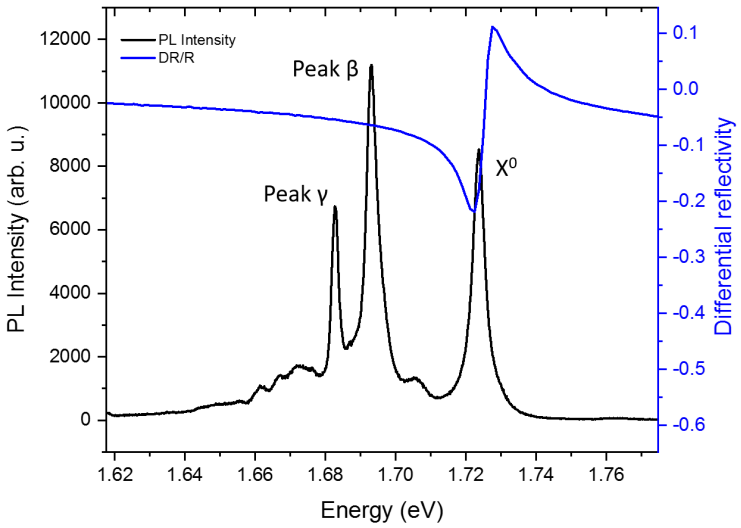

Figure 3.3: The black curve (same as Fig. (3.2) (b)) shows the photoluminescence spectrum of a WSe_2 monolayer encapsulated in hBN excited by a helium-neon laser. The blue one is a differential reflectivity measure of the same sample and it is defined as $(R_{\text{sig}} - R_{\text{ref}})/R_{\text{ref}}$ where R_{sig} is the reflected light coming from the monolayer while R_{ref} is the reflection from the heterostructure withouth the monolayer. Both spectra are obtained at $T = 4\,\text{K}$.

emission coming from the two other peaks at lower energy (peak β at 1.69 eV and peak γ at 1.68 eV). Please note that in addition to absorption also energy relaxation towards the lower energy states has to be efficient. The results are shown in Fig. (3.4).

The black curve shows again the PL spectra of an encapsulated sample under helium-neon excitation at $T = 4\,\text{K}$. The two blue curves are the PLE data and represent the total intensity emitted by peak β (full squares) and by peak γ (empty squares) as a function of the excitation laser energy. See Chapter 2 for a full description of PLE.

As one can see the PLE resonances perfectly match the energy position of the X^0 peak in PL. Moreover, the linewidths measured from PL and PLE data are very similar. These are other two strong proofs that the peak identification is correct.

There is also another experimental result which can be used to prove it, that is the dependence of the emission intensity on the power density of the exciting laser. We can indeed excite the monolayer with a helium-neon laser, measure the area below the X^0 peak and plot it as a function of the incident power in a log-log scale. The data are shown in Fig. (3.5)

The black squares in panel (a) represent the energy integrated PL intensity of the neutral exciton at different powers while the black line is the linear fit to the data. In a log-log graph the dependence of the integrated PL intensity as a function of the incident power gives an indication of the available electronic states. Saturation of the PL intensity would suggest a limited number of available electronic states (for example emission from defects) whereas linear proportionality between emission and excitation power is typically expected for

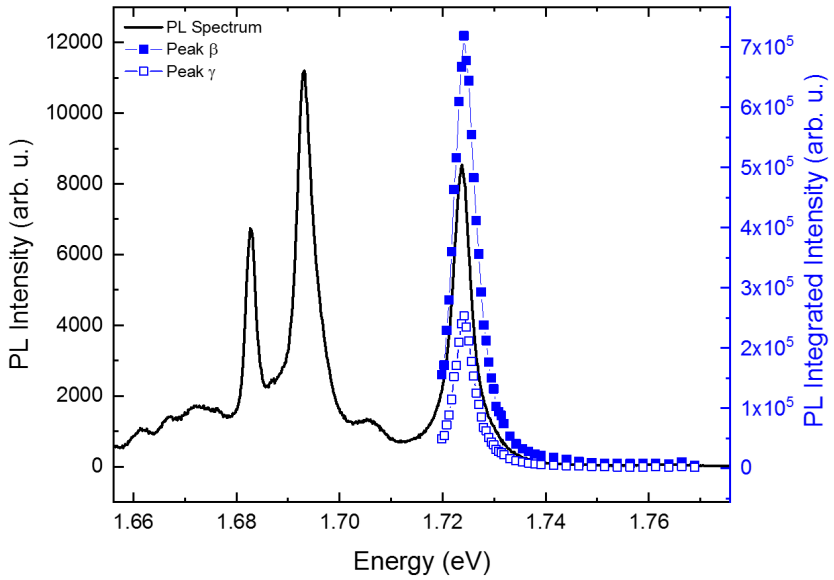

Figure 3.4: Comparison of the energy position of the neutral exciton PL emission at low temperature ($T = 4\,\mathrm{K}$) of a WSe_2 monolayer under 632.8 nm excitation (same curve as Fig. (3.2) (b) and Fig. (3.3)) with the position of the resonances in the photoluminescence excitation (PLE) scan. We resonantly excite the neutral exciton while detecting the emission from the two peaks (labelled peak β and peak γ) at lower energy. When the laser is detuned from the strictly resonant energy, the intensity of the two peaks drops as photons are not absorbed anymore by the material. The data are the same shown in Fig. (2.10) in Chapter 2 where the integrated intensity of peak β and peak γ was added.

intrinsic, not defect related, PL emission.

A particular case is a linear behaviour with a slope equal to one (two). It means that if we double the incident power we double (multiply by four) the number of excitons which in turn emit a twice as (four times) intense signal when they recombine. If the PL emission does not originate from exciton recombination but is instead defect related, a saturating behaviour is expected because when a certain power (i.e. number of incident photons) is reached all the available states will be occupied. Therefore, a further increase of the power will not change the PL emission intensity. However, if the defect density is large, the saturation may require higher powers than those reached in an experiment. That's why this measure alone is not a proof of the nature of the transition but is consistent with the behaviour of the neutral exciton.

Another method to identify the neutral exciton is checking the polarization of the PL signal. WSe_2 monolayer emission presents strong valley polarization and coherence which means that the PL signal shows the same circular and linear polarization as the exciting laser. These data are shown in Fig. (3.6)

As it can be seen the neutral exciton is co-circularly polarized with the laser. This means that after the successful initialization of one of the valleys (electrons can be excited just in one of the two valleys if the exciting polarization is purely circular) the excitons recombine before scattering to the other polarization state.

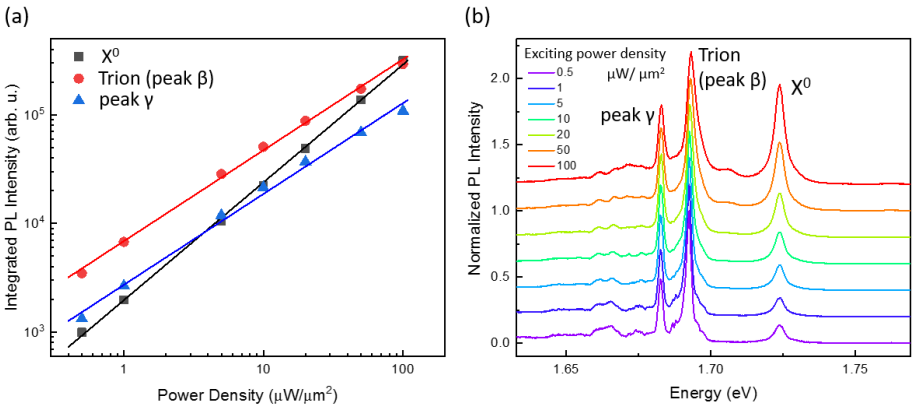

Figure 3.5: Data from an encapsulated WSe_2 monolayer at $T = 4\,K$. (a) Dependence of the energy integrated photoluminescence intensity of the neutral exciton (black squares), of the trion (peak β, red circles) and of peak γ (blue triangles) as a function of the incident power density over two orders of magnitude. The black, red and blue lines are the best linear fits to the data and have a slope $m = 1.08$ for X^0, $n = 0.84$ for peak β and $l = 0.84$ for peak γ. (b) Waterfall plot which shows the normalized PL spectra as a function of the exciting power density.

Moreover, the emission of the neutral exciton results co-polarized even after linear excitation i.e. valley coherence is successfully generated and maintained [131]. As linearly polarized light can be seen as a coherent superposition of circularly polarized waves with a well defined phase difference, the fact that the emitted PL keeps the direction of linear polarization means that this phase difference is conserved through the absorption of the photon and the subsequent relaxation to the X^0 state.

Only X^0 so far displayed both linear and circular polarization following non-resonant excitation. The trion is a three particle complex and there is no well defined phase relationship between the incident photon polarization and the photon emitted by an exciton that captures an additional carrier.

It is important to note that the wavelength used for exciting the sample in these polarization measurements is 669.5 nm and it is chosen on purpose as it corresponds to the energy of the A-exciton first excited state, labelled A:2s (see section (3.3) for the explaination of the notation). This is why X^0 (i.e. the A:1s state) is so intense compared to the other peaks. More details will be provided later in this chapter, in section (3.3). However, substantial PL polarization can be obtained with an energy excitation not resonant with a particular excited state such as that provided by an helium-neon laser (632.8 nm or 1.96 eV) [132].

3.1.2 Identification of the charged exciton: trion

Many of the characteristic of the peak at 1.69 eV (peak β) can be already observed in the images presented before. First, it is located approximately at the same distance from X^0 than the trion (charged exciton) peak in samples exfoliated on SiO_2: about 31 meV. That's why it is very tempting to call it trion, as we will do in the following, for simplicity.

Let's consider the reflectivity spectrum in Fig. (3.3): the trion transition is

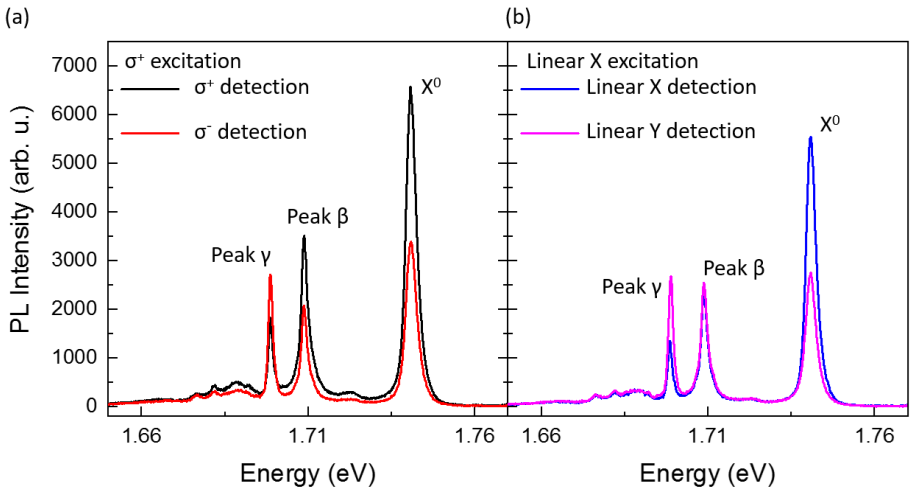

Figure 3.6: (a) $T = 4\,\mathrm{K}$ PL spectra showing the σ^+ and σ^- emission of an encapsulated WSe_2 monolayer after excitation with a σ^+ polarized laser with a power density of $20\,\mu\mathrm{W}/\mu\mathrm{m}^2$ and an energy of 1.852 eV (669.5 nm). The neutral exciton is co-polarized with the laser. (b) The same but this time the basis is linear and the laser is linearly polarized in an arbitrary direction labelled as X.

not observed, while in PL is the dominant transition. We thus deduce that the absorption of light by this complex is very small but the radiative recombination seems to be very efficient. From these facts we can also deduce that the effective doping in encapsulated monolayers is very small but not zero, as the absorption of light by charged excitons is not strong but still some trions have to exist as we see them in photoluminescence.

If we look at Fig. (3.5) we see that also the trion intensity (red circles) evolves linearly with the power density (at least in the explored power range) but the slope is smaller than one and equal to 0.84. This means that an increase of incident photons corresponds to a smaller increase of emitted photons by the trion. That's why at higher energy the neutral exciton becomes almost as intense as the trion, as can be seen in the panel (b) of Fig. (3.5).

Another interesting observation regards the polarization of the trion. Similar to monolayers exfoliated on Si/SiO_2 the trion shows valley polarization but not valley coherence [133].

It is clear that for identifying a charged compound the ideal situation would be being able to change the charge density in the monolayer. This can be done by effectively doping the sample in a device which will be better described later in Chapter 5. These charge tunable devices allowed us to study the PL emission and reflectivity contrast of an encapsulated WSe_2 monolayer as a function of gate voltage. We will show that at negative voltage the transition associated to the neutral exciton disappears, replaced by a transition which is necessarily due to the negatively charged trion. Moreover, this transition is actually a doublet. The details about this experiment and the explanation of the data will be the subject of Chapter 5.

It is important to note at this point that the energy distance of the "trion" peak from X^0 is ~ 31 meV which almost correspond to one Longitudinal Optical

phonon (LO) energy which in WSe_2 is of 32 meV [134]. We will discuss this issue later in this chapter, in section (3.4).

3.1.3 Origin of the optical transition at 1.68 eV

We have so far analysed the two peaks at 1.72 eV (X^0) and at 1.69 eV (trion). We will now discuss the peak at 1.68 eV (peak γ). It presents very interesting qualities. Its very narrow FWHM (2 meV) at a well defined energy seems to rule out a defect origin (usually broad emission). It does not appear in reflectivity and also in PL vanishes when the doping is increased, similarly to the neutral exciton (see Chapter 5). Its power dependence (PL intensity versus laser power) is linear with the same slope as the trion but it also seems to show saturation, as shown in panel (a) of Fig. (3.5) (blue triangles).

However, the most peculiar behaviour is observable in polarization: the peak is both cross-circularly and cross-linearly polarized with respect to the exciting laser as it can be seen in Fig. (3.6). In particular this behaviour appears to be the same over a broad range of excitation energies. As a linear polarization is more surprising we decided to map it: we excite the sample at three fixed linear polarization direction and we detect the PL emission at different angles as shown in panel (a) of Fig. (3.7).

The graph shows the integrated photoluminescence intensity as a function of the detection angle. It is clearly shown that the emission from peak γ does not depend on the linear polarization direction of the exciting laser or on the position of the detection spot on the monolayer sample, as shown in panel (b) of Fig. (3.7). Similar results are obtained when we excite and detect the PL signal at the same angle rotating both simultaneously: the maximum of PL is at the same angle suggesting that the emission is stronger along that direction. The results are shown in Fig. (3.7) (c). We also observe the same trend for different excitation energies as shown in panel (d).

This behaviour is typical from samples which present some physical anisotropy such as elongated quantum dots or nano-rods. However, the spatial de-localization of the peak and the nature of the heterostructure definitely exclude this explanation. Please note that we cannot exclude strain along a certain axis in the sample, possibly induced during the thermal annealing and subsequent cool-down of the structure performed during the fabrication procedure (see section (2.1)). The identification of the peak required thus more detailed studies which are presented in the next section. We will show that this peak is the dark exciton and that it has an optical dipole out of the monolayer plane.

3.2 Dark exciton (spin-forbidden) transitions

When the data presented above were collected, on the transition we labelled so far peak γ, there were indications of the existence of a low energy, optically inactive state in monolayer WSe_2 where the excitons would have relaxed and subsequently recombined non-radiatively [58]. This idea came mainly from the fact that the PL intensity from this material increases as a function of temperature: as T is increased, more and more excitons can reach the radiative level at higher energy thus, increasing the PL signal. A similar behaviour was observed in CdSe nano-crystals [135].

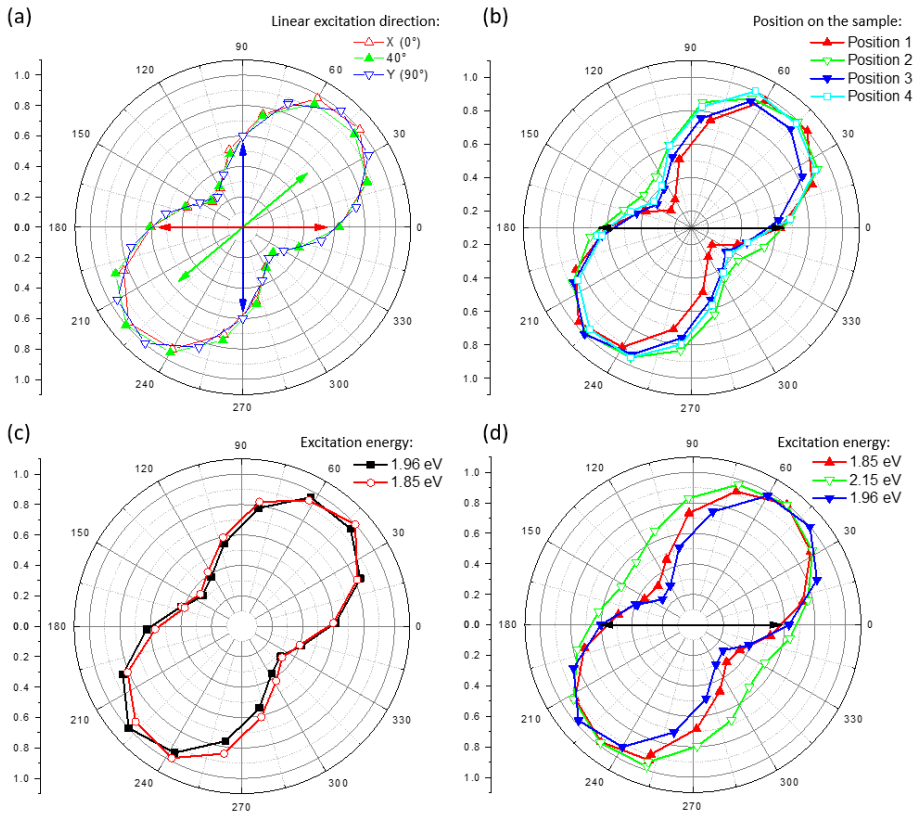

Figure 3.7: Data from an encapsulated WSe_2 monolayer at $T = 4\,K$. (a) Integrated PL intensity as a function of the detection angle for three different directions of the polarization of the exciting laser (a helium-neon, 632.8 nm), marked by green, red and blue double arrows. The X direction was arbitrarily defined and considered as the origin of the angle axis. As it can be seen the maximum of the emission does not depend on the laser polarization direction. In panel (b) the laser polarization direction is kept fixed at 0° (X-direction) while the spectra are collected from different spots on the monolayer sample surface. (c) The polarization of the laser is rotated and the detection angle is rotated accordingly: in this scheme we excite and detect along the same direction of polarization. The two curves correspons to two different excitation energies (1.96 eV from a helium-neon and 1.85 eV from an OPO). (d) The laser polarization direction is kept fixed at 0° (X-direction) while the excitation energy is varied.

Even if the nature of this "dark" state was unclear, it was suggested that it could originate from a spin-orbit splitting of the conduction band [58] idea which is broadly accepted today, although the exact order of bright and dark states also depends on the Coulomb exchange interaction [136]. A sketch useful for the explanation is shown in Fig. (3.8).

As one can see the conduction band is splitted in such a way that the low energy branch can host only spin states which have opposite direction with respect to those present in the upper valence band branch (the lower branch has been omitted). As a consequence an optical transition between the lowest

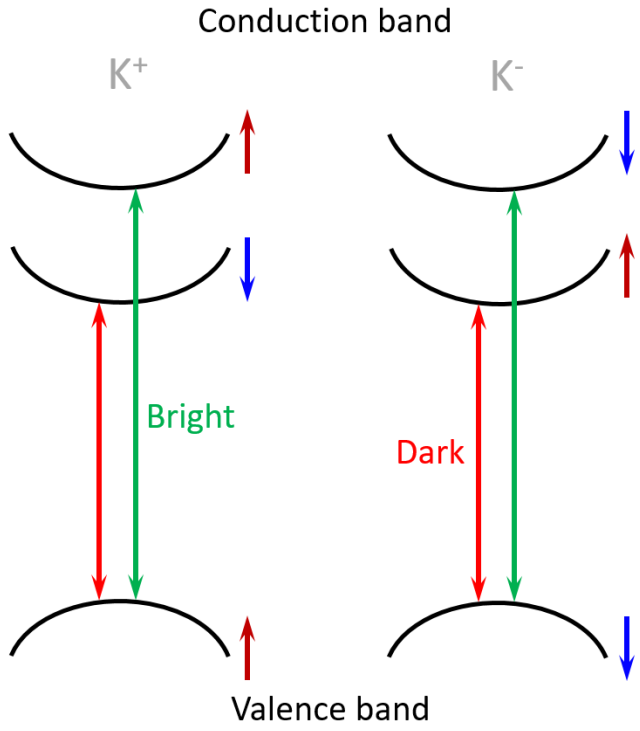

Figure 3.8: Sketch of the two K-valleys in a WSe_2 monolayer with the conduction band splitted by the spin-orbit interaction. The low energy state is, in principle, non-radiative as it is spin forbidden. For simplicity we omitted to show the lower branch of the valence band and all the spins are shown in the electron picture.

branch of the conduction band and the upper one of the valence band would be spin forbidden. This is the first of the two selection rules that must be satisfied in order to have a transition: the initial and final states must have the same spin orientation. This makes the excitons residing in the lower state optically dark as they can't emit light. The "bright" excitons about which we have talked so far (the neutral excitons X^0) are thus due to the recombination of an electron in the upper conduction band with a hole in the upper valence band.

The spectral separation between these two exciton states has been predicted to be around 30 meV [63] which is reasonably close to the value of 40 meV that we measured between the bright exciton X^0 and the peak that we labelled as peak γ. This is the reason why we suspected that peak γ was actually the dark exciton. However, if this is the case how is it possible that we observe this transition in PL? How can we prove this hypothesis?

Another ingredient essential to understand our observation is the fact that, as a consequence of the symmetry of the involved conduction and valence states, the band-to-band transitions are predicted to be anisotropic for light oscillating parallel to the plane of the monolayer or perpendicular to it. This is in analogy to experiments performed on III-V quantum wells, which showed that heavy-hole absorption is negligible when the incident light is polarized perpendicularly to the layers [137]. This is the second selection rule concerning the optical dipole

orientation: certain transitions are allowed just for a particular direction of oscillation of light. Both the spin and the optical dipole selection rules have to be satisfied in order to observe a transition.

We will show in the following that peak γ is indeed the dark exciton and it is coupled only to light polarized out of the plane of the monolayer. In particular, this polarization state is not well defined in the classic experimental configuration in which the light propagates perpendicularly to the monolayer. This explains the surprising findings on polarization of the emission.

3.2.1 Optical transitions for normal and in-plane excitation geometry

All the experiments on TMDs monolayer up to 2017 were performed in the configuration sketched in Fig. (3.9).

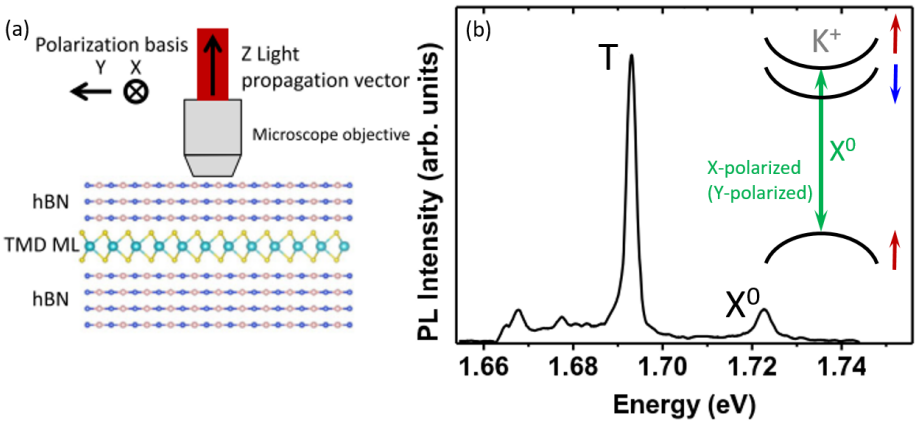

Figure 3.9: (a) Sketch of the usual experimental conditions used for studying a TMD monolayer. Light propagates perpendcular to the plane of the monolayer thus forcing the polarization to lay inside it. (b) PL emission of a WSe_2 monolayer excited with an helium-neon laser (1.96 eV) obtained in the configuration shown in panel (a) at $T = 13$ K. The inset shows a sketch of the K^+ valley where the electronic transition associated to the neutral exciton is indicated by a green arrow [92].

The light propagates along the z-direction and thus it can be polarized only in the monolayer plane (xy). In the left panel a spectrum of a WSe_2 monolayer obtained in this configuration is shown, using a microscope objective with low NA, i.e. we mainly collect light from excitons with optical dipoles in the monolayer plane. The neutral exciton transition is visible, being both spin and optical dipole allowed. Please note the absence of peak γ which (as we will prove) is only coupled to light oscillating out of the monolayer plane. For proving this, it is necessary to change the excitation scheme in such a way that both polarization directions become accessible. A theoretically simple but experimentally challenging way to do it is exciting the sample not from the top, but from the side as shown in Fig. (3.10). In this condition both in-plane and out-of-plane polarizations of light are accessible as the laser is propagating along y-direction.

The spectra in panel (b) clearly show that when the light oscillates out of the monolayer plane a new, intense transition appears. This transition has the

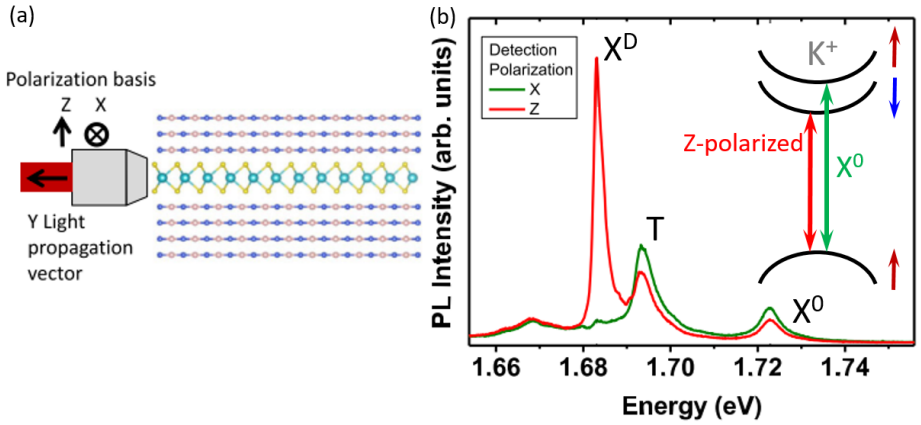

Figure 3.10: (a) Sketch of the experimental conditions we used for clarifying the nature of peak γ. Light propagates in the plane of the monolayer thus giving us access to both polarization states. (b) PL emissions at $T = 13\,\mathrm{K}$ of a WSe_2 monolayer excited by an helium-neon laser (1.96 eV) obtained in the configuration shown in panel (a). The two curves correspond to the in-plane polarization component of the PL emission (green) and to the out-of-plane one (red). The inset shows a sketch of the K^+ valley where the electronic transitions associated to the neutral exciton and to the dark exciton are indicated respectively by a green and a red arrow [92].

same linewidth of peak γ (observed previously, when exciting from the top and collecting the signal with a high NA objective) and it is at the same spectral distance from X^0. If we rotate the polarization of the light making it parallel to the x-direction the PL emission from the new transition disappears as we return in the same conditions of the normal incidence experiment. We thus deduce that peak γ is indeed a z-polarized transition. Moreover, thanks to a theoretical analysis performed in reference [92] by our collaborator M. Glazov and our group, we proved that the dark exciton is a z-polarized transition. This, and the predicted energy separation between the dark and the bright states, proves that peak γ is the dark exciton X^D.

Howerver, we stated above that the dark exciton is spin forbidden. This means that even if the optical dipole selection rule is satisfied in the side-incidence experimental configuration the spin selection rule is not. Therefore, we can deduce that in our real sample spin mixing has to be present and the spin selection rule is relaxed. The fact that spin mixing is present in WSe_2 monolayers was indeed proved by tracking the intensity of X^D as a function of an in-plane applied magnetic field [138]. Indeed, the spin-mixing is stronger when an in-plane field is applied and as a consequence the dark exciton should become brighter. This has been observed by Zhang et al. [138] and Molas et. al [139]

These results clarify the nature of the peak appearing at 1.68 eV in the encapsulated WSe_2 monolayers. However, if the dark exciton is really a z-polarized transition, why we do observe it in normal incidence configuration? Which means, why we do observe it in a configuration in which the optical dipole selection rule is not satisfied?

3.2.2 Excitons with in-plane and out-of plane dipoles

When we compare the spectrum in panel (b) of Fig. (3.9) with those we showed before (e.g. the one in Fig. (3.2)) we note that in the first one the dark exciton X^D is absent. This is actually not surprising as we demonstrated that the peak corresponds to a z-polarized transition which cannot emit light out of the plane of the monolayer. But if this is the case why we observed it in normal incidence configuration in Fig. (3.2) or in Fig. (3.6)?

We need to consider the high numerical aperture objective (NA= 0.82) used for our experiments. With reference to the Fig. (3.11), our objective is able to collect light propagating at high angles θ from the optical axis of the lens system. That light clearly contains a component polarized along the z-direction and thus allowed us to observe the dark exciton emission as shown in panel (d) of Fig. (3.11).

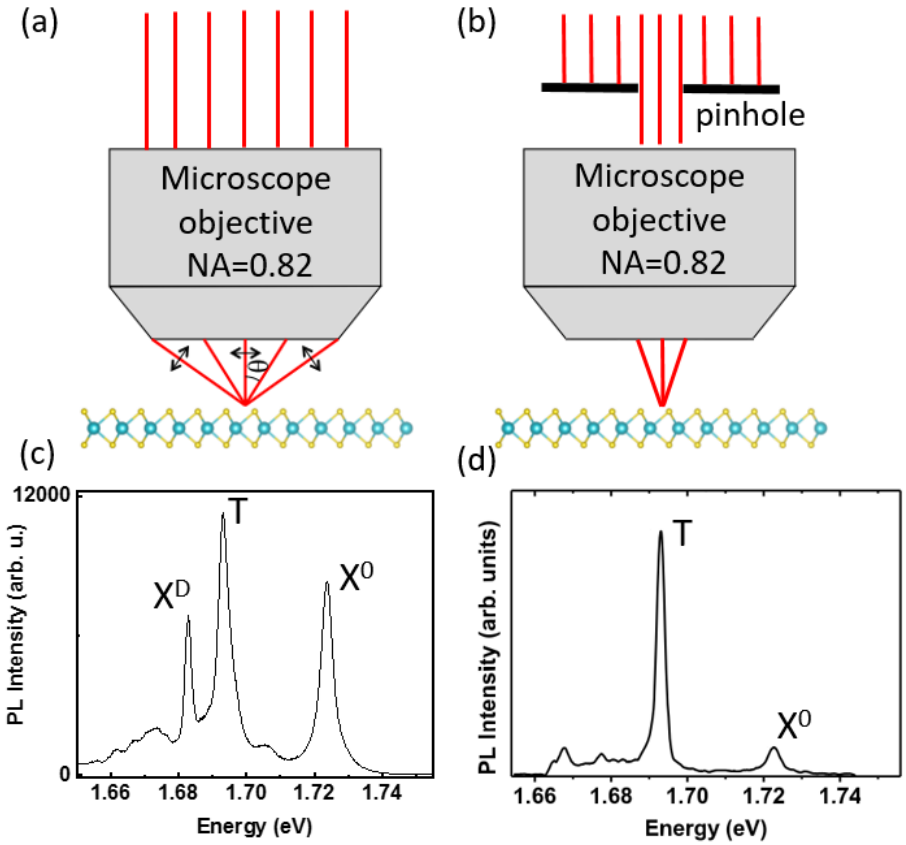

Figure 3.11: (a) Sketch of the microscope objective and of how the high numerical aperture allows us do detect the (z-polarized) dark exciton. (b) Variant of panel (a) in which the presence of a pinhole allows only the collection of light emitted perpendicularly to the sample surface. (c) PL spectrum of an encapsulated WSe_2 monolayer at $T = 4\,\mathrm{K}$ excited by a 1.96 eV laser in a normal incidence configuration with an high NA objective (NA=0.82), corresponding to the panel (a) excitation scheme. (d) Same as (c) but with the spectra obtained in the experimental configuration shown in (b).

For obtaining a spectra such as the one in Fig. (3.9) we have to put a pinhole in front of the objective for exciting and collecting only paraxial rays with almost no z-component. As a consequence the emission from the dark exciton is suppressed and only the bright exciton X^0 (dipole and spin allowed) and the trion appear in the spectrum. In reality the experiment we actually performed was slightly more challenging as it is more efficient to put the pinhole in the Fourier plane of the microscope objective and not directly in the beam path [92].

Side excitation is not the only way in which the dark exciton can be observed directly. At the same time we were working on this experiment, in Harvard, Zhou et al. were coupling X^D to surface plasmon polaritons [140]. Their experiment was the following: a WSe_2 monolayer encapsulated in hBN is placed on top of an atomically smooth silver film whose surface plasmon polaritons (SPPs) are strongly polarized in the z-direction. Thus, optical transitions are coupled to the SPPs by the near-field much more efficiently if they have an optical dipole oriented out-of-plane. The surface plasmons excited by the optical transitions in the monolayer are then converted again in far-field (FF) light with an appropriate out-coupling structure. In this way a transition with an optical dipole oriented out-of-plane (i.e. the dark exciton) is enhanced with respect those whose optical dipole lies in the plane. The device fabricated by Zhou et al. is shown in Fig. (3.12) .

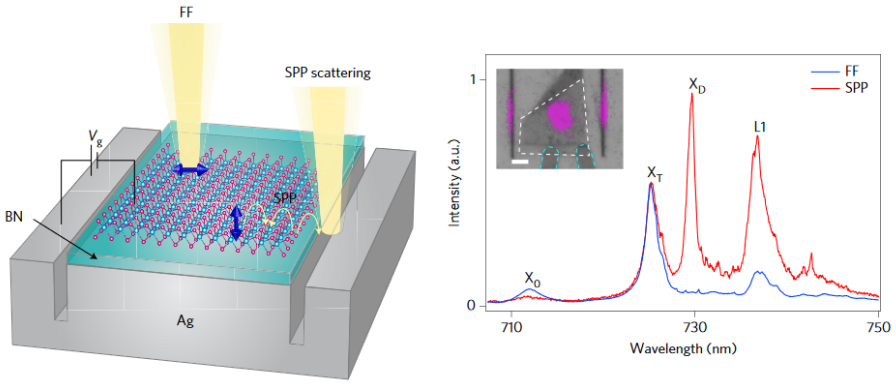

Figure 3.12: (a) Device used for coupling the dark exciton of a WSe_2 monolayer to a surface plasmon polariton which is in turn converted again into far-field light and detected. (b) Comparison between the spectrum obtained detecting directly the light emitted by the WSe_2 monolayer ($T = 4\,K$ excited at 660 nm) with the one out-coupled by the plasmonic structure. The dark exciton emission is strongly enhanced in the latter and it is the strongest transition. Both figures are reprinted from [140].

Their experimental configuration allowed them to directly detect the far-field light emitted by the monolayer from the same spot of laser excitation or the out-coupled light due to the scattered surface plasmon. The two spectra obtained in this way are compared in the panel (b) of the Fig. (3.12). The SPP photoluminescence spectrum shows an additional peak with a linewidth of 2 meV and at approximately 40 meV from X^0. From this observation we can deduce as well that the peak is associated with a transition with an out-of-plane optical dipole that preferentially couples to SPPs.

With the device fabricated in Harvard it also possible to change the charge density inside the monolayer as the silver film acts as a gate electrode. In this way it was possible to show that the emission from the neutral and the dark excitons disappear simultaneously when the doping is changed. It is also worthy to notice that Zhou et al. [140] also fabricated a similar device but with a $MoSe_2$ monolayer instead. In this case no new transitions appear in the SPP photoluminescence spectrum. This is not surprising as for the molibdenum compounds the spin-orbit splitting of the conduction band has been predicted to have a different sign. This results in the bright state as the the lowest energy transition, with the dark state above in energy not visible in PL. [63, 60, 58, 62, 33]. We also confirmed this in our original work by performing side-excitation experiments in encapsulated WS_2 and $MoSe_2$ monolayers. In the tungsten compound, the dark exciton is observed at a spectral distance of 55 meV from the bright neutral exciton while no trace of X^D is observed in the $MoSe_2$ monolayer [92].

After our initial work we proceeded in investigating the dark exciton transition in encapsulated WSe_2 monolayers. In particular we placed the heterostructure inside a magneto-cryostat measuring the behaviour of the dark exciton in an out of plane magnetic field up to 9 T [93]. What we observed is that a new transition becomes brighter on the low energy side of the dark exciton as shown in panel (b) of Fig. (3.13).

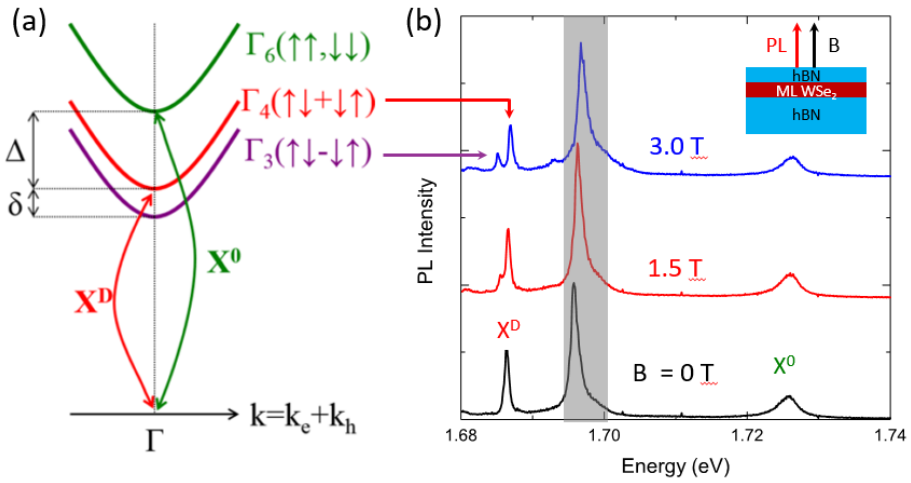

Figure 3.13: (a) Sketch of the exciton fine structure. The symmetry of the exciton states is marked on the figure where the arrows represent the electron spin components. In an applied magnetic field the states with symmetry Γ_3 and Γ_4 are coupled and an additional transition emerges. (b) Optical spectra of an encapsulated WSe_2 monolayer at $T = 4$ K for different magnetic fields. As the intensity of the field increases, the splitting and the mixing of the Γ_3 and Γ_4 states increase as well.

Indeed, it was predicted that the short-range exchange interaction between the electron and the hole should also lift the double degeneracy of dark neutral excitons (i.e. of the bottom conduction band) [141, 142]. This concept is shown in the sketch presented in panel (a) of Fig. (3.13). The new transition should be completely dark as, contrary to the high energy one which is coupled to z-

oscillating light, it is dipole forbidden. Thanks to the collected data, we were able to measure this fine-structure splitting which we found to be 0.6 ± 0.1 meV. We were also able to measure the dark exciton X^D lifetime: $\tau^D = 110 \pm 10$ ps. This is in agreement with having a lower oscillator strength than the bright exciton X^0, which recombines on a timescale of 1 ps [101].

3.3 Exciton excited states

As we saw in the previous sections, encapsulating a WSe_2 monolayer in-between hexagonal boron nitride led to a much clearer PL spectrum without defect-related peaks and with only three spectrally narrow transitions, two of which have now been unambiguously identified. The peak at higher energy (1.72 eV) is the bright neutral exciton X^0 while the one at 1.68 eV is the dark (neutral) exciton X^D. The transition in the middle, at 1.69 eV is tentatively ascribed to the trion. The reflectivity spectrum of the same encapsulated WSe_2 monolayer, shown in Fig. (3.3), is also very clear with only a single transition appearing around 1.72 eV, this peak is the bright neutral exciton X^0. However, if we take a look on a broader spectral range we note that this peak is not the only one appearing. In the panel (a) of Fig. (3.14) more transitions are clearly visible.

The most energetic one, about 430 meV above the neutral exciton is associated to the B-exciton, which is an exciton formed by an electron in the conduction band and an hole in the lowest branch of the valence band, as discussed in Chapter 1. This identification is made possible by the large spectral distance between the two excitons, of the same order of magnitude of the valence band spin-orbit splitting. The broadening mechanism for B-exciton transitions as compared to A-excitons ones are still under discussion. It could for example be due to very fast relaxation towards the A-exciton states.

In between these states other two less intense but narrower transitions appear which are believed to be the first two A-exciton excited state, at 133 meV and 156 meV above the X^0 state. In analogy with an hydrogen atom an electron in an exciton can occupy different energy levels which we will label with the principal quantum number n. When the electron-hole pair is in the most tightly bound state, n is equal to 1 and the recombination from this level is responsible for the neutral A-exciton (X^0) emission. We can label this transition A:1s where s stems for the s-shell zero angular momentum state (in analogy with the hydrogen atom). Thus, from now on we will refer to X^0 mainly as A:1s. When the recombination happens from an excited level the energy of the emitted photon will be higher. We claim that the transitions in Fig. (3.14) are due to the recombination of an exciton in its first and second excited state where n is equal to 2 and 3. We thus labelled these transitions A:2s and A:3s respectively and claim that they are the first two states of the Rydberg-like series for the neutral A-exciton (see also Chapter 1).

Reflectivity is not the only measurement which show the presence of these high energy states. They appear in particular in hot photoluminescence (photoluminescence from a level which is at higher energy) when the laser is tuned to resonantly excite the B:1s exciton transition (2.15 eV). These results are shown in panel (b) of Fig. (3.14). First we have performed PL excitation around the B-exciton observing a great increase in the emission from the A-exciton and its excited states. The integrated PL intensity of the A-exciton peak are indicated

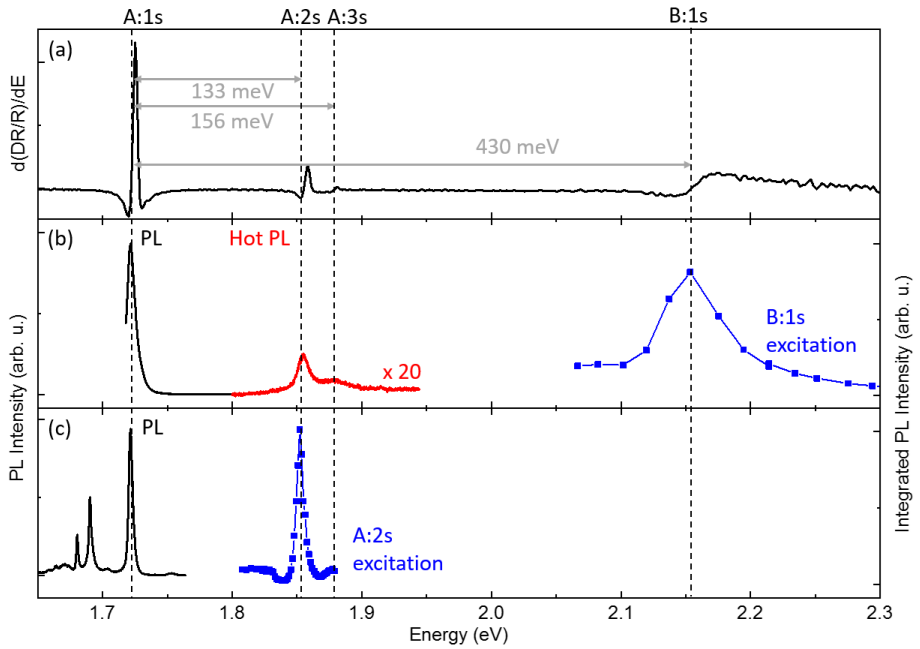

Figure 3.14: Low temperature ($T = 4\,\mathrm{K}$) data from a WSe_2 monolayer encapsulated in hBN. (a) First derivative of the differential reflectivity spectrum with respect to energy. Four transition are clearly visible and they are: the neutral A-exciton A:1s (X^0) at 1.72 eV, the first two A-exciton excited states A:2s (1.85 eV) and A:3s (1.88 eV) and the neutral B-exciton B:1s at 2.15 eV. (b) Photoluminescence spectrum of the neutral exciton with its excited states following the exact resonant excitation of the B-exciton at 2.15 eV. The red part of the curve was multiplied by 20 for making the excited states visible. The blue dots are the integrated photoluminescence intensity of the neutral exciton while the laser is scanned throug the B-exciton transition (photoluminescence excitation scan). (c) Similar to (b) but the PLE is performed across the excited states observing the emission from the neutral exciton, A:1s state. The black spectrum is obtaind for resonat A:2s excitation at 1.85 eV.

by blue dots in Fig. (3.14) (b). The resonance associated with the B-exciton is clearly visible. The PL and hot PL spectra correspond to the one obtained on resonance (laser energy at 2.15 eV). It is a single spectrum but its high energy part has been multiplied by 20 to make the excited states more visible. As indicated by the dashed lines connecting panels a-b-c, the spectral position of the peaks A:1s, A:2s, A:3s and B:1s is the same, independently of the used experimental technique.

In panel (c) we show the results of PLE around the A:2s excited state. A resonance in absorption is clearly visible: when the laser is tuned in resonance with the first excited state (1.85 eV) the emission from the A:1s is greatly enhanced. Again the energy position of the A:2s resonance matches the one obtained previously, with the other optical spectroscopy techniques. As for the reflectivity measurements, PLE shows that strong light absorption is present around 1.85 eV. This has to be related to a real electronic transition which we identify as an excited exciton state.

3.3.1 Oscillator strength of exciton states

Our measurements are not the only ones to show the presence of excited exciton states in TMDs monolayers [143, 50, 46, 144, 47, 145] but in our reflectivity spectra they appear to be very intense, as shown for monolayer WSe_2 in panel (a) of Fig. (3.14). One immediate explanation comes again from the improved optical quality which follows the hBN encapsulation. Indeed, the marked reduction of the linewidths has as an immediate side effect the improvement of the visibility of the transitions as the total intensity should not change. However, this effect is not enough to explain the experimentally observed relative intensity between A:1s and its excited states.

To develop a simple explanation, we start assuming that both the electron and the hole are confined in two dimensions, in a slab between two dielectrics. Thus, the electric potential deviates from the classic $1/r$ Coulomb law. Two consequences of this new 2D potential are a different energy spacing between the excited states and a deviation of the oscillator strengths of A:ns states, from the standard 3D hydrogen series. For this 2D Coulomb potential, the oscillator strength can be defined as follows:

$$f_n = \frac{f_1}{(2n-1)^3} \tag{3.1}$$

As a consequence the ratio between A:2s and A:1s intensity should be equal to 1/27 in our monolayer, while we observe a value close to 1/7. This argument was used to question the interpretation of these transitions as excited A-exciton states. This issue had to be addressed to convince the community of the correctness of the hypothesis.

First, we note that the SiO_2/hBN/ML/hBN heterostructure acts like a cavity. If we shine light on it, the wavelength dependent reflection will strongly change as a function of the relative layer thickness. In [146] we modelled the total reflection with the transfer matrix method formalism to simulate the response of a MoS_2 monolayer encapsulated in hBN (whose thickness has been measured by AFM) and exfoliated on top of a SiO_2/Si substrate where the SiO_2 layer is 83 nm thick. The obtained results matched very well with the experimental data as shown by the red curve in panel (c) of Fig. (3.15).

Additionally, we proved that changing the thickness of the layers has a great impact on the visibility of the different peaks. In other words, the measured differential reflectivity spectrum has to be convoluted: the visibility of the transitions depends on their intrinsic oscillator strength but also strongly on where they are spectrally positioned with respect to the underlying oscillations that come from interference effects in the multilayer van der Waals structure. As a result, the visibility for instance of the A:2s compared to the A:1s can be amplified or diminished. Therefore we can not extract the ratio of the oscillator strength directly from reflectivity, we need to model the underlying oscillations in addition. The results of our calculations for different hBN and SiO_2 thicknesses are shown in panel (c) of Fig. (3.15).

Moreover, in reference [146] we provide a quantitative analysis of the energies and oscillator strengths of the A-exciton Rydberg series and demonstrate its consistency with experimental observations. The potential used to describe the electron-hole interaction in an encapsulated sample is the Keldysh potential [52, 53] also referred to as Rytova-Keldysh potential:

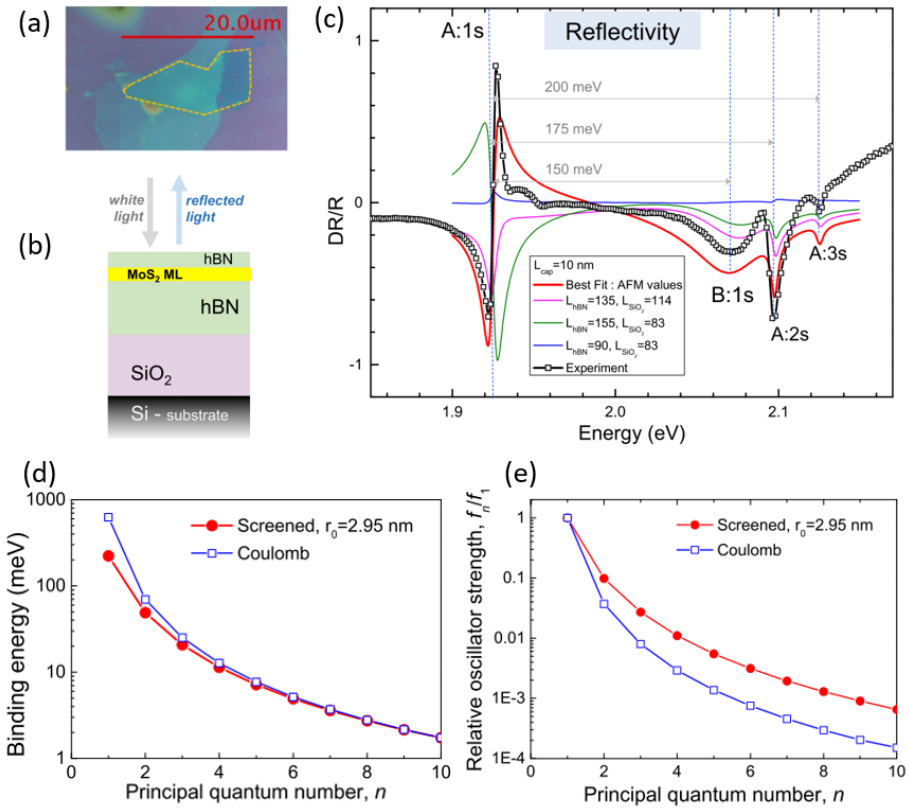

Figure 3.15: (a) Optical microscope image of a MoS_2 flake encapsulated in hBN. The scale bar is 20 μm. (b) Schematic of sample structure, the top (bottom) hBN layers are 7 ± 3 nm (130 ± 5 nm) thick as determined by AFM, the SiO_2 layer is 83 nm thick. (c) Differential reflectivity measurement $(R_{sig} - R_{ref})/R_{ref}$ performed with a power-stabilized white halogen lamp. The strong transition at lower energy (1.92 eV) is due to the A:1s absorption. At higher energies, three more transitions are clearly visible; the broader one at 2.07 eV is due to the B-exciton while the other two are the A:2s and A:3s excited A-exciton states, at 2.07 eV and 2.12 eV respectively. Model simulations using the thickness of the two hBN layers as determined by AFM are shown by the bold, red curve. Additional simulations (fine magenta, green, and blue) for different hBN and SiO_2 thicknesses show how the depth and shape of the exciton resonances depends on the thickness of the individual layers. The exciton resonance parameters are as follows: the energy position of A:1s exciton was tuned to the observed A:1s peak. binding energies of excited states are calculated and shown in panel (d). Radiative damping for the lowest lying states $\Gamma_{0,A:1s} = \Gamma_{0,B:1s} = 1$ meV, for excited states found from calculation and shown in panel (e). Nonradiative damping $\Gamma_A = 2.5$ meV, $\Gamma_B = 25$ meV. Refractive indices: $n_{\mathrm{hBN}} = 2.2$, $n_{\mathrm{SiO_2}} = 1.46$, $n_{\mathrm{Si}} = 3.5$. (e) Results from calculations which show the exciton binding energies as a function of principal quantum number n for ML MoS_2. The red dots are obtained for the screened potential in Eq. (3.2) ($r_0 = 2.95$ nm) while the blue squares for an unscreened 2D Coulomb potential. (e) Same as (d) but for the relative oscillator strength of the A-exciton excited states, normalized to the value of A:1s. The picture is taken from [146].

$$V(r) = -\frac{e^2}{8\epsilon_0 r_0}\left[H_0\left(\frac{\kappa r}{r_0}\right) + Y_0\left(\frac{\kappa r}{r_0}\right)\right] \tag{3.2}$$

where e is the fundamental charge, ϵ_0 is the vacuum permittivity, r_0 a screening length characterizing the material, H_0 and Y_0 the Struve and Neumann functions, respectively and κ is the average dielectric constant of the surrounding environment.

Starting from this 2D screened potential, we performed numerical calculations in order to estimate the exciton binding energy in encapsulated monolayer MoS_2. In doing so we consider the dielectric constant to be an effective value which takes into account the new dielectric environment in which the monolayer is placed. The chosen value is $\kappa = 4.5$, as in reference [147]. The screening distance is adjusted to match the experimental energy separation between the peaks. We found that both the binding energy (222 meV) and the relative intensity ($\sim 1/9$ and $1/27$ for A:2s and A:3s respectively) deviates from the 2D unscreened Coulomb potential as shown in panel (d) and (e) of Fig. (3.15). Even if these results were obtained for monolayer MoS_2 they are general and can thus explain our observation on WSe_2 as well. The combination of a heterostructure dependent reflectivity contrast and of a screened Coulomb potential can perfectly explain the enhanced visibility of the excited exciton states.

3.3.2 Excited states in magnetic fields

The definitive experiment which proved that the transitions observed in Fig. (3.14) are excited exciton states comes form magneto-optics and was performed in Los Alamos by Stier et al. [147]. Since long time, high field magneto-optical spectroscopy has been used for identify excited exciton states in other system such as III-V and II-VI semiconductors [148, 149, 150, 151, 152]. The reason is that each excited state undergoes a different shift as a function of the applied field.

In particular if the excited exciton, ns (with n the principal quantum number), is small compared to the characteristic magnetic length l_B of the system (weak field limit), the diamagnetic shift is quadratic in B and follows the equation:

$$\Delta E_{dia} = \frac{e^2}{8m_r}\langle r_\perp^2\rangle B^2 = \sigma B^2 \qquad ; \qquad \text{if } l_b \gg r_{ns} \tag{3.3}$$

Where $m_r = \frac{m_e m_h}{m_e + m_h}$ is the reduced mass of the exciton, σ is the diamagnetic coefficient and $\langle r_\perp^2\rangle$ is the expectation value of the radial coordinate perpendicular to B. This means that the larger the exciton, the less bound the particle is, the stronger will be its shift in a magnetic field. In the limit of strong field instead, when $l_B \ll r_{ns}$ the diamagnetic shift becomes proportional to B. From data obtained in this strong field limit the reduced mass can be deduced directly, independently from the model used. When the two lengths are comparable the behaviour of the diamagnetic shift as a function of the magnetic field is intermediate. The data obtained by Stier et al. are presented in Fig. (3.16) for hBN encapsulated WSe_2 monolayers.

From the pictures we can see the very different energy shifts of the 2s, 3s and 4s excited states of the A-exciton. In particular, the fits of the data, shows that 1s and 2s have a parabolic behaviour. At high field 3s start to increase

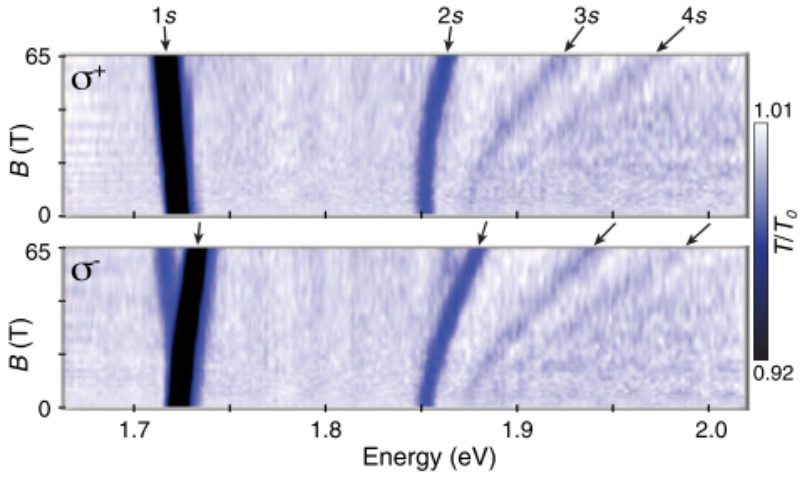

Figure 3.16: The contour plot shows the normalized transmission spectra of a WSe_2 monolayer encapsulated in hBN at $T = 4\,K$ as a function of energy and applied magnetic field. Darker colour means higher absorption as indicated by the legend on the left. Both components of circular polarization σ^+ and σ^- are detected. It is obvious that each peak shifts differently in the magnetic field and that the shift is larger for larger n. The picture is taken from [147].

linearly with the magnetic field while 4s become visible only when it is already in the linear regime. The fact that the data are in such a good agreement with the equations is a strong proof that the observed transitions are indeed excited exciton states. Moreover, the spectral positions (relatively to 1s) at zero magnetic field for 2s and 3s found by Stier et al. [147] are in excellent agreement with those we found in our encapsulated WSe_2 monolayers. We thus deduce that the peaks labelled A:2s and A:3s in our spectrum in Fig. (3.14) are real electronic transitions and not mere phonon replicas, as claimed in [115].

3.4 Exciton-phonon coupling

In this section we want to introduce another important phenomenon which appears to be ubiquitous in transition metal dichalcogenides [134, 153, 154, 155, 156, 157, 158, 159] and in semiconductor nanostructures in general [160, 161, 162, 163, 164, 165, 166]: the exciton-phonon interaction. It affects the optical properties of a system in many ways including energy relaxation, dephasing and linewidths broadening with temperature [167]. Phonon emission is also the process with which excitons lose energy and relax to a lower laying state.

A result of the exciton-phonon interaction are two very important processes called single and double-resonant Raman scattering which will be introduced in the following.

3.4.1 Raman scattering and Raman features

Raman scattering is a form of inelastic scattering of electromagnetic radiation by a material. This means that the scattered photons have a different energy from the incident ones. Generally, when a photon is scattered by a material it undergoes an elastic scattering (Rayleigh scattering) thus changing its propagation direction but keeping its energy constant. However, it may happen that some photons lose (gain) energy thus giving it to (absorbing it from) the medium. These energy exchanges are mediated by the vibrations of the material i.e. by phonons in the case that the considered material is a crystal.

In a very simple picture in which only one type of phonon is present, if we shine a laser onto a crystal and we detect the back-scattered light we will observe a strong reflection at the same energy (Rayleigh scattering) and two additional peaks (Raman features) on both the low and high energy side of the main emission. The first peak is called Stokes mode while the second anti-Stokes mode. The detection of scattered light from a material is called Raman spectroscopy. The energy separation between the incident laser and the different Raman features corresponds to the phonon energies ($E_{\text{phonon}} = E_{\text{laser}} - E_{\text{Raman}}$) and from them it is thus possible to deduce the different crystal vibration modes [168, 169, 170, 171].

In particular, this technique was used to distinguish between monolayer and multilayer flakes of TMDs [172, 173] as the type and intensities of the vibrational modes change when we consider one or more monolayers. If for example we consider $MoTe_2$, both monolayer and bilayer exhibit sharp PL peaks [174]. Raman spectroscopy is thus a very effective way to distinguish between the two as the absence of the low-energy A_{1g} phonon-related peak is a clear signature of a monolayer, as can be observed in panel (a) of Fig. (3.17)

These data are obtained in a so called non-resonant configuration as neither the laser energy nor the scattered Raman light are resonant with an electronic state, as depicted in the cartoon in Fig. (3.17). However, if the Raman line is resonant with a real transition it can be amplified and this can thus strongly modify the overall light emission. This process is called single-resonant Raman scattering and it is illustrated in panel (b) of Fig. (3.17).

In particular the excitation laser was tuned approximately 20 meV above the A:1s exciton transition which is close to the energy of the A_1' phonon. As the laser energy is moved in a photoluminescence excitation spectroscopy experiment we observe the narrow Raman line shifting as well. Indeed, the distance between the laser line and the associated Raman features is fixed by the energy of the phonons in the material. At the beginning, the Raman line is on the low energy side of the PL emission of the A:1s $MoTe_2$ exciton and is not very intense (Fig. (3.17) (b), upper panel). But when the laser is moved, the Raman line energy (i.e. laser energy minus phonon energy, $E_{\text{laser}} - E_{\text{phonon}}$) matches the one of A:1s. As a result the Raman scattering signal becomes very intense and is superimposed on the PL signal. We can distinguish between the PL and the Raman contributions thanks to the very different linewidths (Raman features roughly inherit the narrow linewidth of the Ti:Sapphire laser used for the experiment, see Fig. (3.17) (b), middle panel). When the laser is moved at even higher energies the Raman line is detuned from the exciton resonance and appears like a small shoulder on the high energy side of the peak. For further detuning, only the PL emission remains as shown in Fig. (3.17) (b), bottom

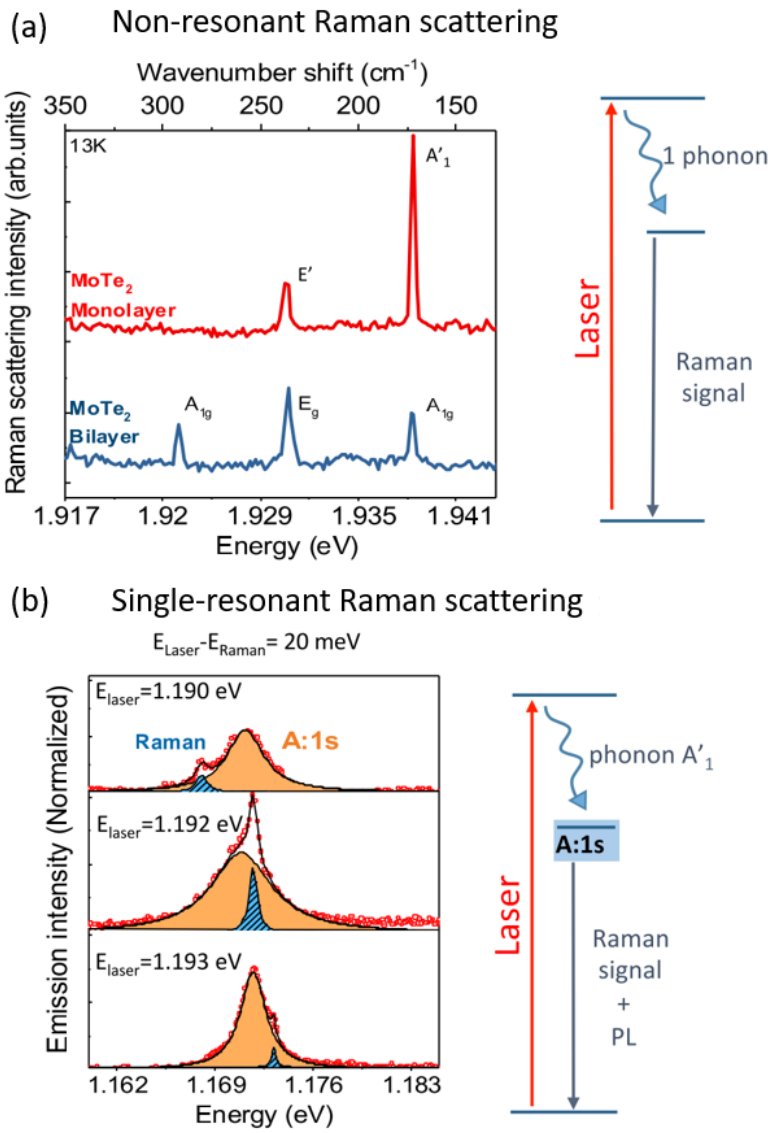

Figure 3.17: (a) $T = 4\,\mathrm{K}$ non-resonant Raman scattering spectra of a $MoTe_2$ mono- and bi-layer and sketch of the process. Both the laser and the scattering light are in a spectral region where the material does not have an electronic transition with a pronounced resonance. This technique is used for identifying different Raman peaks, which means different lattice vibrations (b) Single-resonant Raman scattering data (left) and scheme of the process (right) for the same sample of panel (a). In addition to PL emission (orange peak), we see a spectrally sharper feature (shaded blue) superimposed on the PL, which shifts with the excitation energy of the laser. This peak corresponds to light scattered by the A_1' phonon, which is particularly efficient as the final state after the scattering corresponds to a real electronic state. This picture is taken from [83].

panel.

It is important to note that for this single-resonant Raman scattering the Raman signal is amplified by the proximity of the electronic state. This also happens in other monolayers, such as WSe_2 and $MoSe_2$ [167, 169]. In the following, relevant data will be presented. However, before doing that, we have to introduce an even more complex form of interaction between phonons and excitons.

3.4.2 Double-resonant Raman scattering

In addition to non-resonant and sinlge-resonant, a third possible scenario of exciton-phonon interaction is called double-resonant Raman scattering. This process happens when both the laser excitation energy and the final state after the scattering (Raman feature) match two real electronic transitions. In order for this to happen, the energy separation between the two electronic transitions has to be equal to the energy of a phonon or multiple phonons in the crystal. This process is made extremely efficient as the scattering cross sections are strongly enhanced [175, 176, 177, 178]. The sketch in panel (c) of Fig. (3.18) describes this scenario.

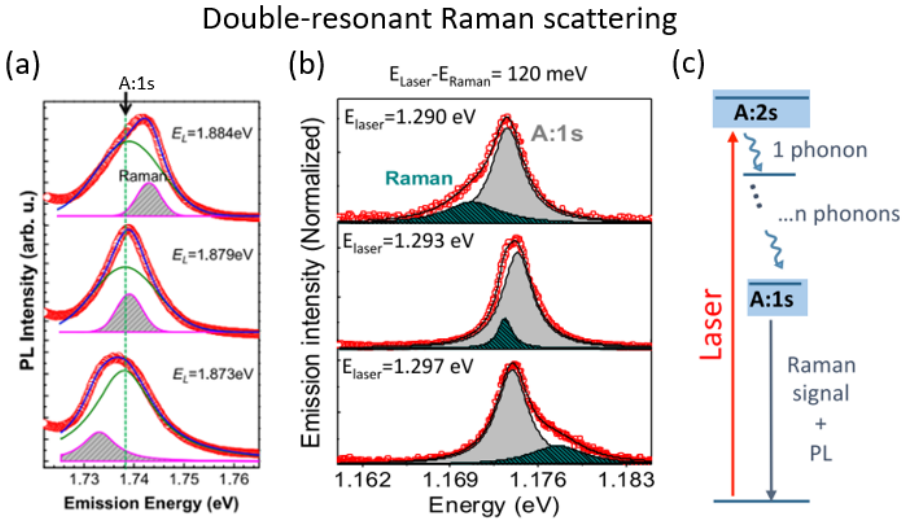

Figure 3.18: (a) $T = 4\,\mathrm{K}$ double-resonant Raman scattering spectra of a WSe_2 monolayer exfoliated on SiO_2. The laser is tuned to resonantly excite the first A-exciton excited state (A:2s) and the light emitted at the A:1s spectral energy is detected. As phonons make relaxation from A:2s towards A:1s very efficient, the detected signal results as a superposition of an enhanced PL emission from the A:1s state and of a broadened and enhanced Raman line. The picture is taken from [179]. (b) Same as (a) but for an encapsulated $MoTe_2$ monolayer. (c) Sketch of the double-resonant Raman process. Both panels (b) and (c) are taken from [83].

This process was indeed observed by Wang et al. in an unencapsulated WSe_2 monolayer [179], in an experiment which shares many points in common with the one described above, in the single-resonant case. As before, the laser is used to excite the material, this time around 140 meV above the A:1s transition. The

main difference is that now this excitation energy matches the one of the first excited exciton state A:2s. When the laser is on the low energy side of the A:2s transition, the PL emission from the A:1s state starts to be enhanced, as shown in Fig. (3.18) (a) top panel. What happens is that a shoulder appears on the low energy side of the PL peak. As the laser is scanned across the excited exciton resonance A:2s also the shoulder (Raman signal) moves appearing on the high energy side when the laser has crossed the resonance (bottom panel of Fig. (3.18) (a)), a strong indication for Raman scattering.

When those data were analysed it was understood that the total emission consisted of two different features: the emission from the neutral exciton A:1s and a narrower line which later was identified as a Raman signal. The claim that two lines were present was made following careful double peak fitting of the data thanks to which the second peak, shifting with the laser and maintaining a spectral distance of 140 meV from it, was identified. In contrast, the energy position of the neutral exciton remained constant both in resonance and non-resonance excitation, as expected. Moreover, those fits allowed to establish that the FWHM of the A:1s state was constant around 15 meV while the one of the Raman feature was smaller, close to 5 meV, as a pulsed Ti:Sapphire laser (ps) was used.

The clear identification of the narrow feature was subsequently performed in a single-resonant Raman experiment where the laser was used for excitation around 60 meV above the A:2s state. Superimposed to the broad hot PL emission form the excited state up to three optical phonon modes (separated by 31 meV) were observed. Multiple Raman features in 2D materials were observed before [178, 134], because of the efficiency of the interaction between excitons and phonons.

Double-resonant Raman scattering has been observed more recently in encapsulated $MoTe_2$ monolayers [83]. In this experiment, as done for WSe_2, the laser was used to excite the first excited exciton state A:2s while the PL signal from the A:1s exciton recombination was detected. The energy separation between these two states A:1s-A:2s is approximately 120 meV for this material. The variation of the exciting laser energy results in a strong change of the PL emission intensity of the A:1s but also of its lineshape, as a Raman feature cross the transition. The data are shown in panel (b) of Fig. (3.18).

Fitting the two different peaks is made difficult by the fact that in this case the Raman line is spectrally broadened as it corresponds to a multi-phonon process. Determining the energies of the two peaks (A:1s and Raman) precisely is thus not possible when the laser is in resonance with A:2s. However, it appears clear that at the resonance (i.e. laser excitation exactly at the A:2s energy) both PL and Raman signals are strongly enhanced as shown in the middle panels of Fig. (3.18) (a) and (b).

Summarizing, we talk about double-resonant Raman scattering when both the laser excitation energy and the Raman feature spectrally overlap with two different electronic transition. If just one between the laser and the Raman line is resonant with an electronic transition we talk instead of a single-resonant Raman scattering process. Finally, if no electronic transition is involved, we talk about non-resonant Raman scattering.

One question which raised following the results presented above was: is it just by chance that the A:1s and the first excited state (A:2s) are separated exactly by phonon multiples? Is it possible that we are actually observing a

mixed exciton-phonon state? In the last part of this chapter we will try to answer this question.

3.4.3 Exciton-phonon coupling in encapsulated WSe_2

During this thesis, the same experiment described above for WSe_2 exfoliated directly on SiO_2 has been repeated on encapsulated WSe_2 monolayer samples, where the narrow linewidths allowed us to have deeper insights. Again, we performed photoluminescence excitation (PLE) spectroscopy on the neutral exciton: we scanned the laser in the energy range where the A:2s transition is and we detected the light coming from A:1s. The data are similar to those of panel (c) in Fig. (3.14). The energy separation between the A:1s and A:2s states is around 130 meV and corresponds almost to the energy of four phonons of 32 meV.

Monitoring the intensity of A:1s, the trion and the dark exciton, we confirmed the position of the A:2s resonance: all the peaks have their maximum when the laser is exactly in resonance with A:2s, as can be seen in panel (b) and (d) of Fig. (3.19). As before, when the excitation energy of the laser approaches the A:2s from the high energy side we see an increasing Raman feature approaching A:1s as shown in panel (a) of Fig. (3.19).

The strictly resonant spectrum (laser excitation energy equal to A:2s energy) is shown in red in panel (b) of Fig. (3.19), together with two others obtained by slightly detuning the laser out of resonance. Note how the central energy is shifted without really changing the lineshape. In the contour plot in Fig. (3.19) (d) a larger set of data is presented. The region between the red and purple dashed lines has been generated using the spectra from panel (a). In the contour plot we can see that after the laser has crossed the resonance the Raman line does not emerge on the other side of the A:1s transition, which is a first sign of anti-crossing. The extracted peak positions of the PL and of the Raman features are shown in panel (c) but they do not show the Raman line moving away from A:1s, on the same side. This would have been a direct observation of anti-crossing which would have proved the strong-coupling nature of the exciton-phonon interaction in monolayer WSe_2 Unfortunately the data didn't allow us to answer whether the exciton-phonon coupling is perturbative or strong.

Summarizing, in this experiment we are looking at the PL emission of A:1s whose energy is fixed and determined by the material under investigation (a monolayer of WSe_2 encapsulated in hBN). The emission is strongly enhanced when the state is excited by resonantly pumping its first excited state A:2s. In the experiment we change the laser excitation energy, which is scanned across the range between 1.9 eV to 1.8 eV, and we observe (in emission) a Raman feature passing through the A:1s resonance.

Actually, not only one but two Raman lines are observed, as one can see in both panel (b) and (d) of Fig. (3.19). One which overlaps the neutral exciton emission (double-resonant) and another around 32 meV above A:1s which is single-resonant, as the initial state (laser energy) is at the A:2s energy, but the final state is not an exciton resonance. These Raman features are separated from the laser by 4×32 meV and 3×32 meV, respectively and they are visible because of the double-resonant and single-resonant Raman scattering process respectively.

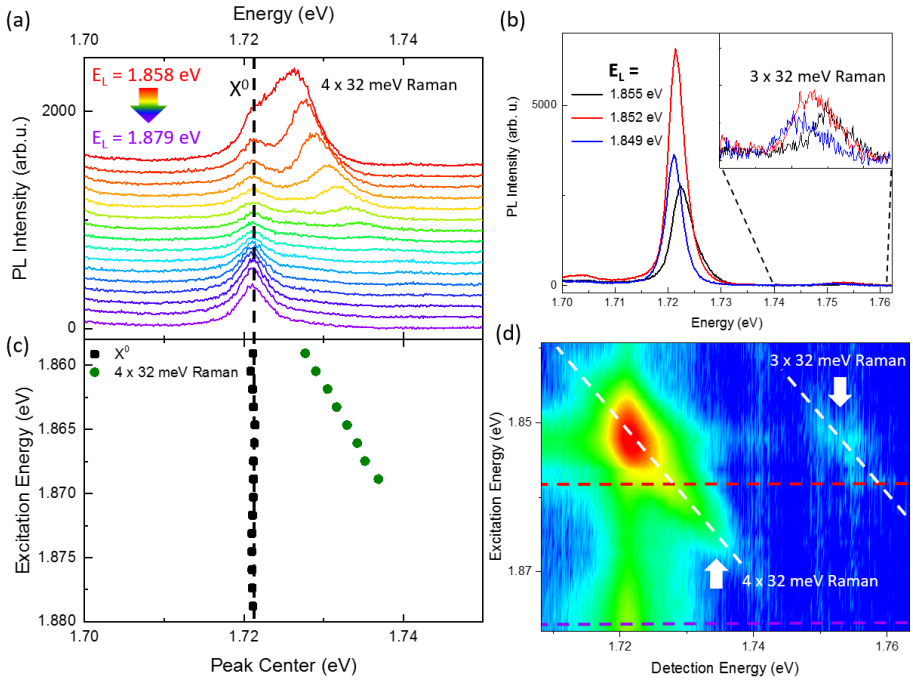

Figure 3.19: Data from an encapsulated WSe_2 monolayer at $T = 4\,\mathrm{K}$. (a) Different emission spectra of A:1s and of the Raman feature at different laser excitation energy (from 1.879 eV for the purple spectrum to 1.858 eV for the red one) as it approaches the A:2s resonance located at 1.852 eV. The spectrum for the strictly resonant excitation is not shown here but in (b) by the red curve. The black and the blue spectra are instead obtained by slightly detuning the laser energy away from A:2s. In the inset, another Raman line appears separated by the first by $\sim 32\,\mathrm{meV}$. (c) The extracted position of the peaks is presented. For energy excitation closer to 2s we were not able to reliably fit the transition with two peaks. (d) The contour plot shows a larger set of data obtained in cross-circular excitation condition. The purple and the red spectra showed in (a) are indicated by dashed lines. The second Raman feature is clearly visible and the withe dashed lines are guides to the eyes and represent the movement of the Raman lines as a consequence of the changing of the laser excitation energy.

As a consequence, a second different single-resonant Raman scattering configuration is possible: the one in which the Raman line at $3 \times 32\,\mathrm{meV}$ from the laser is resonant with the A:1s transition. This situation is realized by moving the laser line 32 meV from A:2s towards A:1s. This second single-resonant Raman scattering condition, with a second resonance in PLE, is shown in Fig. (3.20).

The data presented are qualitatively identical to those of Fig. (3.19). Note how the particular excitation scheme makes visible also a third Raman related line, as highlighted in panel (b) of Fig. (3.20). This line is in a non-resonant configuration.

We can group all these data in a single graph as done in panel (c) and (d) of Fig. (3.20). While moving the exciting laser energy (thick black arrow) through the spectral range 1.9 eV to 1.8 eV (y-axis in panel (c)) makes several Raman features appear. Their movement can be tracked (red, blue and green circles

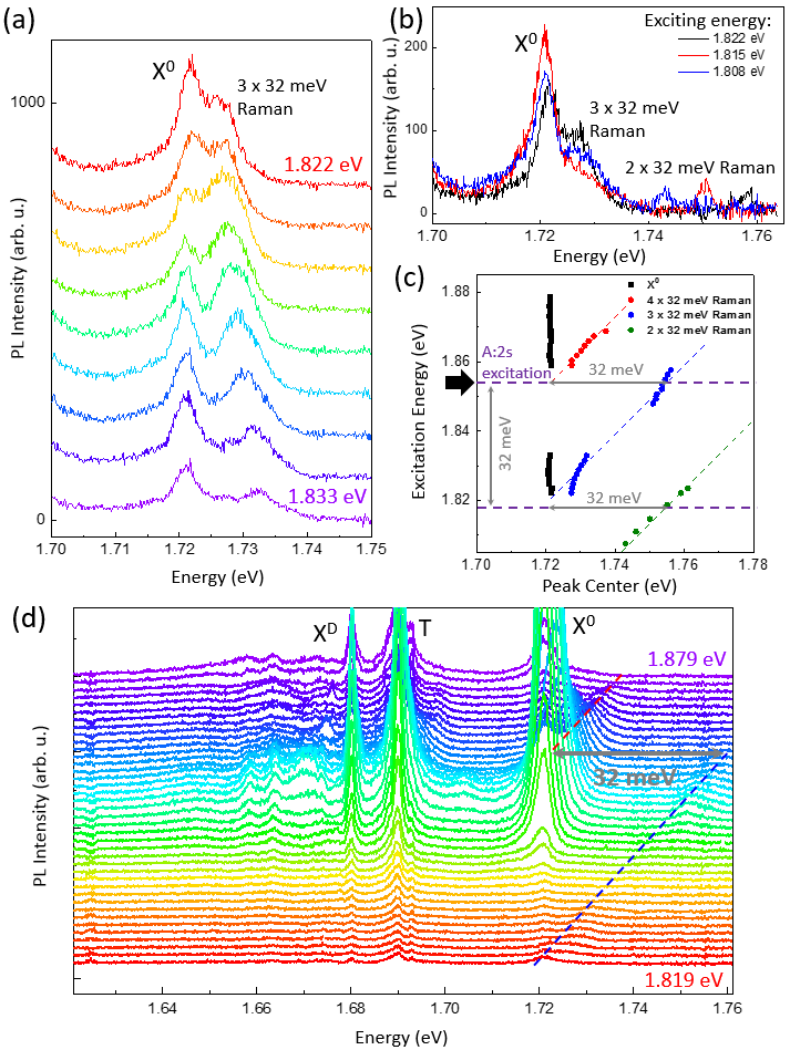

Figure 3.20: Data from an encapsulated WSe_2 monolayer at $T = 4\,\mathrm{K}$. (a) Waterfall plot which shows a Raman line approaching the A:1s transition while the laser is moved from 1.833 eV (purple spectrum) to 1.822 eV (red spectrum). This Raman feature is at a $3 \times 32\,\mathrm{meV}$ distance from the laser. (b) The red spectrum is the resonat excitation one while the other two are slightly detuned. Another Raman feature appears and it is separated by the one which is resonant by $\sim 32\,\mathrm{eV}$ ($2 \times 32\,\mathrm{meV}$ from the laser). (c) Extracted peak positions of A:1s and of three Raman lines (separated by each other by 32 meV) as a function of the excitation energy. The dashed red, blue and green lines represent the movement of the Raman features as a consequence of the movement of the exciting laser. The purple dashed lines represent the position of the laser for having a double- or single-resonant Raman scattering condition. (d) Spectra as a function of the laser excitation energy. The red and blue dashed lines are guides to the eyes and represent the movement of the first two Raman lines (as in panel (c)).

in panel (c)) as they follow the movement of the exciting laser. Note how they are visible only when the double or single-resonant Raman conditions are met (dashed purple lines).

In panel (d) of Fig. (3.20) all the spectra as a function of excitation laser energy are shown. The red and blue dashed lines are guides to the eye which highlight the shift of the Raman lines as the laser is moved.

In the end, we note that the trion is $\sim 31\,\text{meV}$ below the neutral exciton (A:1s). The results which will be presented in Chapter 5 will question the nature of this peak. Given the great importance of exciton phonon interaction in WSe_2, may the so called trion be actually a phonon replica of A:1s? Indeed, even when the monolayer is undoped the transition is dominant in PL but completely absent in reflectivity. When the sample is negatively doped the peak disappears, replaced by a doublet which is visible both in reflectivity and PL but whose intensity is much smaller.

The fact that this peak is quenched when the neutral exciton is quenched in a charge tunable structure and that is at $\sim 32\,\text{meV}$ from it may indicate that this emission relies on the initial presence of excitons and that phonon emission is necessary to observe the peak. Further research is needed tu fully understand the origin of this so called trion peak in samples close to charge neutrality.

3.5 Conclusions

In this chapter we presented the basic optical characterization of monolayer WSe_2 encapsulated in hexagonal boron nitride. The improved optical quality of this class of samples allows us to observe, in the PL spectrum, three main peaks at $1.72\,\text{eV}$, $1.69\,\text{eV}$ and $1.68\,\text{eV}$ respectively. Two of them have been clearly identified as the neutral bright (A:1s or X^0) and the neutral dark (X^D) A-exciton and they appear in the high and in the low energy side of the spectrum respectively. The nature of the peak in the middle (labelled as trion so far) is still under discussion.

The better optical response of encapsulated WSe_2 monolayers also allows us to observe clearly two of the bright neutral A-exciton excited states (A:2s and A:3s). Their spectral position and intensity relatively to the most tightly bound A-exciton (A:1s) was discussed.

In the end we presented our data on exciton-phonon coupling. We showed that the interaction between these two quasi-particles is strong in monolayer WSe_2 and we observed both single-resonant and double-resonant Raman scattering. Unfortunately we were not able to observe a clear trace of anti-crossing between the PL and the Raman signals. This prevented us to understand if the coupling is strong or perturbative.

We stress that the fact that we observe strong Raman features in the WSe_2 spectrum is not only related to the intensity of the interaction between phonons and excitons but also to the comparatively low emission intensity of WSe_2 at low temperature. The same Raman lines will be much less visible in e.g. monolayer $MoSe_2$ whose low temperature PL emission is much more intense.

Chapter 4

Upconversion spectroscopy of exciton states

The pourpose of this chapter is to introduce a non-linear optical process which we term upconversion. Its fingerprint is the observation of photoluminescence emission at higher energy with respect to the excitation laser energy. Thus, for reasons of energy conservation, mechanisms beyond single photon absorption and emission have to be involved in the upconversion process.

In particular, in our experiment we studied a high quality monolayer WSe_2, whose A-exciton linewidth is reduced to 4 meV thanks to encapsulation in hexagonal boron nitride (hBN). The sample is excited by a tunable laser and in particular the energy is tuned to match the A-exciton transition at 1.72 eV. Even if the laser is continuous wave and its power is kept low (of the order of $1\,\mu W\mu m^{-2}$) we surprisingly observe emission from states at higher energy such as the first (A:2s) and second (A:3s) excited states of the A-exciton and the B-exciton as well. Note that these three levels are respectively about 130 meV, 150 meV and 430 meV above the A:1s state. The observation of hot photoluminescence emission, which will be referred subsequently as upconversion photoluminescence, must be the consequence of efficient population of all the involved states.

Similar processes were already observed in traditional nanostructures such as InP/InAs heterojunctions, CdTe quantum wells and InAs quantum dots [180, 181, 182, 183, 184]. In most of these experiments it was assumed that phonons provide additional energy. Instead of considering Stokes Raman features (generated by photons which have inelastically scattered with phonons losing energy) one has to consider the anti-Stokes ones. The scattered photons have thus absorbed the energy from phonons. If we consider the same situation described at the end of Chapter 3 for the double-resonant Raman scattering we may understand why this process may be efficient. Imagine to have two optical transitions separated in energy by exactly one phonon. This can generally be obtained by applying strain [176] electric [185] or magnetic [186] field. If we resonantly excite the low energy transition we may observe photoluminescence emission from the high energy level, which has been populated by absorbing a phonon.

As we are absorbing phonon energy from the lattice, if the process is very intense, it may lead to an effective cooling of the material. This is the explanation

of the laser cooling effect or optical refrigeration of solid [187, 188].

The size of TMD monolayer samples and the fact that their thermal environment is regulated by an external source (like a cryostat) makes laser cooling in the observed system very unlikely. However, the upconversion process has already been observed in monolayer WSe_2 exfoliated on SiO_2 in the group of Xiaodong Xu [189]. Indeed, a PL emission from the neutral exciton A:1s was observed when the laser was tuned to match the energy of the trion, $\sim 32\,\text{meV}$ below it. In this case the application of an external field or strain is not necessary to allow anti-Stokes scattering as the energy difference between the neutral exciton and the trion in WSe_2 is already equal to the energy of the A_1' longitudinal optical phonon.

The main difference between the observation of Jones et al. [189] and ours lays in the fact that the energy separation between the excited and the emitting states is one order of magnitude larger in our case ($32\,\text{meV} \ll 430\,\text{meV}$). If a phonon assisted upconversion can be invoked to explain the emission from the excited A-exciton states this doesn't appear reasonable for the B-exciton. In the following we will describe in detail our experiment and results. We will then try to interpret different observations in a consistent manner. Not everything is clear at this stage. We hope that this manuscript may encourage the discussion and stimulate future research.

4.1 Upconversion emission

In this first section we will characterize the sample under study and we will describe in more details the upconversion emission. This process, is not only a very interesting phenomenon on its own but it also revealed itself as a useful tool to further investigate the sample and TMDs in general. The WSe_2 monolayer we studied was encapsulated in-between two flakes of hBN with the aim of creating a symmetric top-bottom environment and to avoid effects (such as local accumulation of charges in the substrate or adsorbates on the monolayer surface) which tend to deteriorate the optical quality of the sample. More details about the benefits of encapsulation can be found in Chapter 3.

As a proof of the high quality of the sample under study we show in Fig. (4.1) (a) the first derivative of the differential reflectivity spectrum obtain with a white halogen lamp. In the picture, four different features can be recognized and identified. The first at 1.723 eV is the absorption from the A-exciton whose full width at half maximum is just 4 meV. This is the most tightly bound A-exciton level and it will thus be referred to as A:1s.

At slightly higher energy, two closely spaced transitions are observed. The first is 133 meV away from the A:1s, at 1.856 eV, and has a linewidth of about 6 meV while the second appears around 156 meV above A:1s, at 1.879 eV, and its linewidth is 19 meV. These two features were extensively introduced in the previous chapter and are the excited states of the A-exciton. As before, we will refer to these transition as A:2s and A:3s excitons. Finally, about 430 meV above the A:1s exciton the broader signature of the B-exciton (B:1s) is clearly visible at approximately 2.15 eV. As already discussed, the energy difference between A:1s and B:1s is mainly due to the valence band spin-orbit splitting (see Chapter 1)

After this first characterization, performed with differential reflectivity we

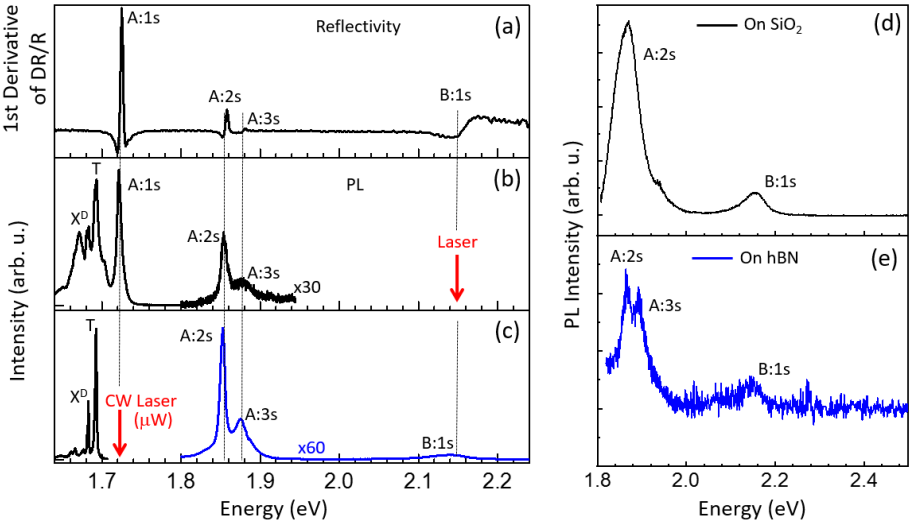

Figure 4.1: All data are obtained at $T = 4\,\mathrm{K}$. (a) First derivative with respect to energy of the differential reflectivity spectrum of an hBN encapsulated WSe_2 monolayer illuminated with a white light source. The A-exciton (A:1s), its excited states (A.2s and A:3s) and the B-exciton (B:1s) are observed and indicated in the figure. (b) PL spectrum of A:1s (alongside with trion, dark exciton and a defect related peak) and hot PL of the excited A-exciton states obtained exciting resonantly the B-exciton. (c) Standard PL (black) and upconversion PL (blue) obtained exciting resonantly the A:1s transition with a continuuous wave Ti:Sapphire laser at low power ($1\,\mu\mathrm{W}\mu\mathrm{m}^{-2}$). (d) Upconversion PL spectrum of a WSe_2 flake exfoliated directly on SiO_2. (e) The same as (d) but with the monolayer exfoliated on hBN (without a capping layer) [116].

also investigated the sample in standard PL measurements. The results are shown in panel (b) of Fig. (4.1). Using a tunable laser source we resonantly excited the B-exciton (indicated by a red arrow) and detected light emitted at lower energies. In the spectrum we can recognize not only the emission coming from the most tightly bound state of the A-exciton (A:1s) but also the hot photoluminescence of the first two excited states. The energy of the photoluminescence peaks matches almost perfectly the one of the reflectivity features. This means that the Stokes shift is negligible and this is a sign of the high homogeneity and quality of the sample as Stokes shift is caused by localization of the excitons around lattice defects. Also the linewidth of the peaks is similar in both techniques further confirming the huge impact of hBN in improving the optical quality of the monolayer.

Please note that the observed features in photoluminescence are visible also when the exciting laser energy is not resonant with B-exciton, i.e. a spectrum similar to the one shown in Fig. (4.1) (b) is obtained when the excitation energy is equal to 1.96 eV (helium-neon laser $\lambda_{exc} = 632.8\,\mathrm{nm}$).

The blue spectrum shown in the panel (c) is instead the one obtained with the upconversion excitation technique. The laser energy is set to match the energy of the A-exciton at 1.723 eV and a very surprisingly strong photoluminescence signal is observed at **higher** energy. This result is striking as the

laser used for excitation is a narrow linewidth, continuous wave Ti:Sapphire and the excitation power was kept low, on the order of $1\,\mu\mathrm{W}\mu\mathrm{m}^{-2}$. Thanks to the previous characterization the identification of the peaks is straightforward. Again, we observe two lines at ≈ 130 meV and 150 meV from the exciting laser (i.e. from A:1s) which are identified as A:2s and A:3s, respectively. At 430 meV above A:1s we can see the emission from the B-exciton instead. The energy position of each peak is perfectly consistent with the one obtained by the other two employed optical techniques.

We also performed photoluminescence in the conventional scheme, which means that we excited A:1s and we looked at the low energy side of the spectrum. We clearly observe two peaks. As we already discussed extensively in Chapter 3 these are the trion and the dark exciton [92] (this latter being the one at lower energy). No sign of these peaks is detected in reflectivity denoting that the monolayer is essentially undoped and that the oscillator strength of the dark exciton is weak. No sign of the biexciton emission is observed, as the exciting power is kept very low. From this fact we deduce that the relaxation from the neutral exciton state towards the trion and the dark exciton is very efficient.

Before discussing the origin of the upconversion emission, we stress that it is not related to hBN encapsulation as the signal was observed also on a WSe_2 monolayer exfoliated on SiO_2 and on a WSe_2 exfoliated on hBN but without the top layer as shown in panel (d) and (e) of Fig. (4.1). When we observed the phenomenon on WSe_2 exfoliated on silicon dioxide, the linewidth of the excited exciton states was much broader. The consequence is that no doublet is discernible and just the peak associated with A:2s is visible. Please note the great difference in intensity between the two signals in panel (d) and (e) of Fig. (4.1). This is possibly due to the cavity effect induced by the hBN/TMD/hBN/SiO_2 heterostructure [146] as discussed in Chapter 3.

After the simple spectra and characterization described on the first part of this chapter, a series of experiments was performed, in the attempt of understanding why this strong emission at higher energy compared to the excitation laser energy is observed.

4.2 Origin of upconversion emission

As a first attempt to unveil more details about the upconversion signal, an upconversion PLE experimet was performed. The exciting laser is tuned across the A:1s resonance (1.723 eV) and the integrated photoluminescence emission from A:2s, A:3s and B:1s states (at 1.856 eV, 1.879 eV and 2.15 eV respectively) is recorded. All the spectra as a function of the exciting energy are used to generate the contour plot shown in panel (a) of Fig. (4.2), where the color represents the photoluminescence intensity.

It is straightforward to see how the upconversion emission is dependent on the excitation energy: as soon as the laser is not resonantly exciting the A-exciton anymore (white line) the signal vanishes. Moreover, the FWHM of the resonance observed in upconversion PLE is about 4 meV which is the linewidth of the A-exciton (see Fig. (4.2) (a) right panel). It is thus clear that the process has to be related to efficient A-exciton generation. Another confirmation of this fact came from experiments which we performed later on a $MoSe_2$ charge tunable sample: as the doping reduces the oscillator strength of the neutral exciton

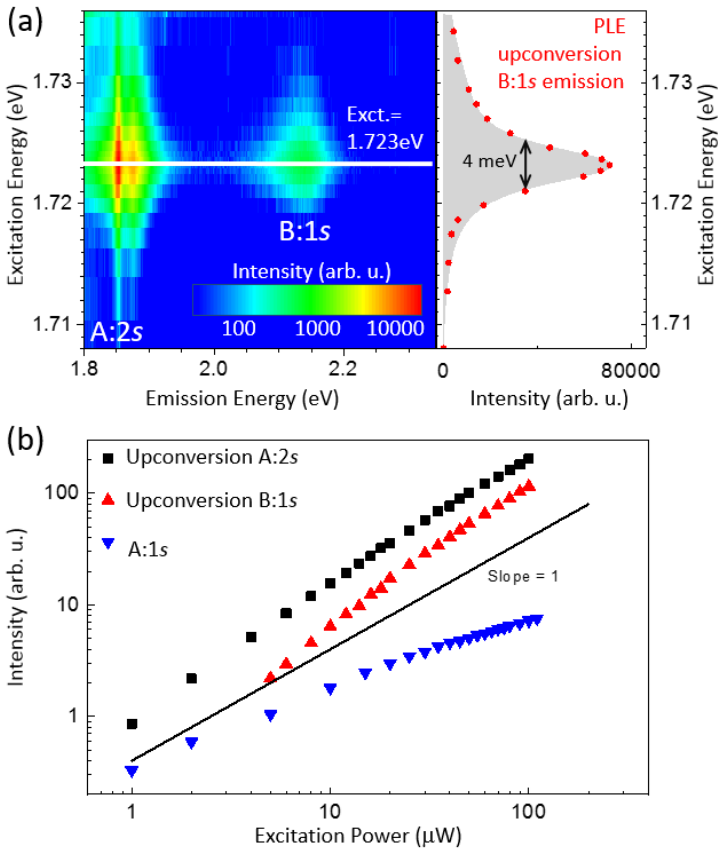

Figure 4.2: All data are from the same encapsulated WSe_2 monolayer and are acquired at $T = 4\,\mathrm{K}$. (a) On the left panel a contour plot is shown where the intensity of the PL emission of A:2s, A:3s and B:1s is plotted as a function of the laser excitation energy (y-axis). A resonance is clearly seen and highlighted in the right panel where the PLE of the B-exciton is shown. (b) Power dependence of the PL emission coming from A:1s (blue triangles) following resonant excitation of the A:2s state, compared with the upconversion power dependence of A:2s and B:1s. This latter emission shows clearly a super-linear behaviour and the slope, in the range $10-100\,\mu\mathrm{W}\mu\mathrm{m}^{-2}$, is twice the one of the A:1s signal (1.1 and 1.25 for A:2s and B:1s respectively and 0.56 for A-exciton) [116].

the upconversion signal is quenched [83]. These results reveal an important characteristic of upconversion: it is a resonant phenomenon.

The link between A-exciton and upconversion is even clearer when one tries to resonantly excite the trion transition, $\sim 32\,\mathrm{meV}$ below in energy: in this configuration, no signal can be detected neither from the excited states nor from the B-exciton. As already mentioned, emission at higher energy than the exciting laser can have different origins [180, 181, 182, 183, 184, 190] but some of them can be ruled out by simply taking into account the great energy separation between the laser energy and the B-exciton emission: 430 meV are indeed too much for considering a process purely based on phonon absorption (such as anti-Stokes Raman scattering [189, 191]) especially at $T = 4\,\mathrm{K}$ as we expect the

number of phonons and their energy to be very low.

Now it is interesting to investigate the power dependence of standard PL and upconversion. If we measure the evolution of the standard PL signal coming from A:1s when a laser is used for the resonant excitation of A:2s we observe that its increase is sub-linear. As we already mentioned in Chapter 3 (subsection (3.1.1)), we would expect a linear increase of A:1s intensity. This can be a consequence of nonlinear effects such as absorption saturation or non-linear (Auger) recombination of excitons which are made very efficient by the fact that we are exciting the sample at a very specific energy, where the absorption probability is strongly enhanced. However, it is interesting that the upconversion emission is instead superlinear and the signal evolves with a slope which is roughly twice the one of the standard PL emission, as shown in Fig. (4.2), panel (b).

This seems to indicate that two excitons created by the laser are necessary to generate a single excited state at higher energy. One possible scenario is an Auger-like process or exciton-exciton annihilation [192, 110, 193, 194] in which two independently created excitons scatter together. As a result, one of the two recombines giving the excess energy to the other one which can now reach an excited energy band indicated by c' in Fig. (4.3). This excited electron-hole pair can then lose energy (phonon emission) and relax to B:1s or the A-exciton excited states.

Please note that an Auger process would be in principle very unlikely as for gaining energy an exciton (an electron in the conduction band, to be precise) has to gain momentum as well, in order to satisfy the bands dispersion curves. Thus, for an Auger process to happen the involved particles should have high kinetic energy [195, 196]. This process is illustrated in panel (a) of Fig. (4.3).

Hovewer, based on a detailed analysis by our collaborators Leonid Golub and Mikhail Glazov (Ioffe Institute, Saint Petersburg) [197], the momentum selection rule can be relaxed. This happens thanks to the strong Coulomb interaction in TMDs, which remove the constraints on the single-electron momentum conservation [198] [199] and thanks to the presence of the excited conduction band. Thus, when the exciton-exciton annihilation process happens, an electron is not forced to be scattered within the same band to a much larger wave-vector state, but it can be directly promoted to the excited conduction band c' [33, 200] with only a minor change in its wave-vector. This of course happens if the energy separation between the two conduction bands is close to the energy provided by the A:1s recombination (i.e. by the incident photons). This means that the following equation must hold:

$$E'_g \lesssim E_g - E_B \tag{4.1}$$

Where E_g is the energy gap, E'_g is the energy separation between the two conduction bands and E_B the exciton binding energy. This is indeed roughly the case for WSe_2 but also $MoSe_2$, MoS_2 and $MoTe_2$ monolayers. See values for E_g and E'_g in [200] and references therein. Upconversion was observed for all of them [83]. A more quantitative analysis which shows how the resonant Auger scattering is much more efficient than the standard one can be found in [83].

The assumption that the high energy states are populated following an Auger scattering process explains the superlinear power-dependence of the upconver-

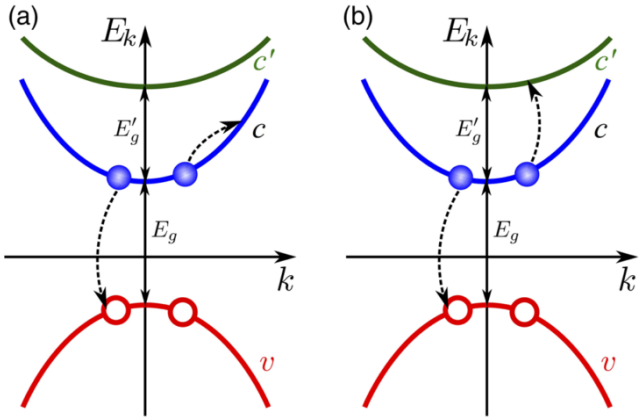

Figure 4.3: Model of the exciton-exciton annhilation in a single-particle picture. Holes are represented by open circles while electrons by blue dots. The dashed arrows represents electronic transitions (a) Standard Auger scattering process in which one electron return to the valence band while the other scatters to a higher energy state without leaving the conduction band. In this intraband process the momentum of the electron in the final state has to be equal to the sum of momenta of the two electrons involved. (b) Resonant Auger scattering where one electron is promoted to an excited conduction band. The wave-vector in the final state can be very small thus lifting the constraints on the wave-vector of the interacting particles [83].

sion signal. Indeed, a consequence of our hypothesis is that the emission of the upconversion signal scales as $N^2_{\text{A:1s}}$, where $N_{\text{A:1s}}$ is the occupation number of the A-exciton level i.e. the number of A-excitons created by the resonant excitation laser. In other words the effect is optically non-linear as the upconversion intensity scales quadratically with the number of photoexcited excitons.

Before detailing the optical process leading to upconversion and explaining why we believe it is Auger driven, it is worthy to briefly discuss the evolution of the upconversion PL signal coming from A-exciton excited states as a function of temperature. The signal is indeed detectable up to room temperature as shown in panel (a) of Fig. (4.4). This result is very important for possible applications but also because it shows how robust the process is. We can see immediately how the linewidth of the transitions gets broader as the temperature is increased. This was predictable and, as for the A:1s state, it is a consequence of the phonon induced broadening [201, 202]. An increase of the energy separation between A:2s and A:3s was also observed. This is surprising and might be due to higher excited states (A:4s and A:5s) contributing to the emission. This would result in a shift of the fitted peak when the fit is performed considering only two peaks. Also the intensity ratio seems to increase abruptly between 100 and 200 K, as shown in panel (b) of Fig. (4.4). Please note that in this experiment the resonant laser follows the bandgap shift with temperature.

4.2.1 Details on upconversion power dependence

In this subsection we will have a closer look at the optical processes which lead to upconversion. In particular we will try to understand how the excitation of

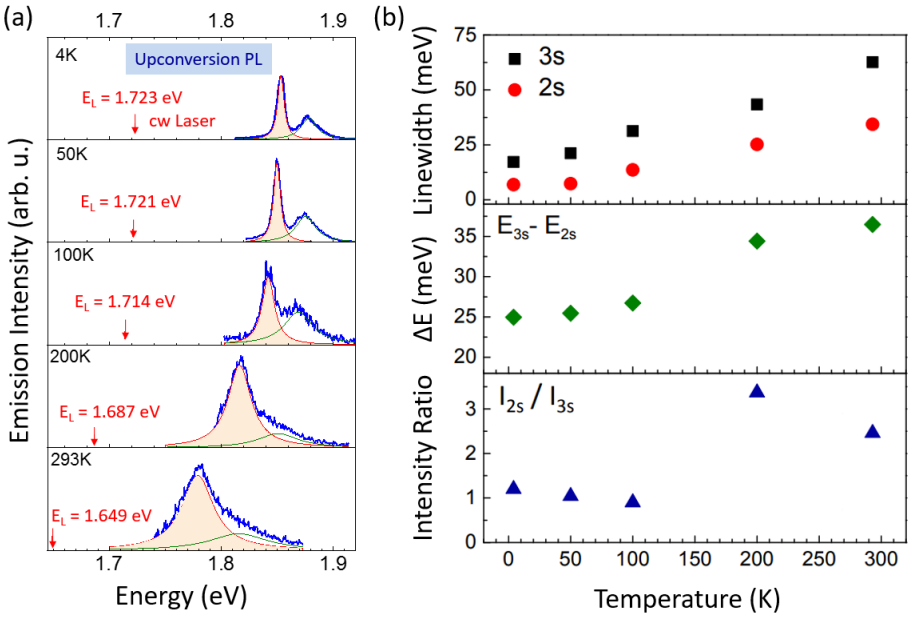

Figure 4.4: (a) Evolution of the upconversion PL signal of the excited A-exciton states of an encapsulated WSe_2 monolayer as a function of temperature. The excitation energy of the laser was tuned to match the moving A-exciton resonance and its position is indicated in each panel by the red arrow. (b) Evolution of linewidth, energy splitting and intensity ratio of A:2s and A.3s as a function of temperature. Each data point is extracted from the spectra on the left [116].

the A:1s state can populate levels at higher energy.

In the so called linear regime one absorbed photon generates one exciton. Hence, under resonant excitation the occupation number $N_{\mathrm{A:1s}}$ is directly proportional to the light intensity I. Thus, the generation rate G in the linear regime can be written as:

$$G = A(1-R)\frac{I}{\hbar\omega} \tag{4.2}$$

where A is the absorption coefficient of the TMD monolayer, R is the reflection coefficient of the whole sample and $\hbar\omega$ the incident photons energy. We stress that some effects such as absorption saturation or nonlinear recombination can prevent the system to be in the linear regime, but this will not affect our conclusions. The exciton occupancy is in general:

$$N_{\mathrm{A:1s}} = G\tau_A \tag{4.3}$$

Where τ_A is the lifetime of exciton. Note that the effects responsible for a sublinear behaviour can be included either in the absorption coefficient $A \equiv A(I)$ or in $\tau_A \equiv \tau_A(N_{\mathrm{A:1s}})$.

Independently of the absorption regime, observing the upconversion signal, and the one from B:1s in particular, is possible if and only if another quantum of energy is involved in the process. This is necessary because the energy conservation law cannot be violated. So either a phonon, a photon or a second exciton should be involved. We exclude the first process as the energy difference

of about 400 meV at $T = 4\,\mathrm{K}$ seems too high to be covered by phonons, Additionally, a clear optical non-linearity is demonstrated by the data in Fig. (4.2) (b) as the upconversion intensity scales quadratically with the number of photoexcited excitons. A closer look at the other two suggested particles is instead necessary.

A general two photon absorption process (2PA) involves a virtual intermediate state and generally a pulsed laser source is required. In this scenario, the generation rate of excitons in the highly energetic state f (electron in the excited conduction band c' in Fig. (4.3)) will be proportional to the square of the incident light intensity [180, 177, 203]:

$$G_f^{2PA} \propto I^2 \tag{4.4}$$

However, in the sample under investigation the energy of the single photon is equal to the A:1s exciton energy. This means that the intermediate state is real in this hypothetical two-photon absorption process (RS-2PA) and it can be seen as a two step process: first an A-exciton is created and then a second photon takes it to the f state. In this process the generation rate of the exciton in the excited state can be written as:

$$G_f^{RS-2PA} \propto N_{\mathrm{A:1s}} I \tag{4.5}$$

Which is a weaker dependence with respect to I^2 as some saturation in the absorption of the first photon may occur. In case of complete saturation of the A:1s state the generation rate becomes:

$$G_f^{RS-2PA} \propto I \tag{4.6}$$

The other scenario to explain the observation of upconversion is the one in which two independently created excitons are involved. In particular, due to the Coulomb interaction between electrons and holes, a redistribution in energy and thus in $\vec{k}$-space may occur. For example, in an Auger-like process two excitons may undergo Coulomb scattering with the result that one electron-hole pair recombines while the other acquires the released energy and reaches the f highly excited state (electron in c'). Please note that the strong Coulomb interaction between electrons and holes strongly localize the exciton in the real space (small Bohr radius) thus delocalizing it in $\vec{k}$-space and relaxing the momentum conservation law. In such a scenario the generation rate can be written as:

$$G_f^{Auger} \propto N_{\mathrm{A:1s}}^2 \tag{4.7}$$

Also note that, as the energy separation between the two conduction bands is close to the energy provided by the A:1s recombination, this process may be called resonant Auger scattering, as sketched in Fig. (4.3) (b).

Now that the possible ways of populating the excited band are described we want to rule out some scenarios. First, we assume that the relaxation from f to A:2s, A:3s and B:1s is linear, which means that the rate of excitons leaving this state is proportional to its occupancy. As a consequence the upconversion signal will be proportional to the generation rate of the excitons in the highly excited state: G_f. Therefore, if we compare the experimental result shown in Fig. (4.2) (b), with the generation rate inferred from the different excitation mechanism we can conclude that the Auger-like process and the real state two

photon absorption (in presence of saturation of the intermediate state) are more likely to be the source of the upconversion signal.

If we further look into the question we may rule out the real state 2PA process as well. This can be obtained using a very simple three level model to describe the complex system we are dealing with. The ground state $|0\rangle$ is represented by the absence of excitons, the first excited level $|\mathrm{A:1s}\rangle$ by the the A-excitons and the third $|f\rangle$ by the electron forming the exciton in the excited conduction band (electron in c' and hole in the valence band).

If we expand the wavefunction of the system over these states and if we introduce the decomposition coefficients, C_0, $C_{\mathrm{A:1s}}$ and C_f respectively, we obtain, from second-order time-dependent perturbation theory:

$$C_0 = 1 \tag{4.8}$$

$$C_{\mathrm{A:1s}} = \frac{V_{A0}}{\hbar\omega - E_{\mathrm{A:1}s} + \mathrm{i}\hbar\Gamma_A} \tag{4.9}$$

$$C_f = \frac{V_{fA}V_{A0}}{(2\hbar\omega - E_f + \mathrm{i}\hbar\Gamma_f)(\hbar\omega - E_{\mathrm{A:1}s} + \mathrm{i}\hbar\Gamma_A)} \tag{4.10}$$

In the equations, ω is the energy of the incident radiation, $E_{\mathrm{A:1s}} = E_g - E_B$ is the excitation energy of the A-exciton, E_f is the energy of the exciton in the final state $|f\rangle$ and Γ_A and Γ_f are the dampings of these states. In Eq. (4.9) and Eq. (4.10), the matrix elements V_{A0} and V_{fA} are the matrix elements of exciton excitation for the processes $v \to c$ and $c \to c'$, respectively. In this simplified approach, the steady-state populations of the A:1s state and of the final state are:

$$N_{\mathrm{A:1}s} = |C_{\mathrm{A:1}s}|^2 = \frac{|V_{A0}|^2}{(\hbar\omega - E_A)^2 + \hbar^2\Gamma_A^2} \tag{4.11}$$

$$N_f = |C_f|^2 = \frac{|V_{fA}|^2}{(2\hbar\omega - E_f)^2 + \hbar^2\Gamma_f^2} \times N_{\mathrm{A:1}s} \tag{4.12}$$

Note that Eq. (4.11) gives the spectral shape of one-photon absorption in the vicinity of A:1s exciton resonance, while Eq. (4.12) gives the spectral shape of the two-photon absorption.

It is instructive to estimate the two-photon absorption induced generation rate of excitons in the excited states. Taking into account that in our model the lifetime of the state $|f\rangle$ reads $\tau_f = 1/(2\Gamma_f)$ the generation rate of the excitons in the $|f\rangle$ state can be as:

$$R_{RS-2PA} = \frac{N_{\mathrm{A:1}s}}{\tau_{RS-2PA}} \quad , \quad \frac{1}{\tau_{RS-2PA}} = \frac{2\Gamma_f|V_{fA}|^2}{(2\hbar\omega - E_f)^2 + \hbar^2\Gamma_f^2} \tag{4.13}$$

The calculation shows that the absolute values squared of the matrix elements take the form:

$$|V_{A0}|^2 = \left|\frac{e\gamma_3}{E_g}\mathcal{E}_\omega\right|^2 \Phi_{1s}^2(0) \quad , \quad |V_{fA}|^2 = \left|\frac{e\gamma_6}{E_g'}\mathcal{E}_\omega\right|^2 . \tag{4.14}$$

Here the normalization area is set to unity, we neglected the difference between $\hbar\omega$ and E_g and E_g' and disregarded the difference of the exciton envelope

functions in the intermediate and final states, $\mathcal{E}_\omega$ is the amplitude of the incident electromagnetic field and $\Phi_{1s}(r)$ is the wavefunction of the most tightly bound exciton (A:1s) in the 2D hydrogenic form. For crude estimates, we put $\Gamma_f = \Gamma_A \equiv \Gamma$ as well as $\gamma_3 = \gamma_6$ where γ_3 and γ_6 are the band structure parameters introduced in [33]. We also assume that the double-resonant condition $2\hbar\omega \approx E_f$, $\hbar\omega \approx E_A$ (which overestimates the rate of transition) and we obtain:

$$\frac{1}{\tau_{RS-2PA}} \sim \Gamma \frac{n_X}{|\Phi_{1s}(0)|^2} \sim \Gamma n_X a_B^2. \tag{4.15}$$

Here $a_B = 1\,\mathrm{nm}$ is the exciton Bohr radius and n_X the A:1s exciton density. We therefore estimate (using a reasonable $\Gamma \sim 1\,\mathrm{meV}$) that $\tau_{RS-2PA} \sim 100\,\mathrm{ns}$ at $n_X = 10^9\,\mathrm{cm}^{-2}$. In contrast, we can estimate the recombination time of the exciton-exciton scattering process schematically shown in Fig. (4.3) (b) thanks to the following equation:

$$\frac{1}{\tau_{Auger}} \sim \frac{n_X}{\hbar k_B T} \left(E_B \frac{a_0^2}{a_B} \right)^2 \tag{4.16}$$

where $a_0 = 0.3\,\mathrm{nm}$ is the lattice constant and $E_B = 0.5\,\mathrm{eV}$ is the exciton binding energy. We find $\tau_{Auger} \sim 25\,\mathrm{ps}$ [83]. Thus, we may conclude that the direct two-photon absorption is weaker than the Auger-like process because of the longer lifetime.

Thus, even if the performed analysis cannot fully rule out the real state two absorption process and even if we may have oversimplified the system under study, we suggest that the exciton-exciton annihilation is more likely to explain the upconversion PL. It is possible that more complex processes, for which the exciton-phonon interaction is involved at one of the steps of the two-photon absorption, also play a role. The more detailed analysis performed in [83] will stimulate further experimental and theoretical studies aimed, in particular, at specifying band parameters of two-dimensional materials. So far the crucial position of the excited conduction bands c' is only taken from theory [33, 200].

4.3 Polarization of the upconversion PL

As discussed above, after resonantly pumping the A-exciton at 1.723 eV we observed strong hot photoluminescence emission at higher energy from A:2s, A:3s and B:1s (at 1.856 eV, 1.879 eV and 2.15 eV respectively). We called this signal upconversion photoluminescence and we explained how these high energy states can be populated. The scenario we propose for this observation involves two photons which creates two excitons. One of these excitons recombines giving its energy to the other electron hole-pair. The second electron is thought to reach a high-energy excited conduction band c'. Subsequently the surviving exciton can relax to the B-exciton level or to the excited A-exciton states and eventually recombine emitting the light we detect as hot PL.

Very interesting results are obtained when we excited the sample with circularly polarised light and we detect the two different polarization states of the upconversion PL. In particular we note that while the emission from the A-exciton excited states is co-circularly polarized with respect to the excited laser

the upconversion PL emission from B:1s is counter-circularly polarized with respect to it. In order to understand this key difference we propose two different scenarios which we will present in the following.

4.3.1 Upconversion emission from the B-exciton

The upconversion PL coming from the B-exciton is counter-circularly polarized with respect to the exciting laser. Moreover, and this is even more surprising, the degree of circular polarization increases with the incident power: the more intense is the σ^+ polarized exciting laser the more the upconversion PL from B-exciton will be σ^- polarized. This is shown in Fig. (4.5)

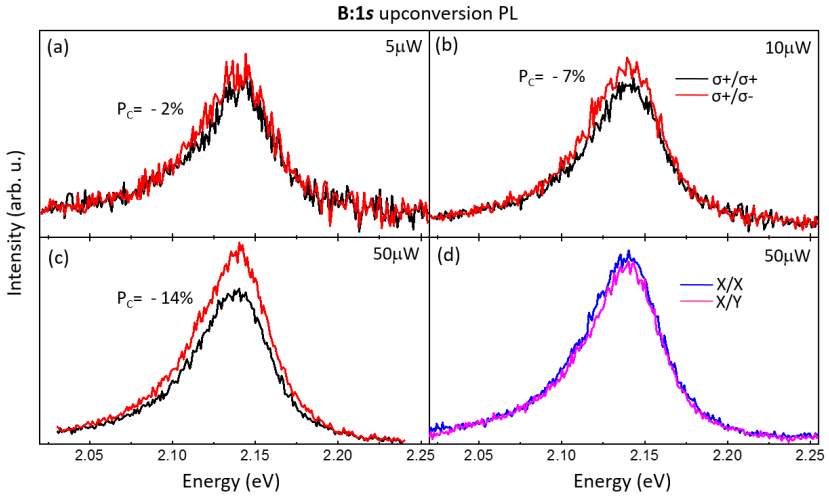

Figure 4.5: All data are obtained at $T = 4\,\mathrm{K}$ from an encapsulated WSe_2 monolayer. (a) σ^+ (black, co-polarized) and σ^- (red, cross-polarized) components of upconversion PL of B:1s following a σ^+ laser excitation with power density of $5\,\mu\mathrm{W}\,\mu\mathrm{m}^{-2}$. (b) Same as (a) but for power density of $10\,\mu\mathrm{W}\,\mu\mathrm{m}^{-2}$. (c) same as (a) but for power density of $50\,\mu\mathrm{W}\,\mu\mathrm{m}^{-2}$. The degree of circular polarization is defined as: $P_c = (I_{\sigma^+} - I_{\sigma^-})/(I_{\sigma^+} + I_{\sigma^-})$ and it is indicated in each panel. It can be noted that as the power density is increased the degree of circular polarization becomes more and more negative indicating cross-polarization with the excitation laser. (d) Linear X (blue, co-polarized) and linear Y (magenta, cross-polarized) components of upconversion PL of B:1s following a linear X laser excitation with power density of $50\,\mu\mathrm{W}\,\mu\mathrm{m}^{-2}$. The emission is not linearly polarized [116].

The observation of circular polarization in this upconversion emission is really surprising as it is expected that the chiral selection rules governing light absorption for states near the valence band and conduction band extrema at the K-point do **not** hold for very high excitation energies. Moreover it is unlikely that the polarization of excitons can survive an Auger-like scattering. In this context we compare the total circular upconversion emission (following circular polarization excitation) with the total linear emission (following linear polarization excitation). The two values are the same thus excluding the necessity of absorbing two photons of different circular polarization for reaching the high energy state [177].

To explain the strong cross-circular emission from the B:1s state we propose a scenario, which is based on boson scattering between A- and B-excitons. Indeed, one fascinating result obtained by the condensed matter community in between this century and the end of the previous one was to show that excitons are particles that follow Bose-Einstein statistics. In this framework, important papers were published showing that excitons in quantum wells undergo selective scattering: an unambiguous evidence for the fact that they behave like bosons [204, 205]. Indeed, bosons preferentially scatter from their initial state if the final quantum state is already occupied thus making the scattering more efficient the more occupied the final state is. In the following, we suggest that this principle is responsible for our observations.

To begin, we assume that the excitation creates an equal population of excitons σ^+ and σ^- in the highly energetic state f because the chiral selection rules should not hold so far from the K-valley extrema. A sketch of the situation after the excitation is depicted in panel (a) of Fig. (4.6).

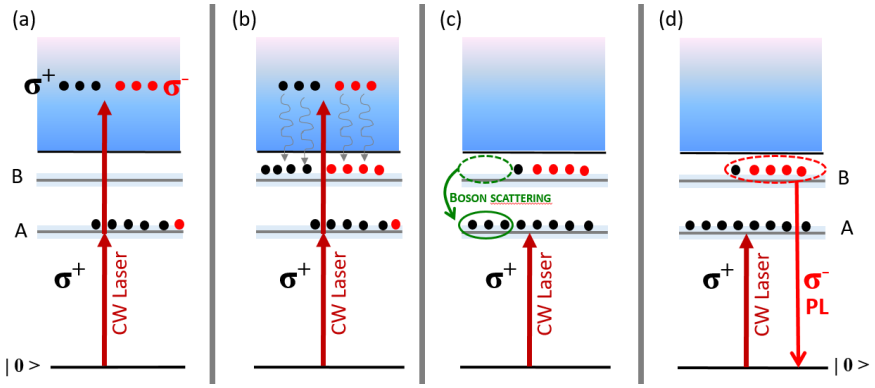

Figure 4.6: Scheme for the explaination of the negative, power dependent, polarization of the B:1s upconversion signal (observed in an encapsulated WSe_2 monolayer) based on the selective boson scattering between A- and B-excitons.

The second assumption is that the relaxation toward the B-exciton state does not favour any of the two polarization states. This means that after excitation we have an equal population of B-excitons in the two polarization states (see panel(b) of Fig. (4.6)).

However, the population of excitons in the σ^+ state will be depleted faster than the one in σ^- thanks to boson scattering (panel (c)). Indeed, it was already proved that excitons behaves like bosons and it is known that bosons preferentially scatter to a final quantum state if this state is already occupied by other bosons. So, because of the A-exciton level in polarization state σ^+ is strongly populated thanks to the σ^+ polarized exciting laser, the scattering probability for B-excitons will be higher in this state than in state σ^-, thus leading to a population imbalance.

At this point the number of σ^- B-excitons will be higher than the σ^+ one which in turn will lead to the σ^- polarized upconversion PL signal from this level as shown in panel (d) of Fig. (4.6). Moreover, the degree of polarization of this signal will increase with power as the scattering probability is proportional to $(1+N^{\sigma^+}_{\mathrm{A:1}s})$ were $N^{\sigma^+}_{\mathrm{A:1}s}$ is the occupancy of the A-exciton level in polarization

state σ^+. Therefore, the more the A:1s is occupied in σ^+ polarization, the faster will be the depletion of B-exciton in the same polarization, the more counter-polarized will be the upconversion emission.

In the end, we note that the linearly polarized excitation of A:1s doesn't induce any linearly polarized upconversion signal from B:1s, as shown in panel (d) of Fig. (4.5). Indeed, linear polarization is related to valley coherence [131] which is too fragile to be maintained during the upconversion and energy relaxation processes.

4.3.2 Rate equation model

For giving a more quantitative description on the possible origin of the build-up of negative polarization we have to write the rate equations which describe the polarization-independent relaxation from the high energy state to B:1s and the polarization dependent scattering from the B- to the A-exciton state. We start writing the generation rate of B-excitons in both polarization states, which is the same, as the relaxation is assumed to be polarization-independent. Thus, if $N_B^{\pm}$ is the occupation number of excitons polarized $\sigma_{\pm}$ we have:

$$G_B = \frac{dN_B^+}{dt} + R_B^+ = \frac{dN_B^+}{dt} + \frac{N_B^+}{\tau_B} + W(1+N_A^+)N_B^+ \tag{4.17}$$

$$G_B = \frac{dN_B^-}{dt} + R_B^- = \frac{dN_B^-}{dt} + \frac{N_B^-}{\tau_B} + W(1+N_A^-)N_B^- \tag{4.18}$$

where $R_B^{\pm}$ are the recombination rates, $N_A^{\pm}$ are the occupancies of $\sigma_{\pm}$ polarized A:1s excitons, τ_B is the lifetime of B-excitons (not related to relaxation towards A-states) while W is the term describing the relaxation rate from B- to A-excitons. In other words the addend $W(1+N_A^{\pm})N_B^{\pm}$ is taking into account the selective boson scattering.

The description presented above is simplified as we do not take explicitly any polarization relaxation of excitons into account. Also a possible multiple step relaxation from B- to A-state was not considered.

The B:1s photoluminescence degree of circular polarization is defined as usual as:

$$P_B = \frac{I_B^+ - I_B^-}{I_B^+ + I_B^-} = \frac{N_B^+ - N_B^-}{N_B^+ + N_B^-} \tag{4.19}$$

An expression for $N_B^{\pm}$ can be obtained from equations Eq. (4.17) and Eq. (4.18) and can be substituted into Eq. (4.19). After some calculation and in the limit of $W\tau_B(1+N_A^{\pm}) \ll 1$ we obtain:

$$P_B = -\frac{1}{2}W\tau_B N_A P_A \tag{4.20}$$

where P_A is the degree of circular polarization of A-excitons and $N_A = N_A^+ + N_A^-$ is the total number of A-excitons. Eq. (4.20) clearly shows that the polarization P_B of the upconversion photoluminescence signal has opposite sign with respect to the polarization of the A-exciton state. Moreover P_B is proportional to the occupation number of A-excitons and so the more excitons are created by the laser the more the upconversion signal will be counterpolarized.

It is also possible to try to estimate P_B. If we assume an incident intensity of $I = 100\,\mu\mathrm{W}/\mu\mathrm{m}^2$ and an A-exciton lifetime $\tau_A = 1\,\mathrm{ps}$ we obtain from Eq. (4.3)

an exciton density $n_X = 10^{10}\,\mathrm{cm}^{-2}$. This value, joint with the value M of the exciton effective mass and with the width of exciton distribution Δ can be used to estimate the occupancy in the A:1s state by means of the equation:

$$N_A = \frac{\hbar^2 n_X}{M\Delta} \tag{4.21}$$

M is estimated to be $0.5\,\mathrm{m}_0$ and in the presence of a population of completely thermalized excitons: $\Delta = k_B T \approx 0.3\,\mathrm{meV}$. So we obtain $N_A \approx 0.05$.

However, we cannot assume thermalization of A-excitons because the sample is under resonant excitation and at low temperature: the exciton-acoustic phonon scattering is weak in TMD crystals and the time between two events strongly exceed the radiative lifetime of excitons [141]. The lowest limit for Δ is coming from the laser linewidth which is extremely sharp in this experiment (around 100 kHz, see subsection (2.2.4)). Taking $\Delta = 3 \times 10^{-2}\,\mathrm{meV}$, $W\tau_B = 0.5$ and $P_A = 100\%$ we obtain $P_B = -15\%$ which is of the same order of magnitude of the value found in our experiment in Fig. (4.5). We therefore conclude that the simple scenario presented here is a possible explanation for the unusual creation of negative polarization that increases with laser power.

4.3.3 Upconversion emission from the excited A-exciton states

Up to now we have discussed the polarization of the emission from the B-exciton, 430 meV above the excitation laser. We will now tackle the description and the interpretation of the polarization of the emission from A:2s and A:3s. The first thing we note is that this emission is strongly co-polarized with respect to the exciting laser, $P_c \approx 25\%$ and it is almost independent on the excitation power. This is shown in panel (a), (b) and (c) of Fig. (4.7), where the three upconversion spectra of the A-exciton excited states obtained at three different powers (5, 10 and $50\,\mu\mathrm{W}/\mu\mathrm{m}^2$ respectively), are presented.

If we compare these results with those obtained from the B-exciton we can clearly see how different the behaviour is. It is thus clear that the scenario based on boson scattering is not suitable to interpret the measured polarization. To explain this different behaviour we suggest that the A-exciton lowest lying state population and its excited states one are coupled. This coupling is made possible by the fact that the separation of $\approx 130\,\mathrm{meV}$ matches the energy of 4 Longitudinal Optical (LO) phonons, as we already discussed in the previous chapter. At this stage we do not have any microscopic model for this "coupling", we merely suggest this scenario based on the surprising results.

To verify this hypothesis we can detune the exciting laser from the strictly A:1s resonant excitation condition and observe the upconversion emission from the excited states. This upconversion PLE is similar to the one shown in Fig. (4.2) (a) but this time the detected spectral range is smaller as we used a more dispersive grating to focus only on the signal coming from the A-exciton excited states. This improved our spectral resolution. The results are shown in Fig. (4.8).

In Fig. (4.8) we can see in addition to the A:2s-A:3s double peak a new feature that moves with the excitation laser. This corresponds to an anti-Stokes Raman mode superimposed to the upconversion PL of the A:2s and A:3s excitons. While

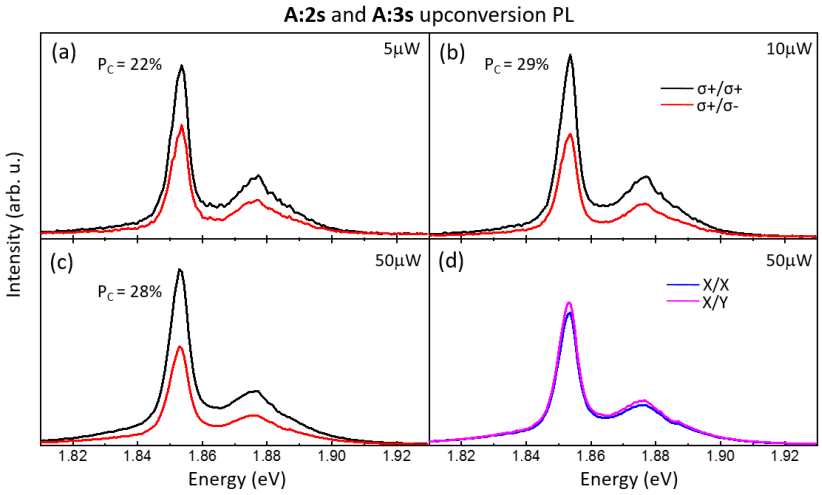

Figure 4.7: All data are obtained at $T = 4\,\mathrm{K}$ from an encapsulated WSe_2 monolayer. (a) σ^+ (black, co-polarized) and σ^- (red, cross-polarized) components of the upconversion PL of A:2s and A:3s following a σ^+ laser excitation with power density of $5\,\mu\mathrm{W}\,\mu\mathrm{m}^{-2}$ (b) Same as (a) but for power density of $10\,\mu\mathrm{W}\,\mu\mathrm{m}^{-2}$. (c) same as (a) but for power density of $50\,\mu\mathrm{W}\,\mu\mathrm{m}^{-2}$. The degree of circular polarization is indicated in each panel and it can be noted that it is weakely dependent on the power density of excitation. (d) (a) Linear X (blue, co-polarized) and liner Y (magenta, cross-polarized) components of the upconversion PL of A:2s and A:3s following a linear X laser excitation with power density of $50\,\mu\mathrm{W}\,\mu\mathrm{m}^{-2}$.

the contour plot in panel (a) of Fig. (4.8) shows the complete set of data, the waterfall one in panel (b) focuses mainly on the high energy side of the excitation (the laser is always at slightly higher energy than the A:1s transition and so is the anti-Stokes Raman line with respect to the A:2s). We can conclude that our detected signal between $1.84 - 1.90\,\mathrm{eV}$ is actually the superposition of a spectrally fixed PL component coming from the excited A-exciton states and one coming from a Raman feature whose spectral position changes with the laser energy. However, we couldn't find a clear trace of anti-crossing between PL and Raman signals, to progress in the understanding of the observed exciton-phonon coupling (strong or perturbative). The linewidths are too broad to trace the position of the two peaks with high accuracy.

Even though a strong coupling was not clearly proved, a clear interaction is present and we think that excitons from the A:1s state, which means from polarization state σ^+, can scatter to the A:2s state thus incrementing the population of the excited excitons in the same polarization state. This is why the subsequent emission is slightly σ^+ polarized.

As already discussed in Chapter 3, a double resonant Stokes scattering was observed [179] proving the relaxation from A:2s to the A:1s state to be efficient as the two states are separated by a phonon energy multiple. What was observed here is the equivalent anti-Stokes process. This may seem very surprising as the system is kept at $T = 4\,\mathrm{K}$ so the phonon absorption suggested here may seem unlikely. First, the process is intrinsically less efficient, secondly it is not clear how the absorbed phonons are generated, considering the temperature at which

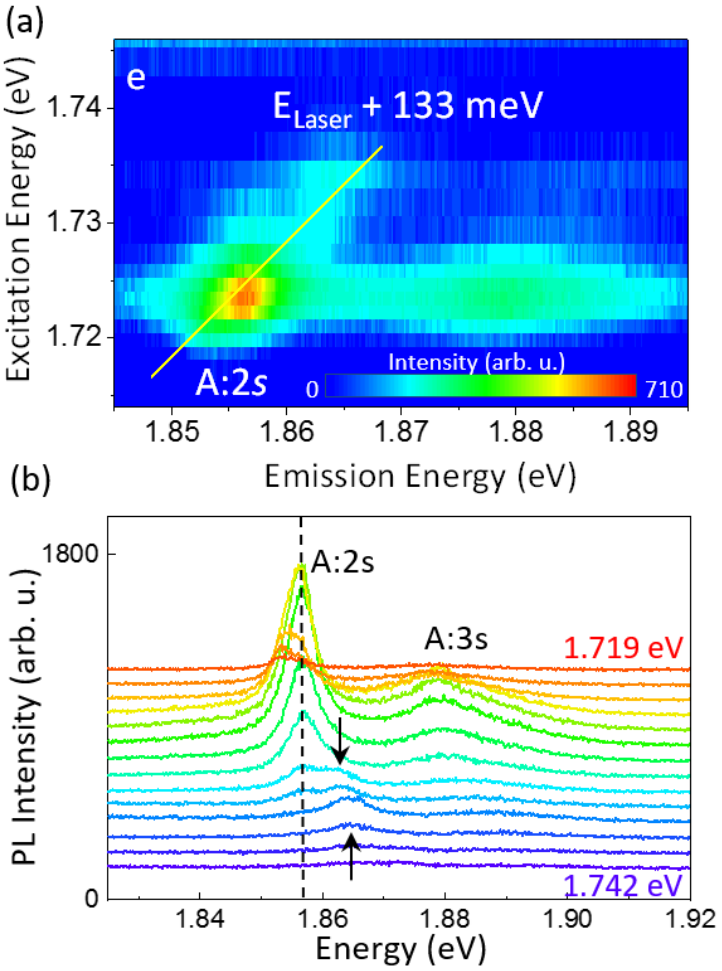

Figure 4.8: All data are obtained at $T = 4\,\mathrm{K}$ from an encapsulated WSe_2 monolayer. (a) Contour plot of A:2s and A:3s upconversion PL intensity as a function of laser excitation energy while it crosses the A:1s transition. As mentioned before, the upconversion signal is quenched when the laser is not resonant with the neutral exciton anymore. A Raman mode moving with the laser energy is clearly visible. (b) Different PL spectra of A:2s, A:3s and of the Raman feature at different laser excitation energy (from 1.742 eV for the purple spectrum to 1.719 eV for the red one) as it approaches and crosses the A:1s resonance located at 1.723 eV. The data are the same presented in panel (a).

the system is kept.

One hypothesis is that they are generated during the relaxation of excitons from the highly excited state f towards the B:1s, A:2s and A:3s states and even more efficiently when the neutral exciton A:1s relaxes towards the trion state. If indeed we consider a standard PLE experiment in which we monitor the trion emission while resonantly exciting the neutral exciton A:1s (in the same conditions of the upconversion PLE) we observe that the trion emission is several orders of magnitude more intense than the upconversion signal, as shown

in panel (c) of Fig. (4.1). This situation may generate enough phonons that then are used to couple the most tightly bound state of the A-exciton (A:1s) with its first excited state.

To conclude, we also point out that, as for the Stokes case described in Chapter 3, the Raman line do not clearly emerge on the low energy side of the A:2s transition. In the anti-Stokes case (panel (b) of Fig. (4.8)) we can see a shift of the energy position of the peak and a broadening of the linewidth but we cannot fit the phonon related line and the A:2s transition separately with high precision. Please note that for the upconversion B-exciton emission, we have no signature of a double-resonant Raman process.

4.4 Conclusions

During this chapter we introduced an upconversion process in monolayer WSe_2. This process leads to very surprising observations and we interpreted it as a non-linear process in which two excitons are independently generated by two photons. Following a resonant Auger scattering, one of them is promoted to an highly excited state f from which it can relax and occupy excitonic states A:2s, A:3s and B:1s which lays at higher energy than the A:1s state we were exciting.

Even if upconversion is an interesting phenomenon which we aim to understand, it can also be seen as a new tool for investigating a material. For example it is a way to gain insight into the exciton-exciton interaction inside a monolayer. This high density regime is interesting in the context of lasing, for which exciton-exciton annihilation (Auger scattering) should of course be as inefficient as possible.

We would like to conclude this chapter with a simple numerical analysis comparison with other works on exciton-exciton scattering. In a general simple case, the rate of the Auger process is described by a parameter R_A. The generation rate of highly energetic excitons (those which gain energy during the scattering) is given by:

$$\frac{dn'_X}{dt} = R_A n_X^2 \tag{4.22}$$

Where n'_X is the density of highly energetic excitons and n_X the density of excitons photoexcited in the A:1s state. In this equation we disregarded the recombination and energy relaxation processes.

For reasonable material parameters [200] the quantity R_A at $T = 4\,\mathrm{K}$ can be estimated to be $1, \ldots 10\,\mathrm{cm}^2/\mathrm{s}$ in our experiment. This quantity can be reduced by a factor $10, \ldots 100$ if the resonant condition, shown in panel (b) Fig. (4.3) is not fulfilled [83].

The experimentally observed Auger rates in the literature are therefore one or two orders of magnitude smaller than the resonant contribution to R_A investigated here [192, 110, 194, 193, 206, 207, 208]. The exact value of R_A will also vary with sample temperature and environment, demonstrating that the exact resonance conditions are not fulfilled in the studied structures. Furthermore, depending on the material, e.g., for tungsten based monolayers, a considerable part of the excitonic population can be in the spin-dark state (see Chapter 3), which also affects the Auger rates because, for the Auger process, at least one exciton should be spin allowed [83]. Our measurements are carried

out at $T = 4\,\mathrm{K}$, whereas many exciton-exciton scattering studies are carried out at elevated temperatures. The absence of disorder in the sample, especially with the hBN encapsulation, may enable us to simultaneously fulfil the energy and momentum conservation in TMD MLs, making additional scenarios for Auger-like processes possible.

Thus, upconversion spectroscopy represents also another way to study the light-matter interaction in TMDs. We can alsouse it to determine the position of the real electronic transitions in a material, and in particular it has been used to find the excited states in monolayers $MoSe_2$ and $MoTe_2$ encapsulated in hBN [83]. The presence and the position of these states was not reported before. When these materials are exfoliated on SiO_2 the A-exciton series spectrally overlaps with the B-exciton one and the transitions are too broad to be fitted.

In general, after our first experiment in WSe_2 we performed upconversion in four out of the five members of the TMDs family as shown in Fig. (4.9). This proves once more the generality of this process for TMDs, which works independently of the material, the substrate and the temperature.

The description of the process we gave before is in principle valid for all the TMDs. As already mentioned, a more complete version of the theory developped by L. Golub and M. Glazov can be found in reference [83]. Even though, several things still need to be understood. For example, we found that the intensity dependence of the upconversion signal as a function of the exciting laser power in monolayer $MoTe_2$ is not superlinear as expected but follows a linear relationship. This is not necessarily in contradiction with our proposed Auger scattering scenario.

The hot photoluminescence from B:1s and A:2s excitons is indeed not ideal for probing quantitatively how many excitons were generated in upconversion. For example the relaxation efficiency towards B:1s or A:2s can be complex. Moreover, hot photoluminescence itself depends on the competition between radiative recombination and relaxation towards the A:1s state. This means that a non-quadratic relationship of the hot luminescence intensity as a function of the laser excitation power can have several origins.

We thus hope that the discussion in this chapter will stimulate more research as we believe that the answers to the proposed questions are of great interest for a deeper understanding of exciton-exciton interactions in these extraordinary materials.

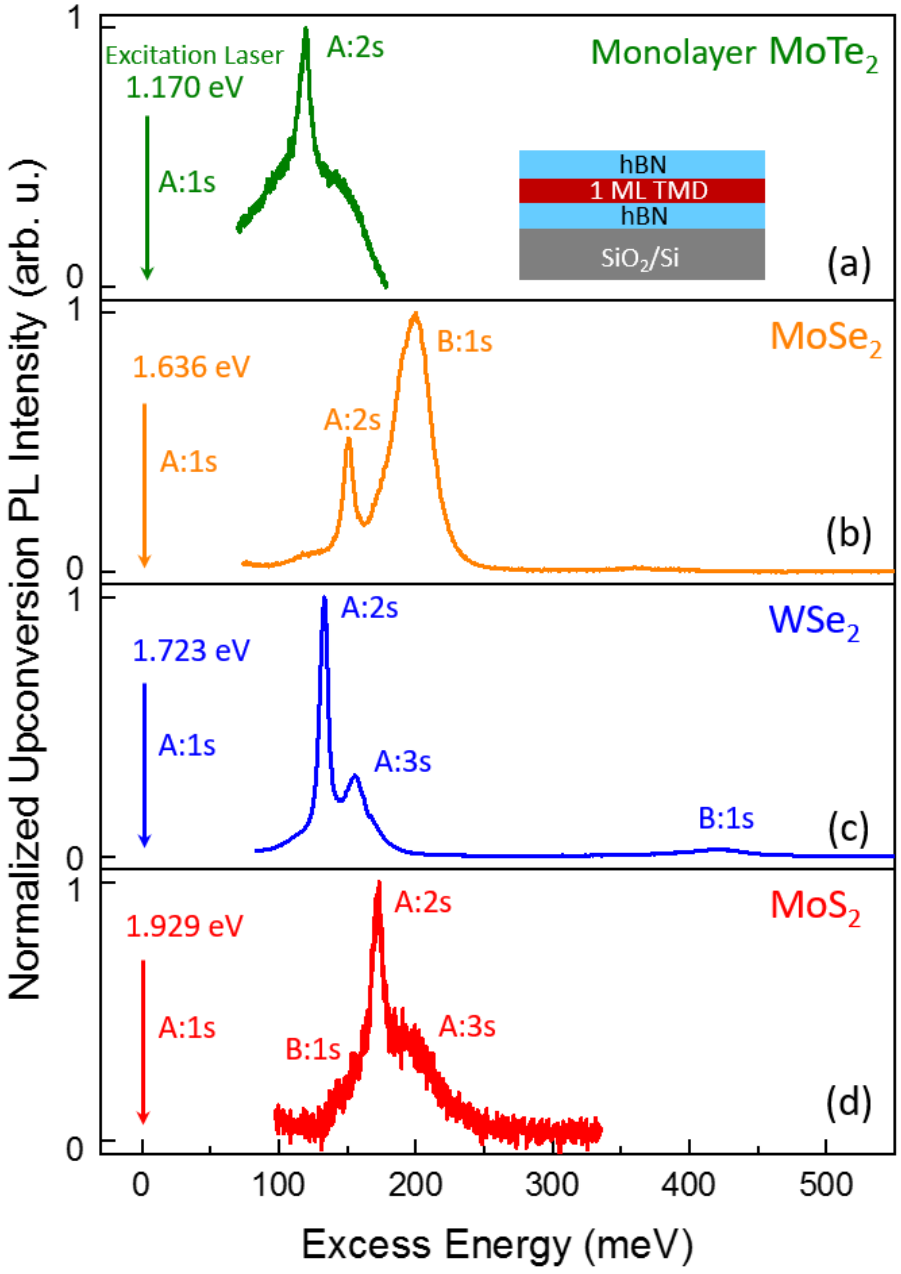

Figure 4.9: $T = 4\,\mathrm{K}$ upconversion emission from: (a) $MoTe_2$, (b) $MoSe_2$, (c) WSe_2 and (d) MoS_2 monolayers encapsulated in hBN. For excess energy we mean the difference between the detected energy and the energy of the exciting laser. All the samples are excited resonantly at the A:1s energy (indicated by the arrow on the left). The emission from the excited states and the B-exciton is observed between 100 and 400 meV above the A:1s state [83].

Chapter 5

Gated devices

In the previous two chapters we have studied WSe_2 monolayers encapsulated in hexagonal boron nitride (hBN) which were fabricated following the procedure described in Chapter 2. This basic van der Waals heterostructure was positioned on top of a Si/SiO_2 substrate. For this type of simple heterostructure, we cannot control the excess carrier concentration in the monolayer. The only way to deduce the doping is by checking the optical signatures of charged excitons (trions) in the spectrum. These quasi-particles are made of an exciton bound to an additional charged carrier. There are thus negatively charged excitons X^- (two electrons and one hole) and positively charged excitons X^+ (one elctron and two holes). The label T we used for indicating the trion in Chapter 3 implies that we don't know if we are looking at the positively or the negatively charged trion. Indeed, if the doping is unknown, it is extremely difficult to deduce the charge of the trion state.

This was even more problematic, when the monolayers were exfoliated directly on SiO_2 due to the broader transition linewidth in earlier studies. The attempts of using chemically doped bulk samples for exfoliation were not very successful as the high surface/volume ratio of the monolayers may result in the extraction or the injection of charges from the surrounding environment. This in turn may lead to a significative difference between the chemical doping of the bulk and the effective one of the exfoliated monolayer.

Thus, for studying charged excitons, the community developed devices for effective doping of monolayers. The way to do it is very simple, it is necessary to contact one side of a monolayer with a metal and to isolate the other from a second electrode which acts like a gate. In this way the charges can be introduced or removed by controlling the electric potential between the two electrodes.

Studying trions in TMDs is interesting because they present several differences with the analougous particles observed in other systems, such as quantum wells kept at low temperature [209]. First, when these particles were observed they were localized around defects while in TMDs they are in principle free to move along the monolayer. This happens because the energy difference in the binding energy is one order of magnitude: in TMDs it is around 30 meV [210, 211], whereas the trion binding energy in a GaAs quantum well is between 1 and 2 meV [212, 213, 214, 215] and around 2.5 meV in CdTe quantum wells [209]. As a consequence of this large value of the binding energy in TMDs, charged excitons are observed up to room temperature [112, 133, 216].

A second difference between trions in classic nanostructures and in TMDs is due to the peculiar bandstructure of the latter. As we mentioned in Chapter 1 the bandgap in a TMD monolayer is located at the K points of the Brillouin zone. Because of the absence of inversion symmetry these non-equivalent K points are, respectively, of K^+ and K^- nature. This means that each of the two valleys can be addressed with a different state of circular polarization thus initializing the valley index [55, 54]. See Chapter 1 for more details.

Moreover, the conduction (valence) band splits in two sub-bands which can host just one of the two possible spin states and which are separated by several tens (hundreds) of meV [32, 54, 58, 59, 217] (see also Chapter 1). This fact gives rise to many different configurations of the valley index and the spin quantum number of the particles composing a trion. For example, in a negatively charged trion, the extra electron can be in the same valley or in the opposite valley of the electron that was optically excited, thus giving rise to small changes in the trion binding energy. The consequence of this can be seen as a fine structure splitting in the spectrum of the negatively charged excitons.

As explained in Chapter 3, the deposition of a monolayer directly on a Si/SiO_2 substrate gives rise to two critical problems. An example spectrum is shown in Fig. (5.1)

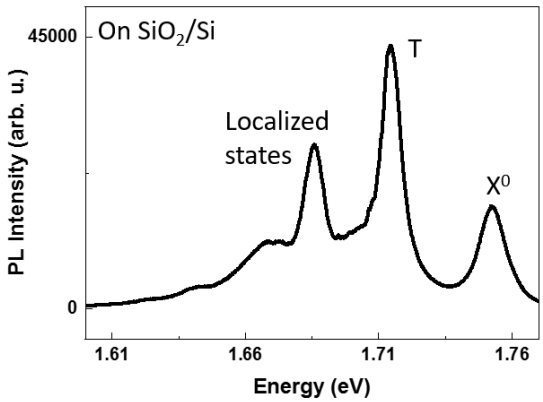

Figure 5.1: Low temperature ($T = 4\,K$) photoluminescene spectrum of a WSe_2 monolayer exfoliated on a Si/SiO_2 substrate and excited by a helium-neon laser (632.8 nm). The labels indicate the peaks according to literature identification: from right to left we have the neutral exciton X^0 (A:1s) the trion T and a peak ascribed to localized excitons.

As one can see the peaks are very broad, X^0 and T have a FWHM of 13 meV and 9 meV respectively. If there is a trion fine structure is very likely that it would be masked by the large value of the full width at half maximum of the trion peak. In the same way, a difference in the binding energy of the positively and the negatively charged trion may not be visible. Moreover, the doping regime is unknown. We observe a trion peak but we cannot determine if we are observing X^+ or X^- (and thus we labelled it as T). For these two reason we decided to encapsulate monolayers in hexagonal boron nitride.

In this chapter we will present our version of a gated device. We will start describing it and the procedure we use for fabricating it. Then, we will proceed with the description of the experimental observations that the effective doping

allowed us to obtain, such as the splitting in the negative trion fine structure. We will compare these results with those obtained in the literature. In the end a theoretical model which aims to interpret the results will be provided.

For the fabrication part I would like to thank Cedric Robert, Emmanuel Courtade and AIME INSA. The theory was developed by Marina Semina and Mikhail Glazov, our collaborators from the Ioffe Institute in Saint Petersburg.

5.1 Sample fabrication and optical spectroscopy

In the following we will briefly describe the fabrication procedure that allowed us to build our charge tunable device which we later investigated using optical spectroscopy techniques.

For the particular sample investigated in this chapter we started patterning some gold electrodes on a standard Si/SiO_2 substrate. A first high quality hBN [89] flake is then mechanically exfoliated and transferred close to one electrode, using the polydimethylsiloxane (PDMS) technique described extensively in Chapter 2. As a next step, a monolayer WSe_2 is deposited on top of the first hBN flake followed by a graphite flake a few monolayers thick. This graphite flake doesn't cover the whole monolayer, which has to be optically excited. The other side of the graphite flake is instead in contact with the gold electrode. In the end, a capping hBN layer is transferred on top of the heterostructure. The schematic and an optical micrograph of the device are shown in Fig. (5.2).

In this device the two electrodes are the Si substrate and the gold patterned on top of the SiO_2 layer. Once the two electrodes are connected to a sourcemeter (a Keithly 2450) the injection or extraction of electrons from the monolayer will be possible through the graphite flake (where the extraction of carriers corresponds to the injection of holes). As shown by Mak et al. [210] the presence of intentional or unintentional doping in TMD monolayers has as a consequence the formation of three particle complexes called trions or charged excitons which leave their signature in the optical spectra. The device we built will thus allow us to study these particles in more detail. We can select which doping regime we want to investigate thus studying positively charged X^+ or negativel charged X^- trions. Due to hBN encapsulation and the resulting increase of the optical quality we will have access to the fine structure details of the trions, so far hidden by spectrally broad lines.

Indeed, already in samples exfoliated on SiO_2 the negatively charged exciton X^- in the n-doping regime was showing hints of a fine structure. This is a consequence of the fact that the extra electron can be either in the same valley or in a different valley compared to the optically generated electron, as explained theoretically [218] and observed experimentally in WSe_2 [189, 90] but also in WS_2 [219, 220, 221, 222]. More details about these observations will be provided in the following.

An important premise is that the charge densities explored during our experiment are small. By this we mean that once a charged exciton is formed it is not influenced by the presence of others trions in the surroundings. However, if the charge density becomes too large we cannot neglect the effects of screening any more. For high charge carrier concentration it is probably more convenient to redefine the problem: instead of considering a three particle approach a many-body physics one would be more convenient. In this case we

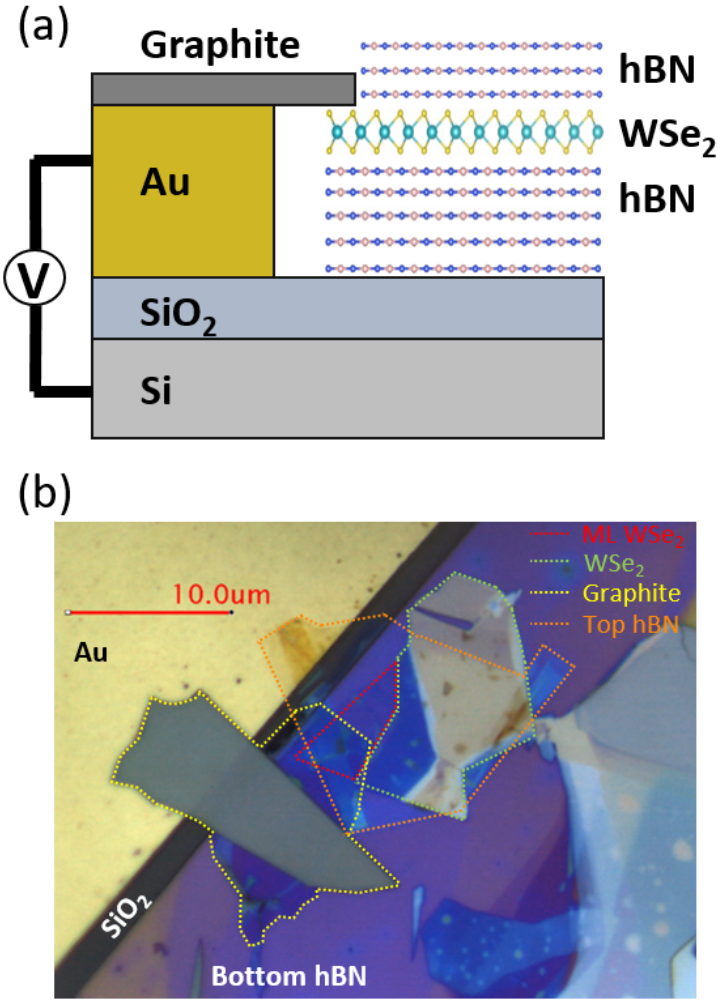

Figure 5.2: (a) Sketch of the gated device fabricated by our group and (b) optical micrograph of it. The application of a voltage between the gold electrode and the Si backgate allows us to effectively dope the monolayer.

would rather consider an exciton immersed in a sea of electrons. This problem has been addressed in a fermi-polaron approach [223]. This approach is very powerful and interesting but is not necessary here to analyse experiments at low carrier densities.

The charge tunable sample is mounted inside a cryostat to perform optical spectroscopy at $T = 4\,\mathrm{K}$. First we discuss the differential reflectivity experiment, where we measured the spectrum from the sample as a function of the gate voltage. The series of data is shown in the contour plot in Fig. (5.3) (a) where the intensity of the first derivative of the differential reflectivity with respect to photon energy is shown.

In Fig. (5.3) we can identify the main features in the spectrum, which means those transitions which show a large oscillator strength for optical absorption

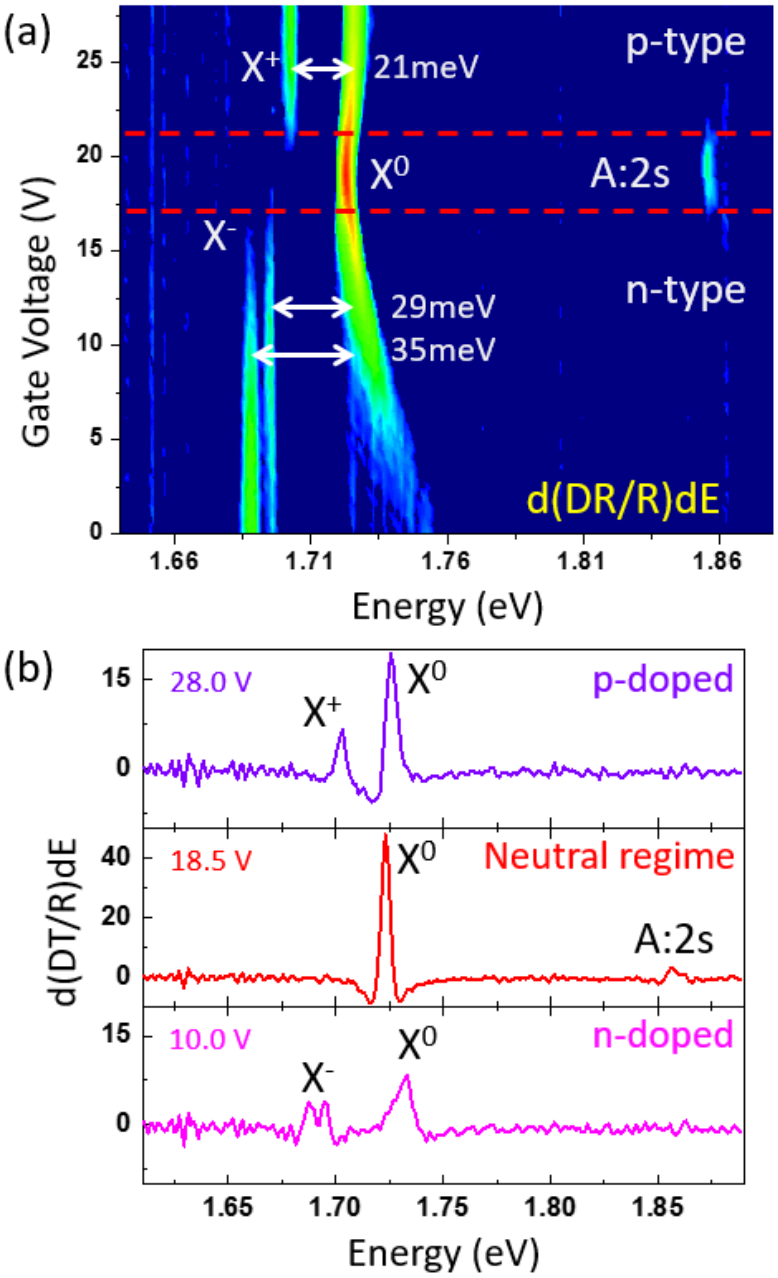

Figure 5.3: (a) Contour plot which shows the first derivative of the differential reflectivity spectra with respect to energy as a function of the gate voltage of an encapsulated and gated WSe_2 monolayer at $T = 4\,\mathrm{K}$. The three doping regimes, p-type, neutral and n-type are clearly visible. The intensity is color coded in a log-scale where dark blue corresponds to < 0.5, while red > 50 (arbitrary units). (b) Spectra corresponding to the three doping regimes extracted from the contour plot on (a).

[49]. Globally, the most intense transition is the one at 1.72 eV which is identified as the neutral exciton and indicated as X^0: this is the A:1s exciton state. In the same gate voltage region a second transition appears at about 130 meV above the neutral exciton. It is thus identified as the A-exciton first excited state (A:2s), as discussed in Chapter 3 and in Chapter 4. Please note how the intensity of both transitions strongly decreases when the voltage is moved from the neutrality condition.

With regard to this, please note how the applied voltage necessary for keeping the sample in the neutrality regime is not zero but it is around 18 V. The reason may be the fact that the graphite automatically injects electrons in the monolayer when no voltage is applied. Indeed, the situation is not the same when we consider a monolayer simply encapsulated in hBN, which is in fact very close to the neutral regime. We can deduce this comparing the reflectivity spectrum in Fig. (3.3) from Chapter 3 with the reflectivity spectrum of our device in the neutral regime, shown in panel (b) of Fig. (5.3).

When we apply a higher voltage than 18 V, i.e. when we extract electrons from the WSe_2, we observe a decrease of the oscillator strength of the neutral exciton X^0. At the same time a peak appears 21 meV at lower energy. This peak is the positive trion and it is labelled X^+. If the voltage is decreased we reach the n-doping regime (the Fermi level reaches the conduction band). Also in this case, the intensity of the neutral exciton strongly decreases but this time not a single feature but a doublet appears at around 30 meV below the X^0. It is the negatively charged exciton X^- and its fine structure splitting of 6 meV is clearly demonstrated. This would have not be possible in a non-encapsulated sample with broad linewidth.

It is worthy to note for future discussions that the two peaks are located at 29 and 35 meV from X^0 which means that both their energies are different from the longitudinal optical (LO) phonon energy which is equal to 32 meV [134]. Moreover, the different evolution of the oscillator strength of X^0 and X^- as a function of voltage clearly shows that the doublet is not a simple phonon replica of the X^0 transition.

Now that all the transitions are identified in absorption we can try to interpret the emission spectra. Unfortunately, the p-type regime is not accessible in photoluminescence. Indeed, the non-resonant excitation laser might generate a sufficiently high carrier concentration in order to screen the applied electric field. In contrast, the white light source has sufficiently low power to avoid this effect. As a result, in photoluminescence we can only study the neutral and the n-type regimes. When increasing the voltage in the device towards the p-type regime, we recorded a current and therefore we did not increase the bias further. The PL spectra are shown in Fig. (5.4).

In the neutral doping regime, we observe a very similar emission compared to the one obtained by ungated WSe_2 encapsulated in hBN. Compare the red curve in panel (b) of Fig. (5.4) with the one shown in Fig. (3.2) in Chapter 3. The main difference is due to a bigger defect related peak (marked as "Loc." in Fig. (5.4)) at ≈ 1.67 eV, on the low energy side of the spectrum, that may also be due to the phonon assisted recombination of indirect excitons [224]. As described in Chapter 3, we observe three main transitions. The one at higher energy (1.72 eV) and with a linewidth of just 4 meV is X^0. Please note that the energy position of X^0 is the same in both reflectivity and PL, indicating that the Stokes shift is negligible. The peak 40 meV at lower energy has been identified

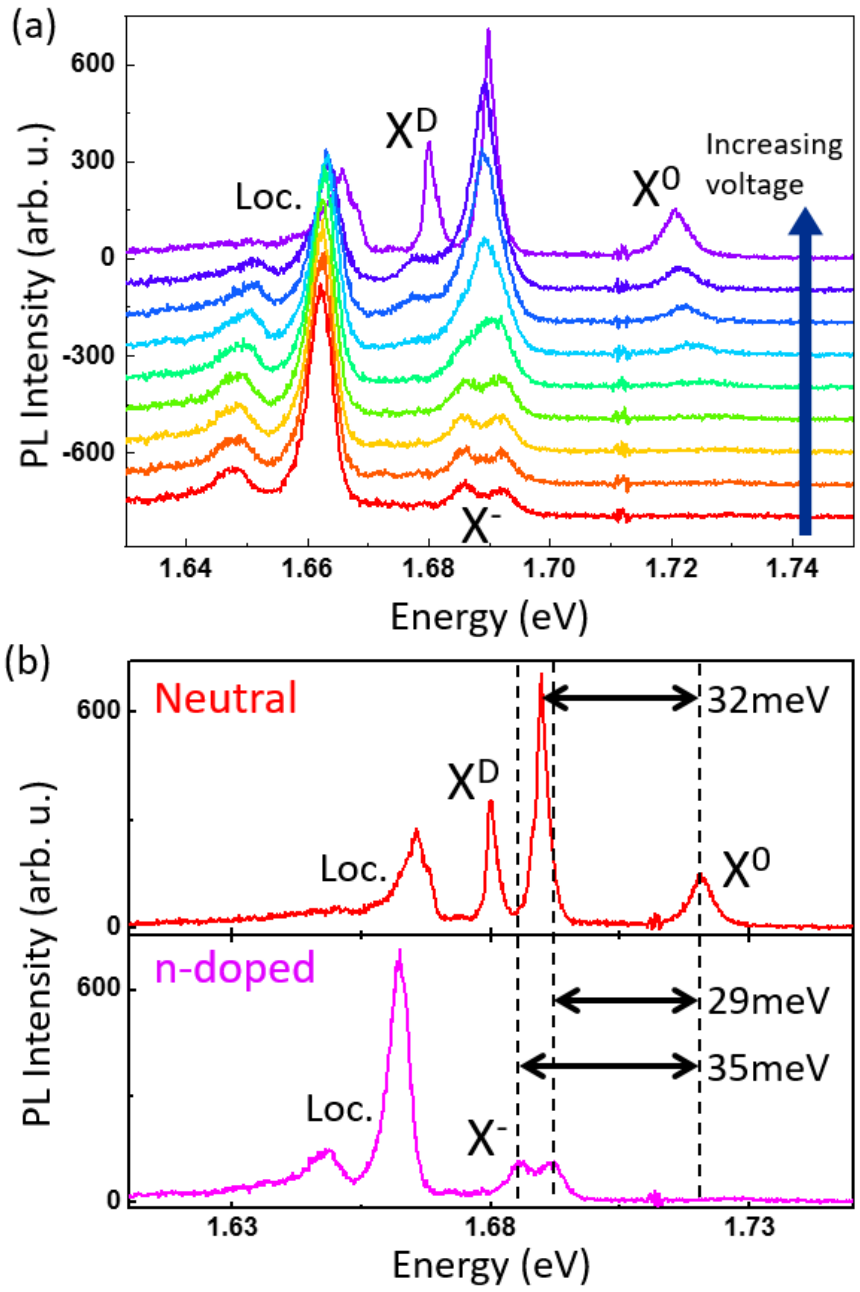

Figure 5.4: (a) Waterfall plot which shows the PL spectra of our charge tunable device as the gate voltage is varied. The WSe_2 monolayer is kept at $T = 4\,K$ and excited by a helium-neon laser (1.96 eV). (b) Two spectra extracted from panel (a). The red one represent the PL emission in the neutral regime and strongly rensamble those obtained in simple encapsulated samples. The magenta spectrum is instead obtained in the n-doping regime. The trion fine structure is clearly visible.

as the dark exciton X^D. So far, we and the whole community ascribed the most intense transition in the middle to the trion.

When we inject electrons in the system, both the PL signals from the bright and the dark neutral excitons completely disappear. The peak in the middle is replaced by a weaker doublet as we approach the n-type regime. The energy separation of the two peaks of this doublet and their spectral distance from X^0 perfectly match with the same values obtained in reflectivity for the negatively charged trion. Hence, we deduce that this doublet is the PL emission of X^-.

This PL data questions the nature of the very intense peak we observe in PL in the neutral regime. This single peak ~ 32 mev below X^0 cannot be the X^+, which is 21 meV away in reflectivity. The X^- is a doublet and therefore it also can't explain this peak. If we look more carefully at the waterfall plot in panel (a) of Fig. (5.4) we actually note how its intensity decreases very similarly to the one of X^0. They disappear at the same voltage. This considerations and the fact that 32 meV is the energy of the LO phonons in WSe_2 make us think that we are actually observing some kind of phonon replica of X^0 or some kind of mixed state between the negative trion and the phonons. Another possibility would be phonon mediated recombination of indirect excitons [224].

In this context, please note that in the n-doping regime a new peak appears on the low energy side of the X^- emission. This peak is separated by the negatively charged exciton doublet by ~ 32 meV and may represent a phonon replica of one of the X^- components. Finally, we stress that the green PL curve in Fig. (5.4) (a), between the neutral and n-type regime, which shows a superposition of the trion doublet and the possibly phonon-related emission, closely resembles the emission PL usually observed in ungated and unencapsulated samples, where the trion peak often appears as an asymmetric peak which appears to have a shoulder.

We now focus on the negative trion fine structure. The presence of two lines with different energy may be understood when we consider that (at least) two negative trion states exist: the one in which the two electrons lay in the same valley (intravalley trion) and the one formed by two electrons in the two different valley (intervalley trion). The energy of these two configurations should be different because of the Coulomb exchange interaction between the involved particles [218].

More in detail, in the intravalley trions, the electrons have to occupy the two branches of the conduction band of the same valley, thus having a different spin. This means that they will form a singlet state. For the intervalley trion, the spin of the two electrons may be the same, they will thus form a spin triplet. It was hence suggested that the electron-hole exchange interaction in the intervalley trion is stronger than the electron-electron one thanks to the Coulomb attraction. This term would be then responsible for the increase of the energy of the intervalley (triplet) state. In other words the intervalley trion is less bound. Here we just repeated the arguments from the literature. The relative signs of the different Coulomb terms are still not known in our point of view. It is therefore difficult to determine which trion configuration is in reality at higher/lower energy.

Experimental results in the literature seem to confirm the presence of a trion fine structure, first in unencapsulated WSe_2 [189] and WS_2 [219, 220, 221] samples and then also in encapsulated WSe_2 [90] and WS_2 [222]. The data obtained by some of these groups are summarized in Fig. (5.5).

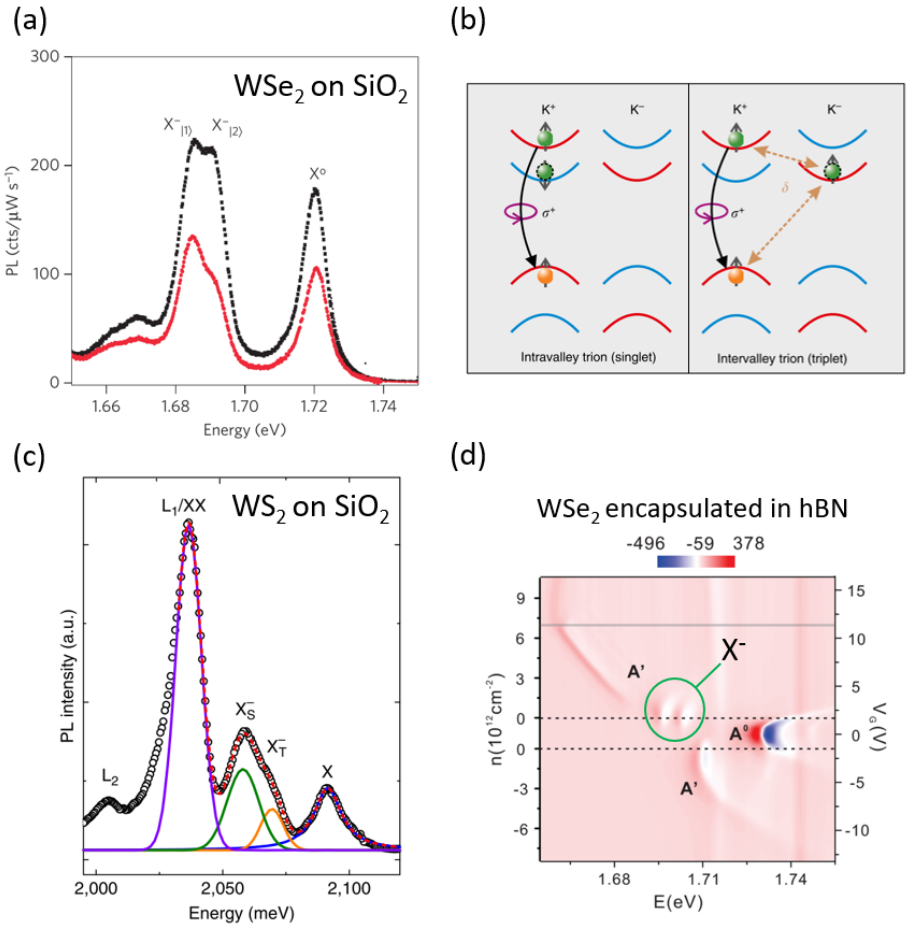

Figure 5.5: (a) Low temperature PL spectrum of an unencapsulated WSe_2 sample where the trion fine structure is observed. The picture has been taken from reference [189]. (b) Sketch of the intravalley and the intervalley trions. Picture taken from Plechinger et al. [220]. (c) Low temperature PL spectrum of an unencapsulated WS_2 sample where a trion fine structure of 11 meV is shown. The picture has been taken from reference [220]. (d) The contour plot shows the first derivative of the reflectivity spectrum with respect to the energy as a function of the electron density. The WSe_2 sample under study was encapsulated in hBN, kept at low temperature and it clearly shows a trion double feature, indicated by a green circle. The picture has been taken from reference [90].

The PL spectrum shown in panel (a) has been taken by Jones et al. and shows a doublet with a splitting of 7 meV from an unencapsulated WSe_2 monolayer. This value agrees with the one of 6 meV predicted by [218]. This, and the fact that both peaks are circularly polarized made the authors assign those lines to the intravalley and intervalley trion which are sketched in panel (b) of Fig. (5.5).

Moreover, the authors observed that the degree of circular polarization of the higher energy component of the doublet is larger than the one of the peak at

lower energy. The authors thus suggested that the intervalley trion is indeed the component of the doublet at higher energy. In their opinion this happens because the high energy branch of the conduction band has a narrower distribution of the momentum of the electrons. This has as a consequence a smaller depolarization rate which depends indeed on the momentum of the electron. Please note that in the experiment performed by Jones et al. the energy separation between the more polarized intervalley trion and the neutral exciton matches the phonon energy. They clearly observe this in upconversion PLE: the trion doublet was excited with a laser and the X^0 emission was detected. However, a resonance appears only when the excitation energy matches the energy of the more polarized trion and not for both the components of the doublet. The energy separation between the resonance and X^0 is 32 eV. Note that this upconversion process has very different microscopic orignin than our exciton-exciton scattering discussed in Chapter 4

Similar results are obtained by Plechinger et al. in WS_2 monolayers deposited on SiO_2 and they are shown in panel (c) of Fig. (5.5). A trion doublet with energy separation of 11 meV is observed and the degree of circular polarization of the state at higher energy (labelled triplet trion X_T^-) is larger than the one of the state at the lower energy (singlet trion). The authors agree with Jones et al. in assigning the high energy component to the intervalley trion and the lower energy peak to the intravalley one.

Finally, a clear double peak is observed by Wang et al. [90], in an encapsulated WSe_2 monolayer, this time in reflectivity. The graph, shown in panel (d) of Fig. (5.5) strongly resembles to the one we presented in Fig. (5.3) (a). The authors agree in assigning the doublet to a fine structure emission of the negatively charged exciton and they say their observation is consisted to an exchange interaction origin of the splitting. However, no further comment is made about the nature of the individual peaks (i.e. which one between the intervalley or the intravalley transition is at higher energy).

In this framework, we try to observe the same polarization difference in our sample with higher optical quality. Hence, we excite the sample with a σ^+ polarized laser and we detect the two circular polarization components of the PL emission. We also found that both the peaks which compose the X^- are cocircularly polarized with the laser, but no appreciable difference in the degree of circular polarization was observed between the two peaks, as shown in Fig. (5.6).

It is indeed true, as suggested by [189] that the depolarization may be different for different X^- species, i.e. for intravalley or intervalley trions. However, in stationary PL this differences may not be noticeable if the PL emission time is faster than the depolarization one. Measurements of these times were not performed for charge tunable samples encapsulated in hBN. So, at this stage, we do not know which of the two trion transitions corresponds to the intervalley and intravalley contribution, respectively.

More recently, a fine structure splitting was also observed in encapsulated WS_2 [222]. Also in this case the authors observed a different degree of circular polarization for the two negative trion states (which are separated by 7 meV). So the polarization of the X^- emission is clearly not well understood by the community and further experiments are needed.

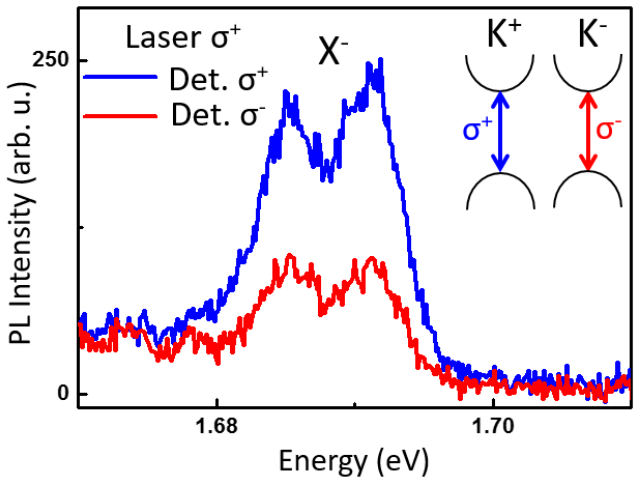

Figure 5.6: Low temperature ($T = 4\,\mathrm{K}$) PL spectrum of the X^- transition in the n-doping regime (gate voltage fixed at 6 V), observed in our gated device. The sample was excited at 1.96 eV. The two spectra represent the two components of circular polarization following a σ^+ excitation.

5.2 Theory of trion binding energies and fine structure

The main experimental results we presented in the previous section were a clear difference in the binding energies of the positive and negative trion and a 6 meV fine structure splitting of the X^- transition. We achieved these unambiguous results for the first time in this field due to hBN encapsulation which allowed us to obtain a better spectral resolution.

In this section we will estimate the trion binding energies, we will discuss why they are different for the positive and the negative complexes and in the end we will explain the origin of the fine structure splitting for the negative trion. This discussion is based on the arguments developed by Marina Semina and Mikhail Glazov with our group [225].

5.2.1 Trion binding energies

In order to calculate the binding energies we have first to define the wave function of the charged excitons. We will do so following the same procedure of [225] in which more details can be found. Our target here is to summarize the main findings.

The wave function describing a free electron in a crystal has the form

$$\psi(\mathbf{r}) = e^{i\mathbf{k}\cdot\mathbf{r}} u(\mathbf{r}) \tag{5.1}$$

Where, for the Bloch's theorem, $u(\mathbf{r})$ is a periodic function with the same periodicity as the crystal. In the equation, $\mathbf{k}$ is the momentum vector and $\mathbf{r}$ the position one. In our case it would be convenient to express the position vector in cylindrical coordinates $\mathbf{r} = (\boldsymbol{\rho}, z)$, where z is perpendicular to the monolayer

plane. As a consequence of the fact that the binding energy of the trion is much smaller than the bangap we can write the trion wave function as the product of the single particles wave functions, i.e. like a product of equations such as Eq. (5.1). We can express it in the following way:

$$\Psi_{i,j;k}(\mathbf{r}_i, \mathbf{r}_j, \mathbf{r}_k) = \frac{e^{i\mathbf{K}\cdot\mathbf{R}}}{\sqrt{S}} \phi(\boldsymbol{\rho}_1, \boldsymbol{\rho}_2) U^{(2)}_{i,j}(\mathbf{r}_i, \mathbf{r}_j) U^{(1)}_k(\mathbf{r}_k) \tag{5.2}$$

The subscripts i and j denote the two identical carriers while k is the unpaired one. Hence if the wave function describes X^+ i and j will represent the two holes h_1 and h_2 while they will represent the two electrons if we are considering the wave function of X^-. In Eq. (5.2) $\mathbf{R} = [m_i(\boldsymbol{\rho}_i + \boldsymbol{\rho}_j) + m_k\boldsymbol{\rho}_k]/M$ is the center-of-mass in-plane coordinate while $\mathbf{K}$ is the center-of-mass wave vector. S in the normalization area, m_i the mass of the identical particles and m_k is the mass of the unpaired one. M is the trion mass and it is thus equal to $2m_i + m_k$. The envelope function describing the in-plane relative motion of the particles is $\phi(\boldsymbol{\rho}_1, \boldsymbol{\rho}_2)$ where $\boldsymbol{\rho}_{1,2} = \boldsymbol{\rho}_{i,j} - \boldsymbol{\rho}_k$. $U^{(2)}_{i,j}(\mathbf{r}_i, \mathbf{r}_j)$ is the Bloch function of the identical particles while $U^{(1)}_k(\mathbf{r}_k)$ is the Bloch function of the unpaired one.

Now, when we consider the hole Bloch function we can neglect the lower lying valence band (spin-orbit splitting Δ_{so} of several hundred meV) and consider just the topmost sub-band [43]. Therefore, the hole Bloch state will not be labelled by two quantum numbers, spin and valley index, but just by the latter: $\tau_\nu = \pm 1$. For the conduction band instead, the spin splitting is only in the tens of meV range and we will thus consider both spin up and spin down states. Thus, we can write the Bloch function for conduction and valence bands as $U^{cb}_{s,\tau}(\mathbf{r})$ and $U^{vb}_{-\tau_\nu}(\mathbf{r})$ respectively. $s = \pm\frac{1}{2}$ is the value of the conduction electron spin projection on the direction perpendicular to the monolayer plane.

Please note that the hole Bloch function is related to the empty valence band state by $U^h_{\tau_\nu}(\mathbf{r}) = \hat{\mathcal{K}} U^{vb}_{-\tau_\nu}(\mathbf{r})$ where $\hat{\mathcal{K}}$ is the time-reversal operator [177]. This means that under the time inversion an empty state in the valence band in valley e.g. K^+ is equivalent to a hole state in valley K^-.

The wavefunction in Eq. (5.2) must be antisymmetric [226] and in order to satisfy this condition, the product $\phi(\boldsymbol{\rho}_1, \boldsymbol{\rho}_2) U^{(2)}_{i,j}(\mathbf{r}_i, \mathbf{r}_j)$ must be antisymmetric as well. We can rewrite the two-particle Bloch function as a symmetric or antisymmetric combination of the single-particle Bloch function:

$$U^{(2)}_{i,j}(\mathbf{r}_i, \mathbf{r}_j) = \frac{1}{\sqrt{2}} \left[U_i(\mathbf{r}_i) U_j(\mathbf{r}_j) + U_i(\mathbf{r}_j) U_j(\mathbf{r}_i)\right] \tag{5.3}$$

$$U^{(2)}_{i,j}(\mathbf{r}_i, \mathbf{r}_j) = \frac{1}{\sqrt{2}} \left[U_i(\mathbf{r}_i) U_j(\mathbf{r}_j) - U_i(\mathbf{r}_j) U_j(\mathbf{r}_i)\right] \tag{5.4}$$

Correspondingly, the envelope function $\phi(\boldsymbol{\rho}_1, \boldsymbol{\rho}_2)$ has to be antisymmetric (with respect to the permutation of the indices 1 and 2, which correspond to i and j as $\boldsymbol{\rho}_{1,2} = \boldsymbol{\rho}_{i,j} - \boldsymbol{\rho}_k$) in the first case or symmetric in the second. From now on we will call a trion symmetric or antisymmetric according to the symmetry of the envelope function. This has as a consequence the fact that in symmetric trions, two identical particles cannot occupy the same Bloch state. This means that spin and/or valley index must differ. In conventional III-V and II-VI quantum wells the symmetric trions are called spin singlet trions and the

antysimmetric trions are called spin-triplet trions [227, 228]. This is the reason why the same notation is used in reference [220].

Now that we defined the trion wavefunction it is possible to calculate the binding energies once the Hamiltonian is known. We can write the effective mass two-particle Hamiltonian, of which the envelope functions $\phi(\boldsymbol{\rho}_1, \boldsymbol{\rho}_2)$ are the eigenfunctions, in the following way:

$$\mathcal{H}_{tr} = -\frac{\hbar^2}{2\mu}\left[\Delta_1 + \Delta_2 + \frac{2\sigma}{\sigma+1}\nabla_1\nabla_2\right] + V(\rho_1) + V(\rho_2) - V(|\boldsymbol{\rho}_1 - \boldsymbol{\rho}_2|), \quad (5.5)$$

where Δ_l and ∇_l are the Laplacian and gradient operators acting on the functions of relative motion $\boldsymbol{\rho}_l$ $(l = 1, 2)$, $\mu = m_e m_h/(m_e + m_h)$ is the reduced mass of the electron-hole pair, $\sigma = m_i/m_k$ is the ratio of effective mass of one of the identical carrier to the effective mass of the non-identical one, i.e., $\sigma = m_e/m_h$ for the X^- trion and $\sigma = m_h/m_e$ for the X^+. Eq. (5.5) is written in terms of the relative motion coordinates $\boldsymbol{\rho}_1$ and $\boldsymbol{\rho}_2$ of identical carriers with respect to the unpaired one. The term $\propto \nabla_1\nabla_2$ accounts for a finite mass ratio σ and is known as Hughes-Eckart term in the theory of atoms and molecules. The kinetic energy $\hbar^2 K^2/2M$ of the trion translational motion is excluded from Eq. (5.5).

In Eq. (5.5) $V(\boldsymbol{\rho})$ is the effective interaction potential (Keldysh potential) taken in the form [46, 52, 53, 51, 229, 230]:

$$V(\boldsymbol{\rho}) = -\frac{\pi e^2}{2r_0\epsilon^*}\left[H_0\left(\frac{\boldsymbol{\rho}}{r_0}\right) - Y_0\left(\frac{\boldsymbol{\rho}}{r_0}\right)\right], \quad (5.6)$$

where r_0 is the effective screening radius, ϵ^* is the effective dielectric constant being the average of the dielectric constants of the substrate and cap layer, H_0 and Y_0 are the Struve and Neumann functions. Note that here we defined the Keldysh potential differently with respect to Eq. (3.2) in Chapter 3 and to some works, such as reference [127]. This is because the parameter r_0 is introduced in a different way with the factor ϵ^* explicitly introduced in the arguments of the H_0 and Y_0 functions rather than in the pre-factor of $V(\boldsymbol{\rho})$, namely, $V(\boldsymbol{\rho}) = \pi e^2/(2r_0)[H_0(\rho\epsilon^*/r_0) - Y_0(\rho\epsilon^*/r_0)]$. This is simply equivalent to the rescaling $r_0 \to r_0/\epsilon^*$.

Please note that Eq. (5.5) and Eq. (5.6) take into account direct electron-hole Coulomb interaction only. Also Eq. (5.2) disregard the effects of short range electron-electron or electron-hole interaction. Those effects can be included later and are accountable for the splitting of the trion states observed in our experiment [225].

The trion binding energy is defined as the difference between the trion energy E^b_{tr} and the one of the neutral exciton E^b_{ex} (as the single particle conduction band splitting do not contribute to the binding energy of the trion). The trion energy is the eigenenergy of the Hamiltonian of Eq. (5.5). Both E^b_{tr} and E^b_{ex} can be calculated using a variational approach as done in [225] and the results of our calculations are in a good agreement with the values obtained by the more sophisticated calculations using the quantum Monte Carlo method in reference [230].

If we consider the effective masses values as is [33] $m_e = 0.28\, m_0$ and $m_h = 0.36\, m_0$ ($\mu = 0.16\, m_0$) and $\epsilon^* = 1$ we obtain exciton binding energies of the order of $10^2 \ldots 10^3$ meV and trion binding energies of $10-100$ meV. These values are in

agreement with previous calculations [46, 229, 230] and are shown as a function of the screening radius in panel (a) of Fig. (5.7)

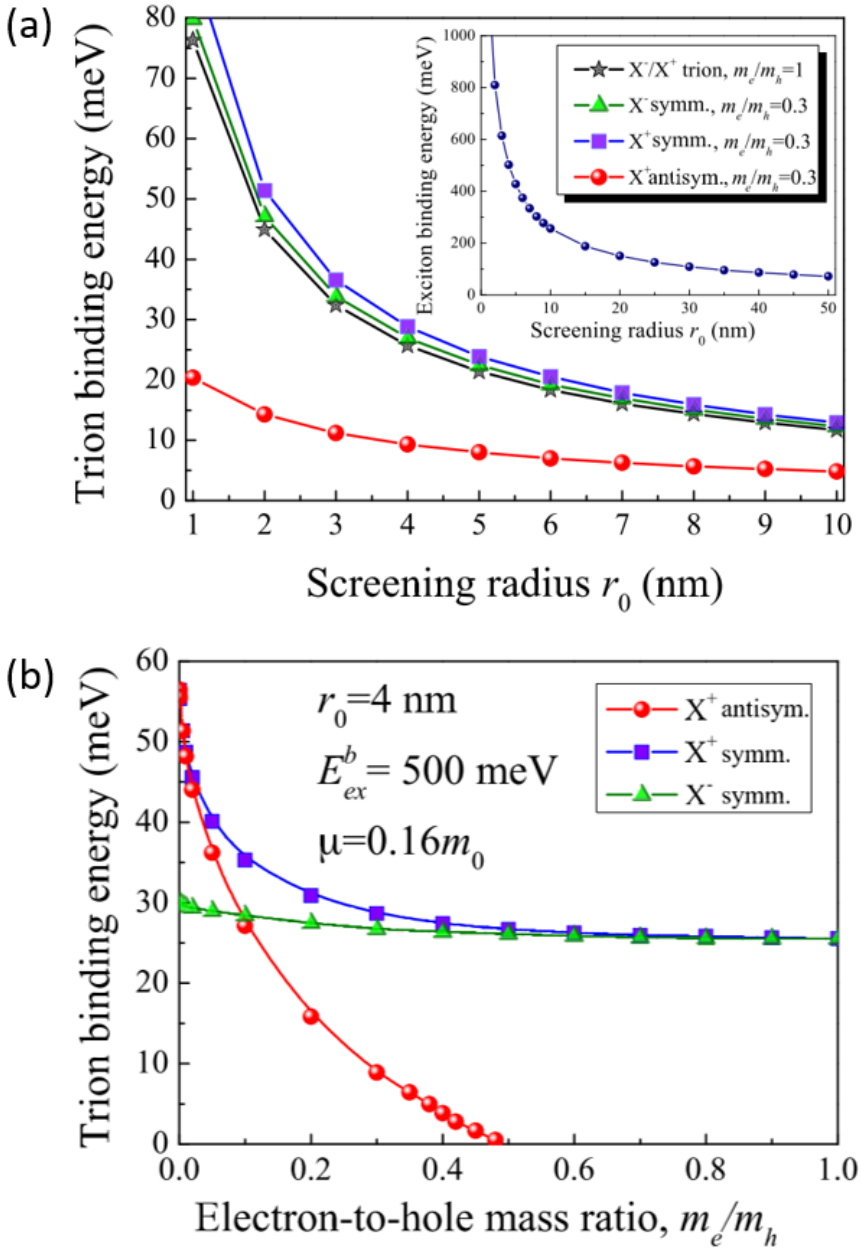

Figure 5.7: Calculated trion binding energies as a function of (a) the screening radius and (b) the electron-hole mass ratio. In order to perform the calculation we fixed the value of the reduced mass at $0.16\,m_0$. In (a) we also fixed $\epsilon^* = 1$ and in (b) $r_0 = 4.0\,nm$.

First, we note that in our model the trion with two heavier carriers, X^+, has a higher binding energy. This is in contradiction with our experimental

findings. Secondly, we see that the $X^{\pm}$ binding energies are not very sensitive to the electron and hole effective mass ratio, at least when this value is between one and 0.3.

For studying these effects we performed new calculations this time fixing the screening radius at $r_0 = 4.0\,\text{nm}$. With $\mu = 0.16\,m_0$ we obtain 500 meV as the binding energy of the exciton for WSe_2. Then we calculate the trion binding energy as a function of the mass ratio $\frac{m_e}{m_h}$ and the results are shown in panel (b) of Fig. (5.7). We can see that when the mass ratio is close to $\frac{m_e}{m_h} = 1$ the binding energies of the positive and negative trions are equal, while for holes much heavier than electrons the binding energy of X^+ becomes larger.

We can now use the model we developed for a direct comparison with our results. Using an average dielectric constant $\epsilon^* = 3.3$, an effective mass $\mu = 0.18\,m_0$ and an effective screening radius $r_0 = 1.36\,\text{nm}$ (which are the values determined by excitonic diamagnetic shifts for an encapsulated WSe_2 monolayer obtained by [129]) our model predict a reasonable value of the exciton binding energy: 206 meV compared with the experimental value $E^b_{tr} = 221\,\text{meV}$ of [129]. However, using $m_e = m_h$ the positively and the negatively charged excitons are predicted to have the same binding energy, equal to 13 meV. This value is too low when compared to our experimental results and it doesn't explain neither the energy separation between the two trion species X^+ and X^- nor the fine structure splitting of the X^-.

A better agreement can be obtained using the following parameters: $\mu = 0.16\,m_0$, $r_0 = 0.64\,\text{nm}$, and $\epsilon^* = 3.3$. In this case we found the exciton binding energy to be 283 meV and for the trions: $E^b_{tr} = 20.6\,\text{meV}$.

Please note that changing the mass ratio in our model cannot explain our experimental results. Indeed, if we do so we would predict a more tightly bound positively charged exciton. This fact came from the so called Hughes-Eckart coefficient in the kinetic energy term of the Hamiltonian in Eq. (5.5):

$$-\frac{\hbar^2}{2\mu}\frac{2\sigma}{\sigma+1}\nabla_1\nabla_2 \tag{5.7}$$

This term increases monotonously with an increase of the mass ratio m_e/m_h and, as a consequence, it predicts that the trion with two lighter carries is less bound.

To explain the lower binding energy of X^+ with respect to the negatively charged exciton one can speculate that the electron is heavier than the hole. However, to justify the 10 meV splitting one has to assume $m_e > 10m_h$ which is not reasonable. Moreover, this wouldn't explain the fine structure splitting of X^-. Thus, the origin of the splitting between the two charged exciton species X^+ and X^- and of the fine structure splitting of X^- has to be found in the short-range contributions to the exchange interaction which where not included in the simple theory described above but which are analyzed in more detail in [225].

5.2.2 Trion fine structure

In WSe_2 monolayers several trion configurations are possible as we need to consider carriers from the valley K^+ and K^- and in each valley two conduction states ($s = \pm\frac{1}{2}$) and one valence state.

We will now analyze the nature of the symmetric trion states. Indeed, in the effective mass approximation, the trion are symmetric when they are in their most tightly bound state [225]. We can thus neglect the contribution from the antisymmetric trions. This is also reasonable as these latter are not stable at any arbitrary electron-hole mass ratio.

When we consider the positively charged exciton X^+ the two holes have to occupy the two valence sub-bands at higher energy in the two different valleys. This is because of the high energy separation between the valence sub-bands of several hundred meV. Therefore, the unpaired electron of the X^+ has four possible states to occupy, which corresponds to the permutation of the two quantum numbers: spin $s_e = \pm\frac{1}{2}$ and valley index $\tau_e = \pm 1$. There are thus four symmetric X^+ states which are illustrated in Fig. (5.8).

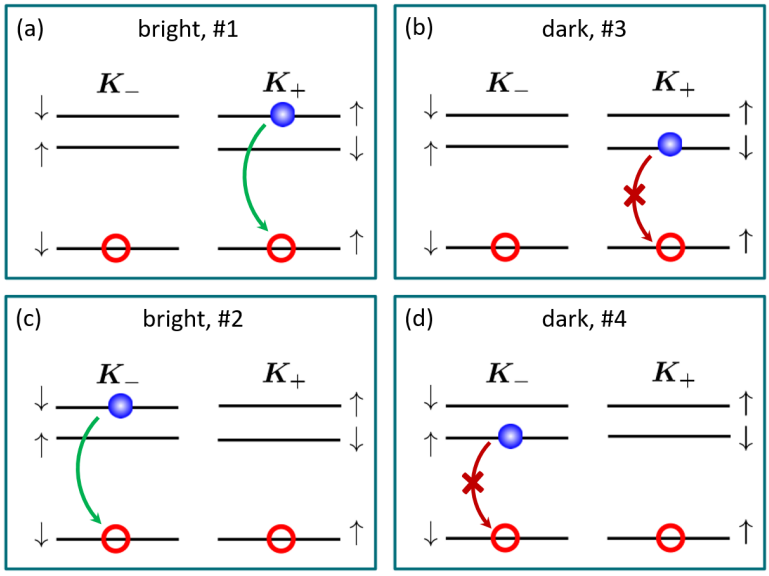

Figure 5.8: Schematic illustration of the symmetric positively charged trions X^+. The blue dot indicate an electron in the conduction band while the red cirles are empty states in the valence band. We remain in the electron picture so optical transitions $\uparrow \Rightarrow \uparrow$ can occur, whereas $\uparrow \Rightarrow \downarrow$ is forbidden. The arrows indicate the spin of the particle in that state and their direction correspond to the one in the WSe_2 bandstructure.

They are paired in two couples related by the time reversal operator, which means that in a considered couple the trion state is the same for holes but with the electron in the opposite valley. Compare for example the states #1 and #2 in Fig. (5.8). This will, for example, change the polarization of the emitted photon if the considered state is optically bright. To prove if the transition is bright (when we consider light propagating perpendicular to the monolayer plane) we have to remember that the allowed transition for the electron is the one from its conduction band state to the valence vacant state with the same spin. This means that the bright states are those sketched in panel (a) and (c) of Fig. (5.8). The other two states are instead optically dark, as already discussed in Chapter 3 and by references [142, 141, 92] for the dark exciton. In fact, the direct interband optical transition between the bottom conduction and the top

valence sub-bands are spin forbidden, as we can intuitively understand looking at the sign of the spin.

Thus the emission from of the X^+ is due to the trions in the states #1 and #2. One corresponds to the σ^+ component and the other to the σ^- one. For this reason the positive trion appears as a single line (in absence of a magnetic field) and does not shows any fine structure.

The situation is very different for the negative trion X^-. It is possible to show that the number of symmetric trion states is equal to twelve. This is made possible by the smaller energy splitting between the spin states in the conduction band. Hence, once we fix the valley index of the unpaired hole we have 6 possible configurations for the two electrons, i.e. one for each possible permutation of the spin and the valley index (taking into account that the particles are identical). These six states (with the hole in valley K^+) are shown in Fig. (5.9)

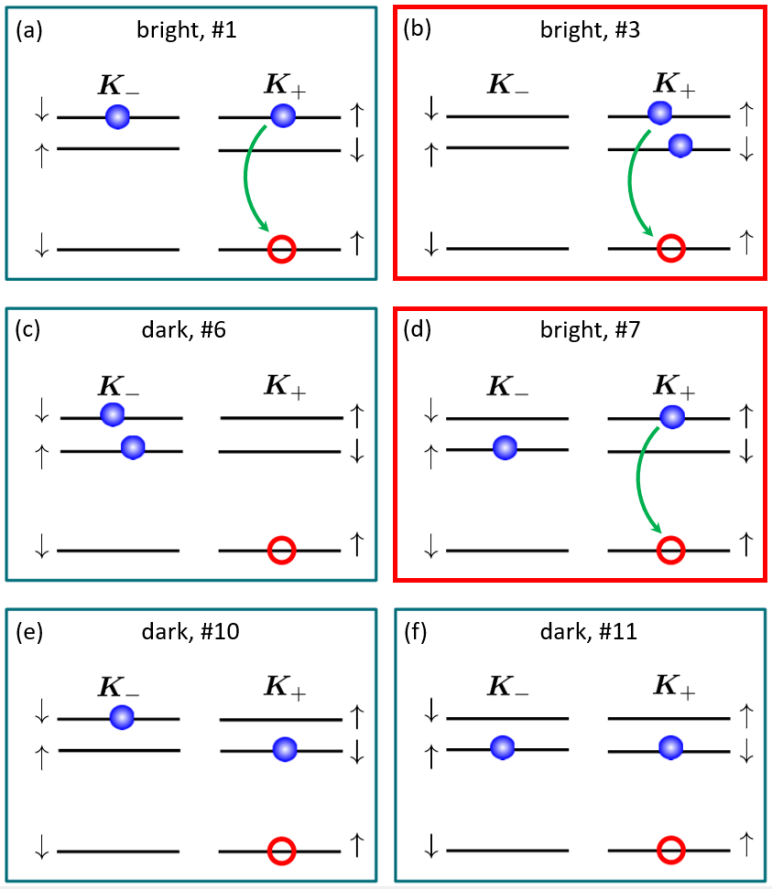

Figure 5.9: Schematic illustration of the symmetric negatively charged trions X^- with the empty valence state in the in valley K^+. The blue dot indicate an electron in the conduction band while the red cirles are empty states in the valence band. The arrows indicate the spin of the particle in that state and their direction correspond to the one in the WSe_2 bandstructure. In the red box are represented the negative trion states responible for the absorption/emission features in the spectrum of WSe_2. There are six other states with the empty valence state in the K^- valley.

As one can see there are three pairs of bright states which are optically active. If we consider the order of the conduction sub-bands in WSe_2 we understand that the state #1 is an "excited trion". Taking into account the spin orbit splitting of the order of 30 meV [58], a reasonable electron density $n_e \lesssim 4 \times 10^{12}\,\mathrm{cm}^{-2}$ and the low temperatures at which the system is kept, we deduce that the number of trions in the excited state #1 is negligible. Thus, excited trion states cannot be responsible for one of the lines appearing in absorption as their formation in a single photon absorption process will require to have electrons occupying the topmost sub-band. Hence, we deduce that the two observed absorption lines are due to the states #3 (intravalley trion) and #7 (intervalley trion), and to the corresponding states with the hole in valley K^-.

To summarize, in absorption in Fig. (5.3) we observe two transitions for the X^-, the intervalley and the intravalley trion, separated in energy by the Coulomb electron-hole exchange energy. As we cannot determine the sign of this term we are not able to say which of the two transition is which.

5.3 Conclusions

In this chapter we studied in detail the positively and negatively charged excitons in an encapsulated WSe_2, both theoretically and experimentally. The trions are clearly observed in photoluminescence and reflectivity, allowing us to observe the energy splitting between X^+ and X^- i. e. they have different binding energies. Moreover, for the latter we where able to cleary resolve a fine structure splitting of 6 meV. We also compared our observation with the results found by other groups.

Using the effective mass approach we presented a model which describes the main experimental findings, we evaluated the binding energies of the trions and we obtained values close to the experimental ones. The symmetry analysis allowed us to identify all the trion states and distinguish between the optically allowed and the optically forbidden ones. Knowledge of the WSe_2 trions is important, as also the dark trion states will play a role in optically probed valley and spin dynamics at long timescales [231].

Chapter 6

Conclusions and outlook

In this final chapter we want to summarize the main results presented in this PhD thesis manuscript and introduce some ideas for future experiments which we would like to perform and which started to stimulate the interest of the community.

The encapsulation of transition metal dichalcogenide monolayers in hexagonal boron nitride led to the observation of high quality optical spectra in which the linewidth of every transition is close to the homogeneous limit $\approx 1\,\mathrm{meV}$ and where the peaks related to defects are strongly reduced in number and in intensity. This improvement in the fabrication procedure was achieved at the beginning of this PhD thesis and allowed us to obtain many new insights in TMD monolayers and especially on WSe_2.

The emission spectrum we observed from the first WSe_2 monolayer encapsulated in hBN contained three spectrally narrow peaks. The peak at higher energy (1.72 eV) was clearly identified as the bright neutral exciton A:1s or (X^0) while the one at lower energy (1.68 eV) is instead the dark exciton X^D. We uncovered the optical dipole selection rules of the dark exciton transition and we proved that it is coupled to light which oscillates normally to the monolayer plane. The exact nature of the peak observed at an intermediate energy (1.69 eV) between the dark and the bright neutral excitons is still under debate.

Thanks to the improved quality of encapsulated sample and to the presence of a cavity effect we were able to observe the excited A-exciton states. With the help of our collaborators Marina Semina and Mikhail Glazov (Ioffe Institute, Saint Petersburg) we model the intensity and the spectral position of these transition obtaining an estimation for the binding energy and thus for the free-particle bandgap.

In monolayer WSe_2 we also discovered a non-linear optical process which we named upconversion. When resonantly exciting the bright exciton transition a PL emission was observed by two of its excited states (A:2s and A:3s) at higher energy, approximately 130 meV, and by the B-exciton as well (430 meV above the laser energy). We tentatively explained the occupation of high energy states as the result of an exciton-exciton Auger-like scattering made efficient by the presence of an excited conduction band in the investigated TMD materials.

In a series of experiments performed in an encapsulated charge tunable WSe_2 monolayer we unveiled more details about the trion states in this system. We clearly observed an energy splitting between the positively and the negatively

charged excitons (X^+ and X^- respectively) and we uncovered a fine structure splitting in the negative trion. A theoretical model explaining our observation was then developed by Marina Semina and Mikhail Glazov where the fine structure splitting is ascribed to the short range Coulomb electron-hole exchange interaction. The origin of the splitting between X^+ and X^- also ascribed to Coulomb exchange terms.

The experimental results presented in this manuscript are indeed in many way surprising and contributed to s better understanding of the light-matter interaction in WSe_2 monolayer. However, considerable work is still required to have a more complete comprehension of TMD monolayers. For example, one hot topic which attracted the interest of many group during the last years is the study of heterobilayer structures in which a monolayer of one of the TMD materials is exfoliated on top of another monolayer (which may be the from the same or from a different compound). The un-perfect alignment (twist angle) and the possible crystal lattice mismatch give rise to a so-called Moiré pattern which is a super-crystal structure that can effectively modulate the amplitude of the bandgap [232, 233].

Our first attempts to fabricate these particular heteostructures gave us interesting results, comparable to the state of the art data reported in the literature [234]. However, the very weak signal obtained from interlayer excitons indicates inefficient coupling between our monolayers. Works to understand this issue are ongoing.

Another interesting topic is the study of commensurately matched homobilayers (no lattice or angle mismatch) which can be obtained simply by exfoliation. In this system we try to better understand the role of the interlayer excitons, which are excitons in which the electron resides in one layer and the hole is delocalized over both [235].

Also indirect excitons, which are formed when at least one between the electron and the hole resides in valley different from K, are being intensely studied. These excitons are important in order to understand why TMDs, despite a strong light matter interaction, still present a low quantum yield. Although recently investigated TMD structures grown by the flux method show considerably higher emission yield [236, 237].

The study of van der Waals heterostructure will be central in the future of this research area. The great number of layered materials which are stable in ambient conditions opens up many possibilities of combining mono- and few-layer crystals. The number of the resulting combinations and the possible functionalities are still far from being predictable but it is very likely that they will show compelling properties. Two dimensional devices may replace existing ones and completely new ones may perform novel tasks. In this framework very interesting studies will be done by combining semiconducting TMDs with ferromagnetic layered materials such as CrI_3 and $CrBr_3$. The presence of a local magnetic field could lift the valley degeneracy of a TMDs monolayer without the need of an external magnetic field [238].

In the very end I would like to present the list of published papers to which I gave my contribution during my three year PhD. Some of them were extensively covered in writing this manuscript, other where instead on different topics (such as GaAs quantum dots) and where left out.

1. F. Cadiz, C. Robert, G. Wang, W. Kong, X. Fan, M. Blei, D. Lagarde, M. Gay, M. Manca, T. Taniguchi, K. Watanabe, T. Amand, X. Marie, P. Renucci, S. Tongay and B. Urbaszek
   "Ultra-low power threshold for laser induced changes in optical properties of 2D molybdenum dichalcogenides" 2D Mater. 2016; 3(4), 045008
   http://iopscience.iop.org/article/10.1088/2053-1583/3/4/045008

2. H. Cai, B. Chen, G. Wang, E. Soignard, A. Khosravi, M. Manca, X. Marie, S. L. Y. Chang, B. Urbaszek and S. Tongay
   "Synthesis of Highly Anisotropic Semiconducting GaTe Nanomaterials and Emerging Properties Enabled by Epitaxy" Adv. Mater. 2017, 29, 1605551
   http://doi.wiley.com/10.1002/adma.201605551

3. M. Manca, M.M. Glazov, C. Robert, F. Cadiz, T. Taniguchi, K. Watanabe, E. Courtade, T. Amand, P. Renucci, X. Marie, G. Wang and B. Urbaszek
   "Enabling valley selective exciton scattering in monolayer WSe_2 through upconversion" Nat Commun. 2017; 8(1) 1-7.
   http://dx.doi.org/10.1038/ncomms14927

4. F. Cadiz, E. Courtade, C. Robert, G. Wang, Y. Shen, H. Cai, T. Taniguchi, K. Watanabe, H. Carrere, D. Lagarde, M. Manca, T. Amand, P. Renucci, S. Tongay, X. Marie and B. Urbaszek
   "Excitonic Linewidth Approaching the Homogeneous Limit in MoS_2-Based van der Waals Heterostructures" Phys. Rev. X. 2017; 7(2): 021026.
   http://link.aps.org/doi/10.1103/PhysRevX.7.021026

5. E. Courtade, M. Semina, M. Manca, M.M. Glazov, C. Robert, F. Cadiz, G. Wang, T. Taniguchi, K. Watanabe, M. Pierre, W. Escoffier, E.L. Ivchenko, P. Renucci, X. Marie, T. Amand and B. Urbaszek
   "Charged excitons in monolayer WSe_2: experiment and theory" Phys. Rev. B. 2017; 085302: 1-12.
   https://doi.org/10.1103/PhysRevB.96.085302

6. C. Robert, T. Amand, F. Cadiz, D. Lagarde, E. Courtade, M. Manca, T. Taniguchi, K. Watanabe, B. Urbaszek and X. Marie
   "Fine structure and lifetime of dark excitons in transition metal dichalcogenide monolayers" Phys. Rev. B **96**, 155423, (2017)
   https://doi.org/10.1103/PhysRevB.96.155423

7. C. Robert, M. A. Semina, F. Cadiz, M. Manca, E. Courtade, T. Taniguchi, K.Watanabe, H. Cai, S. Tongay, B. Lassagne, P. Renucci, T. Amand, X. Marie, M. M. Glazov and B. Urbaszek
   "Optical spectroscopy of excited exciton states in MoS2 monolayers in van der Waals heterostructures" Phys. Rev. Materials 2, 011001(R) (2018)
   https://doi.org/10.1103/PhysRevMaterials.2.011001

8. M. Manca, G. Wang, T. Kuroda, S. Shree, A. Balocchi, P. Renucci, X. Marie, M. V. Durnev, M. M. Glazov, K. Sakoda, T. Mano, T. Amand,

and B. Urbaszek.
"Electrically tunable dynamic nuclear spin polarization in GaAs quantum dots at zero magnetic field" Appl. Phys. Lett. 112, 142103 (2018)
https://doi.org/10.1063/1.5024619

9. F. Cadiz, C. Robert, E. Courtade, M. Manca, L. Martinelli, T. Taniguchi, K. Watanabe, T. Amand, A. C. H. Rowe, D. Paget, B. Urbaszek, and X. Marie
"Exciton diffusion in WSe_2 monolayers embedded in a van der Waals heterostructure" Appl. Phys. Lett. 112, 152106 (2018)
https://doi.org/10.1063/1.5026478

10. S. Shree, M. Semina, C. Robert, B. Han, T. Amand, A. Balocchi, M. Manca, E. Courtade, X. Marie, T. Taniguchi, K. Watanabe, M. M. Glazov, and B. Urbaszek
"Observation of exciton-phonon coupling in $MoSe_2$ monolayers" Phys. Rev. B **98**, 035302, (2018)
https://doi.org/10.1103/PhysRevB.98.035302

11. B. Han, C. Robert, E. Courtade, M. Manca, S. Shree, T. Amand, P. Renucci, T. Taniguchi, K. Watanabe, X. Marie, L.E. Golub, M.M. Glazov and B. Urbaszek
"Exciton states in monolayer $MoSe_2$ and $MoTe_2$ probed by upconversion spectroscopy" Phys. Rev. X **8**, 031073, (2018)
https://doi.org/10.1103/PhysRevX.8.031073

12. N. Morell, S. Tepsic, A. Reserbat-Plantey, A. Cepellotti, M. Manca, I. Epstein, A. Isacsson, X. Marie, F. Mauri, A. Bachtold
"Optomechanical measurement of thermal transport in two-dimensional MoSe2 lattices" Nano Lett. 2019, 19 (5), pp 3143âĂŞ3150
https://pubs.acs.org/doi/10.1021/acs.nanolett.9b00560

Bibliography

[1] Feynman, R. There's plenty of room at the bottom. In *Feynman and computation*, 63–76 (CRC Press, 2018).

[2] Drexler, K. E. Molecular engineering: An approach to the development of general capabilities for molecular manipulation. *Proceedings of the National Academy of Sciences* **78**, 5275–5278 (1981).

[3] Schneiker, C. *et al.* Scanning tunnelling engineering. *Journal of Microscopy* **152**, 585–596 (1988).

[4] Trimmer, W. S. Microrobots and micromechanical systems. *Sensors and actuators* **19**, 267–287 (1989).

[5] Stroscio, J. A. & Eigler, D. Atomic and molecular manipulation with the scanning tunneling microscope. *Science* **254**, 1319–1326 (1991).

[6] Moore, G. E. Cramming more components onto integrated circuits. *Electronics* **38**, 114–117 (1965).

[7] Rosencher, E. & Vinter, B. *Optoelectronics* (Cambridge University Press, 2002).

[8] Frindt, R. Single crystals of mos2 several molecular layers thick. *Journal of Applied Physics* **37**, 1928–1929 (1966).

[9] Wilson, J. & Yoffe, A. The transition metal dichalcogenides discussion and interpretation of the observed optical, electrical and structural properties. *Advances in Physics* **18**, 193–335 (1969).

[10] Bromley, R., Murray, R. & Yoffe, A. The band structures of some transition metal dichalcogenides. iii. group via: trigonal prism materials. *Journal of Physics C: Solid State Physics* **5**, 759 (1972).

[11] Joensen, P., Frindt, R. & Morrison, S. R. Single-layer mos2. *Materials research bulletin* **21**, 457–461 (1986).

[12] Novoselov, K. S. *et al. Science* **306**, 666 (2004).

[13] Novoselov, K. S. *et al. Proc. Natl Acad. Sci. USA* **102**, 10451 (2005).

[14] Zhang, Y., Tan, Y.-W., Stormer, H. L. & Kim, P. Experimental observation of the quantum hall effect and berry's phase in graphene. *nature* **438**, 201 (2005).

[15] Geim, A. K. & Grigorieva, I. V. Van der waals heterostructures. *Nature* **499**, 419—425 (2013).

[16] Novoselov, K. S. *et al.* Two-dimensional gas of massless dirac fermions in graphene. *nature* **438**, 197 (2005).

[17] Meric, I. *et al.* Current saturation in zero-bandgap, top-gated graphene field-effect transistors. *Nature nanotechnology* **3**, 654 (2008).

[18] Balandin, A. A. *et al.* Superior thermal conductivity of single-layer graphene. *Nano letters* **8**, 902–907 (2008).

[19] Bunch, J. S. *et al.* Impermeable atomic membranes from graphene sheets. *Nano letters* **8**, 2458–2462 (2008).

[20] Lee, C., Wei, X., Kysar, J. W. & Hone, J. Measurement of the elastic properties and intrinsic strength of monolayer graphene. *science* **321**, 385–388 (2008).

[21] Feng, J. *et al.* Metallic few-layered vs2 ultrathin nanosheets: high two-dimensional conductivity for in-plane supercapacitors. *Journal of the American Chemical Society* **133**, 17832–17838 (2011).

[22] Watanabe, K., Taniguchi, T. & Kanda, H. Direct-bandgap properties and evidence for ultraviolet lasing of hexagonal boron nitride single crystal. *Nature materials* **3**, 404 (2004).

[23] Xi, X. *et al.* Strongly enhanced charge-density-wave order in monolayer nbse 2. *Nature nanotechnology* **10**, 765 (2015).

[24] Ding, W. *et al.* Prediction of intrinsic two-dimensional ferroelectrics in in 2 se 3 and other iii 2-vi 3 van der waals materials. *Nature communications* **8**, 14956 (2017).

[25] Huang, B. *et al.* Layer-dependent ferromagnetism in a van der waals crystal down to the monolayer limit. *Nature* **546**, 270 (2017).

[26] Wang, G. *et al.* Colloquium: Excitons in atomically thin transition metal dichalcogenides. *Reviews of Modern Physics* **90**, 021001 (2018).

[27] Splendiani, A. *et al.* Emerging photoluminescence in monolayer mos2. *Nano Letters* **10**, 1271 (2010).

[28] Mak, K. F., Lee, C., Hone, J., Shan, J. & Heinz, T. F. Atomically thin mos_2: A new direct-gap semiconductor. *Phys. Rev. Lett.* **105**, 136805 (2010).

[29] Yun, W. S., Han, S. W., Hong, S. C., Kim, I. G. & Lee, J. D. Thickness and strain effects on electronic structures of transition metal dichalcogenides: 2h-mX_2 semiconductors (m = mo, w; x = s, se, te). *Phys. Rev. B* **85**, 033305 (2012).

[30] Zhao, W. *et al.* Origin of indirect optical transitions in few-layer mos2, ws2, and wse2. *Nano Letters* **13**, 5627–5634 (2013).

[31] Li, T., & Galli, G. Electronic properties of mos2 nanoparticles. *The Journal of Physical Chemistry C* **111**, 16192–16196 (2007).

[32] Zhu, Z. Y., Cheng, Y. C. & Schwingenschlögl, U. Giant spin-orbit-induced spin splitting in two-dimensional transition-metal dichalcogenide semiconductors. *Phys. Rev. B* **84**, 153402 (2011).

[33] Kormanyos, A. *et al.* k.p theory for two-dimensional transition metal dichalcogenide semiconductors. *2D Materials* **2**, 022001 (2015).

[34] Lopez-Sanchez, O., Lembke, D., Kayci, M., Radenovic, A. & Kis, A. Ultrasensitive photodetectors based on monolayer mos2. *Nature Nanotechnology* **8**, 497–501 (2013).

[35] Perkins, F. K. *et al.* Chemical vapor sensing with monolayer mos2. *Nano Letters* **13**, 668–673 (2013).

[36] Radisavljevic, B., Whitwick, M. B. & Kis, A. Integrated circuits and logic operations based on single-layer mos2. *ACS Nano* **5**, 9934–9938 (2011). PMID: 22073905.

[37] Wang, H. *et al.* Integrated circuits based on bilayer mos2 transistors. *Nano Letters* **12**, 4674–4680 (2012).

[38] Cheng, R. *et al.* Electroluminescence and photocurrent generation from atomically sharp wse2/mos2 heterojunction pn diodes. *Nano Letters* **14**, 5590–5597 (2014).

[39] Lopez-Sanchez, O. *et al.* Light generation and harvesting in a van der waals heterostructure. *Acs Nano* **8**, 3042–3048 (2014).

[40] Pospischil, A., Furchi, M. M. & Mueller, T. Solar-energy conversion and light emission in an atomic monolayer pn diode. *Nature nanotechnology* **9**, 257–261 (2014).

[41] Ross, J. S. *et al. Nature Nanotechnology* **9**, 268 (2014).

[42] Gross, E. Gross, ef, and na karryev, 1952b,âĂIJexciton optical spectrum,âĂİ dokl. akad. nauk sssr 84, 471. In *Dokl. Akad. Nauk SSSR*, vol. 84, 471 (1952).

[43] Cheiwchanchamnangij, T. & Lambrecht, W. R. L. Quasiparticle band structure calculation of monolayer, bilayer, and bulk mos_2. *Phys. Rev. B* **85**, 205302 (2012).

[44] Ramasubramaniam, A. Large excitonic effects in monolayers of molybdenum and tungsten dichalcogenides. *Phys. Rev. B* **86**, 115409 (2012).

[45] Qiu, D. Y., da Jornada, F. H. & Louie, S. G. Optical spectrum of mos2: Many-body effects and diversity of exciton states. *Phys. Rev. Lett.* **111**, 216805 (2013).

[46] Chernikov, A. *et al.* Exciton binding energy and nonhydrogenic rydberg series in monolayer ws_2. *Phys. Rev. Lett.* **113**, 076802 (2014).

[47] Wang, G. *et al.* Giant enhancement of the optical second-harmonic emission of wse_2 monolayers by laser excitation at exciton resonances. *Phys. Rev. Lett.* **114**, 097403 (2015).

[48] Shinada, M. & Sugano, S. Interband optical transitions in extremely anisotropic semiconductors. i. bound and unbound exciton absorption. *Journal of the Physical Society of Japan* **21**, 1936–1946 (1966).

[49] Klingshirn, C. *Semiconductor Optics* (Springer, Berlin Heidelberg New York, 2007), 3rd edn.

[50] He, K. *et al.* Tightly bound excitons in monolayer wse_2. *Phys. Rev. Lett.* **113**, 026803 (2014).

[51] Cudazzo, P., Tokatly, I. V. & Rubio, A. Dielectric screening in two-dimensional insulators: Implications for excitonic and impurity states in graphane. *Phys. Rev. B* **84**, 085406 (2011).

[52] Rytova, N. S. Screened potential of a point charge in a thin film. *Proc. MSU, Phys., Astron.* **3**, 30 (1967).

[53] Keldysh, L. PisâĂŹma zh. eksp. teor. fiz. 29, 716 (1979). *JETP Lett* **29**, 658 (1979).

[54] Xiao, D., Liu, G.-B., Feng, W., Xu, X. & Yao, W. Coupled spin and valley physics in monolayers of mos_2 and other group-vi dichalcogenides. *Phys. Rev. Lett.* **108**, 196802 (2012).

[55] Cao, T. *et al.* Valley-selective circular dichroism in mos_2. *Nature Communications* **3**, 887 (2012).

[56] Zhang, Y. *et al.* Direct observation of the transition from indirect to direct bandgap in atomically thin epitaxial mose2. *Nature Nanotechnology* **9**, 111–115 (2014).

[57] Miwa, J. A. *et al.* Electronic structure of epitaxial single-layer mos_2. *Phys. Rev. Lett.* **114**, 046802 (2015).

[58] Kosmider, K., González, J. W. & Fernández-Rossier, J. Large spin splitting in the conduction band of transition metal dichalcogenide monolayers. *Phys. Rev. B* **88**, 245436 (2013).

[59] Molina-Sánchez, A., Sangalli, D., Hummer, K., Marini, A. & Wirtz, L. Effect of spin-orbit interaction on the optical spectra of single-layer, double-layer, and bulk MoS_2. *Physical Review B* **88**, 045412 (2013).

[60] Liu, G.-B., Shan, W.-Y., Yao, Y., Yao, W. & Xiao, D. Three-band tight-binding model for monolayers of group-vib transition metal dichalcogenides. *Phys. Rev. B* **88**, 085433 (2013).

[61] Kormányos, A., Zólyomi, V., Drummond, N. D. & Burkard, G. Spin-orbit coupling, quantum dots, and qubits in monolayer transition metal dichalcogenides. *Phys. Rev. X* **4**, 011034 (2014).

[62] Wang, G. *et al.* Spin-orbit engineering in transition metal dichalcogenide alloy monolayers. *Nature Comms.* 10110 (2015).

[63] Zhang, X.-X., You, Y., Zhao, S. Y. F. & Heinz, T. F. Experimental evidence for dark excitons in monolayer wse_2. *Phys. Rev. Lett.* **115**, 257403 (2015).

[64] Arora, A. *et al.* Excitonic resonances in thin films of WSe ₂ : from monolayer to bulk material. *Nanoscale* **7**, 10421–10429 (2015).

[65] Withers, F. *et al.* Wse2 light-emitting tunneling transistors with enhanced brightness at room temperature. *Nano Letters* **15**, 8223–8228 (2015).

[66] Dyakonov, M. Spin physics in semiconductors. *Springer Series in Solid-State Science, Springer-Verlag Berlin* **157** (2008).

[67] Yao, W., Xiao, D. & Niu, Q. Valley-dependent optoelectronics from inversion symmetry breaking. *Phys. Rev. B* **77**, 235406 (2008).

[68] Mak, K. F., He, K., Shan, J. & Heinz, T. F. Control of valley polarization in monolayer mos_2 by optical helicity. *Nat. Nanotechnol.* **7**, 494 (2012).

[69] Sallen, G. *et al.* Robust optical emission polarization in mos_2 monolayers through selective valley excitation. *Phys. Rev. B* **86**, 081301 (2012).

[70] Zeng, H., Dai, J., Yao, W., Xiao, D. & Cui, X. Valley polarization in mos_2 monolayers by optical pumping. *Nat. Nanotechnol.* **7**, 490 (2012).

[71] Rycerz, A., Tworzydlo, J. & Beenakker, C. J. *Nature. Phys.* **3**, 172 (2007).

[72] Xiao, D., Yao, W. & Niu, Q. Valley-contrasting physics in graphene: Magnetic moment and topological transport. *Phys. Rev. Lett.* **99**, 236809 (2007).

[73] Behnia, K. Condensed-matter physics: polarized light boosts valleytronics. *Nature nanotechnology* **7**, 488–489 (2012).

[74] Schaibley, J. R. *et al.* Valleytronics in 2d materials. *Nature Reviews Materials* **1**, 16055 (2016).

[75] Dey, P. *et al.* Gate-controlled spin-valley locking of resident carriers in wse 2 monolayers. *Physical review letters* **119**, 137401 (2017).

[76] Jin, C. *et al.* Imaging of pure spin-valley diffusion current in ws2-wse2 heterostructures. *Science* **360**, 893–896 (2018).

[77] Glazov, M. M. *et al.* Exciton fine structure and spin decoherence in monolayers of transition metal dichalcogenides. *Phys. Rev. B* **89**, 201302 (2014).

[78] Maialle, M. Z., de Andrada e Silva, E. A. & Sham, L. J. Exciton spin dynamics in quantum wells. *Phys. Rev. B* **47**, 15776–15788 (1993).

[79] Zhu, C. *et al.* Exciton valley dynamics probed by kerr rotation in wse 2 monolayers. *Physical Review B* **90**, 161302 (2014).

[80] Dufferwiel, S. *et al.* Exciton-polaritons in van der waals heterostructures embedded in tunable microcavities. *Nature communications* **6**, 8579 (2015).

[81] Liu, X. *et al.* Strong light–matter coupling in two-dimensional atomic crystals. *Nature Photonics* **9**, 30–34 (2015).

[82] Castellanos-Gomez, A. *et al.* Deterministic transfer of two-dimensional materials by all-dry viscoelastic stamping. *2D Materials* **1**, 011002 (2014).

[83] Han, B. *et al.* Exciton states in monolayer $mose_2$ and $mote_2$ probed by upconversion spectroscopy. *Physical Review X* **8**, 031073 (2018).

[84] Lezama, I. G. *et al.* Indirect-to-direct band gap crossover in few-layer mote2. *Nano letters* **15**, 2336–2342 (2015).

[85] Haigh, S. *et al.* Cross-sectional imaging of individual layers and buried interfaces of graphene-based heterostructures and superlattices. *Nature materials* **11**, 764 (2012).

[86] Koma, A. Van der waals epitaxy - a new epitaxial growth method for a highly lattice-mismatched system. *Thin Solid Films* **216**, 72–76 (1992).

[87] Mayorov, A. S. *et al.* Micrometer-scale ballistic transport in encapsulated graphene at room temperature. *Nano letters* **11**, 2396–2399 (2011).

[88] Cassabois, G., Valvin, P. & Gil, B. Hexagonal boron nitride is an indirect bandgap semiconductor. *Nature Photonics* **10**, 262 (2016).

[89] Taniguchi, T. & Watanabe, K. Synthesis of high-purity boron nitride single crystals under high pressure by using ba-bn solvent. *Journal of Crystal Growth* **303**, 525 – 529 (2007).

[90] Wang, Z., Zhao, L., Mak, K. F. & Shan, J. Probing the spin-polarized electronic band structure in monolayer transition metal dichalcogenides by optical spectroscopy. *Nano Letters* **17**, 740–746 (2017).

[91] Withers, F. *et al.* Light-emitting diodes by band-structure engineering in van der waals heterostructures. *Nature materials* **14**, 301 (2015).

[92] Wang, G. *et al.* In-plane propagation of light in transition metal dichalcogenide monolayers: optical selection rules. *Physical review letters* **119**, 047401 (2017).

[93] Robert, C. *et al.* Fine structure and lifetime of dark excitons in transition metal dichalcogenide monolayers. *Physical Review B* **96**, 155423 (2017).

[94] Manca, M. *et al.* Electrically tunable dynamic nuclear spin polarization in gaas quantum dots at zero magnetic field. *Applied Physics Letters* **112**, 142103 (2018).

[95] Marvin, M. Microscopy apparatus (1961). US Patent 3,013,467.

[96] Wilson, T. & Sheppard, C. *Theory and practice of scanning optical microscopy*, vol. 180 (Academic Press London, 1984).

[97] El Allali, M., So, C., Veje, E., Tidemand-Petersson, P. *et al.* Experimental determination of the gaas and ga 1- x al x as band-gap energy dependence on temperature and aluminum mole fraction in the direct band-gap region. *Physical Review B* **48**, 4398 (1993).

[98] Lien, D.-H. *et al.* Engineering light outcoupling in 2d materials. *Nano Letters* **15**, 1356–1361 (2015).

[99] Radisavljevic, B., Radenovic, A., Brivio, J., Giacometti, i. V. & Kis, A. Single-layer mos 2 transistors. *Nature nanotechnology* **6**, 147 (2011).

[100] Kioseoglou, G. *et al.* Valley polarization and intervalley scattering in monolayer mos[sub 2]. *Applied Physics Letters* **101**, 221907 (2012).

[101] Lagarde, D. *et al.* Carrier and polarization dynamics in monolayer mos_2. *Phys. Rev. Lett.* **112**, 047401 (2014).

[102] Dickinson, R. G. & Pauling, L. The crystal structure of molybdenite. *Journal of the American Chemical Society* **45**, 1466–1471 (1923).

[103] Cadiz, F. *et al.* Well separated trion and neutral excitons on superacid treated mos2 monolayers. *Applied Physics Letters* **108**, 251106 (2016).

[104] Amani, M. *et al.* Near-unity photoluminescence quantum yield in mos2. *Science* **350**, 1065–1068 (2015).

[105] Cadiz, F. *et al.* Ultra-low power threshold for laser induced changes in optical properties of 2d molybdenum dichalcogenides. *2D Materials* **3**, 045008 (2016).

[106] Korn, T., Heydrich, S., Hirmer, M., Schmutzler, J. & Schüller, C. Low-temperature photocarrier dynamics in monolayer mos_2. *Applied Physics Letters* **99**, 102109 (2011).

[107] Mai, C. *et al.* Many-body effects in valleytronics: Direct measurement of valley lifetimes in single-layer mos2. *Nano Letters* **14**, 202–206 (2014).

[108] Wang, Q. *et al.* Valley carrier dynamics in monolayer molybdenum disulfide from helicity-resolved ultrafast pump–probe spectroscopy. *ACS Nano* **7**, 11087–11093 (2013).

[109] Wang, H., Zhang, C. & Rana, F. Ultrafast dynamics of defect-assisted electron-hole recombination in monolayer mos2. *Nano Letters* **15**, 339–345 (2015). PMID: 25546602, `http://dx.doi.org/10.1021/nl503636c`.

[110] Kumar, N. *et al.* Exciton-exciton annihilation in mose 2 monolayers. *Physical Review B* **89**, 125427 (2014).

[111] Yang, L. *et al.* Long-lived nanosecond spin relaxation and spin coherence of electrons in monolayer mos2 and ws2. *Nature Physics* (2015).

[112] Shang, J. *et al.* Observation of excitonic fine structure in a 2d transition-metal dichalcogenide semiconductor. *ACS Nano* **9**, 647–655 (2015). PMID: 25560634.

[113] He, Z. *et al.* Biexciton formation in bilayer tungsten disulfide. *ACS Nano* **10**, 2176–2183 (2016). URL http://dx.doi.org/10.1021/acsnano.5b06678. PMID: 26761127, http://dx.doi.org/10.1021/acsnano.5b06678.

[114] Cadiz, F. *et al.* Excitonic linewidth approaching the homogeneous limit in mos_2-based van der waals heterostructures. *Phys. Rev. X* **7**, 021026 (2017).

[115] Jin, C. *et al.* Interlayer electron–phonon coupling in wse 2/hbn heterostructures. *Nature Physics* **13**, 127 (2017).

[116] Manca, M. *et al.* Enabling valley selective exciton scattering in monolayer wse2 through upconversion. *Nature Comms.* **8**, 14927 (2017).

[117] Chow, C. M. E. *et al.* Unusual exciton-phonon interactions at van der waals engineered interfaces. *Nano Letters* (2017).

[118] Ajayi, O. *et al.* Approaching the intrinsic photoluminescence linewidth in transition metal dichalcogenide monolayers. *2D Materials* (2017).

[119] Wang, Z., Shan, J. & Mak, K. F. Valley-and spin-polarized landau levels in monolayer wse 2. *Nature nanotechnology* **12**, 144 (2017).

[120] Wierzbowski, J. *et al.* Direct exciton emission from atomically thin transition metal dichalcogenide heterostructures near the lifetime limit. *Scientific reports* **7**, 12383 (2017).

[121] Chen, S.-Y. *et al.* Superior valley polarization and coherence of 2 s excitons in monolayer wse 2. *Physical review letters* **120**, 046402 (2018).

[122] Nagler, P. *et al.* Zeeman splitting and inverted polarization of biexciton emission in monolayer ws 2. *Physical review letters* **121**, 057402 (2018).

[123] Chen, S.-Y., Goldstein, T., Taniguchi, T., Watanabe, K. & Yan, J. Coulomb-bound four-and five-particle intervalley states in an atomically-thin semiconductor. *Nature communications* **9**, 3717 (2018).

[124] Dean, C. *et al.* Graphene based heterostructures. *Solid State Communications* **152**, 1275–1282 (2012).

[125] Neumann, A. *et al.* Opto-valleytronic imaging of atomically thin semiconductors. *Nature Nanotechnology* doi:10.1038/nnano.2016.282 (2017).

[126] Sallen, G. *et al.* Dark-bright mixing of interband transitions in symmetric semiconductor quantum dots. *Phys. Rev. Lett.* **107**, 166604 (2011).

[127] Stier, A. V., McCreary, K. M., Jonker, B. T., Kono, J. & Crooker, S. A. Exciton diamagnetic shifts and valley Zeeman effects in monolayer WS2 and MoS2 to 65 Tesla. *Nature Communications* **7**, 10643 (2016). 1510.07022.

[128] Mitioglu, A. A. *et al.* Magnetoexcitons in large area cvd-grown monolayer mos_2 and $mose_2$ on sapphire. *Phys. Rev. B* **93**, 165412 (2016).

[129] Stier, A. V., Wilson, N. P., Clark, G., Xu, X. & Crooker, S. A. Probing the influence of dielectric environment on excitons in monolayer wse2: Insight from high magnetic fields. *Nano Letters* **16**, 7054–7060 (2016).

[130] Raja, A. *et al.* Coulomb engineering of the bandgap and excitons in two-dimensional materials. *Nature Communications* **8**, 15251 (2017).

[131] Jones, A. M. *et al.* Optical generation of excitonic valley coherence in monolayer wse2. *Nat. Nanotechnol.* **8**, 634–638 (2013).

[132] Wang, G. *et al.* Control of exciton valley coherence in transition metal dichalcogenide monolayers. *Phys. Rev. Lett.* **117**, 187401 (2016).

[133] Wang, G. *et al.* Valley dynamics probed through charged and neutral exciton emission in monolayer wse2. *Phys. Rev. B* **90**, 075413 (2014).

[134] Zhang, X. *et al.* Phonon and raman scattering of two-dimensional transition metal dichalcogenides from monolayer, multilayer to bulk material. *Chem. Soc. Rev.* **44**, 2757–2785 (2015).

[135] Crooker, S. A., Barrick, T., Hollingsworth, J. A. & Klimov, V. I. Multiple temperature regimes of radiative decay in cdse nanocrystal quantum dots: Intrinsic limits to the dark-exciton lifetime. *Applied Physics Letters* **82**, 2793–2795 (2003).

[136] Echeverry, J. P., Urbaszek, B., Amand, T., Marie, X. & Gerber, I. C. Splitting between bright and dark excitons in transition metal dichalcogenide monolayers. *Phys. Rev. B* **93**, 121107 (2016).

[137] Weiner, J. *et al.* Strong polarization-sensitive electroabsorption in gaas/algaas quantum well waveguides. *Applied physics letters* **47**, 1148–1150 (1985).

[138] Zhang, X.-X. *et al.* Magnetic brightening and control of dark excitons in monolayer wse2. *Nature Nanotechnology* **doi:10.1038/nnano.2017.105**, – (2017).

[139] Molas, M. *et al.* Brightening of dark excitons in monolayers of semiconducting transition metal dichalcogenides. *2D Materials* **4**, 021003 (2017).

[140] Zhou, Y. *et al.* Probing dark excitons in atomically thin semiconductors via near-field coupling to surface plasmon polaritons. *Nature Nanotechnology* **doi:10.1038/nnano.2017.106**, – (2017).

[141] Slobodeniuk, A. & Basko, D. Spin–flip processes and radiative decay of dark intravalley excitons in transition metal dichalcogenide monolayers. *2D Materials* **3**, 035009 (2016).

[142] Dery, H. & Song, Y. Polarization analysis of excitons in monolayer and bilayer transition-metal dichalcogenides. *Phys. Rev. B* **92**, 125431 (2015).

[143] Ye, Z. *et al.* Probing Excitonic Dark States in Single-layer Tungsten Disulfide. *Nature* **513**, 214–218 (2014).

[144] Zhu, B., Chen, X. & Cui, X. Exciton Binding Energy of Monolayer WS2. *Scientific Reports* **5**, 9218 (2015).

[145] Hill, H. M. *et al.* Observation of excitonic rydberg states in monolayer mos2 and ws2 by photoluminescence excitation spectroscopy. *Nano letters* **15**, 2992–2997 (2015).

[146] Robert, C. *et al.* Optical spectroscopy of excited exciton states in mos 2 monolayers in van der waals heterostructures. *Physical Review Materials* **2**, 011001 (2018).

[147] Stier, A. V. *et al.* Magnetooptics of exciton rydberg states in a monolayer semiconductor. *Physical review letters* **120**, 057405 (2018).

[148] Miura, N. *Physics of semiconductors in high magnetic fields*, vol. 15 (Oxford University Press, 2008).

[149] Knox, R. Theory of excitons (1963).

[150] Akimoto, O. & Hasegawa, H. Interband optical transitions in extremely anisotropic semiconductors. ii. coexistence of exciton and the landau levels. *Journal of the Physical Society of Japan* **22**, 181–191 (1967).

[151] MacDonald, A. & Ritchie, D. Hydrogenic energy levels in two dimensions at arbitrary magnetic fields. *Physical Review B* **33**, 8336 (1986).

[152] Edelstein, W., Spector, H. N. & Marasas, R. Two-dimensional excitons in magnetic fields. *Physical Review B* **39**, 7697 (1989).

[153] Sekine, T., Izumi, M., Nakashizu, T., Uchinokura, K. & Matsuura, E. Raman scattering and infrared reflectance in 2h-mose2. *Journal of the Physical Society of Japan* **49**, 1069–1077 (1980).

[154] Molina-Sánchez, A. & Wirtz, L. Phonons in single-layer and few-layer mos_2 and ws_2. *Phys. Rev. B* **84**, 155413 (2011).

[155] Rice, C. *et al.* Raman-scattering measurements and first-principles calculations of strain-induced phonon shifts in monolayer mos_2. *Phys. Rev. B* **87**, 081307 (2013). URL `http://link.aps.org/doi/10.1103/PhysRevB.87.081307`.

[156] Horzum, S. *et al.* Phonon softening and direct to indirect band gap crossover in strained single-layer $mose_2$. *Phys. Rev. B* **87**, 125415 (2013).

[157] Ribeiro-Soares, J. *et al.* Group theory analysis of phonons in two-dimensional transition metal dichalcogenides. *Phys. Rev. B* **90**, 115438 (2014).

[158] Slobodeniuk, A. & Basko, D. Exciton-phonon relaxation bottleneck and radiative decay of thermal exciton reservoir in two-dimensional materials. *Physical Review B* **94**, 205423 (2016).

[159] Jakubczyk, T. *et al.* Impact of environment on dynamics of exciton complexes in a ws2 monolayer. *2D Materials* **5**, 031007 (2018).

[160] Lee, J., Koteles, E. S. & Vassell, M. Luminescence linewidths of excitons in gaas quantum wells below 150 k. *Physical Review B* **33**, 5512 (1986).

[161] Hameau, S. *et al.* Strong electron-phonon coupling regime in quantum dots: evidence for everlasting resonant polarons. *Physical review letters* **83**, 4152 (1999).

[162] Tatham, M., Ryan, J. & Foxon, C. Time-resolved raman measurements of intersubband relaxation in gaas quantum wells. *Physical review letters* **63**, 1637 (1989).

[163] Gindele, F. *et al.* Excitons, biexcitons, and phonons in ultrathin cdse/znse quantum structures. *Physical Review B* **60**, 8773 (1999).

[164] Borri, P. *et al.* Ultralong dephasing time in ingaas quantum dots. *Physical Review Letters* **87**, 157401 (2001).

[165] Besombes, L., Kheng, K., Marsal, L. & Mariette, H. Acoustic phonon broadening mechanism in single quantum dot emission. *Physical Review B* **63**, 155307 (2001).

[166] Urbaszek, B. *et al.* Temperature-dependent linewidth of charged excitons in semiconductor quantum dots: Strongly broadened ground state transitions due to acoustic phonon scattering. *Physical Review B* **69**, 035304 (2004).

[167] Shree, S. *et al.* Observation of exciton-phonon coupling in mose 2 monolayers. *Physical Review B* **98**, 035302 (2018).

[168] Gołasa, K. *et al.* Multiphonon resonant raman scattering in mos2. *Applied Physics Letters* **104**, 092106 (2014).

[169] Soubelet, P., Bruchhausen, A., Fainstein, A., Nogajewski, K. & Faugeras, C. Resonance effects in the raman scattering of monolayer and few-layer mose 2. *Physical Review B* **93**, 155407 (2016).

[170] Miranda, H. P. *et al.* Quantum interference effects in resonant raman spectroscopy of single-and triple-layer mote2 from first-principles. *Nano letters* **17**, 2381–2388 (2017).

[171] Froehlicher, G., Lorchat, E., Zill, O., Romeo, M. & Berciaud, S. Rigid-layer raman-active modes in n-layer transition metal dichalcogenides: interlayer force constants and hyperspectral raman imaging. *Journal of Raman Spectroscopy* **49**, 91–99 (2018).

[172] Lee, C. *et al.* Anomalous lattice vibrations of single- and few-layer mos2. *ACS Nano* **4**, 2695–2700 (2010). URL `http://pubs.acs.org/doi/abs/10.1021/nn1003937`. PMID: 20392077, `http://pubs.acs.org/doi/pdf/10.1021/nn1003937`.

[173] Tonndorf, P. *et al.* Photoluminescence emission and raman response of monolayer mos 2, mose 2, and wse 2. *Optics express* **21**, 4908–4916 (2013).

[174] Froehlicher, G., Lorchat, E. & Berciaud, S. Direct versus indirect band gap emission and exciton-exciton annihilation in atomically thin molybdenum ditelluride (mote 2). *Physical Review B* **94**, 085429 (2016).

[175] Miller, R., Kleinman, D. & Gossard, A. Observation of doubly resonant lo-phonon raman scattering with gaas-algaas quantum wells. *Solid State Communications* **60**, 213 – 216 (1986).

[176] Cerdeira, F., Anastassakis, E., Kauschke, W. & Cardona, M. Stress-induced doubly resonant raman scattering in gaas. *Phys. Rev. Lett.* **57**, 3209–3212 (1986).

[177] Ivchenko, E. L. *Optical spectroscopy of semiconductor nanostructures* (Alpha Science, Harrow UK, 2005).

[178] Guo, H. *et al.* Double resonance raman modes in monolayer and few-layer $mote_2$. *Phys. Rev. B* **91**, 205415 (2015).

[179] Wang, G. *et al.* Double resonant raman scattering and valley coherence generation in monolayer wse_2. *Phys. Rev. Lett.* **115**, 117401 (2015).

[180] Seidel, W., Titkov, A., André, J., Voisin, P. & Voos, M. High-efficiency energy up-conversion by an" auger fountain" at an inp-aiinas type-ii heterojunction. *Physical review letters* **73**, 2356 (1994).

[181] Hellmann, R. *et al.* Low-temperature anti-stokes luminescence mediated by disorder in semiconductor quantum-well structures. *Physical Review B* **51**, 18053 (1995).

[182] Poles, E., Selmarten, D. C., Mićić, O. I. & Nozik, A. J. Anti-stokes photoluminescence in colloidal semiconductor quantum dots. *Applied physics letters* **75**, 971–973 (1999).

[183] Paskov, P. *et al.* Photoluminescence up-conversion in inas/gaas self-assembled quantum dots. *Applied Physics Letters* **77**, 812–814 (2000).

[184] Chen, S. *et al.* Efficient upconversion of photoluminescence via two-photon absorption in bulk and nanorod zno. *Applied Physics B* **108**, 919–924 (2012).

[185] Agulló-Rueda, F., Mendez, E. & Hong, J. Doubly resonant raman scattering induced by an electric field. *Physical Review B* **38**, 12720 (1988).

[186] Gubarev, S., Ruf, T. & Cardona, M. Doubly resonant raman scattering in the semimagnetic semiconductor cd 0.95 mn 0.05 te. *Physical Review B* **43**, 1551 (1991).

[187] Pringsheim, P. Zwei bemerkungen über den unterschied von lumineszenz- und temperaturstrahlung. *Zeitschrift für Physik* **57**, 739–746 (1929).

[188] Nemova, G. & Kashyap, R. Laser cooling of solids. *Reports on Progress in Physics* **73**, 086501 (2010).

[189] Jones, A. M. *et al.* Excitonic luminescence upconversion in a two-dimensional semiconductor. *Nature Physics* **12**, 323 (2016).

[190] Ovsyankin, V. & Feofilov, P. Mechanism of summation of electronic excitations in activated crystals. *Soviet Journal of Experimental and Theoretical Physics Letters* **3**, 322 (1966).

[191] Zhang, J., Zhang, Q., Wang, X., Kwek, L. C. & Xiong, Q. Resolved-sideband raman cooling of an optical phonon in semiconductor materials. *Nature Photonics* **10**, 600 (2016).

[192] Mouri, S. *et al.* Nonlinear photoluminescence in atomically thin layered wse 2 arising from diffusion-assisted exciton-exciton annihilation. *Physical Review B* **90**, 155449 (2014).

[193] Yu, T. & Wu, M. W. Valley depolarization dynamics and valley hall effect of excitons in monolayer and bilayer mos_2. *Phys. Rev. B* **93**, 045414 (2016). URL `https://link.aps.org/doi/10.1103/PhysRevB.93.045414`.

[194] Sun, D. *et al.* Observation of rapid exciton-exciton annihilation in monolayer molybdenum disulfide. *Nano Letters* **14**, 5625–5629 (2014). PMID: 25171389.

[195] Abakumov, V., Perel, V. I. & Yassievich, I. *Nonradiative recombination in semiconductors*, vol. 33 (Elsevier, 1991).

[196] Polkovnikov, A. S. & Zegrya, G. G. Auger recombination in semiconductor quantum wells. *Physical Review B* **58**, 4039 (1998).

[197] Glazov, M. M. *et al.* Intrinsic exciton-state mixing and nonlinear optical properties in transition metal dichalcogenide monolayers. *Phys. Rev. B* **95**, 035311 (2017).

[198] Kavoulakis, G. & Baym, G. Auger decay of degenerate and bose-condensed excitons in cu 2 o. *Physical Review B* **54**, 16625 (1996).

[199] Wang, F., Wu, Y., Hybertsen, M. S. & Heinz, T. F. Auger recombination of excitons in one-dimensional systems. *Physical Review B* **73**, 245424 (2006).

[200] Rybkovskiy, D. V., Gerber, I. C. & Durnev, M. V. Atomically inspired kp approach and valley zeeman effect in transition metal dichalcogenide monolayers. *Phys. Rev. B* **95**, 155406 (2017).

[201] Dey, P. *et al.* Optical coherence in atomic-monolayer transition-metal dichalcogenides limited by electron-phonon interactions. *Phys. Rev. Lett.* **116**, 127402 (2016).

[202] Selig, M. *et al.* Excitonic linewidth and coherence lifetime in monolayer transition metal dichalcogenides. *Nature Communications* **7**, 13279 (2016).

[203] Berkelbach, T. C., Hybertsen, M. S. & Reichman, D. R. Bright and dark singlet excitons via linear and two-photon spectroscopy in monolayer transition-metal dichalcogenides. *Physical Review B* **92**, 085413 (2015).

[204] Tassone, F. & Yamamoto, Y. Exciton-exciton scattering dynamics in a semiconductor microcavity and stimulated scattering into polaritons. *Physical Review B* **59**, 10830 (1999).

[205] Butov, L. *et al.* Stimulated scattering of indirect excitons in coupled quantum wells: Signature of a degenerate bose-gas of excitons. *Physical Review Letters* **86**, 5608 (2001).

[206] Yuan, L., Wang, T., Zhu, T., Zhou, M. & Huang, L. Exciton dynamics, transport, and annihilation in atomically thin two-dimensional semiconductors. *The journal of physical chemistry letters* **8**, 3371–3379 (2017).

[207] Hoshi, Y. *et al.* Suppression of exciton-exciton annihilation in tungsten disulfide monolayers encapsulated by hexagonal boron nitrides. *Physical Review B* **95**, 241403 (2017).

[208] Robert, C. *et al.* Exciton radiative lifetime in transition metal dichalcogenide monolayers. *Phys. Rev. B* **93**, 205423 (2016).

[209] Kheng, K. *et al.* Observation of negatively charged excitons x^- in semiconductor quantum wells. *Phys. Rev. Lett.* **71**, 1752–1755 (1993).

[210] Mak, K. F. *et al.* Tightly bound trions in monolayer mos2. *Nature Materials* **12**, 207 (2013).

[211] Ross, J. S. *et al.* Electrical control of neutral and charged excitons in a monolayer semiconductor. *Nature communications* **4**, 1474 (2013).

[212] Finkelstein, G., Shtrikman, H. & Bar-Joseph, I. Optical spectroscopy of a two-dimensional electron gas near the metal-insulator transition. *Physical review letters* **74**, 976 (1995).

[213] Shields, A., Osborne, J., Simmons, M., Pepper, M. & Ritchie, D. Magneto-optical spectroscopy of positively charged excitons in gaas quantum wells. *Physical Review B* **52**, R5523 (1995).

[214] Buhmann, H. *et al.* Electron-concentration-dependent quantum-well luminescence: Evidence for a negatively charged exciton. *Physical Review B* **51**, 7969 (1995).

[215] Finkelstein, G., Shtrikman, H. & Bar-Joseph, I. Negatively and positively charged excitons in gaas/al x ga 1- x as quantum wells. *Physical Review B* **53**, R1709 (1996).

[216] McCreary, K. M. *et al.* The effect of preparation conditions on raman and photoluminescence of monolayer ws 2. *Scientific reports* **6**, 35154 (2016).

[217] Song, Y. & Dery, H. Transport theory of monolayer transition-metal dichalcogenides through symmetry. *Phys. Rev. Lett.* **111**, 026601 (2013).

[218] Yu, H., Liu, G.-B., Gong, P., Xu, X. & Yao, W. Dirac cones and dirac saddle points of bright excitons in monolayer transition metal dichalcogenides. *Nature communications* **5**, 3876 (2014).

[219] Boulesbaa, A. *et al.* Observation of two distinct negative trions in tungsten disulfide monolayers. *Physical Review B* **92**, 115443 (2015).

[220] Plechinger, G. G. plechinger, p. nagler, a. arora, r. schmidt, a. chernikov, ag del águila, pcm christianen, r. bratschitsch, c. schüller, and t. korn, nat. commun. 7, 12715 (2016). *Nat. Commun.* **7**, 12715 (2016).

[221] Molas, M. R. *et al.* The optical response of monolayer, few-layer and bulk tungsten disulfide. *Nanoscale* **9**, 13128–13141 (2017).

[222] Vaclavkova, D. *et al.* Singlet and triplet trions in ws2 monolayer encapsulated in hexagonal boron nitride. *Nanotechnology* **29**, 325705 (2018).

[223] Sidler, M. *et al.* Fermi polaron-polaritons in charge-tunable atomically thin semiconductors. *Nature Physics* **13**, 255 (2017).

[224] Lindlau, J. *et al.* Identifying optical signatures of momentum-dark excitons in transition metal dichalcogenide monolayers. *arXiv preprint arXiv:1710.00988* (2017).

[225] Courtade, E. *et al.* Charged excitons in monolayer wse 2: Experiment and theory. *Physical Review B* **96**, 085302 (2017).

[226] Landau, L. D. & Lifshitz, E. M. Quantum mechanics: non-relativistic theory (1977).

[227] Sergeev, R. & Suris, R. The triplet state of x+ trion in 2d quantum wells. *physica status solidi (b)* **227**, 387–396 (2001).

[228] Astakhov, G. Gv astakhov, dr yakovlev, vv rudenkov, pcm christianen, t. barrick, sa crooker, ab dzyubenko, w. ossau, jc maan, g. karczewski, and t. wojtowicz, phys. rev. b 71, 201312 (r)(2005). *Phys. Rev. B* **71**, 201312 (2005).

[229] Berkelbach, T. C., Hybertsen, M. S. & Reichman, D. R. Theory of neutral and charged excitons in monolayer transition metal dichalcogenides. *Physical Review B* **88**, 045318 (2013).

[230] Szyniszewski, M., Mostaani, E., Drummond, N. D. & Fal'ko, V. Binding energies of trions and biexcitons in two-dimensional semiconductors from diffusion quantum monte carlo calculations. *Physical Review B* **95**, 081301 (2017).

[231] Yanhao Tang, J. S., Kin Fai Mak. Long valley lifetime of dark excitons in single-layer wse2. *arXiv preprint arXiv:1903.12586* (2019).

[232] Zhang, C. *et al.* Interlayer couplings, moiré patterns, and 2d electronic superlattices in mos2/wse2 hetero-bilayers. *Science advances* **3**, e1601459 (2017).

[233] Tran, K. *et al.* Evidence for moiré excitons in van der waals heterostructures. *Nature* 1 (2019).

[234] Lindlau, J. *et al.* The role of momentum-dark excitons in the elementary optical response of bilayer wse 2. *Nature communications* **9**, 2586 (2018).

[235] Gerber, I. C. *et al.* Interlayer excitons in bilayer mos 2 with strong oscillator strength up to room temperature. *Physical Review B* **99**, 035443 (2019).

[236] Edelberg, D. *et al.* Hundredfold enhancement of light emission via defect control in monolayer transition-metal dichalcogenides. *arXiv preprint arXiv:1805.00127* (2018).

[237] Luo, Y., Liu, N., Hone, J. C. & Strauf, S. Single photon emission in wse_2 up 160 k by quantum yield control. *arXiv preprint arXiv:1903.00126* (2019).

[238] Zhong, D. *et al.* Van der waals engineering of ferromagnetic semiconductor heterostructures for spin and valleytronics. *Science Advances* **3**, e1603113 (2017).

Summary in french

In this first and only appendix, you can read a summary of the present manuscript written in french. I would really like to thank Thierry Amand without whose help this would have been impossible.

Brève introduction aux dichalcogénures de métaux de transition

Les cristaux lamellaires constituent un groupe de matériaux formés par une série de plans atomiques empilés les uns sur les autres. De fortes liaisons chimiques covalentes maintiennent les atomes d'un plan cristallin donné entre eux, tandis que ce sont des forces attractives de van der Waals qui sont responsable de la cohésion d'ensemble des plans cristallins. Il est possible de détacher un feuillet du cristal massif et obtenir ainsi un véritable cristal bidimensionnel, car la liaison de van der Waals est notablement plus faible que la liaison covalente.

Avec l'isolation du graphène, simple feuillet d'atomes de carbones disposés en nid d'abeille [12, 13], le plus étudié des cristaux bidimensionnels (2D), de nombreuses techniques pour produire, caractériser et manipuler des feuillets dont l'épaisseur ne dépasse pas quelques plans atomiques ont été mises au point, ce qui a conduit en retour à un développement rapide des recherches dans le domaine des matériaux 2D. Le grand intérêt porté à ces matériaux est motivé par les propriétés fascinantes présentées par le graphène.

Suivant cette découverte, la communauté scientifique a entrepris des recherches sur différentes familles de matériaux lamellaires, dans l'espoir que d'autres propriétés extraordinaires pourraient être découvertes dans différentes monocouches. Parmi celle-ci, celle qui nous intéresse particulièrement est la famille des dichalcogénures de métaux de transitions et tout spécialement le groupe VI des dichalcogénures de formule chimique MX_2, où M représente l'atome métallique (molybdène ou tungstène) et X représente un atome de chalcogène (soufre, sélénium ou tellure). La structure cristalline de ces matériaux est montrée dans la Fig.(1,a). Nous nous référerons dorénavant à ce sous-groupe de matériaux simplement sous le nom de dichalcogénures de métaux de transition (TMDs).

Les travaux concomitants de Splendiani [27] et Mak [28] ont montré que les mono-feuillets de MoS_2 sont des semi-conducteurs à gap direct, avec une forte émission radiative dans le spectre visible. Par contre, contrairement au cas précédent, sous forme de cristal massif ou même amincis jusqu'à obtenir des bicouches, ces cristaux présentent un gap indirect, comme le montre la Fig.

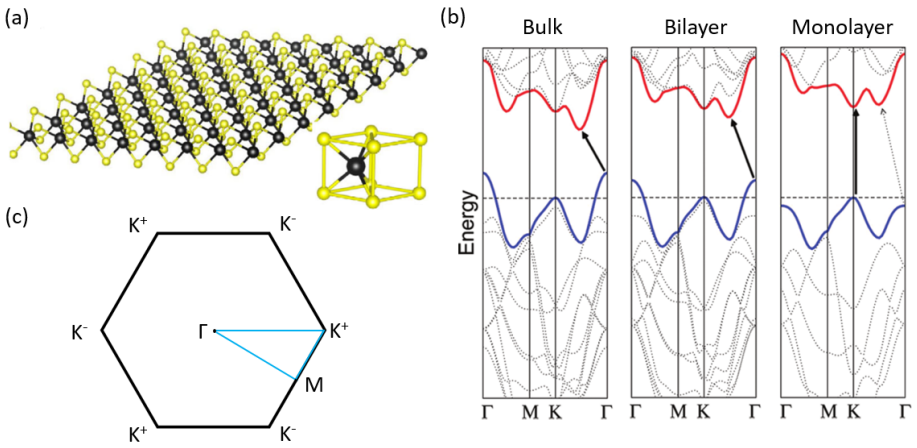

Figure 1: (a) Modèle de la structure cristalline d'une monocouche de TMD et cellule élémentaire de Wigner correspondante. Les sphères jaunes représentent les atomes de chalcogène tandis que les noires les atomes métalliques (images tirées de la référence [26]). (b) Structure de bande calculée de MoS_2 sous forme de cristal massif (à gauche), bicouche (au milieu) et monocouche (à droite). On voit sur ces trois panneaux que le semi-conducteur passe d'une structure de bande indirecte à directe (images tirées de la référence [27]). (c) Schéma de la zone de Brillouin hexagonale d'une monocouche où les principaux points caractéristiques sont indiqués. Les traits bleu clair indiquent les chemins le long desquels la structure de bande du panneau (b) à droite est calculée.

(1,b). Ce passage de gap indirect à direct renforce l'interaction lumière-matière de ces matériaux et conduit en particulier à un accroissement de quatre ordres de grandeur de l'émission de la photoluminescence.

Une autre conséquence de l'exaltation de l'interaction lumière-matière et le fait que l'épaisseur des cristaux 2D n'est que de quelques plans atomiques est la présence d'effets excitoniques très forts. Dans un semi-conducteur, un électron et un trous s'attirent mutuellement du fait de l'interaction coulombienne. En particulier, dans les TMDs l'effet d'écran diélectrique sur l'interaction de Coulomb est réduite, et du fait du fort confinement quantique des porteurs perpendiculairement à la couche, l'attraction coulombienne entre électrons et trous est exaltée et donne lieu à des états fortement liés appelés excitons, situés en dessous du gap.

Ces quasi-particules ont été initialement découvertes dans Cu_2O [42], mais dans les TMD mono-feuillet, leur énergie de liaison est très grande (des centaines de meV), de sorte que le spectre présente un caractère excitonique dominant, même à température ambiante. Le caractère excitonique se manifeste par une raie d'absorption ou d'émission dans le spectre optique il est manifeste également dans les spectres de réflectivité, située en dessous du gap électronique du matériau.

Les excitons possèdent beaucoup de similitudes avec l'atome d'hydrogène, par exemple une série de niveaux discrets présentant une forte analogie avec la série de Rydberg. Des états excitoniques excités ont été bien sûr observés dans ces cristaux monocouches [46].

De manière remarquable, les extrema de bandes dans les TMDs mono-

feuillets ne sont pas situés au centre de la zone de Brillouin (appelé point Γ) mais à sa frontière, aux points appelés points K, comme indiqué sur la figure (1c). De plus, du fait de l'absence de symétrie d'inversion présentée par les TMDs mono-feuillets, ces points K se répartissent en deux sous-ensembles non équivalents, appelés K^+ et K^- .

Un autre résultat fondamental obtenu par Xiao et al. [54] and by Cao et al. [55] à partir du calcul de structure de bande des TMDs est que l'on peut exciter sélectivement l'une ou l'autre des vallées situées au voisinage de ces deux familles de points par des photons de différentes hélicités. Nous appellerons dorénavant les vallées K^+ et K^- celles excités par de la lumière de polarisation circulaire respectives σ^+ et σ^-.

De plus, Xiao et al. [54] ont également considéré que le fort couplage spin-orbite induit par les atomes métalliques, relativement lourds, et le fait que leurs orbitales d sont impliquées dans la formation des états électroniques de conduction et de valence, donne lieu à un clivage important de la bande de valence. En conséquence, il n'y a qu'un seul état de spin possible dans chaque sous-bande, et l'ordre est renversé dans deux vallées adjacentes (non-équivalentes) de la zone de Brillouin. Cette situation est décrite en détail dans la figure (2a).

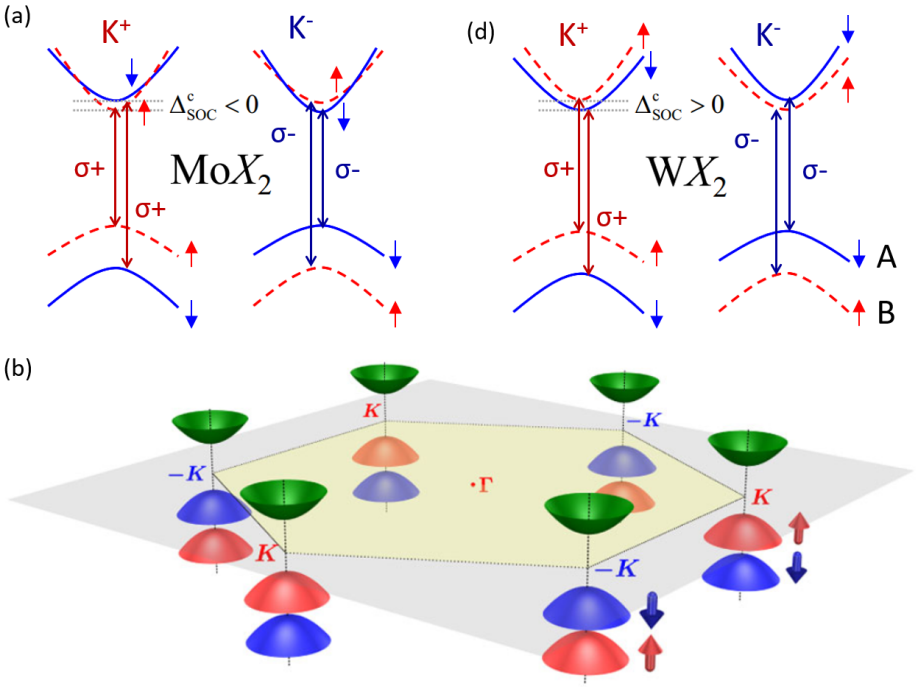

Figure 2: (a) Le schéma montre le clivage de la bande de valence et de conduction dans les deux vallées K^+ et K^- à la fois pour les composés à base de tungstène et de molybdène. Notez que l'ordre du clivage des bandes de conduction est inversé lorsque l'on passe de Mo à W. La double flèche indique les bandes impliquées dans une transition excitonique de la série A ou B, et leur couleur symbolise les règles de sélection chirales (D'après G. Wang et al. [26]) (b) Schéma de la première zone de Brillouin hexagonale dans les TMDs; le clivage de la bande de conduction n'est pas visible à cette échelle (D'après la référence [55]).

Le clivage de la bande de valence est très significatif, se montant typiquement à 0.2 eV pour les molybdénides MoX_2 et 0.4 eV pour pour les tungsténides WX_2 [32, 43, 54, 56, 57]. Il a été montré ultérieurement que la bande de conduction était également clivée, mais la différence d'énergie entre les deux sous-bandes est plus faible d'un ordre de grandeur (quelques dizaines de meV typiquement) [33, 54, 58, 59, 60, 61]. Du fait de la présence des deux bandes de valence, il y a deux types de transitions excitoniques possibles, que nous conviendrons d'appeler exciton A ou B.

Du fait des règles de sélection optiques gouvernant les transitions près des minima des vallées situées aux points K, les électrons qui y sont photo-générés ont une orientation de spin bien définie. Ceci signifie que certaines transitions sont interdites du fait de la conservation du spin dans les transitions dipolaires électriques. Dans les composés molybdénides, la transition optique permise en spin vers l'exciton A est favorisée, car elle correspond à la recombinaison d'un exciton construits avec des états des bandes d'électrons et de trous les plus basses en énergie [58, 60]. Dans les tungsténides tels WS_2 et WSe_2 au contraire, les excitons les plus bas en énergie sont construits à partir de bandes entre lesquelles les transitions optiques sont interdites car elles correspondent à des états de spin opposés, comme nous le montrons dans la figure (2a).

Une autre conséquence des règles de sélections optiques est le caractère chiral des transitions. A partir des propriétés de symétrie du système, on peut déduire qu'une transition se produisant dans l'une des vallées inéquivalentes, par exemple K^+, peut être obtenue sélectivement avec des photons ayant une polarisation circulaire bien définie : dans le cas présent il s'agit de la polarisation circulaire droite que nous appellerons dorénavant σ^+. En revanche, l'autre vallée pourra être excitée sélectivement avec une polarisation circulaire gauche, appelée σ^- [54, 55, 67, 68, 69, 70].

En définitive, nous avons la possibilité de générer et de détecter une polarisation de spin/vallée de façon optique. Les dichalcogénures de métaux de transitions constituent donc un système idéal pour étudier le degré de liberté correspondant à l'état de vallée dans le cadre de la valléetronique [71, 72, 73, 74].

Techniques expérimentales

Exfoliation

La technique utilisée pour obtenir un feuillet atomique unique en partant d'un cristal massif est appelée clivage micromécanique, mais on s'y réfère souvent comme la technique de l'exfoliation dite "du ruban adhésif". De fait, c'est le seul outil nécessaire pour réaliser cette exfoliation à partir du cristal 3D.

Un cristal massif d'un matériau lamellaire est appliqué sur un ruban adhésif et retiré de façon répétée. Puis le ruban est mis en contact avec une feuille de Polydimethylsiloxane (PDMS) adhérant à une lame de verre [82], ce qui a pour effet de transférer sur le polymère les feuillets exfoliés. On cherche ensuite parmi ces derniers les cristaux qui sont mono-feuillets. Le processus est donc aléatoire, et donc la feuille de PDMS est examinée soigneusement au microscope. Pour ce faire, la lame de verre est montée sur un système de positionnement micromécanique dans les trois directions, x,y et z. Une fois le mono-feuillet trouvé, il peut être transféré de façon déterministe sur un substrat cible (en général

une plaquette de silicium recouvert d'une couche d'environ 90 nm de dioxyde de silicium placé au sommet d'un système de positionnement micromécanique xyz. Le transfert réalisé, un recuit thermique est généralement pratiqué pour améliorer l'adhésion du mono-feuillet au substrat. Ce recuit est effectué en plaçant le substrat sur une plaque chauffée à 150 °C à l'air à la pression ambiante.

La technique décrite précédemment suppose la possibilité the voir effectivement la monocouche. Ce problème n'est pas trivial car la monocouche a une épaisseur d'envron 0.6 nm. Heureusement, la forte interaction lumière-matière présentée par les TMDs rend possible l'identification d'un mono-feuillet par simple mesure du contraste de l'image dans un microscope optique. Une des grandes forces des cristaux 2D est la possibilité de combiner différentes monocouches en les empilant les unes sur les autres. Il en résulte un matériau artificiel assemblé selon une séquence choisie que l'on appelle hétéro-structure de van der Waals [15].

La fabrication de telles structures s'effectue très simplement en utilisant de façon répétée la technique de transfert décrite ci-dessus. Il est bien sûr très important de contrôler la position de la couche déposée sur la précédente avec une grande précision spatiale, ce que l'on effectue au moyen de micromanipulateurs.

Les structures les plus courantes fabriquées dans notre laboratoire sont les échantillons encapsulés [87], dans les quelles un mono-feuillet de TMD est placé entre deux lamelles de nitrure de bore hexagonal (hBN) de grande qualité [89]. Nous expliquerons plus en détail l'intérêt de cette hétéro-structure au chapitre 3.

En pratique, on colle sur un cristal massif de hBN un ruban adhésif que l'on décolle ensuite, et ce de façon répétée. On peut ainsi transférer quelques centaines de lamelles de hBN de l'adhésif au PDMS. Puis, au moyen d'un microscope optique situé dans notre poste de transfert, nous cherchons une lamelle convenable, c'est-à-dire plane et d'une épaisseur d'environ 100 nm (cette valeur peut changer selon les applications). La lamelle choisie est ensuite transférée sur un substrat, l'ensemble étant recuit (à 150 °C pendant 10 minutes à l'air). Après que la couche inférieure de hBN ait été transférée, on doit répéter l'opération pour le monofeuillet de TMD. Finalement, une seconde lamelle plus fine (≈ 10 nm) est utilisée pour encapsuler la monocouche déposée au préalable sur hBN, ce qui a pour effet de la protéger de l'environnement. Notez qu'un recuit thermique est effectué après chaque étape de la procédure de fabrication.

Techniques expérimentales

Ce travail de thèse peut être défini comme une étude par spectroscopie optique à basse température de matériaux dont l'épaisseur ne dépasse pas quelques plans atomiques. Les ensembles expérimentaux doivent donc satisfaire les conditions suivantes.

Les échantillons doivent pouvoir être maintenus à des températures cryogéniques. Il est clair que la présence de vibrations de réseau altère les propriétés optiques des TMDs, en particulier en induisant un élargissement thermique des raies spectrales. Ainsi, pour révéler des effets fins, il est préférable de réaliser les études à basse température, lorsque le nombre de phonons et leur énérgie thermique est réduite. Un seconde exigence est la nécessité d'une haute résolution spatiale, car l'aire des feuillets à analyser ne s'étend en général pas au-delà de quelque dizaines de μm^2. Pour atteindre une excitation d'irradiance suffisante

et être en mesure d'analyser les fluctuations spatiales des propriétés optiques sur la surface de l'échantillon, il est donc nécessaire d'avoir une tache d'excitation laser proche de la limite de diffraction, ce qui nécessite en retour l'emploi d'un objectif de fort grandissement.

De plus, de façon à caractériser un échantillon malgré sa petite taille, il est nécessaire de pouvoir le déplacer par rapport à l'objectif du microscope dans les trois directions de l'espace avec une grande précision spatiale. Ceci peut être réalisé grâce à trois moteurs pas à pas piézoélectriques qui permettent le contrôle de la position de l'échantillon dans les trois directions, et en particulier de placer la tache d'excitation avec une précision nanométrique.

Si l'ensemble expérimental est sensible à la position du laser d'excitation laser, il est impératif de réduire les vibrations externes qui ont pour effet de déplacer la tache d'excitation et de moyenner le spectre sur une grande surface pendant le temps d'acquisition: l'effet serait le même que si l'on utilisait une tache d'excitation plus grande. Pour cette raison, les cryostats utilisés présentent des vibrations mécaniques très faibles.

Une autre condition requise pour l'accomplissement du dessin de ce travail de thèse est l'obtention d'une haute résolution en polarisation. Ceci est nécessaire pour mettre au jour les propriétés de polarisation de vallée des dichalcogénures ainsi que le couplage spin/vallée dont ils sont le siège. En effet, nous avons vu qu'en excitant un mono-feuillet de TMD avec une lumière polarisée circulairement on excite sélectivement les électrons dans l'une des deux vallées K. Pour ce faire, le degré de polarisation circulaire du laser d'excitation sera maintenu autour de 99% tout au long des expériences décrites plus loin. Les composants optiques principaux pour contrôler le degré de polarisation sont des jeux de lames quart-d'onde, des prismes polariseurs de Glan-Taylor et des lames biréfringentes à cristaux liquides.

Il est également important de présenter des différentes techniques de spectroscopie qui seront utilisées par la suite pour connaitre le type d'information qu'il est possible d'en tirer. Le contraste de réflectivité noté DR/R (appelée réflectivité différentielle par certains auteurs) est la seule technique ne requérant pas l'emploi d'un laser. Cette technique est proche de la spectroscopie d'absorption, car les informations que l'on peut en tirer sont similaires. Le principe est d'exciter l'échantillon avec une source de lumière blanche (lampe halogène) et de détecter le spectre réfléchi. Si l'échantillon absorbe à une certaine longueur d'onde, le spectre de réflectivité présentera une oscillation et le contraste de réflectivité présentera un creux à cette longueur d'onde.

Généralement, les spectres de réflectivité apparaissent sur un fond continu important, ce qui rend leur détection difficile. De plus, une partie du signal peut être généré par le substrat lui-même. C'est pourquoi un second spectre est enregistré sur le substrat tout près de l'échantillon. Ce second spectre est le spectre de référence. Ce dernier est soustrait au spectre relevé sur l'échantillon (d'où le nom de réflectivité différentielle) et normalisé en divisant par le spectre de référence. De façon remarquable ici, il n'est pas nécessaire de recourir ici à des techniques de réflectivité modulée, comme c'est souvent le cas avec les semiconducteurs et leurs nanostructures classiques, du fait des forces d'oscillateur très élevées des excitons dans les TMDs.

Une autre technique qui sera utilisée extensivement est la spectroscopie de photoluminescence (PL). Un laser dont l'énergie spectrale est plus grande que le gap est utilisé pour exciter l'échantillon. Les excitons se forment et recombinent

radiativement. Les photons émis, dont l'énergie est maintenant plus faible que celle des photons d'excitation, constituent un pic d'émission dans les spectres de PL. Ces derniers sont en général beaucoup plus riches que les spectres de réflectivité. Ceci se produit car des niveaux de défauts sont souvent présents à des énergies plus faibles que le gap excitonique. Dans ce cas, les excitons peuvent relaxer (en émettant un ou plusieurs phonons) vers l'un de ces états de défauts et recombiner radiativement. Ceci provoque l'apparition de plusieurs pics situés en dessous du gap excitonique. Si l'on a un grand nombre de défauts, le pic correspondant aux excitons libres peut même disparaître au profit des pics d'excitons piégés.

Une autre technique plus complexe mais extrêmement utile est la spectroscopie d'excitation de la photoluminescence (PLE). Celle-ci consiste à enregistrer des spectres de PL d'une raie d'émission donnée en fonction de l'énergie d'excitation (en utilisant par exemple un laser accordable). Si tous les autres paramètres sont maintenus constants (en premier lieu l'énergie de détection), cette dépendance donnera des informations sur les propriétés d'absorption du matériau et la relaxation d'énergie subséquente vers les états détectés.

Spectroscopie optique des dichalcogénures de métaux de transition

Nous discutons maintenant des spectres optiques des TMDs. Depuis le début des recherches sur ces cristaux, les mono-feuillets étaient transférés sur des plaquettes de silicium présentant une couche d'oxyde superficielle. Après cette étape de transfert, l'ensemble du substrat et de l'échantillon sont chargés dans un cryostat et peuvent être refroidis à basse température, autour de 4 K. La première caractérisation de base est faite au moyen de la technique du contraste de réflectivité, car les spectres sont ainsi plus simples à interpréter. Des résultats typiques peuvent être vus sur la figure (3) où les spectres des quatre composés les plus étudiés de la famille des TMDs sont présentés.

Comme on l'observe clairement, le spectre de réflectivité chaque matériau présente deux transitions: celle associée à l'exciton A, et celle associée à l'exciton B, notés respectivement X^0_A et X^0_B. Grâce à cette caractérisation, il est donc possible d'assigner une position spectrale aux excitons et en particulier celle de l'exciton A. Les spectres de photoluminescence des quatre composés sont présentés sur la figure (4), où l'on a porté simultanément les composantes co-polarisées ou contra-polarisées à celle du laser d'excitation. Pour identifier les pics, on doit utiliser différentes approches. Comme nous l'avons déjà mentionné, l'exciton A neutre peut être identifié en contrôlant simplement la position du pic d'émission le plus haut en énergie et en la comparant avec celle relevée sur le spectre de réflectivité.

Les pics repérés par la lettre L correspondent à des états d'exciton localisés soit par des défauts. On peut le déduire en observant l'évolution du spectre en augmentant la température. L'augmentation de l'énergie thermique favorise alors la probabilité d'échappement des excitons localisés du puits de potentiel associé à leur défaut et les pics d'états localisés disparaissent progressivement.

Le trion (ou exciton chargé) peut être identifié dans les dispositifs où il est effectivement possible de doper le matériau et par des prédictions théoriques concernant son énergie de liaison, qui est directement mesurable par l'écart de la raie correspondante par rapport à celle de X^0. Noter que l'on ne considère

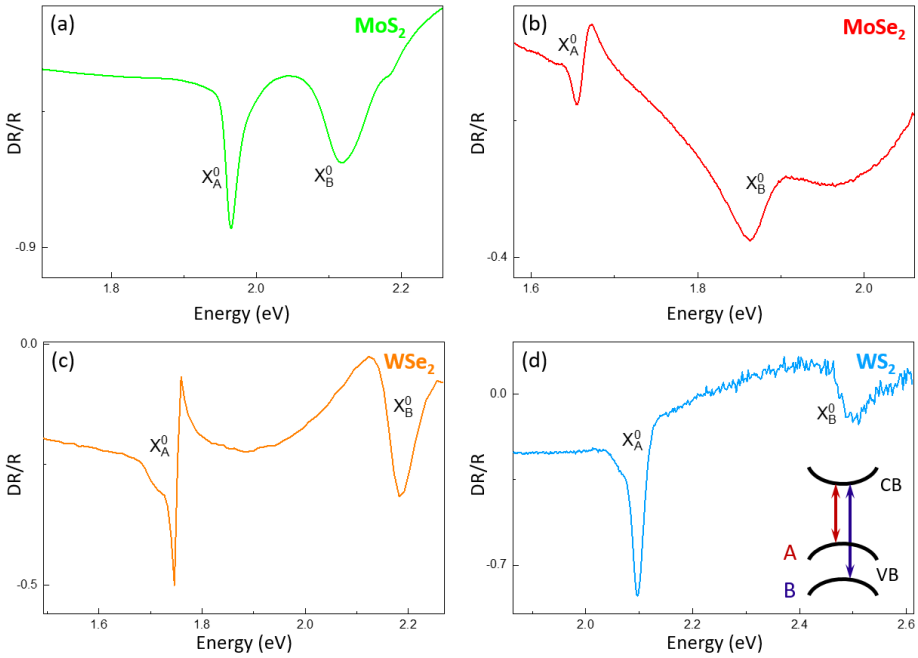

Figure 3: Spectres de réflectivité de mono-feuillets de (a) MoS_2, (b) $MoSe_2$, (c) WSe_2 et (c) WS_2, obtenus au moyen d'une lampe halogène. La température est de 4 K.

pas l'exciton B en photoluminescence. En effet la photoluminescence chaude de cet état est extrêmement faible car les excitons B relaxent préférentiellement vers les états de la série excitonique A qui recombinent ensuite radiativement.

Comme nous l'avons discuté au chapitre 1, la structure de bande particulière des TMDs conduit au verrouillage entre état de spin et de vallée dans une bande donnée, avec pour conséquence la possibilité d'excitation sélective des deux vallées inéquivalentes en lumière polarisée, σ^+ ou σ^-. Comme le temps de relaxation de la polarisation des excitons est comparable ou un peu plus long que le temps de recombinaison, le déséquilibre entre les populations d'excitons créés par un laser polarisé circulairement est partiellement conservé pendant leur temps de vie pour certains composés de la famille des TMDs. Comme on le voit clairement sur les figures (4a,c), l'émission de la PL est co-polarisée avec la polarisation circulaire du laser d'excitation.

Transitions optiques dans WSe_2

Le but de ce chapitre est de montrer les améliorations portées au processus de caractérisation des mono-feuillets de WSe_2, ainsi que les propriétés optiques récemment découvertes qu'elles ont permises.

En effet, dans les trois dernières années, de grands progrès ont été réalisées dans la fabrication d'échantillon. Il en a résulté une grande amélioration de la réponse optique du matériau [115, 116, 117, 114, 118, 119, 120, 121, 122, 123] et une réduction considérable des largueurs de raies spectrales, ces dernières at-

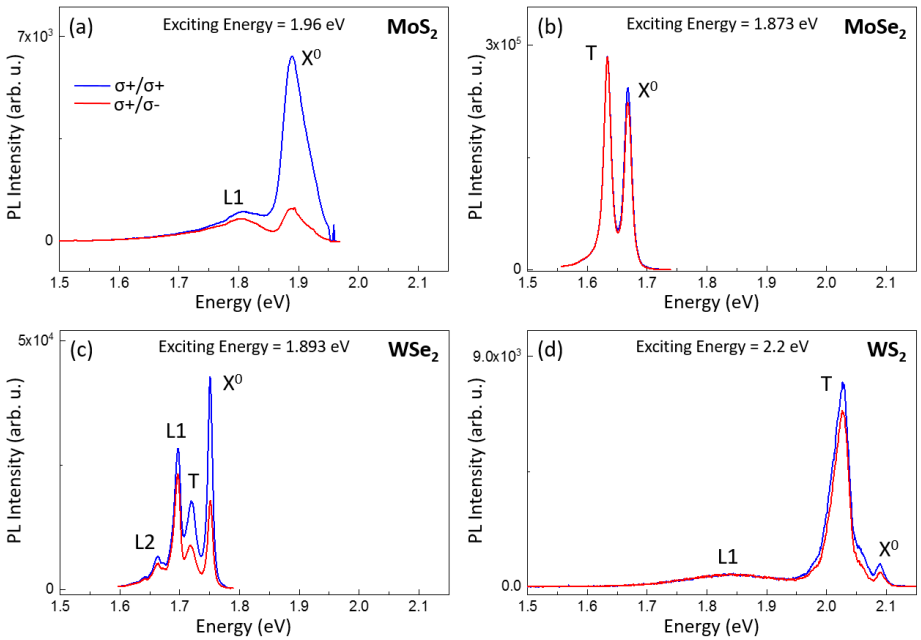

Figure 4: Spectres d'émission de PL polarisés circulairement pour des mono-feuillets de (a) MoS_2, (b) $MoSe_2$, (c) WSe_2 et (c) WS_2, obtenus sous excitation par un laser polarisé σ^+. La température est de 4 K. L'énergie d'excitation diffère pour les quatre échantillons et est indiquée dans chaque panneau. Noter que nous avons omis l'indice A dans le symbole de l'exciton comme il n'y a pas d'ambigüité en PL

teignant récemment la limite de l'élargissement homogène, soit autour de 1 meV à $T = 4$ K.

Cette amélioration a été procurée par l'encapsulation dans des platelets de nitrure de bore, le procédé consistant à élaborer une hétéro-structure de van der Waals en exfoliant un mono-feuillet et en le transférant sur un platelet épais d'un cristal de hBN (d'épaisseur typique ≈ 100 nm), puis en recouvrant le tout par un platelet beaucoup plus fin de hBN (≈ 10 nm).

Cette technique n'est pas nouvelle. Déjà en 2010 Dean et al. ont montré qu'insérer un feuillet de graphène entre de platelet de hBN améliorait considérablement de la mobilité électronique [124]. Le grand changement dans la qualité optique des mono-feuillets de TMD obtenu en les encapsulant dans hBN est montré sur la figure (5).

Comme on peut le constater, la largueur spectrale des raies associées aux transitions excitoniques X^0 (mais aussi des autres transitions) dans les échantillons directement exfoliés sur SiO_2 sont larges et dominées par l'élargissement homogène. Quand nous considérons les feuillets exfoliés sur hBN à $T = 4$ K, toutes les raies deviennent très fines, présentant des largeur de moins de 5 meV. Nous nous concentrerons dorénavant dans ce chapitre sur le WSe_2 sur Si/SiO_2 et dans hBN dont les spectres de PL sont présentés sur les planches (a) et (b) de la figure (6) respectivement.

La différence principale est la réduction de la largueur de raie des transitions optiques. Le pic le plus énergétique est identifié comme l'exciton neutre X^0

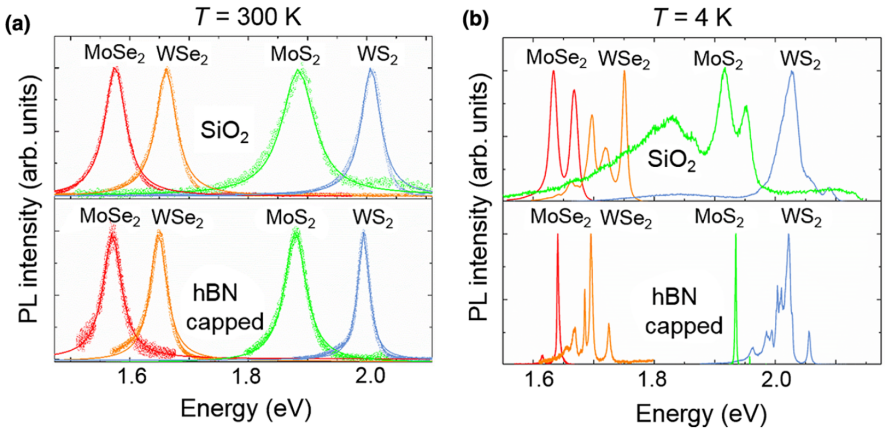

Figure 5: Spectres de photoluminescence de quatre TMDs enregistrés à (a) $T = 300\,\mathrm{K}$ et (b) $T = 4\,\mathrm{K}$. Dans la partie supérieure des planches (a) et (b), nous montrons les spectres de PL de mono-feuillets exfoliés sont déposés sur SiO_2. Dans la partie inférieure, la monocouche exfoliée est déposée sur un platelet de nitrure de bore hexagonal d'épaisseur $\approx 100\,\mathrm{nm}$ puis recouverte par un mince feuillet de hBN d'épaisseur $\approx 10\,\mathrm{nm}$. L'hétéro-structure est placée sur une plaquette de silicium recouverte d'une fine couche d'oxyde SiO_2.

comme le montre immédiatement la comparaison entre la PL et le contraste de réflectivité dans la figure (6b).

Quand le mono-feuillet est déposé sur un substrat de SiO_2/Si la raie de l'exciton neutre présente une largeur de $\approx 13\,\mathrm{meV}$. Celle-ci se réduit à $\approx 4\,\mathrm{meV}$ lorsqu'il est encapsulé dans hBN.

Une autre façon de sonder l'absorption de la lumière par le matériau est d'utiliser l'excitation de la photoluminescence: nous faisons varier l'énergie d'un laser Ti:Sa autour de la transition de X^0 et nous détectons la PL émise par deux autres raies à plus basse énergie. Les résultats sont présentés sur la planche (c) de la figure (6).

La courbe noire montre de nouveau le spectre de PL d'un échantillon encapsulé sous excitation par un laser hélium-néon à $T = 4\,\mathrm{K}$. Les deux courbes bleues représentent les données de PLE et représentent respectivement l'intensité totale émise par le pic β et par le pic γ en fonction de l'énergie du laser d'excitation (voir le chapitre 2 du texte principal pour une description complète de la PLE).

Comme on le constate, les résonances de PLE coincident parfaitement à la position énergétique du pic de PL de X^0. De plus, les largeurs des courbes de PL et de PLE sont très semblables. Un autre résultat expérimental confirme que le premier pic est bien X^0, à savoir la variation de l'intensité d'émission en fonction de la densité de puissance du laser d'excitation. Nous pouvons en effet exciter le mono-feuillet avec un laser hélium-néon, mesurer l'aire située sous le pic X^0 et tracer le graphe de cette aire en fonction de la densité de puissance excitatrice en échelles Log-Log., comme on le montre figure (6d). Dans un tel graphe, la variation de l'intensité de PL en fonction de la puissance incidente donne une indication du nombre d'états électroniques disponibles. Un comportement linéaire avec une pente unité indique que si nous doublons la

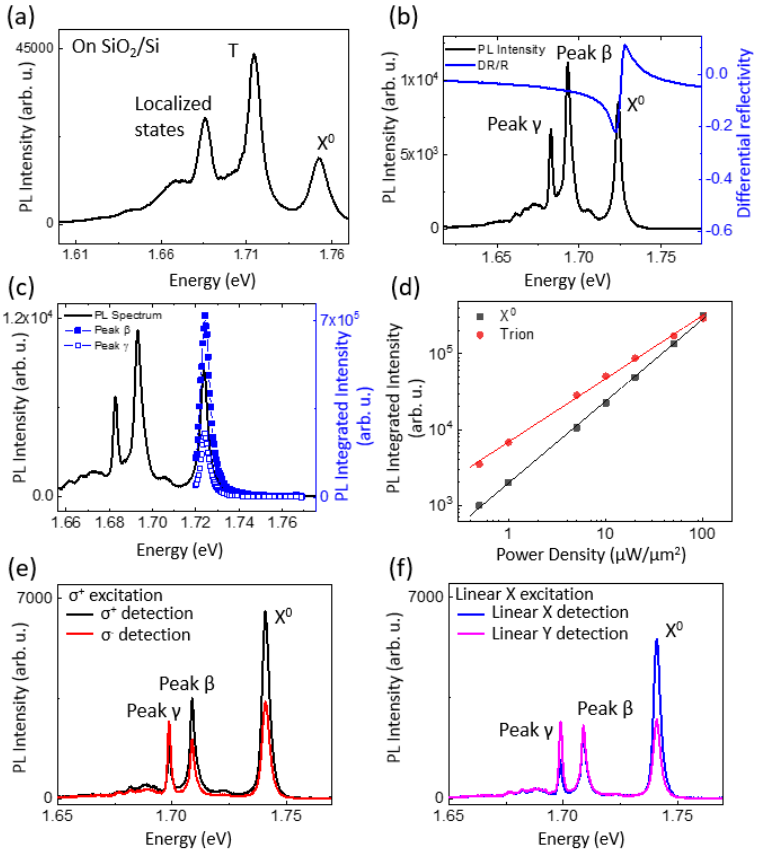

Figure 6: Tous les spectres sont mesurés à $T = 4\,\mathrm{K}$ et concernent, sauf indication contraire, un échantillon encapsulé dans hBN. (a) Les spectres tracés en noir montrent les spectres de photoluminescence d'un mono-feuillet de WSe_2 excité par un laser hélium-néon (632.8 nm) (a) exfolié et déposé sur Si/SiO_2 (b) encapsulé dans hBN . Planche (b) en bleu: contraste de réflectivité mesuré sur le même échantillon qu'en PL, défini par $(R_{signel} + R_{ref})/R_{ref}$ où R_{signel} est le spectre de lumière réfléchie provenant du mono-feuillet tandis que R_{ref} est la réflexion de l'hétéro-structure en l'absence de mono-feuillet. (c) Comparaison entre la position en énergie de la raie de PL de l'exciton neutre sous excitation à 632.8 nm et celle des résonances excitoniques en excitation de la photoluminescence (PLE), où nous excitons de façon résonante l'exciton neutre et détectons la PL émise par les deux pics (marqués par les lettre β et γ). Quand le laser est désaccordé de l'énergie de stricte résonance, l'intensité des deux pics chute car les photons ne sont plus absorbés par le matériau. (d) Dépendance de l'intensité de PL intégrée de l'excitation neutre (carrés noirs) et du pic β (cercles rouges) en faisant varier la densité de puissance du laser d'excitation sur deux ordres de grandeurs. Les graphes noir et rouge représentent le meilleur ajustement par régression linéaire des données avec une pente de m = 1.08 pour X^0 et $n = 0.84$ pour le pic β identifié plus loin comme le trion (exciton chargé). (e) Spectres de PL en mulière polarisée montrant les composantes circulaires droites (σ^+) et gauche (σ^-) sous un laser d'excitation polarisé en σ^+ de densité de puissance $20\,\mu\mathrm{W}/\mu\mathrm{m}^2$ et d'énergie 1.852 eV (669.5 nm). L'exciton neutre est co-polarisé avec le laser. (f) Idem, mais en base linéaire, le laser étant polarisé dans une direction arbitraire notée x.

puissance incidente, le nombre d'excitons est doublé ce qui se traduit en retour par le doublement de l'intensité émise. Cette mesure n'est pas à elle seule une preuve de la nature de la transition, mais est cohérente avec le comportement des excitons neutres.

Une autre méthode permettant l'identification de l'exciton neutre est la mesure de la polarisation de l'émission de la PL. Les mono-feuillets de WSe_2 présentent des états de vallée fortement polarisés et une forte cohérence entre vallée, ce qui se traduit par un signal de PL présentant la même polarisation, circulaire ou linéaire, que le laser d'excitation. Lorsque nous effectuons l'expérience, et en effet nous observons que l'exciton neutre est co-polarisé avec le laser d'excitation, comme le montre la planche (e) de la figure (6). De plus, l'émission de l'exciton neutre est polarisée comme le laser même si celui-ci est polarisé linéairement, i.e. la cohérence inter-vallée peut être générée efficacement et se maintient suffisamment pour être détectée (figure 6f).

Une identification claire du pic à 1.69 eV n'est toujours pas faite (pic β de la figure (6)). Cependant, il est situé approximativement à la même distance de X^0 que le pic du trion dans les échantillons exfoliés sur SiO_2 environ 31 meV. C'est pourquoi il est tentant de l'attribuer au trion, comme nous le ferons par simplicité dans la suite. Ajoutons que ce pic présente une réduction significative de la largueur de raie, de ≈ 10 meV à 4 meV.

Considérons le spectre de réflectivité de la planche (b) de la figure (6): la transition attribuée au trion n'est pas visible, tandis qu'en PL c'est la contribution dominante. Nous en déduisons donc que l'absorption de la lumière par ce complexe est très faible mais que le taux de recombinaison radiatif semble très efficace. De ces données nous pouvons aussi déduire que le dopage effectif dans les échantillons encapsulés est très faible mais néanmoins non nul puisque l'absorption est faible mais que pourtant les trions sont présents puisque nous les observons en photoluminescence.

Si nous considérons la dépendance en puissance sur la figure (6d), nous observons que l'intensité d'émission de la raie du trion croît linéairement avec la densité de puissance (au moins dans le domaine de puissance exploré) mais que la pente de la droite ajustée aux données, s'élevant à 0.84, est inférieure à l'unité.

Une autre observation intéressante concerne le taux de polarisation de l'émission du trion. De même que sur les mono-feuillets exfoliés sur Si/SiO_2, l'émission du trion selon nos données est co-polarisée sous excitation circulaire, mais qu'il n'y a pas de cohérence de vallée [133] (pas de polarisation linéaire sous excitation linéaire). Cependant, pour identifier un complexe chargé, il serait idéal de pouvoir changer la densité de charge dans le mono-feuillet. Cela peut être fait effectivement en chargeant le dopage de l'échantillon dans un dispositif qui sera présenté au chapitre 5.

Jusqu'ici nous avons analysé deux pics, l'un à 1.72 eV (X^0) et l'autre à 1.69 eV (trion). Nous discutons maintenant le pic situé à 1.68 eV. Il montre des propriétés singulières. La raie d'émission correspondante est très étroite puisqu'elle ne s'élève qu'à ≈ 2 meV (FWHM), et sa position en énergie bien définie semble écarter son attribution à un défaut. Elle n'apparaît pas en réflectivité et en PL, elle disparaît lorsque le dopage s'accroît, comme l'exciton neutre. Son intensité croît linéairement avec la puissance de l'excitation, mais présente une saturation.

Cependant, le comportement le plus intriguant est observé en lumière polar-

isée: son pic est contra-polarisé avec le laser à la fois en polarisation circulaire et linéaire, comme on le voit figure (6e,f). Le diagramme polaire de l'intensité de la polarisation linéaire en fonction de la polarisation linéaire d'analyse réalisé montre que l'émission atteint son maximum à environ 45° de la direction x définie arbitrairement indépendamment de la direction de la polarisation du laser d'excitation ou de la position de l'échantillon. L'identification de cette raie nécessite donc une étude plus détaillée.

Lorsque nous avons relevé les mesures précédentes, il y avait des indications sur l'existence d'états optiquement inactifs situés à plus basse énergie dans WSe_2, états vers lesquels les excitons relaxeraient pour se recombiner ensuite non radiativement [58]. Cette idée prenant son origine principalement dans le fait l'intensité de la PL émise par ce type d'échantillon augmente en fonction de la température: losque celle-ci s'accroît, de plus en plus d'excitons peuvent atteindre les niveaux radiatifs plus élevés en énergie ce lui a pour effet d'augmenter le signal de PL. Un comportement similaire a été observé dans les nanocristaux de CdSe [135].

Même si la nature de cet état noir n'était pas claire, il y avait l'idée que l'existence de ces états pourrait prendre son origine dans le clivage spin-orbite de la bande de conduction [64], une idée largement acceptée aujourd'hui, bien que l'ordre exact dépende aussi de l'interaction d'échange coulombienne.

La première des deux règles de sélection qui doit être satisfaite dans les transitions dipolaires électriques est que les états initiaux et finaux doivent avoir la même orientation de spin. Dans les composés tungsténides les états de spin de la branche de conduction la plus basse ont des orientations de spin essentiellement opposées par rapport à celles de la bande de valence supérieure. Ainsi, l'état fondamental de l'exciton correspond à une transition interdite en spin et est optiquement inactif.

Les transitions associées aux excitons brillants dont nous avons parlé jusqu'à présent correspondent à la recombinaison d'un électron de la bande de conduction supérieur avec un trou dans la bande de valence la plus haute. L'écart entre états brillants et noirs a été prédit autour de 30 meV [63] ce qui est en accord raisonnable avec la valeur mesurée qui est de 40 meV. C'est la raison pour laquelle nous avons suspecté ce pic de correspondre en fait à un état d'exciton noir.

Une autre règle de sélection concerne également l'orientation du dipôle associé à la transition doit être satisfaite: certaines transitions optiques ne sont couplées qu'à des directions d'oscillation de la lumière particulières, i.e. à des modes de polarisations donnés. Les règles de sélections dipolaires et de spin doivent être simultanément vérifiées pour qu'une transition optique soit possible et observable. Nous avons montré que le pic γ est en effet un état d'exciton noir et est couplé seulement à la lumière polarisée perpendiculairement au plan d'incidence. En particulier, cet état de polarisation n'est pas bien défini dans la configuration expérimentale dans laquelle la lumière se propage perpendiculairement au mono-feuillet. C'est pourquoi nous le caractérisons en excitant l'échantillon par la tranche, comme nous le montrons en figure (7). Dans cette configuration expérimentale la polarisation dans le plan et perpendiculairement au plan sont simultanément accessibles et le laser se propage dans le plan de la couche dans la direction y.

Les spectres présentés à la figure (7b) montrent clairement que lorsque la lumière oscille perpendiculairement au plan du mono-feuillet, une nouvelle tran-

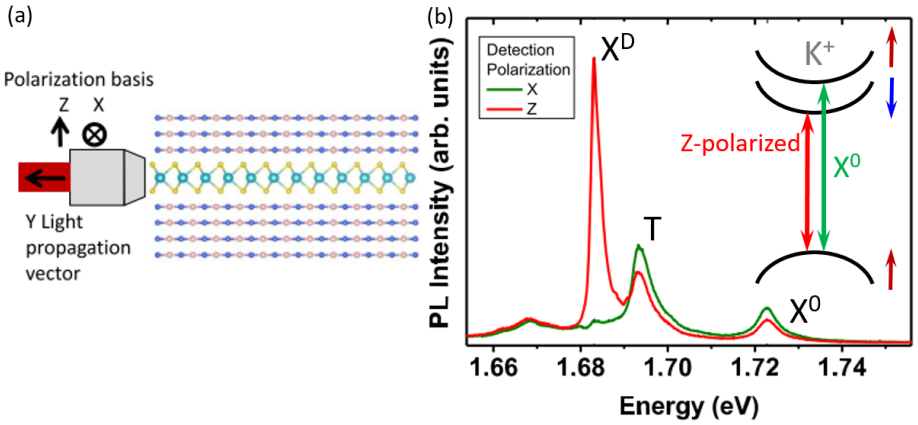

Figure 7: (a) Schéma de principe de la configuration expérimentale utilisée pour élucider la nature de la raie spectrale γ. La lumière se propage dans le plan du mono-feuillet, ce qui permet de l'exciter dans les deux états de polarisation (TE et TM). (b) spectres de l'émission de PL à $T = 13\,\mathrm{K}$ d'un mono-feuillet de WSe_2 excité par un laser à hélium-néon (1.96 eV) obtenus dans la configuration montrée dans la planche (a). Les deux courbes correspondent à l'émission polarisée dans le plan (en vert) et perpendiculaire au plan (en rouge). L'insert montre un schéma de la vallée K^+ où les transitions électroniques associées à l'exciton neutre "brillant" et "noir" sont indiquées respectivement par une flèche verte ou rouge [92].

sition intense apparaît. Cette transition produit une raie de même largeur spectrale que lorsque nous excitions l'échantillon avec une lumière se propageant perpendiculairement à la surface de l'échantillon, et à la même distance énergétique de X^0. Si nous effectuons une rotation de la polarisation pour l'amener dans la direction x parallèle à la surface, la PL associée à la nouvelle transition disparaît alors que nous revenons dans les mêmes conditions de polarisation que lorsque l'on excite perpendiculairement à la surface. Nous en déduisons que la raie γ est polarisée selon la direction z comme le dipôle associé à cette transition et l'identifions comme provenant de la recombinaison d'un état sombre de l'exciton.

Pourtant, nous avons indiqué précédemment que la transition de l'exciton noir vers l'état fondamental était interdite du point de vue du spin. Nous en déduisons qu'il doit exister un certain mélange dans l'état de spin ce qui lève (partiellement) la règle de sélection en spin. Par ailleurs, il a été montré sous champ magnétique appliqué dans le plan de l'échantillon [138] qu'il était possible de coupler les états de spin opposés des bandes de conduction proches du gap, ce qui a permis de mettre en évidence l'existence des états sombres.

L'exciton sombre est détecté aussi dans une direction z perpendiculaire à l'échantillon du fait de la grande ouverture numérique de l'objectif utilisé dans l'expérience, permettant ainsi la détection partielle de la lumière polarisée selon l'axe z.

L'excitation par la tranche n'est pas la seule méthode pour observer l'exciton sombre. Au moment où nous effectuions ces experiences, Zhou et al. le mettaient en évidence en couplant ces modes avec des plasmons-polaritons de surface [140].

Etats excités des excitons

Si nous inspectons sur une plage d'énergie plus large le spectre de réflectivité d'un échantillon de WSe_2 encapsulé, nous remarquons que le pic de l'exciton X^0 situé à 1.72 eV n'est pas le seul à apparaître dans un échantillon non dopé intentionnellement. Dans la planche (a) de la figure (8), d'autres transitions sont clairement visibles.

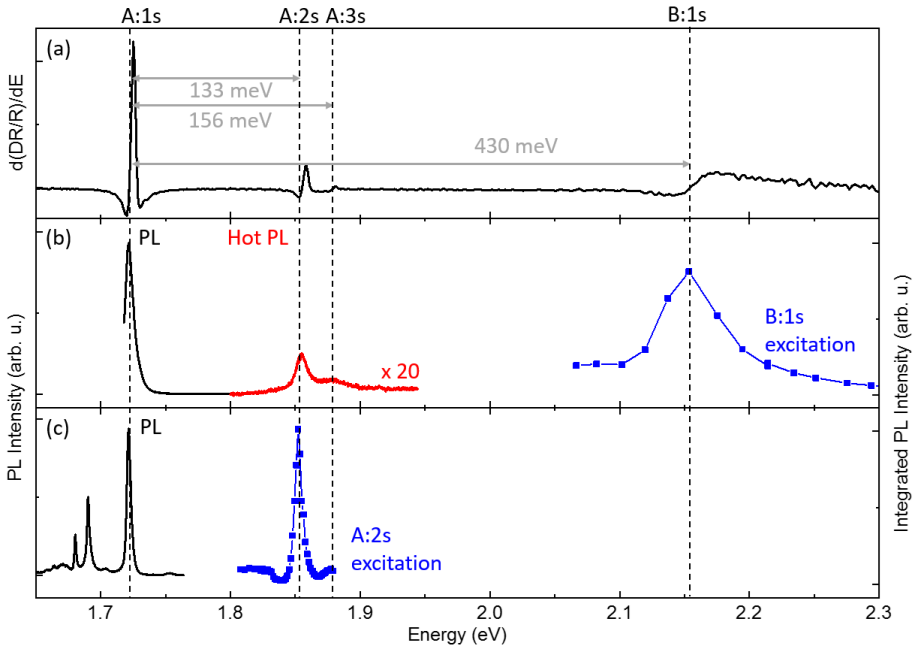

Figure 8: (a) Spectres relevés à basse température ($T = 4\,\mathrm{K}$) d'un mono-feuillet de WSe_2 encapsulé dans hBN. (a) Dérivée première du spectre de contraste de réflectivité en fonction de l'énergie. Quatre transitions sont clairement visibles. (b) Spectre de photoluminescence de l'exciton neutre avec ses premiers états excités sous excitation résonante avec l'exciton B:1s à $\sim 2.15\,\mathrm{eV}$. Le spectre de PL, en rouge, a été amplifié d'un facteur 20 pour rendre les états excités plus visibles. Les points bleus représentent le spectre d'excitation de l'exciton neutre, dont l'intensité est intégrée, lorsque le laser d'excitation accordable traverse la position spectrale de l'exciton B. Le spectre de PL (en rouge) est relevé à une énergie d'excitation qui correspond au maximum de la réponse en PL de l'exciton A. (c) Même méthode qu'en (b) mais pour une excitation quasi résonante avec la transition de l'exciton A:2s. Le spectre en noir est la réponse en PL de l'exciton A:1s obtenu pour une excitation à 1.85 eV strictement résonante avec l'état A:2s.

La plus énergétique, située à environ 430 meV au-dessus de l'exciton neutre est associée à l'exciton B. Cette identification repose sur le fait que la séparation en énergie entre les deux excitons est du même ordre de grandeur que le clivage spin-orbite des deux bandes de valence supérieures. Entre les deux états, deux pics moins intenses mais plus étroits apparaissent à 133 meV et 156 meV au-dessus de l'état A:1s que nous attribuons aux deux premiers états excités de l'exciton. Nous les identifions donc aux états A:2s et A:3s respectivement.

Le réflectivité n'est pas la seule technique de mesure révélant la présence

de ces états à haute énergie. Ils apparaissent en particulier dans la photoluminescence chaude (i.e. émise par un niveau à plus haute énergie que le niveau fondamental) lorsque le laser est accordé sur la transition de l'exciton B:1s. Ces résultats sont montrés sur la planche (b) de la figure (8).

Dans la planche (c), nous montrons maintenant le résultat de l'excitation de la photoluminescence (PLE) pour une excitation résonante avec l'état excité A:2s. Comme pour les expériences de réflectivité, la PLE montre qu'il y a une forte absorption de la lumière autour de 1.85 eV. Ceci doit être mis en relation avec une transition électronique réelle que nous identifions comme un état excité.

L'expérience qui prouve de façon définitive que les transitions observées dans la figure (8) correspondent à des états excités est une expérience de magnéto-optique et a été réalisée à Los Alamos par Stier et al. [147]. En effet, chaque état excité est sujet à un décalage en énergie spécifique en fonction du champ magnétique appliqué, et dans ces expériences, celui-ci est en parfait accord avec la loi simple décrivant le décalage diamagnétique des états excitoniques.

Couplage exciton-phonon

Un autre phénomène important et qui semble omniprésent dans les TMDs est l'interaction exciton-phonon [134, 153, 154, 155, 156, 157, 158, 159]. Une des manifestations de cette interaction est la diffusion Raman, avec des effets très marqués en résonance simple ou double.

L'effet Raman est une forme de la diffusion inélastique des ondes électromagnétiques par un matériau, avec un échange d'énergie avec les vibrations du réseau. Dans une description très simple ù un seul type de phonon est présent, si nous illuminons au moyen d'un laser un matériau et détectons la lumière rétrodiffusée, nous observons un fort signal de diffusion élastique (diffusion Rayleigh sans modification de l'énergie des photons) et deux raies additionnelles situées en énergie de part et d'autre du signal élastique (les pics Raman). Le pic le plus bas en énergie est appelé la raie Stokes, tandis que le second est appelé la raie anti-Stokes. L'analyse des composantes spectrales de la diffusion de la lumière par un matériau est appelée spectroscopie Raman. Lorsque les échanges d'énergie se font avec le réseau, la mesure des écarts entre les pics Raman et le pic Rayleigh permet de déterminer l'énergie des modes phonons du réseau impliqués, et à partir de ceux-là il est ainsi possible de déduire les différents modes vibratoires du cristal [168, 169, 170, 171].

Si une raie Raman est résonante avec une transition réelle, elle est exaltée, ce qui a pour conséquence de modifier considérablement l'intensité de la radiation émise. Ce processus est appelé diffusion Raman simplement résonante. Si maintenant le signal de diffusion Raman et le laser d'excitation sont simultanément résoanants avec des transitions optiques réelles, on parle d'effet Raman doublement résonant.

Nous avons réalisé de type d'expérience sur des mono-feuillets de WSe_2 encapsulés dans hBN où la séparation en énergie entre les états d'exciton A:1s et A:2s est proche de 130 meV, ce qui correspond pratiquement à la somme des énergies de quatre phonons de 32 meV. Ainsi, si nous excitons de façon résonante l'état A:2s, nous attendons une réplique Raman résonante avec l'état A:1s. Notons qu'il s'agit alors d'un processus Raman multi-phononique.

Nous avons réalisé des expériences d'excitation de la photoluminescence de X^0 : nous faisons varier l'énergie du laser d'excitation autour de A:2s et nous

détectons la lumière à l'énergie de l'exciton A:1s. Lorsque l'énergie d'excitation se rapproche de la résonance avec A:2s du côté des hautes énergies, nous voyons croître un signal Raman qui se rapproche progressivement de X^0 comme le montre la planche (a) de la figure (9).

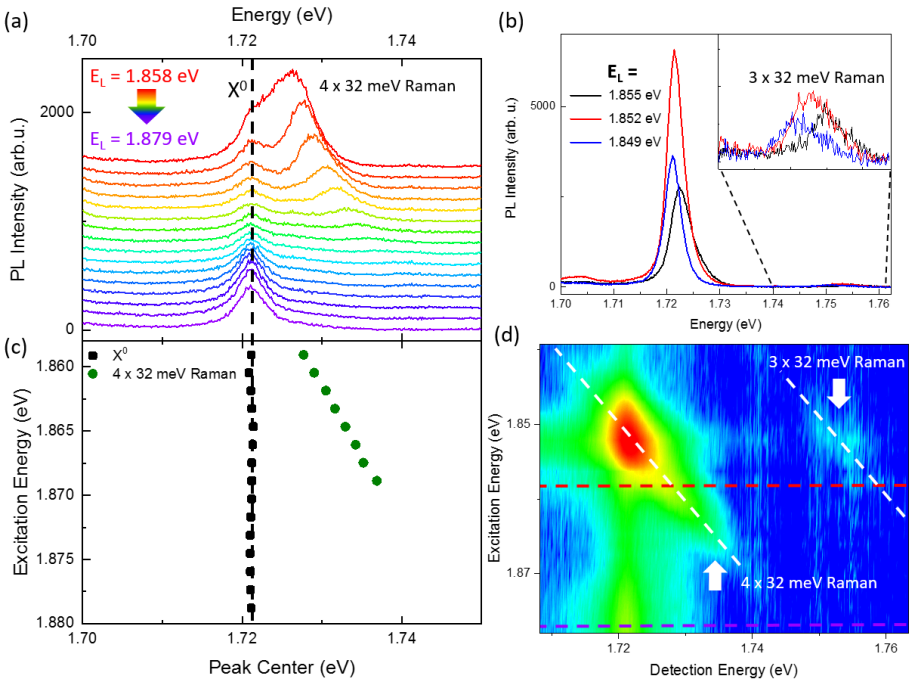

Figure 9: Spectres relevés sur un mono-feuillet de WSe_2 encapsulé dans hBN à $T = 4\,\mathrm{K}$. (a) Différents spectres de PL et du signal Raman pour différentes énergies d'excitation (de 1.879 eV pour le spectre en violet à 1.858 eV pour celui en rouge) lorsque celles-ci se rapprochent la résonance de l'état A:2s située à 1.852 eV. Le spectre obtenu pour une excitation strictement résonante avec A:2s n'est pas présenté ici mais en (b). (b) Le spectre en rouge correspond à une excitation strictement résonante tandis que les deux autres sont obtenu en désaccordant légèrement le laser. Dans l'insert, une autre réplique Raman apparaissant à plus haute énergie, séparée de 32 meV de réplique principale. (c) Position des pics extraits des spectres précédents. Pour les énergies les plus proches de A:2s, il ne nous a pas été possible de séparer de façon fiable les deux contributions (Raman et luminescence) par l'ajustement d'un modèle. (d) Représentation topographique des niveaux d'intensité émise en fonction des énergies de détection et d'excitation, ces dernières étant en polarisation circulaire croisée. Le spectre en violet et celui en rouge de la planche (a) sont indiqués par des tirets. La seconde réplique Raman, plus faible, est néanmoins clairement visible.

Chaque spectre de la figure présente l'émission de la PL de l'état A:1s de X^0 et de la réplique Raman lorsque le laser s'approche de la résonance avec A:2s. Le spectre en condition de stricte résonance avec A:2s est présentée en figure (9b).Un plus grand ensemble de mesures est résumé dans la représentation topographique de l'intensité émise par l'échantillon en fonction des énergies d'excitation et de détection sur la planche (d). Nous pouvons y observer que, contrairement à ce que nous attendions, la réplique Raman ne réapparaît pas au-dessous de la transition A:1s lorsque l'énergie du laser d'excitation est abaissée

en dessous de la résonance avec l'état A:2s. La position des pics Raman et de luminescence qui en est extraite est représentée dans la planche (c). Ce fait traduit une baisse notable de l'efficacité de la diffusion Raman dès que l'énergie d'excitation est plus faible que l'énergie de la transition A:2s.

En résumé, dans cette expérience nous analysons la PL de l'état excitonique A:1s dont l'énergie est fixée et déterminée par le matériau étudié. L'émission est fortement exaltée lorsque l'on excite le premier état excité A:2s de façon résonante. Nous avons varié l'énergie du laser d'excitation sur une plage allant de 1.9 eV à 1.8 eV.

Dans les planches (b) et (d) de la figure (9), deux raies provenant de l'interaction exciton-phonon sont observées. L'une chevauche l'émission de l'exciton neutre (Raman doublement résonant) et l'autre environ 32 meV au-dessus (Raman simplement résonant). Ces répliques sont séparées du laser d'un écart de 4×32 meV et 3×32 meV respectivement. Comme l'intensité des répliques Raman est exaltée même en configuration simplement résonante, nous pouvons faire varier l'énergie du laser de 32 meV de A:2s vers A:1s. Ce faisant, toutes les répliques Raman se déplacent de la même façon. La condition de simple résonance se manifeste lorsque la seconde réplique Raman chevauche la raie de luminescence de X^0 (voir texte principal).

Spectroscopie de conversion de luminescence

Dans ce chapitre nous présentons les études réalisées sur un mono-feuillet de WSe_2 de grande qualité, présentant une largueur de raie excitonique de 4 meV du fait de son encapsulation dans des platelets de nitrure de bore hexagonal (hBN). Les spectres de réflectivité et de PL sont présentés sur les planches (a) et (b) respectivement de la figure (10). Le mono-feuillet est alors excité avec un laser accordé à la résonance avec la transition associée à l'état d'exciton A:1s. Même si le laser fonctionne en régime stationnaire et que sa puissance soit maintenue à des niveaux très bas (de l'ordre de $1\,\mu\mathrm{W}\mu\mathrm{m}^{-2}$), nous avons observé de façon étonnante l'émission d'états situés à plus haute énergie tels que le premier et le second état excité, notés respectivement A:2s et A:3s (en analogie avec le modèle hydrogénoide à 2D) de la série excitonique A, ainsi que l'état de l'exciton B:1s. Notez que ces trois états sont à des niveaux d'énergie situés à envire 130 meV, 150 meV et 430 meV au-dessus de celui de l'exciton A:1s. Nous appellerons dorénavant ce type d'émission le phénomène de "conversion de photoluminescence" (en anglais "up-conversion photoluminescence"), comme décrit sur la planche (c) de la figure (10).

Cet effet n'est pas dû à l'encapsulation dans hBN car il a été observé aussi sur des échantillons exfoliés sur SiO2, ainsi que sur hBN mais en l'absence de couche d'encapsulation supérieure, comme on le montre sur les planches (d) et (e) de la Fig. (10). De plus, cet effet se manifeste jusqu'à la température ambiante (voir le texte principal).

Afin de révéler davantage les caractéristiques de cet effet, nous avons procédé à une expérience de PLE. Le laser d'excitation est accorder de façon à traverser la résonance avec l'exciton A:1s, et l'émission de photoluminescence intégrée spectralement des états excités de l'exciton A et B :1s est mesurée. L'ensemble des spectres obtenus permet de construire la représentation topographique montrée sur la planche (a) de la figure (11), où les couleurs représentent l'intensité

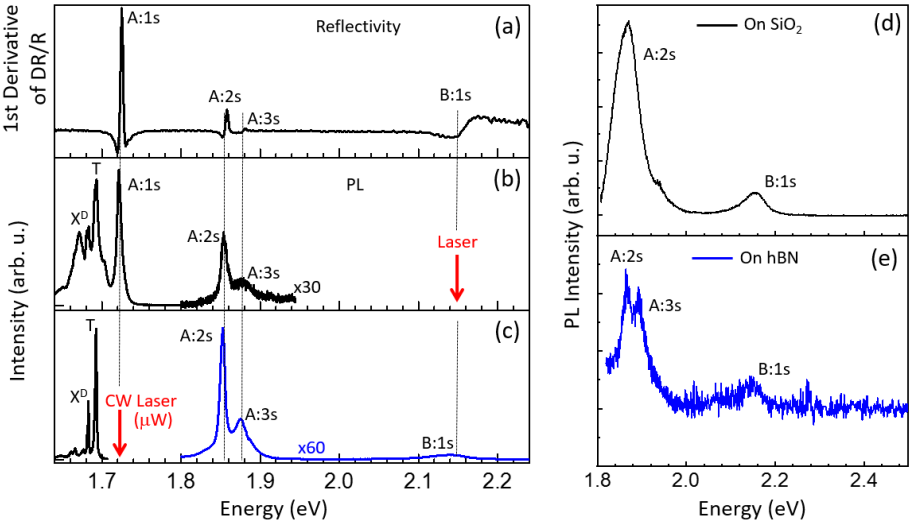

Figure 10: (a) Spectres de réflectivité obtenus à $T = 4\,\mathrm{K}$ sur un mono-feuillet de WSe_2 encapsulé à partir d'une source de lumière blanche. L'exciton A, ses états excités et l'exciton B sont observés. (b) Spectre de PL de A:1s (montrant aussi le trion, l'exciton sombre et un pic lié à un état de défaut) ainsi que la PL chaude des état excités de l'exciton A obtenus en exciton l'exciton B de façon résonante. (c) spectre de PL classique (en noir) et spectre de "conversion de photoluminescence" (en bleu) obtenus en excitant de façon résonante la transition A:1s. (d) Spectre de "conversion de photoluminescence" obtenu à $T = 4\,\mathrm{K}$ sur un mono-feuillet exfolié directement sur SiO2.(e) même expérience qu'en (d), mais en exfoliant le mono-feuillet sur hBN sans couche d'encapsulation supérieure [116].

de photoluminescence.

On voit directement comment l'émission de conversion de luminescence dépend de l'énergie d'excitation: dès que le laser est désaccordé par rapport à la résonance avec l'exciton A:1s (figurée par le trait continu blanc), le signal converti disparaît. De plus, la largueur de la résonance observée en PLE sur le signal de conversion est d'environ 4 meV (FWHM), ce qui correspond à la largueur de raie de l'état A:1s. Il est donc clair que le processus doit être mis en relation avec un taux de génération efficace de l'exciton A.

Une autre confirmation de cet effet vient d'expériences qui furent effectuées plus tard sur des échantillons de MoSe2 à charge ajustable : comme le dopage réduit la force d'oscillateur de l'exciton neutre, le signal de conversion de luminescence diminue [83]. Ces résultats révèlent une caractéristique importante de la conversion de luminescence: c'est un phénomène résonant.

Si nous mesurons l'évolution de la PL du signal de conversion en fonction de la puissance d'excitation du laser d'excitation, nous constatons qu'il évolue de façon super-linéaire comme on le voit en représentation en échelle log-log. En particulier, la pente est approximativement le double de celle de l'exciton A, comme on le voit sur la figure (11,b). Cela signifie que doubler le nombre d'excitons A dans le système produit une augmentation d'un facteur quatre du nombre d'excitons B et d'excitons dans des états excités. En retour, cela semble indiquer que deux excitons photo-générés par le laser se combinent pour

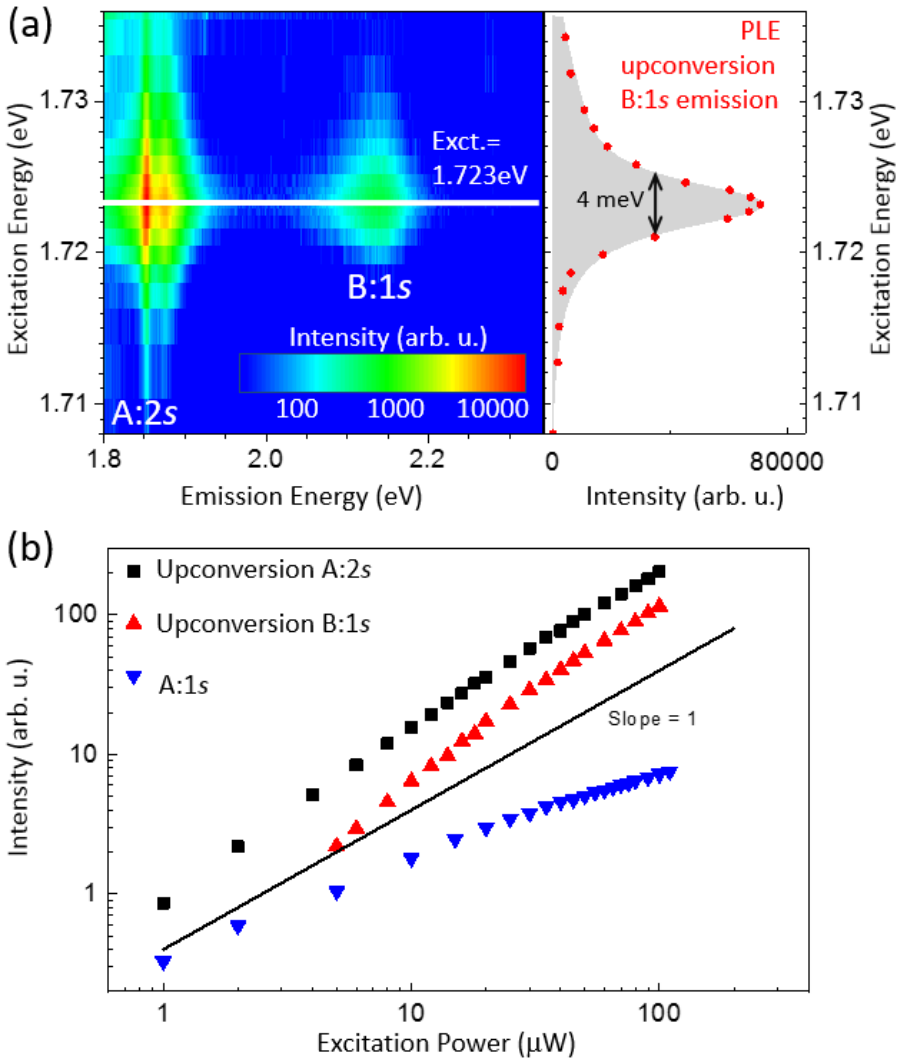

Figure 11: Les données suivantes sont obtenues à $T = 4\,\mathrm{K}$ à partir du même monofeuillet de WSe_2 encapsulé dans hBN. (a) Sur la planche de gauche est portée une représentation topographique de l'intensité d'émission de PL de A:2s, A:3s et B:1s en fonction de l'énergie du laser d'excitation (en ordonnée). Une résonance apparaît clairement comme on le voit de façon plus explicite pour l'exciton B dans la planche de droite qui présente le spectre d'excitation de sa PL. (b) Comparaison de la dépendance en puissance de l'intensité intégrée de la PL de l'exciton A:1s (triangles bleus) sous excitation résonante avec l'état A:2s,.avec celle de l'intensité de "conversion de luminescence" de l'exciton:2s et B:1s sous excitation résonante avec A:1s. Cette dernière montre clairement un comportement super-linéaire et la pente dans le domaine $10 - 100\,\mu\mathrm{W}/\mu\mathrm{m}$, est le double de celle de l'intensité de l'émission de A:1s (1.1 et 1.25 pour A:2s, et B:1s respectivement, et 0.56 pour l'exciton A:1s) [116].

former une seule quasi-particule excitée dont l'énergie est doublée initialement. La paire électron-trou formée relaxe ensuite vers les états qui luminescent.

Un scénario possible d'explication de ces phénomènes serait un processus de type Auger, i.e. l'annihilation exciton-exciton [192, 110, 193, 194], processus dans le quel deux excitons créés indépendamment diffusent l'un avec l'autre selon un processus coulombien. Il en résulte que l'un des excitons recombine non radiativement, cédant son énergie à l'autre exciton qui peut maintenant atteindre une bande d'énergie d'états excités, c'. La paire électron-trou ainsi produite peut alors perdre son énergie (par émission de phonons) et relaxer vers B:1s ou des états excités de l'exciton A. Noter toutefois qu'un processus de type Auger devrait en principe être très peu probable dans la mesure où un exciton (ou plus précisément son électron dans la bande de conduction) doit gagner en impulsion aussi de façon à se retrouver sur un état de bande d'énergie existant.

Cependant sur la base d'une analyse détaillée effectuée par nos collaborateurs Leonid Golub et Mikhail Glazov (Institut Ioffe, Saint Pétersbourg) [197], les règles de sélection en impulsion peuvent être en partie levées du fait de la forte interaction coulombienne dans les TMDs, ce qui en retour lève la contrainte sur la conservation de l'impulsion de l'électron [198, 199], et ce grâce à la présence d'une bande d'énergie de conduction plus énergétique.

Emission de l'exciton B par conversion de de luminescence

Des résultats intéressants sont obtenus lorsque nous excitons l'échantillon par de la lumière polarisée circulairement et que nous résolvons en polarisation le signal de conversion de luminescence. En particulier, nous notons que tandis que l'émission des états excités de l'exciton A est co-polarisée avec le laser d'excitation, le signal de conversion émis par l'exciton B:1s est quant à lui contra-polarisé. Afin de comprendre cette différence, nous proposons deux scenarii différents que nous présentons dans la suite.

En ce qui concerne l'exciton B, nous notons que le signal de conversion qui en émane n'est pas seulement contra-polarisé avec le laser d'excitation mais aussi que le degré de polarisation circulaire croît avec la puissance incidente : plus le laser d'excitation polarisé σ^+ est intense, plus le taux de polarisation de l'émission de l'exciton B est polarisée σ^-.

Afin d'expliquer le caractère contra-polarosé de l'émission de B:1s, nous proposons basé sur la diffusion entre les excitons B et A. En effet, les bosons diffusent préférentiellement depuis leur état initial vers l'état final si celui-ci est déjà peuplé, et ce d'autant plus efficacement que la population de l'état final est grande. Dans la suite, nous suggérons que c'est ce principe général qui est responsable de nos observations.

Pour commencer, nous supposons que l'excitation crée une population égale d'exciton de chiralité $|+1\rangle$ et $|-1\rangle$ dans la bande excitée c' car les règles de sélection chirales ne peuvent être maintenues si loin des minima des vallées K (i.e. pour des états aussi hauts en énergie). Un schéma décrivant cette situation juste après l'excitation est présenté sur la planche (a) de la Fig. (12).

La deuxième hypothèse est que la relaxation vers l'état d'exciton B:1s ne favorise aucune des deux chiralités. Cela signifie qu'après l'excitation, nous avons une population égale d'excitons B de chiralité $|+1\rangle$ et $|-1\rangle$ (voir planche (b)).

Cependant, la population d'exciton $|+1\rangle$ sera déplétée plus rapidement que celle des excitons $|-1\rangle$, du fait de leur caractère bosonique. (planche (c)). En effet, on sait que les excitons se comportent comme des bosons en régime de

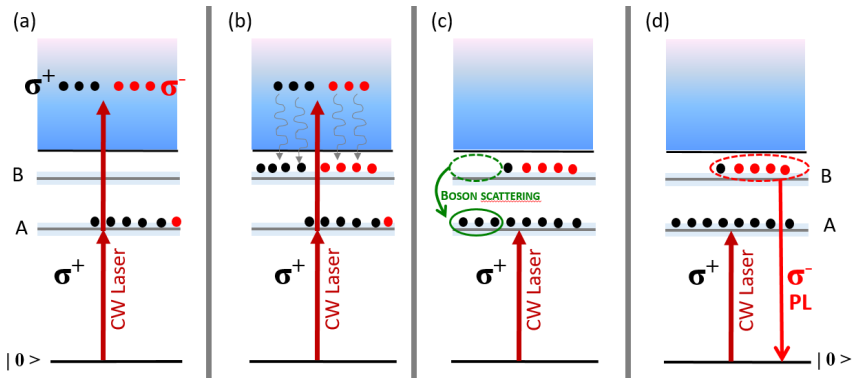

Figure 12: Schéma d'explication de l'apparition d'une polarisation circulaire négative du signal de "conversion de photoluminescence" de l'exciton B:1s en fonction de la puissance d'excitation résonante de l'exciton A:1s en polarisation circulaire, basé sur la diffusion stimulée sélective en polarisation apparaissant entre l'exciton A et B du fait du caractère bosonique des excitons.

faible densité, et il est connu que les bosons diffusent préférentiellement vers des états quantiques déjà peuplés par des bosons de même nature. Ainsi, comme l'état $|+1\rangle$ du niveau A:1s est fortement peuplé du fait de l'excitation laser polarisée σ^+, la probabilité de diffusion des excitons B de chiralité $|+1\rangle$ sera plus élevée vers les états d'excitons $|+1\rangle$ du niveau A:1s que vers les états $|-1\rangle$, ce qui conduit au déséquilibre des populations d'excitons B de chiralités opposées.

Le nombre d'excitons B dans l'état $|+1\rangle$ sera donc plus faible que celui des excitons B dans l'état $|-1\rangle$, ce qui conduit à une émission de conversion de luminescence polarisée σ^- comme le montre la planche (d) de la figure (12). De plus le degré de polarisation de ce signal va croître avec la puissance d'excitation, car la probabilité de diffusion est proportionnelle au nombre d'occupation de l'exciton A:1s dans la vallée K^+. Il s'ensuit que plus ce dernier est occupé, plus efficace sera la déplétion de l'exciton B dans la même vallée, et plus le signal de conversion de luminescence émis par l'exciton B sera contra-polarisé avec le laser d'excitation.

Emission des états excités de l'exciton A par conversion de de luminescence

Nous discutons maintenant du signal de conversion de luminescence émis par les excitons A:2s et A:3s qui montrent aussi des propriétés intéressantes en polarisation. Le premier point est que cette émission est nettement co-polarisée avec le laser d'excitation, atteignant $P_c \approx 25\%$, et est presque indépendante de la puissance d'excitation.

Nous suggérons que la population de l'état fondamental de l'exciton A et ses états excités sont couplés. Ce couplage est rendu possible du fait que la séparation en énergie entre A:1s et A:2s d'environ 130 meV correspond à la somme des énergies de quatre phonons optiques longitudinaux (LO), comme nous l'avons déjà indiqué dans le chapitre précédent. Afin de vérifier cette hypothèse, nous pouvons désaccorder le laser d'excitation de la résonance stricte avec l'état A:1s et observer l'émission des états excités par conversion de luminescence.

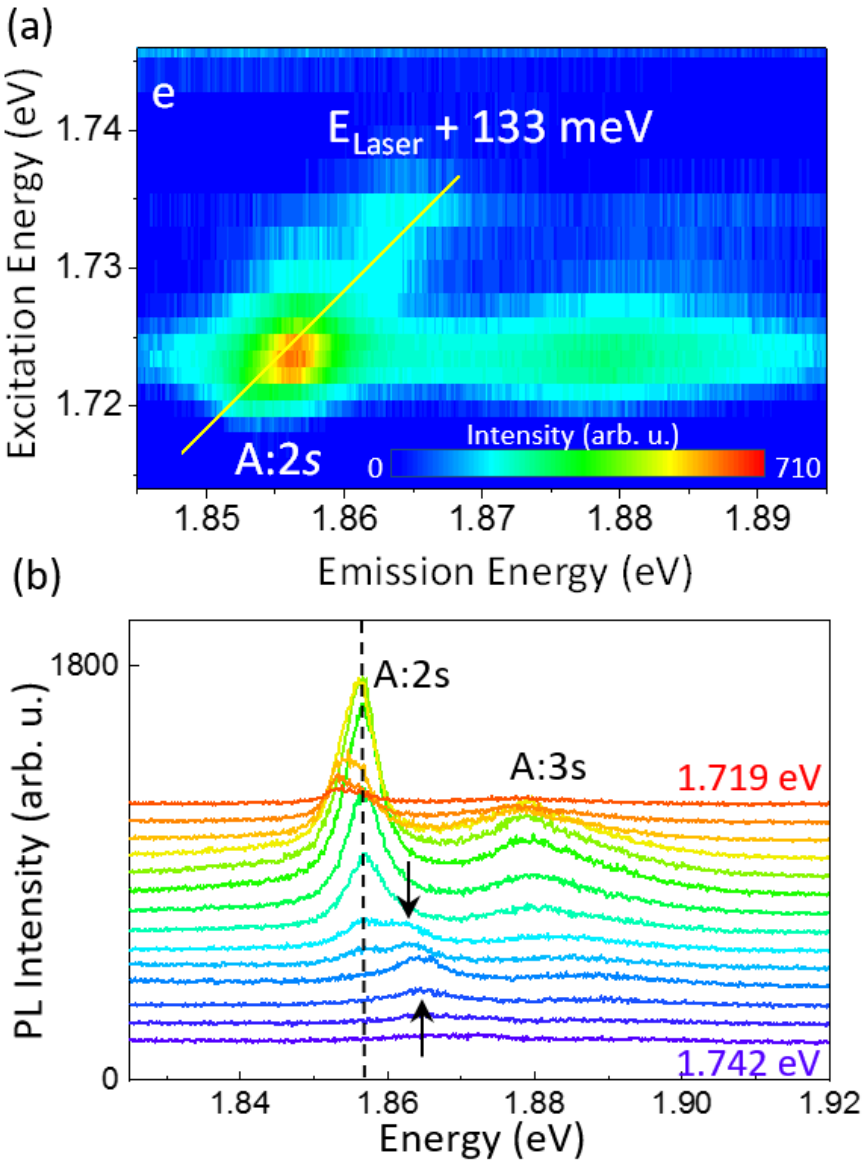

Figure 13: Les données suivantes sont obtenues à $T = 4\,\mathrm{K}$ à partir d'un mono-feuillet de WSe_2 encapsulé dans hBN (a) Représentation topographique de l'intensité de PL de l'exciton A:2s et A:3s en fonction des énergies d'émission et d'excitation du laser lors de la traversée de la résonance avec la transition de l'exciton A:1s. Comme mentionné précédemment, le signal de "conversion de luminescence" est fortement atténué lorsque le laser d'excitation n'est pas résonant avec la transition A:1s. Une réplique Raman se déplaçant comme l'énergie du laser est clairement visible. (b) Différents spectres de A:2s et A:3s ainsi que de la réplique Raman pour différentes énergies d'excitation (de 1.742 eV pour le spectre en violet à 1.719 eV pour le spectre en rouge) tandis que l'on approche de la résonance avec la transition de l'exciton A:1s, située à 1.723 eV. Ces spectres sont obtenus à partir des mêmes données que celles de la planche (a).

Dans la figure (13), nous pouvons voir en plus du double pic de A:2s et A:3s une nouvelle structure qui se translate comme l'énergie du laser d'excitation. Cette structure correspond à une émission Raman sur un mode anti-Stokes superposée au signal de conversion de luminescence de l'exciton A:2s. Tandis que la représentation topographique résume l'ensemble des données relevées, la représentation des spectres en cascade met l'accent sur la partie située à plus haute énergie que l'excitation (le laser varie ici dans un domaine d'énergies un peu supérieures à celle de la transition A:1s, et par suite les raies Raman anti-Stokes sont aussi situées à des énergies un peu supérieures à A:2s.

Nous pouvons conclure que le signal détecté est en fait la superposition d'une composante de PL d'énergie fixe provenant de l'émission des états excités de l'exciton A et d'une autre provenant du signal Raman. Ceci est discuté plus en détail dans le texte principal.

Même si nous n'avons pas prouvé complètement clairement le couplage fort entre A:1s et A:2s (nous ne voyons pas d'anti-croisement, une forme de couplage est bien présent et nous pensons que les excitons de l'état fondamental A:1s, donc de chiralité $|+1\rangle$, peuvent diffuser vers les états A:2s, ce qui a pour effet d'accroître la population d'états excités de la même vallée. C'est pourquoi l'émission qui s'ensuit est polarisée en σ^+.

Dispositifs à dopage ajustable

Afin d'étudier les excitons chargés (trions), la communauté scientifique a développé des dispositifs permettant de doper efficacement un mono-feuillet. Le principe en est simple : il suffit de déposer un contact métallique d'un côté du feuillet et, après avoir au préalable déposé un isolant de l'autre côté, déposer une autre électrode métallique qui agit comme un grille. De cette façon des charges peuvent être amenées ou ôtées du mono-feuillet en contrôlant la tension appliquée entre les deux électrodes.

Pour l'échantillon présenté en particulier dans ce chapitre, nous avons commencé à déposer un réseau d'électrodes d'or sur un substrat standard de Si/SiO_2. Un premier platelet de hBN de haute qualité [89] est alors mécaniquement exfolié et transféré au voisinage d'une électrode au moyen de PDMS. Ensuite, un mono-feuillet de WSe_2 est déposé au-dessus du platelet de hBN suivi du transfert d'un platelet de graphite de quelques monocouches atomiques. Ce dernier ne couvre pas toute la surface du mono-feuillet, afin de pouvoir l'exciter optiquement. l'autre face du platelet de graphite est par contre en contact avec l'électrode d'or. Pour finir, une couche de hBN d'encapsulation est déposée au sommet de l'hétérostructure.

Dans ce dispositif, les deux électrodes sont le substrat de Si et le réseau de fils d'or déposé sur la couche de SiO_2. Une fois que les deux électrodes sont connectées à un source-mètre (Keithley 2450) l'injection ou l'extraction des électrons du mono-feuillet devient possible (ici, l'extraction d'électrons correspond à l'injection de trous).

La conséquence du dopage est l'apparition d'excitons chargée ou trions dans le spectre optique. Avec l'échantillon que nous avons fabriqué, il nous est possible de sélectionner le régime de dopage que nous voulons explorer, ce qui nous permet d'étudier les excitons chargés positivement X^+ ou négativement X^-. Du fait de l'encapsulation dans hBN, l'augmentation de la qualité optique corréla-

tive nous permet d'accéder au détail de la structure fine des trions, qui était jusqu'à maintenant non visible du fait de la largueur trop importante des raies.

L'échantillon à charge ajustable est monté à l'intérieur d'un cryostat afin de réaliser la spectroscopie optique à 4 K. Nous discuterons d'abord des expériences de réflectivité différentielle, où nous avons mesuré les spectres en fonction de la tension de grille appliquée. L'ensemble des données est montrée en représentation topographique sur la figure (14) où l'on a reporté l'intensité de la dérivée première du contraste de réflectivité (i.e. la réflectivité différentielle) en fonction de l'énergie des photons.

Sur la figure (14), nous pouvons identifier les caractéristiques spectroscopiques principales, c'est-à-dire les transitions qui présentent une grande force d'oscillateur pour les transitions optiques [49]. Globalement, la transition la plus intense correspond à l'exciton neutre, noté X^0. Dans le même domaine de tension appliquée apparaît une seconde transition située à environ 130 meV au-dessus de l'exciton neutre. Celle-ci est identifiée comme le premier état excité de l'exciton (A:2s). L'intensité du signal correspondant à ces deux transitions décroît rapidement dès que l'on quitte la région de neutralité de l'échantillon.

A plus forte tension appliquée, i.e. lorsque nous extrayons des électrons de WSe_2, la force d'oscillateur de l'exciton devient évanescente et un nouveau pic apparaît, situé 21 meV en dessous de l'énergie de l'exciton. Ce pic est identifié comme le trion positif, et est noté X^+. Inversement lorsque la tension appliquée est abaissée en dessous de la région de neutralité, nous atteignons le régime de dopage de type n. (Le niveau de Fermi rejoint alors la bande de conduction. Comme précédemment, la force d'oscillateur de l'exciton devient évanescente, mais cette fois c'est un doublet qui apparaît à environ 30 meV en dessous de X^0. Ce doublet est attribué aux états optiquement actifs du trion négatif X^-, le clivage de 6 meV étant attribué à l'échange coulombien à courte portée. La structure fine de X^- n'aurait pas été visible dans un échantillon non encapsulé.

Remarquons que les deux pics observés sont situées plus précisément à 29 meV et 35 meV en dessous de X^0, énergies distinctes de celle des phonons optiques qui vaut 32 meV [134]. De plus, les comportements différents des forces d'oscillateur de X^0 et de X^- en fonction de la tension appliquée montre clairement que ce doublet n'est pas une réplique phonon de X^0. Après avoir identifié toutes ces transitions, il est maintenant possible d'entreprendre l'interprétation des spectres d'émission présentés sur la figure (15).

Dans le régime neutre, nous observons une émission très semblable à celle des échantillons de WSe_2 encapsulés dans hBN mais montés sans grille. Comme décrit dans le chapitre 3, nous observons trois transitions principales. Celle située à plus haute énergie et de largueur 4 meV correspond à X^0. Le pic situé 40 meV en dessous a été identifié à l'exciton sombre. La transition la plus intense entre les deux est attribuée jusqu'à présent par la communauté comme due au trion.

Lorsque nous injectons des électrons dans WSe_2, les signaux de PL à la fois de l'exciton brillant et de l'exciton sombre disparaissent simultanément. Le pic intermédiaire est maintenant remplacé par un doublet de plus faible intensité. La séparation des deux pics et leur distance à X^0 correspond parfaitement à celle mesurée dans les expériences de réflectivité précédemment décrites. Nous en déduisons donc que ce doublet correspond au signal de photoluminescence du trion négatif X^-.

Ces données de obtenues en PL en régime dopé soulèvent une question sur

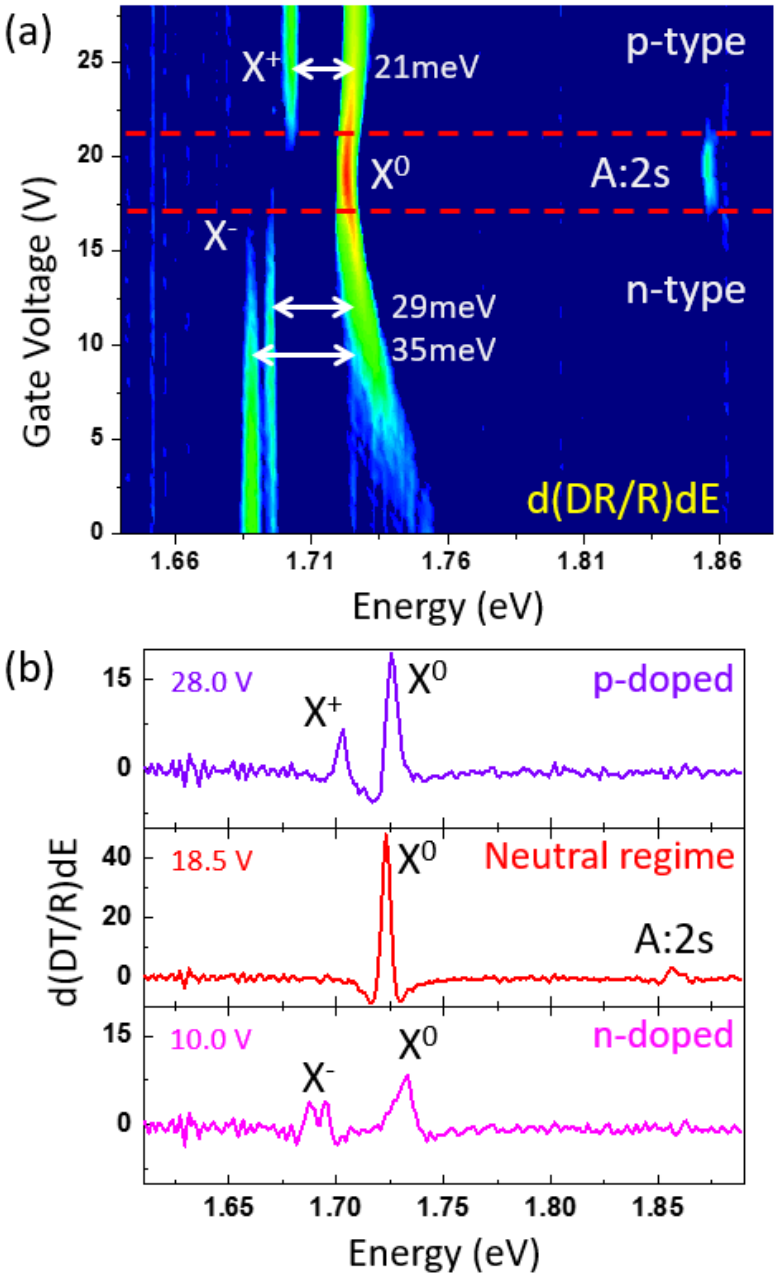

Figure 14: Représentation topographique de la dérivée première des spectres de contraste de réflectivité en fonction de l'énergie en fonction de la tension appliquée à la grille du dispositif. Les trois régimes de dopage, type p, neutre et type n sont clairement visibles. L'intensité est codée en fausses couleurs en échelle logarithmique, de sorte que le bleu nuit correspond à moins de 0.5 tandis que le rouge à plus de 50. (b) Spectres correspondant à trois régimes de dopage extraits de la représentation topographique de la planche (a).

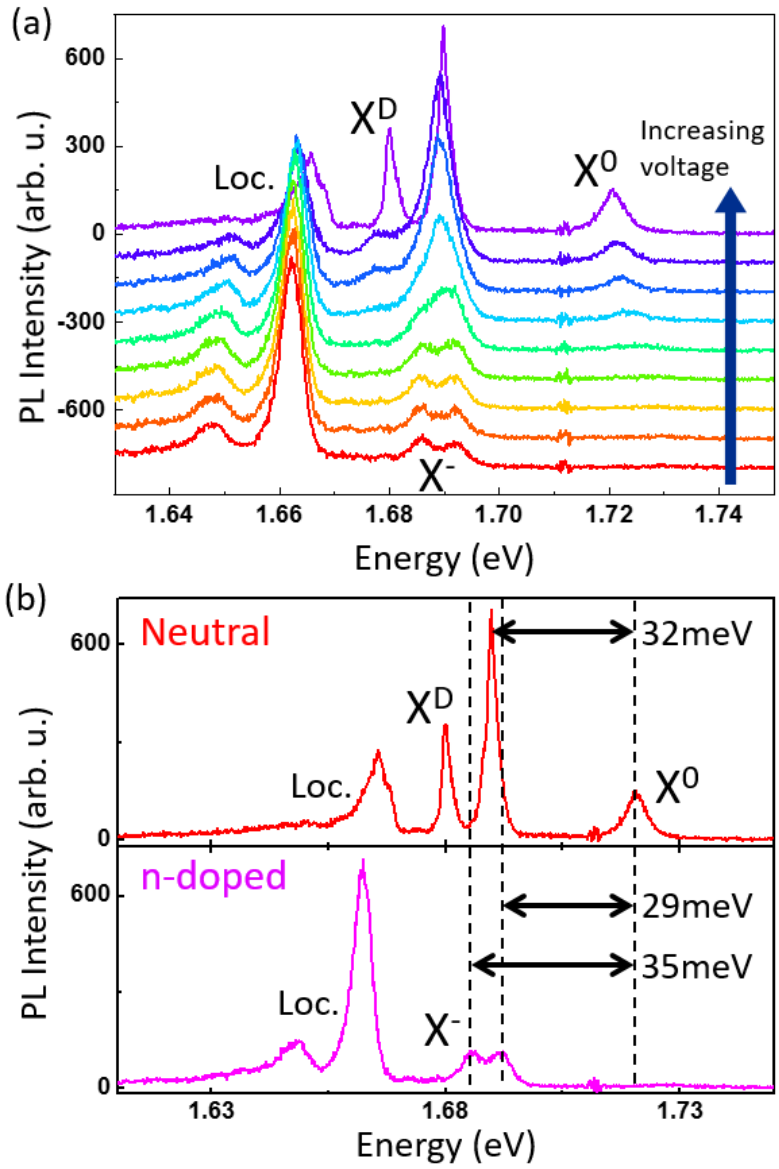

Figure 15: (a) Représentation en cascade des spectres de PL de notre dispositive à charge adjustable (cf. fig. 14) lorsque l'on fait varier la tension de grille. Le monofuillet de WSe_2 est maintenu à $T = 4\,K$ est excité par un laser hélium-néon (1.96 eV). (b) Deus spectres extraits de la planche (a). En rouge, spectre d'émission de PL dans le régime neutre, très similaire à ceux obtenus à partir d'échantillons simples encapsulés. En revanche, le spectre en magenta est obtenu en régime dopé. La structure fine du trion négatif est clairement visible.

la nature du pic intense observé en PL obtenues en régime de neutralité. Le pic observé à 32 meV au-dessous de l'exciton ne peut correspondre au trion X^+ observé en réflectivité en régime de dopage p. De même le trion X^- observé en régime de dopage n, du fait de sa structure en doublet, ne peut correspondre

à ce pic. Si nous observons de plus près la planche (a) de la figure (15), nous observons en fait que son intensité décroît comme celle de X^0 lorsque l'on quitte la région de neutralité de l'échantillon, les deux raies disparaissant à la même tension appliquée. Cette constatation ajoutée au fait que l'énergie d'un phonon LO dans WSe_2 est précisément de 32 meV milite en faveur de l'interprétation de cette raie comme étant due à une émission d'exciton direct assistée par l'émission d'un phonon LO, un processus du second ordre où l'état virtuel intermédiaire serait un état d'exciton lié à un électron localisé (i.e. un trion localisé) situé à une énergie quasi-résonante avec l'énergie de l'exciton libre moins un phonon LO. Un scénario alternatif attribuerait ce pic à la recombinaison radiative d'un exciton indirect assistée par émission d'un phonon LO [234].

Nous abordons maintenant l'interprétation de la structure fine du trion X^-. La présence de d'un doublet peut être comprise si nous considérons le fait que deux types d'états de trions brillants existent et prédominent dans notre expérience: l'un où les deux électrons sont la même vallée (intra-valley trion), et l'autre où les deux électrons sont dans deux vallées différentes (inter-valley trion). L'énergie de ces deux configurations diffère du fait de l'interaction d'échange coulombienne à courte portée entre les particules constitutives du trion [218]. Cette interaction est aussi responsable de la séparation en énergie entre X^+ et le doublet de X^- comme le montre l'analyse théorique effectuée par nos collaborateurs de l'Institut Ioffe. Le modèle développé par M. Semina et M. Glazov explique aussi nos principaux résultats expérimentaux et permet d'identifier les configurations de trions pertinentes pour l'interprétation de nos spectres de réflectivité et d'émission.

Conclusions et perspectives

Dans le chapitre final, nous résumons les résultats principaux obtenus le long de ce manuscrit de thèse de doctorat, et introduisons quelques idées pour des expériences futures que nous aimerions réaliser et qui ont commencé à stimuler l'intérêt de la communauté scientifique. Nous proposons d'une part sur le plan des techniques, de perfectionner encore les techniques de transfert, afin d'améliorer la qualité des spectres et d'affiner leur interprétation. D'autre part, nous proposons d'ouvrir le champ d'investigation aux hétéro-structures de van der Waals: hétéro-bicouches (comment $WSe_2/MoSe_2$), ou structures hybrides composés d'un matériau magnétique ($CrBr_3$ ou CrI_3) et d'un mono-feuillet de TMD afin par exemple de tester des effets de proximité.